THE UNIVERSITY OF QUEENSLAND

AUSTRALIA

Adsorption analysis of carbon dioxide, hydrocarbons and moisture on carbon

Ali Shahtalebi

M.Sc. (University of Tehran)

A thesis submitted for the degree of Doctor of Philosophy at

The University of Queensland in 2016

School of Chemical Engineering

Abstract

This thesis presents a fundamental investigation on the role of the structure of microporous silicon carbide-derived carbon (SiCDC) and its functionalisation in the adsorption equilibria and transport of gases. The SiCDCs with different particle size distributions were synthesized in our laboratory and characterized using a combination of techniques including scanning electron microscopy (SEM), high resolution transmission electron microscopy (HRTEM), X-ray diffraction (XRD), helium pycnometry, thermogravimetric analyses (TGA), nuclear magnetic resonance (NMR), X-ray photoelectron spectroscopy (XPS), Fourier transform infrared (FTIR), Raman spectroscopy, and gas adsorption.

Based on the characterisation results, a bidisperse pore structure model is proposed for the synthesized SiCDC to explain the kinetics. In the mathematical modelling of adsorption kinetics, the internal structure of SiCDC is assumed to have ultra-microporous grains with larger particle scale micropores forming the intergrain pathways. It is shown that CH_4 adsorption kinetics is governed by two distinct diffusional resistances, arising from slow grain scale diffusion in ultra-micropores and faster particle scale diffusion in large micropores. For CO_2, it is found that the adsorption kinetics is strongly influenced by a barrier resistance at the grain surface where entry into the ultra-microporosity occurs. The uptake of CO_2 in the bidisperse pore structure of CDCs occurs through rapid diffusion in the large particle-scale micropores, in which a Henry law isotherm holds, and a combination of barrier resistance at the grain surface and diffusional resistance in the grain interior with a Langmuirian isotherm. It is shown that the grain scale activation energies are comparable with values for carbon molecular sieves, and consistent with values expected for the size range of the ultra-micropores, while the activation energies for transport in the larger particle scale micropores are comparable to those for conventional activated carbons.

The experimental uptake-based data are compared with self-diffusivities obtained through equilibrium molecular dynamics (EMD) simulations using a realistic model of SiCDC developed by the hybrid reverse Monte Carlo (HRMC) method. It is observed that MD-based CO_2 diffusivities are as much as two orders of magnitude larger than the CO_2 particle scale diffusion coefficients, however such discrepancy is not found for CH_4. The quasi elastic neutron scattering (QENS) measurements for CH_4 suggests a smaller activation energy barrier compared to the results obtained from MD simulations and experimental kinetic uptake. The difference between the activation energies obtained from the experimental uptake

measurements and MD simulations suggests that there are some internal barriers and structural constrictions which are not captured by QENS measurement and MD simulation.

This thesis also presents an investigation on the effect of fluorine doping of microporous CDC on its structural as well as hydrophobic/hydrophilic character. The morphology and structure of samples fluorinated to three different F/C ratios are characterized by several analysis techniques and gas adsorption. It is shown that stronger C-F bonds are formed at high levels of fluorination and increasing fluorination level leads to a decrease of specific surface area and total pore volume. It is demonstrated that fluorination has little effect on the ultra-microporosity at low levels of fluorination, but leads to significant decrease at high levels of fluorination. The comparison of the CO_2 uptake-time curves for the fluorinated and non-fluorinated samples shows slightly slower uptake with increasing fluorination level, largely due to decrease in pore volume and surface area. By the application of different semi-empirical models to the experimental water adsorption isotherms of fluorinated and non-fluorinated CDCs, the effects of fluorine-doping on the adsorption mechanism is also analysed. The comparison of different model parameters with characterization results of the samples is used as the methodology to understand the water adsorption mechanism in virgin and fluorinated CDCs. It is demonstrated that with increasing the level of fluorination the hydrophobic character of the low and medium fluorinated CDCs remains almost constant while high level of fluorination decreases the hydrophobicity. It is shown that fluorine doping causes blockage of the carbon pores for the nonpolar argon molecules while allowing polar H_2O molecules to grow into clusters and migrate into the internal volume of the micropores.

The findings of this thesis should aid better understanding of the gas adsorption and diffusion mechanism in microporous CDCs.

Declaration by author

This thesis is composed of my original work, and contains no material previously published or written by another person except where due reference has been made in the text. I have clearly stated the contribution by others to jointly-authored works that I have included in my thesis.

I have clearly stated the contribution of others to my thesis as a whole, including statistical assistance, survey design, data analysis, significant technical procedures, professional editorial advice, and any other original research work used or reported in my thesis. The content of my thesis is the result of work I have carried out since the commencement of my research higher degree candidature and does not include a substantial part of work that has been submitted to qualify for the award of any other degree or diploma in any university or other tertiary institution. I have clearly stated which parts of my thesis, if any, have been submitted to qualify for another award.

I acknowledge that an electronic copy of my thesis must be lodged with the University Library and, subject to the policy and procedures of The University of Queensland, the thesis be made available for research and study in accordance with the Copyright Act 1968 unless a period of embargo has been approved by the Dean of the Graduate School.

I acknowledge that copyright of all material contained in my thesis resides with the copyright holder(s) of that material. Where appropriate I have obtained copyright permission from the copyright holder to reproduce material in this thesis.

Publications during candidature

Journal papers

1- Ali Shahtalebi, Maimonatou Mar, Katia Guérin, Suresh K. Bhatia, ″Effect of fluorine doping on structure and CO_2 adsorption in silicon carbide-derived carbon″, *Carbon*, Vol. 96, pp. 565-577 (2016).

2- Ali Shahtalebi, Pradeep Shukla, Amir H. Farmahini, Suresh K. Bhatia, ″Barriers to diffusion of CO_2 in microporous carbon derived from silicon carbide″, *Carbon*, Vol. 88, pp. 1-15 (2015).

3- Ali Shahtalebi, Amir H. Farmahini, Pradeep Shukla, Suresh K. Bhatia, ″Slow diffusion of methane in ultramicropores of silicon carbide-derived carbon″, *Carbon*, Vol. 77, pp. 560-576 (2014).

4- Ali Shahtalebi, Maimonatou Mar, Katia Guérin, Suresh K. Bhatia, ″Fluorination Induced Changes in Hydrophobicity of Silicon Carbide Derived Nanoporous Carbon″, *J. Phys. Chem. C*, submitted (2016).

5- Amir H. Farmahini, Ali Shahtalebi, Herve Jobic, Suresh K. Bhatia, ″Influence of Structural Heterogeneity on Diffusion of CH_4 and CO_2 in Silicon Carbide-Derived Nanoporous Carbon″, *J. Phys. Chem. C*, Vol. 118, pp. 11784-11798 (2014).

Conferences

1- Ali Shahtalebi, Maimonatou Mar, Katia Guérin, Suresh K. Bhatia, ″CO_2 adsorption on fluorinated SiC-derived carbon″. *9^{th} International Mesostructured Material Symposium (IMMS-9)*, Brisbane Convention & Exhibition Centre, Brisbane, Australia (August 2015).

2- Suresh K. Bhatia, Amir H. Farmahini, Ali Shahtalebi, ″Effect of ultra-microporosity on equilibrium and transport of gases in carbons as revealed by simulation and experiment″. *Characterization of Porous Materials (CPM-7)*, Delray Beach, Florida, USA (May 2015).

3- Amir H. Farmahini, Ali Shahtalebi, Herve Jobic, Suresh K. Bhatia, ″Influence of structural heterogeneity on the transport of gases in microporous silicon carbide-derived carbon″. *OZ Carbon 2014 as part of RACI National Congress*, Adelaide, Australia (December 2014).

4- Ali Shahtalebi, Amir H. Farmahini, Pradeep Shukla, Suresh K. Bhatia, ″Diffusion of Methane in Silicon Carbide Derived Carbon: Experiment and Simulation″ *Carbon2014 Conference*, Jeju Island, South Korea (June-July 2014).

5- Amir H. Farmahini, Ali Shahtalebi, Suresh K. Bhatia ″Computational and experimental characterization of microporous silicon-carbide derived carbon″ *10th International Symposium on the Characterization of Porous Solids (COPS-X)*, Granada, Spain (May 2014).

Publications included in this thesis

Ali Shahtalebi, Amir H. Farmahini, Pradeep Shukla, Suresh K. Bhatia, ″Slow diffusion of methane in ultramicropores of silicon carbide-derived carbon″, *Carbon*, Vol. 77, pp. 560-576 (2014) – Incorporated as Chapter 3.

Contributor	Statement of contribution
Ali Shahtalebi (Candidate)	Conducted experiments (90%) Analysis and interpretation of data (80%) Wrote the paper (100%) Edited the paper (50%)
Amir H. Farmahini	Performed EMD simulations (100%)
Pradeep Shukla	Conducted experiments (10%) Analysis and interpretation of data (20%)
Suresh K. Bhatia	Edited the paper (50%)

Ali Shahtalebi, Pradeep Shukla, Amir H. Farmahini, Suresh K. Bhatia, ″Barriers to diffusion of CO2 in microporous carbon derived from silicon carbide″, *Carbon*, Vol. 88, pp. 1-15 (2015) – Incorporated as Chapter 4.

Contributor	Statement of contribution
Ali Shahtalebi (Candidate)	Conducted experiments (100%) Analysis and interpretation of data (90%) Wrote the paper (100%) Edited the paper (60%)
Pradeep Shukla	Analysis and interpretation of data (10%)
Amir H. Farmahini	Performed EMD simulations (100%)
Suresh K. Bhatia	Edited the paper (40%)

Ali Shahtalebi, Maimonatou Mar, Katia Guérin, Suresh K. Bhatia, ″Effect of fluorine doping on structure and CO_2 adsorption in silicon carbide-derived carbon″, *Carbon*, Vol. 96, pp. 565-577 (2016) – Incorporated as Chapter 5.

Contributor	Statement of contribution
Ali Shahtalebi (Candidate)	Conducted experiments (90%) Analysis and interpretation of data (90%) Wrote the paper (100%) Edited the paper (70%)
Maimonatou Mar	Conducted experiments (10%)
Katia Guérin	Analysis and interpretation of data (10%)
Suresh K. Bhatia	Edited the paper (30%)

Contributions by others to the thesis

- Fluorine-doped samples were prepared in the laboratory at Institut de Chimie de Clermont-Ferrand, Université Blaise Pascal, France.
- The Centre for Microscopy and Microanalysis (CMM) at the University of Queensland is acknowledged for providing facilities, and the scientific and technical assistance with TEM, SEM, XRD, and XPS analysis. XPS measurements were carried out by Dr. Barry Wood at the Centre for Microscopy and Microanalysis. The author acknowledges Dr. Xuechao Gao and Mr. Alireza Hosseinmardi for the helpful discussions and assistance with TEM, SEM and XPS analysis.

Statement of parts of the thesis submitted to qualify for the award of another degree

None

Acknowledgments

I would like to express my sincere respect and appreciation to Prof. Suresh Bhatia for his invaluable guidance, continuous encouragement, and strong support throughout my Ph.D. study. It was a great pleasure and honor to work under his supervision.

I would like to thank my co-supervisor Prof. Victor Rudolph and milestone committee members Dr. Greg Birkett and Prof. Joe Diniz da Costa for their guidance and helpful recommendations.

I sincerely thank Dr. Pradeep Shukla for spending a lot of time with me on laboratory experiments and modelling works. His extensive discussions around my research have been very helpful. I want to thank him for all his generous help, valuable discussions, and friendship.

I am grateful to all my colleagues, the members in Prof. Suresh Bhatia's group and those research fellows in School of Chemical Engineering who helped me during this Ph.D. study in particular Dr. Jun-Seok Bae, Dr. Xuechao Gao, Dr. Mauricio Rincon Bonilla, Dr. Hui An, Dr. Julius Motuzas, Dr. Marc Hampton, Dr. Sandeep Sarathy, Mr. Alireza Hosseinmardi, and Mr. Lang Liu for their helpful discussions and assistance with my research works.

Thanks should also go to the School of Chemical Engineering for the UQ International (UQI) scholarships and the Centre for Microscopy and Microanalysis at the University of Queensland for the facilities, and the scientific and technical assistance. I wish also to thank Dr. Barry Wood for the XPS measurements carried out at the Centre for Microscopy and Microanalysis.

Finally, I would like to dedicate this thesis to my parents and my sister, Roza for their endless love, support and encouragement throughout my life.

Keywords

carbide-derived carbon, microporous materials, characterisation, adsorption kinetics, ultra-microporosity, fluorination, simulation, density functional theory.

Australian and New Zealand Standard Research Classifications (ANZSRC)

ANZSRC code: 090499, Chemical Engineering not elsewhere classified, 40%

ANZSRC code: 090403, Chemical Engineering Design, 40%

ANZSRC code: 090401, Carbon Capture Engineering (excl. Sequestration), 20%

Fields of Research (FoR) Classification

FoR code: 0904, Chemical Engineering, 100%

تقدیم به پدر، مادر و خواهرم رُزا

This thesis is dedicated to my parents and
my sister, Roza

Table of Contents

List of Figures

List of Tables

List of Abbreviations

AC	Adsorption Chamber
AC	Activated Carbon
ACF	Activated Carbon Fibre
BET	Brunauer-Emmett-Teller
CDC	Carbide-Derived Carbon
CMS	Carbon Molecular Sieve
CNT	Carbon Nanotube
DFT	Density Functional Theory
DFT-FWT	Density Functional Theory – Finite Wall Thickness
DFT-IWT	Density Functional Theory – Infinite Wall Thickness
DR	Dubinin–Radushkevich
DS	Dubinin-Serpinsky
DS	Dubinin–Stoeckli
EMD	Equilibrium Molecular Dynamics
EOS	Equation of State
FTIR	Fourier transform infrared spectroscopy
GCMC	Grand Canonical Monte Carlo
GHG	Greenhouse Gas
GP	Grand thermodynamic Potential
GSE	Gibbsian Surface Excess
HIAST	Heterogeneous Ideal Adsorbed Solution Theory
HPVA	High-Pressure Volumetric Analyser
HRMC	Hybrid Reverse Monte Carlo
HRTEM	High Resolution Transmission Electron Microscopy
IAST	Ideal Adsorbed Solution Theory
IUPAC	International Union of Pure and Analytical Chemistry
LAMMPS	Large-scale Atomic/Molecular Massively Parallel Simulator
LJ	Lennard-Jones
MD	Molecular Dynamics
MOF	Metal Organic Frameworks
MPSD	Micropore Size Distribution
MPTA	Multicomponent Potential Theory of Adsorption
MSA	Micropore Surface Area
MSD	Mean-Squared Displacement
NLDFT	None Local Density Functional Theory
ODE	Ordinary Differential Equation
PFG-NMR	Pulse Field Gradient-Nuclear Magnetic Resonance
PM	Permanent Magnet
PPM	Parallel-Path Model
PSD	Pore Size Distribution
PWTD	Pore Wall Thickness Distribution
QENS	Quasi-Elastic Neutron Scattering
RAST	Real Adsorbed Solution Theory
SAED	Selected-Area Electron Diffraction
SANS	Small Angle Neutron Scattering
SEM	Scanning Electron Microscopy
SiC-DC	Silicon Carbide-Derived Carbon
SSA	Specific Surface Area
TEM	Transmission Electron Microscopy

TGA	Thermogravimetric Analyses
TST	Transition State Theory
VST	Vacancy Solution Theory
XPS	X-ray Photoelectron Spectroscopy
XRD	X-ray Diffraction
ZLC	Zero Length Column

Chapter 1 : Introduction

1.1 Background

The fundamental understanding of adsorption (equilibrium and kinetics) of gases in microporous materials is of great practical importance in gas separation and storage technologies. Adsorbents used in gas adsorption processes have a specific pore structure and an appropriate range of pore size distribution (PSD) in which different gas molecules can diffuse at different rates leading to the separation of each component. Within the last two decades, there has been an explosive growth in materials science which has introduced a wealth of new materials such as metal organic frameworks (MOFs) [1], and nanostructured carbonaceous materials which can provide us desired adsorbents for gas adsorption processes [2]. For the optimal design and operation of an adsorption process, a detailed investigation combining experimental characterization and adsorption studies is necessary to obtain a comprehensive understanding of the impact of pore structure and the PSD of the adsorbent on adsorption behaviour. Such fundamental understanding of the pore structure of the adsorbents, along with investigation of the adsorption equilibria and the transport of gases in their internal structure is very important for synthesizing advanced porous adsorbents for specific applications.

Recently nanoporous carbide-derived carbons (CDCs) have emerged as very promising carbonaceous porous materials for gas mixture separation and energy storage because of their unique characteristics such as tuneability of their pore structure, high surface area and pore volume [3, 4]. Carbide Derived Carbons (CDCs) represent a large family of porous carbon structures ranging from amorphous carbon to highly ordered structures, which are attracting attention in CH_4 and H_2 storage, or gas mixture separation such as CO_2 capture [5, 6]. The gas separation and storage is only one of many examples of applications of CDCs which is currently extensively studied. Due to the variety of CDC structures [3], there are numerous potential applications such as catalyst supports for fuel cells, supercapacitor electrodes, electrodes for Li-air and Li-ion batteries, and tribological applications [3].

Although extensive effort has been devoted to the adsorption equilibria and the dynamics of gases in porous adsorbents in the literature [7, 8] and it has been a topic of considerable importance and significance in the field of gas adsorption, however our knowledge in adsorption equilibria and kinetics on CDC materials is very limited.

1.2 Objectives

The aim of this thesis is to investigate the role of microporous structure of carbide derived carbons (CDCs) on adsorption equilibria and kinetics.

The detailed objectives of this thesis are to:

- Synthesize microporous SiCDCs using halogenation method;
- Explore the effects of synthesis conditions and SiC precursor on the characterization of the synthesized samples;
- Characterize synthesized SiCDCs by different analysis techniques;
- Measure the adsorption equilibrium and kinetics of CO_2 and hydrocarbons on the synthesized SiCDCs;
- Functionalising the microporous SiCDCs using fluorination;
- Investigate the characterization of the fluorine doped SiCDCs with the aim of assessing its suitability for CO_2 capture;
- Examine the hydrophilic/hydrophobic characteristics of fluorine-doped SiCDCs and gain more insights into the effects of level of fluorination on the water adsorption properties;

1.3 Outline of the thesis

The thesis consists of seven chapters

Chapter 1 provides brief background information and the aim and objectives of thesis.

Chapter 2 carries out a review in the research areas related to this thesis, which include: (i) the structure of the carbide-derived carbons (CDCs) with their characteristics in the existing literature, (ii) experimental techniques (volumetric and gravimetric) for the measurement of the adsorption isotherms with the adsorption isotherm models presented in literature for the porous adsorbents, (iii) the adsorption kinetics and transport in porous adsorbents and the methods for the diffusivity measurement, (iv) water adsorption in carbon materials, and (v) functionalisation and surface modification of carbon materials.

Chapter 3 presents methane uptake kinetics in SiCDC using an experimental volumetric method. In this chapter it will be shown that SiCDC has a bidisperse micropore distribution, with the microporosity comprising significant ultra-micropores. Based on the models

reviewed for activated carbon (AC) and other bidisperse structure porous adsorbents in chapter 2, the internal structure of SiCDC is assumed to have ultra-microporous topologically connected networks in small independent domains called grains with larger micropores forming the inter-grain spaces. It will be demonstrated that the kinetics of CH_4 adsorption is governed by two distinct diffusional resistances, arising from slow diffusion in the grain ultra-micropores and faster diffusion in the larger particle scale micropores forming the intergrain pathways. The low-density macroscopic uptake kinetics data will be compared with self-diffusivities obtained from microscopic molecular dynamics (MD) simulations and quasi-elastic neutron scattering (QENS) measurements. The characterization results obtained from structural analysis of SiCDC, and the predictions of the experimental adsorption isotherm using the finite wall thickness model (FWT-NLDFT) approach [9], with the adsorption dynamics studies will be used to gain more understanding of the microstructure of the CDC.

Chapter 4 illustrates the presence of significant surface barrier resistance for the diffusion of CO_2 in the synthesized SiCDCs. The diffusion of CO_2 in the disordered microporous SiCDC at various temperatures and loading, using the volumetric technique is investigated. Experimental adsorption uptake kinetics and equilibrium data for CO_2 are obtained and the dependence of the uptake kinetics on loading and temperature is investigated using the bipore model incorporating a grain surface barrier resistance. In addition, isotherm predictions obtained by grand canonical Monte Carlo (GCMC) simulation, and CO_2 self-diffusivities obtained from molecular dynamics simulation, using the atomistic model of disordered microporous SiCDC are compared with those from the experimental low pressure CO_2 data.

Chapter 5 presents a combination of characterization and experimental adsorption studies on fluorine-doped CDCs. The adsorption properties, microstructure of fluorine doped CDCs and the nature and the strength of the C-F bonds of the fluorinated CDCs is investigated. Virgin and fluorinated SiCDCs have been characterized by a variety of microscopic techniques as well as gas adsorption, to gain understanding of their structure and adsorption properties. It is shown that after the fluorination of the SiCDCs, the bimodal micropore size distribution of the sample is preserved. Experimental adsorption uptake kinetics data for CO_2 on virgin and fluorinated samples are interpreted using the bipore model incorporating the grain surface barrier resistance presented in chapter 4. It is shown for the diffusion of CO_2 in both the virgin and fluorinated samples, surface barrier resistance is present which indicates the

presence of structural constrictions and large entry barriers near the grain surface of fluorinated samples.

Chapter 6 presents an investigation on the effect of fluorine doping on experimental water vapor adsorption and hydrophobicity/hydrophilicity of microporous silicon carbide-derived carbon (SiCDC). Water adsorption isotherms are volumetrically measured on fluorinated and non-fluorinated SiCDC samples. By the application of different semi-empirical isotherm models to the experimental water adsorption isotherms of fluorinated and virgin samples, the adsorption mechanism is evaluated. The fluorinated and non-fluorinated samples are characterized using XPS and NMR analysis techniques. The comparison of the characterization results of the samples with model parameters is used as the methodology to understand the water adsorption mechanism in virgin and fluorinated SiCDCs.

Chapter 7 summarizes the important findings and conclusions from the present study of adsorption equilibrium and kinetics on carbide-dervied carbons. Some recommendations for future studies and further research are also presented in chapter 7.

1.4 References

[1] Sumida K, Rogow DL, Mason JA, McDonald TM, Bloch ED, Herm ZR, et al. Carbon dioxide capture in metal–organic frameworks. Chem Rev (Washington, DC, U S). 2011;112(2):724-81.

[2] Webley PA. Adsorption technology for CO2 separation and capture: a perspective. Adsorption. 2014;20(2-3):225-31.

[3] Presser V, Heon M, Gogotsi Y. Carbide-Derived Carbons–From Porous Networks to Nanotubes and Graphene. Adv Funct Mater. 2011;21(5):810-33.

[4] Gogotsi Y, Nikitin A, Ye H, Zhou W, Fischer JE, Yi B, et al. Nanoporous carbide-derived carbon with tunable pore size. Nat Mater. 2003;2(9):591-4.

[5] Presser V, McDonough J, Yeon S-H, Gogotsi Y. Effect of pore size on carbon dioxide sorption by carbide derived carbon. Energy & Environmental Science. 2011;4(8):3059-66.

[6] Lozano-Castello D, Cazorla-Amoros D, Linares-Solano A, Oshida K, Miyazaki T, Kim Y, et al. Comparative characterization study of microporous carbons by HRTEM image analysis and gas adsorption. The Journal of Physical Chemistry B. 2005;109(31):15032-6.

[7] Do DD. Adsorption analysis: equilibria and kinetics: Imperial College Press; 1998.

[8] Kärger J, Ruthven DM, Theodorou DN. Diffusion in nanoporous materials: John Wiley & Sons; 2012.

[9] Nguyen TX, Bhatia SK. Probing the pore wall structure of nanoporous carbons using adsorption. Langmuir. 2004;20(9):3532-5.

Chapter 2 : Literature review

This chapter covers five main areas related to the objectives of this thesis. These areas are: (1) the structure of the carbide-derived carbons (CDCs) with their characteristics, (2) experimental techniques for the measurement of the adsorption isotherms with the adsorption isotherm models presented in literature for the porous adsorbents, (3) adsorption kinetics and transport in porous adsorbents and the methods for the diffusivity measurement, (4) water adsorption in carbon, and (5) functionalisation and surface modification of carbon materials.

2.1 Carbide-derived carbons (CDCs)

Carbide-derived carbons (CDCs) [1], are attracting increasing attention as a very promising carbonaceous microporous material for different applications such as gas separation and storage [2-7], and electrochemical energy storage [1], owing to their unique characteristics such as tunable pore structure, high surface area [8, 9] and their ease of synthesis from natural carbides [1, 10, 11]. The pore structure of CDCs can be relatively well controlled by selecting the appropriate precursor, synthesis and post treatment conditions [3, 9, 11-13]. The synthesis techniques have allowed the pore size of CDCs to be engineered and tailored to suit a wide range of applications [1]. Among different techniques for synthesizing CDCs, physical (thermal decomposition) or chemical processes (halogenation) are more attractive methods in which the selective extraction of the metal changes the carbide structure into pure carbon [1, 14]. Halogenation (most commonly, chlorination) is one of the most economic and scalable techniques for the CDC synthesis [14]. The following reaction (equation (2-1)) shows the carbon formation by selective carbide etching using chlorination method [1]

$$\mathrm{SiC(s)} + 2\mathrm{Cl_2(g)} \rightarrow \mathrm{SiCl_4(g)} + C(s) \qquad (2\text{-}1)$$

Since the structure of carbon is templated by the SiC structure in this method, atomic level control can be achieved, and the silicon extraction is layer by layer [8]. In this synthesis process a high level of control over the resulting amorphous porous carbon pore structure is possible by changing the synthesis conditions and post treatment conditions [14]. In most cases for the CDC experimental synthesis, the carbide powder is loaded into the hot zone of a tube furnace of the experimental set-up, and chlorination begins after the sample is purged with an inert gas to reach the desired temperature. After the completion of the chlorination process, the samples are cooled down under a flow of an inert gas (such as argon) to remove

the residual metal chlorides [14, 15]. In Figure 2-1 a schematic experimental set-up for the chlorination of carbide is illustrated, in which chlorination can be carried out over a broad temperature range depending on the carbide precursor.

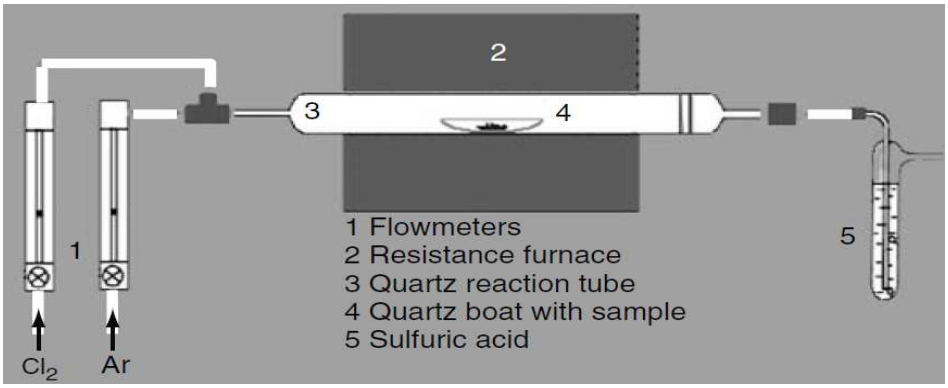

Figure 2-1. Schematic diagram of experimental set-up for CDC synthesis [14].

A variety of carbon structures can be obtained depending on experimental conditions, such as amorphous and nano-crystalline graphitic carbon, carbon onions, nanotubes, fullerene-like structures, nanocrystalline diamond, and ordered graphite have been reported [16-20]. CDCs from different carbide precursors have been investigated by different research groups using a combination of characterization techniques to understand the microstructural changes occurring during their preparation and post- synthesis treatment [3, 11, 12, 15]. Specific BET surface areas of up to 3000 m^2g^{-1} [21] with small pore sizes have been reported [2, 3, 8, 11, 12, 15, 18, 22, 23]. Gogotsi and co-workers [8] have shown the porosity of the CDCs can be tuned with sub-angstrom accuracy in a wide range by controlling the halogenation temperature [8].

2.2 Characterization of carbons

Reliable characterization of the structure of the porous material is a key factor in the synthesis of samples with desired adsorptive properties. Bhatia and co-workers [11, 12] have used a combination of experimental techniques including X-ray diffraction (XRD), Transmission Electron Microscopy (TEM), Helium Pycnometry as well as gas adsorption to characterize the porous CDCs and study of the effect of operating conditions such as chlorination temperature, post heat treatment and carbide precursor on the microstructure of CDCs [11, 12]. In this section some of the techniques for the characterization of CDCs are reviewed.

2.2.1 X-ray diffraction (XRD)

The XRD technique in which an X-ray diffractometer is used to record the X-ray intensities scattered from the examined samples provide information about the degree of crystallization degree of the samples. Figure 2-2 shows a typical example of x-ray diffraction pattern of CDCs obtained from titanium silicon carbide at different temperatures [15]. The higher sharp and narrower 002 peaks in the XRD patterns are indicative of better stack of graphene layers and ordering processes in amorphous carbon while wider 002 peaks indicate disordered carbons [15].

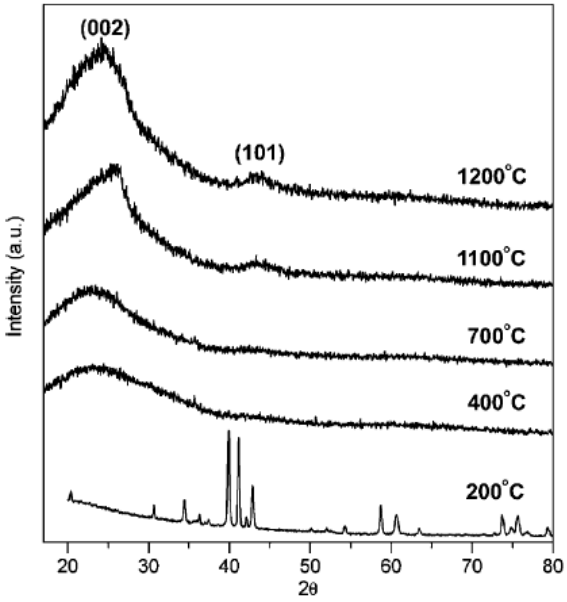

Figure 2-2. X-ray diffraction pattern of CDCs prepared from titanium silicon carbide at different temperatures [15].

The XRD technique can be used to determine the characteristic of carbon crystallites such as interlayer spacing, d_{002}, and crystallite sizes along the c- and a- axes, L_c and L_a respectively. The interlayer spacing, d_{002}, is obtained from the (002) peak using the Bragg equation as follow:

$$d_{002} = \frac{\lambda}{2\sin\theta} \tag{2-2}$$

where θ is the scattering angle for the peak position and λ is the x-ray wavelength. By using the Scherrer equation (equation (2-3)) and the half-width of the (002) reflection peak, the

average thickness of the graphitic crystals (mean particle size) in (002) direction (L_c) and also L_a is obtained [24].

$$L = \frac{K\lambda}{B\cos\theta} \tag{2-3}$$

where L is L_c or L_a, B is the half-width of the peaks in radians, and K is the shape factor. The L_c and L_a are named stack height and stack width.

2.2.2 Transmission electron microscopy

Transmission electron microscopy (TEM) has been widely used to characterize carbide-derived carbons. TEM images of porous carbons can provide information about pore shape as well as the pore size [25]. Figure 2-3 illustrates a typical example of TEM images of CDCs showing the evolution of the carbon structure with increasing synthesis temperature [2].

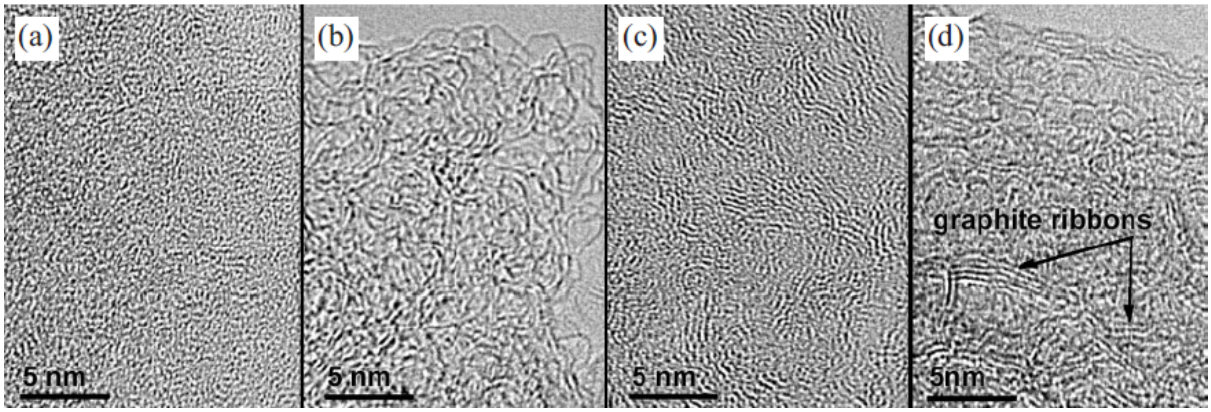

Figure 2-3. TEM images of TiC based CDCs synthesized at (a) 400, (b) 800, (c) 1000, and 1200 °C [2].

TEM images have shown that CDCs with low synthesis temperature ranges are completely amorphous while graphitization and formation of a graphitic shell on particles is observed at higher synthesis temperatures [8, 11].

2.2.3 Helium pycnometry

Another technique used for the characterization of CDCs is the helium pycnometry. Pycnometer determines density and volume of a sample in any shape by measuring the pressure change of helium when it expands from one chamber containing the sample into another chamber without sample [26]. The variation of helium (skeletal) density for CDC

samples which have been prepared at different chlorination temperature and also their heat treatment forms has been observed in some works [3, 11, 12]. Nguyen et al. [12] have shown a slightly gradual increase in the helium density of nano-sized CDCs (Figure 2-4) with increasing synthesis temperature. In their work it is shown that the helium density of synthesized CDC nanoparticles (2.5-2.7 g/cm^3) is higher than the density of graphite which is 2.27 g/cm^3.

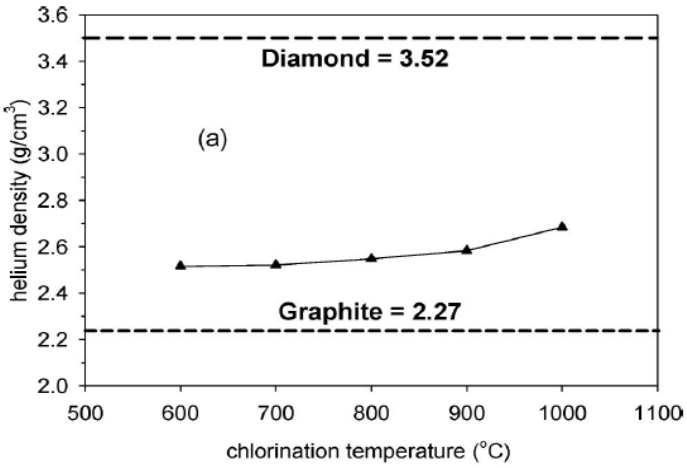

Figure 2-4. Helium density of SiC-based CDC with increasing synthesis temperature [12].

Different techniques have been used to characterize the pore structure and porosity of porous carbons, however because of the highly disordered nature and complex microstructure of porous carbons, the accurate characterization of the pore morphology and topology of the porous carbons even with modern visualization techniques such as HRTEM or X-ray diffraction is impractical. The methods based on the analysis of gas adsorption data including equilibrium and kinetics studies can provide a powerful complement to these characterization methods for interpreting the internal structures of porous carbons. In the next following sections, the gas adsorption isotherm measurement techniques and models as well as diffusion kinetic studies in porous materials is reviewed.

2.3 Adsorption equilibrium on porous adsorbents

Adsorption can be physical (physisorption) or chemical (chemisorption) according to the nature of the intermolecular forces between adsorptive with the surface of a solid. The intermolecular forces between the adsorptive and adsorbent are held by van der Waals and electrostatic forces, however in chemisorption which is not dealt with in this thesis the

intermolecular forces involved lead to the formation of chemical bonds, and therefore chemical adsorption is not reversible [27]. The relation between the amount adsorbed and the equilibrium pressure of the gas at constant temperature is known as the adsorption isotherm. Various types of apparatus and measurement techniques are used for the adsorption isotherm measurement [28] which may be divided into two groups: (a) volumetric methods (measuring the changes of pressure of gas in a confined and calibrated volume) and (b) gravimetric methods (measuring the change in mass of the adsorbent). These two experimental techniques as well as the review on the adsorption isotherm models are presented in this section.

2.3.1 Experimental measurement techniques

One important concept in the isotherm measurements is the excess (Gibbs) adsorption or Gibbsian Surface Excess (GSE). All experimental methods for isotherm measurements give the excess amount adsorbed [29], which has to be related with its absolute amount adsorbed. In the adsorption process, the adsorbed phase volume and compositions cannot be measured experimentally. Sircar explained that this problem has been resolved by the model proposed by Gibbs [30]. This model illustrates that adsorption of adsorbates can be quantified by variables called Gibbsian Surface Excesses (GSE) which can be measured experimentally [29, 30]. The GSE model for adsorption from a multicomponent bulk gas mixture at pressure (P), temperature (T), and gas-phase mole fraction (y_i) of component i have been shown in Figure 2-5.

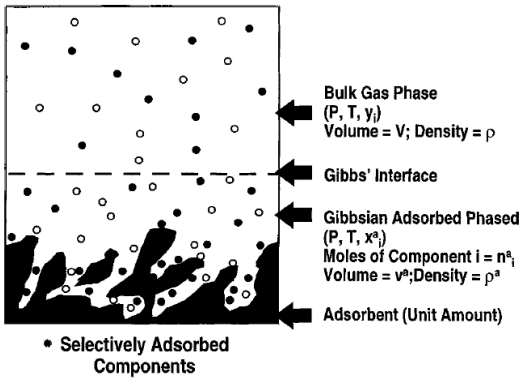

Figure 2-5. Gibbsian model for gas adsorption [30].

In this model, the adsorbed phase is separated from the bulk gas phase by choosing an interface which is called Gibbs Interface. The volume of chamber is v^T and the total void volume (v^0) for the system of Figure 2-5 is given by

$$v^0 = v + v^a \tag{2-4}$$

where v and v^a are the volumes of bulk gas phase and the adsorbed phase respectively. A mass balance for the component i of the gas mixture yields

$$n_i^0 = n_i^m + v^0 \rho y_i \tag{2-5}$$

$$n_i^m = n_i^a - v^a \rho y_i = v^a [\rho^a X_i^a - \rho y_i] \tag{2-6}$$

$$n_i^a = v^a \rho^a X_i^a ; X_i^a = \frac{n_i^a}{n^a} ; n^a = v^a \rho^a \tag{2-7}$$

where n_i^0 is the total moles of component i present in the adsorption system of Figure 2-5 and ρ is the molar density of the bulk gas phase at P, T, and y_i. The variable n_i^m is called the GSE for component i of the gas mixture. n_i^a, n^a, ρ^a, and X_i^a are the amount of component i adsorbed, the total amount of all components adsorbed, the molar density of the adsorbed phase, and the adsorbed phase mole fraction of component i respectively. Since n_i^0, v^0, ρ can be measured experimentally, thus n_i^m which is independent of the location of the Gibbs interface can be measured experimentally [30]. The experimental techniques measure the equilibrium GSE of a pure gas or those for the components of a gas mixture under conditions of the experiments [29].

One of the most employed experimental techniques for the measurement of adsorption isotherms is volumetric technique. This technique is based on a mass balance principle which employs measurements of pressures, volumes and temperatures. There is an equilibrium chamber in the volumetric apparatus which is filled with the adsorbent. The void volume is obtained from the measured values of the temperature, pressure, and amount of helium injected into the chamber. It is assumed that helium is not significantly adsorbed. The void volume obtained from the injected known quantities of helium is used in the measurements of adsorption [30, 31].

Another experimental technique which is widely used for the adsorption isotherm measurements is gravimetric technique. In this technique the adsorbent is exposed to the gas at constant experimental conditions (pressure and temperature), and at equilibrium the change of mass of the adsorbent is measured. Various designs of gravimetric analysers are available which usually consist of three parts including gas dosing system, microbalance and adsorption chamber (AC) [32]. Figure 2-6 [30] shows a typical gravimetric adsorption experiment.

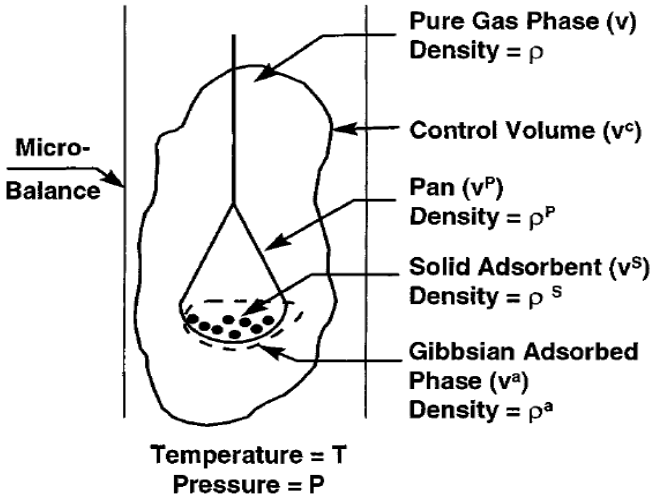

Figure 2-6. Gravimetric adsorption experiment [30].

The basket (pan) containing the adsorbent sample is usually suspended from a permanent magnet (PM). The microbalance in this technique only shows the difference between the sample's weight and its buoyancy force which includes the volume of the porous sample. The buoyancy effect at high gas pressure where the density of the sorptive gas becomes so high is very important. It is this quantity which normally is not known exactly and therefore has to be approximated [33]. Therefore, in gravimetric method like the volumetric method, there are no direct methods to measure both the absolute amount adsorbed and the adsorbed phase density (or adsorbed phase volume), and the only measurable quantity is the excess amount adsorbed.

For mixed gas adsorption, the composition and the molecular weights of the adsorbed phase are not known. Thus, only the total mass GSE can be estimated gravimetrically because the composition of the adsorbed phase cannot be obtained directly from the experimental data.

Van Ness [34] has developed a thermodynamic method using the Gibbs adsorption isotherm (isotherm based on Gibbs approach) for calculation of the adsorbed phase composition from the total amount adsorbed. Myers [35] has developed a new procedure for calculating the composition of the adsorbed phase from gravimetric data which requires only a few mixture points. Friederich and Mullins [36] have also used the gravimetric method to measure the adsorption equilibria of gas mixtures on homogeneous carbon black. Buss [37] has used the gravimetric method to study the mixture adsorption of methane and carbon dioxide on activated carbon and used the gravimetric method proposed by Van Ness to obtain the composition of the adsorbed phase for the binary mixtures.

2.3.2 Adsorption isotherm models

The structure of porous materials can be characterized by the pore size distribution (PSD) in terms of the pore width. According to the International Union of Pure and Analytical Chemistry (IUPAC) recommendation [38], the pores in porous materials are categorized based on their size range into three different kinds:

(i) Pores with larger widths than 50 nm are called macropores;
(ii) Pores with widths between 2 nm and 50 nm are called mesopores;
(iii) Pores with widths smaller than 2 nm are called micropores.

In 1985 IUPAC classified the adsorption isotherms into six types [39]. In 2015 Thommes et al. [40] have refined the original IUPAC classifications of adsorption isotherms and the associated hysteresis loops since new characteristic types of isotherms have been identified over the past 30 years. Their proposed updated classification of adsorption isotherms in their IUPAC Technical Report is shown in Figure 2-7. Type I as reversible isotherms are related to microporous solids having relatively small external surfaces such as some activated carbons, molecular sieve zeolites and certain porous oxides. For nitrogen and argon adsorption at 77 K and 87 K, these type isotherms are given by microporous materials with narrow micropores mainly smaller than 1 nm in width. Type I(b) isotherms are generally observed in materials with PSDs over a broader range including wider micropores and possibly narrow mesopores smaller than 2.5 nm [40]. The reversible Type II and Type III isotherms are observed in nonporous or macroporous solids. Type IVa and Type IVb are usually observed in mesoporous adsorbents. These types suggest the formation of two surface layers in which the initial monolayer-multilayer adsorption on the mesopore walls is followed by capillary

condensation. In Type IVa isotherm, hysteresis is present with capillary condensation. The Type V isotherm which is usually observed for water adsorption on hydrophobic microporous and mesoporous adsorbents is attributed to relatively weak interactions between adsorptive with the adsorbent. The stepwise Type VI isotherm suggests layer by layer adsorption on a highly uniform nonporous surface and has been observed in argon or krypton adsorption on graphitised carbon blacks at low temperature [40]

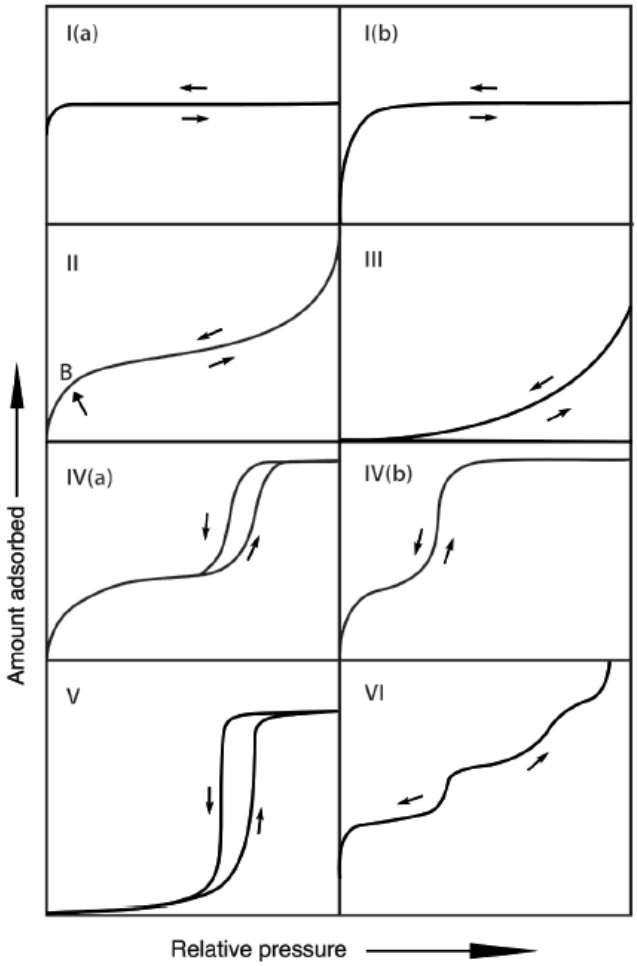

Figure 2-7. Updated classification of adsorption isotherms [40]**.**

Various theoretical model equations have been developed to describe microporous adsorption equilibria ranging from simple equations such as the Langmuir isotherm to theories based on statistical mechanics and molecular simulations. The adsorption isotherm models can be classified into four main approaches: (1) Langmuir approach, (2) Gibbs approach, (3) Potential theory approach and (4) the statistical mechanics. They are briefly discussed in this section.

2.3.2.1 Langmuir approach

Langmuir isotherm [41] has been widely used to describe adsorption processes for decades. In deriving Langmuir isotherm equation, it is assumed that a molecule occupies one definite site on a homogeneous surface, and each site can accommodate only one molecule. By equating the rates of adsorption and desorption, the Langmuir equation follows

$$C_{\mu} = C_{\mu S}\frac{bP}{1+bP} \tag{2-8}$$

where C_{μ} is the adsorbed amount, P is the equilibrium pressure, $C_{\mu s}$ is the adsorption capacity and b is the equilibrium or Langmuir constant. The Langmuir isotherm follows Henry's law form at very low pressure which is a linear form ($C_{\mu}= C_{\mu s}bP$ or $C_{\mu}= K_H P$) in which K_H is called Henry's law constant.

The Freundlich equation is one of empirical equations for the description of equilibria data. This equation is expressed as follows

$$C_{\mu} = KP^{1/n} \tag{2-9}$$

where K and n are constants which depend on temperature. Freundlich equation does not follow Henry law at low pressure, and it does not have a finite limit at high pressures. By different assumptions for the system, different isotherm equations can be derived based on the Langmuir isotherm. By assuming non-uniform surfaces, the Langmuir-Freundlich (Sips) isotherm can be written as [42]

$$C_{\mu} = C_{\mu S}\frac{(bP)^{1/n}}{1+(bP)^{1/n}} \tag{2-10}$$

where the parameter n characterises the heterogeneity of the system. This heterogeneity could be due to solid surface or adsorbate or a combination of both. This equation has been widely used for hydrocarbon adsorption on activated carbon [43]. The Toth isotherm model which is also frequently used is expressed as follows

$$C_{\mu} = C_{\mu S}\frac{bP}{[1+(bP)^{t}]^{1/t}} \tag{2-11}$$

The parameter *t* which characterises the heterogeneity of the system is normally less than unity. The Toth equation has two end limits at both low and high pressures, while the Sips equation does not follow the Henry law at low pressures.

Based on statistical thermodynamic analysis, Nitta et al. [44] have developed a multi-site occupancy model for homogeneous surface on the basis of Langmuir isotherm. This isotherm equation is expressed as follows

$$KP = \frac{\theta}{(1-\theta)^{\nu}} \tag{2-12}$$

where ν is the vacancy occupancy of the adsorbate. This isotherm has been also recommended for the gas mixture adsorption on homogeneous adsorbents [45]. This model assumes each molecule occupies multi sites on a homogeneous surface instead of one definite site. Staudt et al. [46] have proposed generalized form of the Langmuir-Freundlich isotherm for single and multicomponent with introducing characteristic exponent α_i. For single component system, it is written as

$$C_{\mu} = C_{\mu S}\alpha_{\infty}\frac{(bP)^{\alpha}}{1+(bP)^{\alpha}} \tag{2-13}$$

and for multicomponent systems it is presented as

$$C_{\mu,i} = C_{\mu S,i}\alpha_{\infty,i}\frac{(b_i P_i)^{\alpha_i}}{1+\sum(b_k P_k)^{\alpha_i}} \tag{2-14}$$

where α_i characterises the energetic heterogeneity of the surface [47]. In this equation α depends on pressure and temperature.

Dreisbach et al. [48] have used a generalized dual site Langmuir isotherm to describe the experimental adsorption data of methane, nitrogen, carbon dioxide and their binary and ternary mixtures on activated carbon. This isotherm is expressed as follows

$$C_{\mu}(P,T) = C^{P}_{\mu\infty}\alpha^{P}_{\infty}\frac{(b^{P}P)^{\alpha^{P}}}{1+(b^{P}P)^{\alpha}} + C^{S}_{\mu\infty}\alpha^{S}_{\infty}\frac{(b^{S}P)^{\alpha^{S}}}{1+(b^{S}P)^{\alpha}} \tag{2-15}$$

where *"P"* and *"S"* indicate primary and secondary adsorption sites. It is shown that this isotherm model describes properly single gas adsorption equilibria in a wide range of pressure.

Brunauer et al. [49] proposed a theory (BET theory) on the basis of Langmuir approach considering multilayer adsorption. The BET equation which is used for measuring surface area of porous adsorbents [50, 51] is expressed as

$$\frac{1}{n[\left(\frac{p_0}{p}\right)-1]}=\frac{c-1}{n_m c}\left(\frac{p}{p_0}\right)+\frac{1}{n_m c} \tag{2-16}$$

where p and p_0 are the equilibrium and the saturation pressure of adsorbates at the temperature of adsorption, n is the adsorbed gas quantity, n_m is the monolayer adsorbed gas quantity, and c is the BET constant.

2.3.2.2 Gibbs approach

The gas adsorption equilibrium on porous solids can be also described based on the fundamental equations in classical thermodynamics. Myers and Prausnitz [52] have proposed the following expressions based on the classical thermodynamics approach for the internal energy and Gibbs free energy of a two dimensional adsorbed phase

$$d\left(n^a U\right)=Td\left(n^a S\right)-\pi d\left(n^a V\right)+\sum \mu_i^{\,a}\, dn_i^a \tag{2-17}$$

$$d\left(n^a G\right)=-\left(n^a S\right)dT+\left(n^a a\right)d\pi+\sum \mu_i^{\,a}\, dn_i^a \tag{2-18}$$

where U, G, S, V and P are the molar internal energy, Gibbs free energy, entropy, volume respectively, μ_i is the chemical potential of component i, n_i is the number of moles of component i per unit volume of the fluid, and the total number of moles per unit volume of the fluid is given by $n=\sum n_i$. For a two dimensional adsorbed phase, the pressure P is replaced by the spreading pressure π and the molar volume by the molar area a. The superscript a represents the adsorbed phase.

The Gibbs adsorption isotherm is expressed as follows

$$-\left(n^a a\right) d\pi + \sum n_i{}^a d\mu_i{}^a = 0 \tag{2-19}$$

In the equilibrium condition the chemical potentials of each component in both adsorbed and gaseous phases are the same and for any change in the equilibrium conditions,

$$d\mu_i^a = d\mu_i^g \equiv RTd(\ln\ f_i^g) \tag{2-20}$$

The superscript *g* represents the gaseous phase.

For pure systems, the following equation is obtained [52, 53]

$$\left(\frac{d\pi}{d\ln f}\right)_T = \frac{n}{A}RT \tag{2-21}$$

where A is a constant equal to the specific area of the adsorbent ($A = n^a a$). From this equation different isotherm equations can be obtained if the equations of state are known.

For the mixtures most of the models presented for multicomponent adsorption equilibria predict the equilibrium adsorbed amount from single-component adsorption data at the same temperature [53, 54]. One of the most widely used models for the prediction of multicomponent adsorption equilibria is the ideal adsorbed solution theory (IAST). The IAST which assumes that the mixture behaves as an ideal solution at constant spreading pressure and temperature is presented by the following equations [52, 54]

$$f_i = f_i{}^0(\pi)x_i \tag{2-22}$$

$$\frac{\pi A}{RT} = \int_0^{f_i^0} n_i d(\ln\ f_i) \tag{2-23}$$

$$\frac{1}{n_t} = \sum \frac{x_i}{n_i^0} \tag{2-24}$$

$$n_i = x_i n_t \tag{2-25}$$

where f_i is the fugacity of the pure component i in the bulk gas phase, f_i^0 is the fugacity for component i at the solution temperature, T, and the spreading pressure, π, of the binary mixture when the adsorbed and bulk gas phases are in equilibrium, R is the ideal gas constant,

and x_i is the mole fraction of component i in the adsorbed phase. At equilibrium, each component has the same spreading pressure, and by equating the spreading pressures for all components, the unknowns (π_i, f_i^0, and x_i) can be calculated. The ability of IAST to predict the mixture adsorption depends on the characteristics of the adsorbent and the behaviour of the molecules in mixture binding to the surface [55]. The ability of IAST to predict mixture adsorption has been investigated by different research groups [43, 56-61].

The Gibbs approach has been also used by Suwanayuen and Danner [62] to develop an isotherm based on vacancy solution theory which can be used for more than one adsorbate. In this approach the surface is considered to be composed of an imaginary entity defined as vacuum space that acts as the solvent for the system and adsorbed species. Ding and Bhatia [63] have improved the vacancy solution theory to heterogeneous adsorbents by considering that vacancies are consumed on adsorption of molecules. They have used a modified version of vacancy solution theory as single isotherm equation for IAST [63]. Cost et al. [61], and Malek and Farooq [43] have investigated the performance of vacancy solution theory and IAST, and in their work it is shown that the simpler extended versions of single component models such as Langmuir or its modified versions provide adequate and numerically convenient means of predictions.

In the literature, the non-ideality of the adsorbed phase is related to the occurrence of non-unity activity coefficients or the surface energetic heterogeneity of the adsorbent [64-67]. The Real Adsorbed Solution Theory (RAST) has improved the IAST with introducing interaction parameters (i.e. activity coefficients) for the components however it requires multicomponent experimental data for the estimation of the interaction parameters [68]. The Heterogeneous Ideal Adsorbed Solution Theory (HIAST) has also improved the IAST assuming an energy distribution to all of the adsorption sites in which the adsorbed solution on each local site is ideal [65, 66].

2.3.2.3 Potential theory approach

In this approach in which the adsorption system is viewed as a gradual concentration of gas molecules toward the solid surface due to a potential field, it is assumed that there is a relationship between this potential field and the volume above the solid surface. On the basis of this approach the Dubinin–Radushkevich (DR) equation [69, 70] is expressed as follows

$$\log W = \log W_0 - (RT / \beta E_0)^2 \log^2 (P_0 / P) \tag{2-26}$$

where W_0 (cm^3/g STP) is the "micropore capacity" and E_0 (kJ/mol) is the characteristic adsorption energy related to the micropore structure. R and T are the universal gas constant and adsorption temperature respectively, and β is an affinity coefficient which depends on the strength of surface molecule interaction.

Based on the potential theory, the multicomponent potential theory of adsorption (MPTA) [71] has been proposed to describe nonideally behaving mixtures in microporous adsorption. This theory uses a bulk-phase equation of state (EoS) for determination of the chemical potentials of the components in the fluid phase and a separate equation to describe the fluid-solid interactions. Monsalvo and Shapiro [72, 73] have shown that the MPTA is successful in description and prediction of supercritical adsorption and strongly non-Langmuirian behaviour. Bjørner et al. [74] have extended the MPTA by applying the cubic-plus-association (CPA) EoS [75] as a mixture model and investigated its predictive capabilities on several sets of complex binary mixtures on industrially microporous adsorbents. The advantage of using the potential theory for predicting gas mixture adsorption equilibria is that by obtaining isotherm information of pure component at one temperature, the mixture equilibria at other temperatures and pressures can be predicted.

2.3.2.4 Statistical mechanics

Models based on the statistical mechanics have been also widely used in both characterizing carbons which gives a more accurate description of the PSD and modelling of gas adsorption. On the basis of statistical mechanics, there are two main approaches in modelling of gas adsorption: (1) density functional theory (DFT) [76], and (2) Monte Carlo simulation, represented by Grand Canonical Monte Carlo (GCMC) simulations. The adsorbed amount in a pore can be related to the overall adsorbed amount as following

$$n(P) = \int_{H_{min}}^{H_{max}} f(H)\rho(P,H)\mathrm{d}H \tag{2-27}$$

From this equation, the pore size distribution of the adsorbent can be derived if the experimental adsorption isotherm and density profiles of the adsorbed phase are known.

Different versions of density functional theory have been developed based on nonlocal free energy, in which have resulted in potentially useful techniques for the surface area and PSD extraction from experimental adsorption isotherms, which are more accurate than the classical methods [77].

In the DFT approach, the local fluid density ρ(**r**) of the adsorbate confined in a pore of a porous material at given chemical potential μ and temperature T is determined by minimization of the grand thermodynamic potential (GP) [78] using an iterative procedure. The GP as a function of the fluid density ρ(**r**) is expressed as

$$\Omega\left[\rho(r)\right] = F\left[\rho(r)\right] - \int dr\,\rho(r)[\mu - U_{ext}(r)] \tag{2-28}$$

where $\Omega[\rho(r)]$ is the grand thermodynamic potential of fluid confined in a pore at a given chemical potential μ and temperature T. $F[\rho(r)]$ is the intrinsic Helmholtz free energy functional and $U_{ext}(r)$ is the external solid-fluid potential imposed by the pore walls [78].

For the determination of the local density profile, the potential models are essential. The Lennard-Jones (LJ) 12-6 potential, and 10-4-3 potential expression have been widely used to estimate the adsorbate-pore wall interaction in carbon materials [79]. However it is shown that 10-4-3 potential expression overestimates the gas-solid interaction in carbon because of its finite pore wall thickness [80]. Bhatia [80] has considered the random distribution of pore wall thickness in carbon as an alternative method. The most common idealization of the pore structure of carbons is considering a collection of independent slit pores (slit pore model) having infinitely thick walls as infinite wall thickness (IWT) model or finite thick walls as finite wall thickness (FWT) [81, 82]. In FWT model, the PSD is obtained by fitting gas adsorption data using nonlocal density functional theory (NLDFT) by assuming finite thick pore walls instead of considering infinitely thick pore walls [81, 82].

2.4 Adsorption kinetics and diffusion

Despite the efforts devoted to the CDC characterization, there has been no published report on the transport of gases in CDCs. Therefore a detailed kinetic investigation is necessary to obtain a comprehensive understanding of the impact of pore structure of CDC materials on adsorption behaviour.

Understanding the dynamics of gases and how a molecule diffuses in the internal structure of a porous material is very important in the field of gas adsorption, and extensive studies over the years have been devoted to it in the literature [83, 84]. Various types of experimental techniques as well as the review on the adsorption kinetics models are presented in this section.

2.4.1 Experimental measurement techniques

Different experimental techniques have been proposed in the literature to measure the diffusion in porous materials. These techniques can be divided into two main techniques: (1) macroscopic techniques such as uptake rate measurement methods, frequency response [85, 86], infrared spectroscopy, chromatographic measurements and the zero-length-column (ZLC) [87], and (2) microscopic techniques such as Pulse Field Gradient NMR (PFG NMR), NMR relaxation, and quasi elastic neutron scattering (QENS).

In 1988, Eic and Ruthven [87] developed the inexpensive ZLC technique for obtaining diffusion coefficients. Since its development it has become widely used and provides a reliable and reproducible macroscopic technique. In this technique, the experimental apparatus (Figure 2-8) is similar to conventional gas chromatography except that the packed column is replaced by a small sample of adsorbent sandwiched between two sintered metal disks [87]. In this technique, the sample is first equilibrated with an adsorptive at low pressure. Then desorption is conducted under a high and steady flow rate of a non-adsorbing carrier gas such as helium to obtain a curve of desorption versus time. The diffusion time constant is obtained by matching the desorption dynamics to the theoretical solution of the diffusion equation [87, 88]. Various solution methods including ‘long time’, ‘short time’ and ‘intermediate time’ [88-90] as well as a moments-base method [91] have been proposed in the literature for ZLC technique. In the original ZLC technique, there are two methods for extracting the relevant parameters. One is the long-time (LT) asymptote of desorption curve [87], which is linear on a semi-logarithmic plot. The other is the short time (ST) approximate method [88], which fits the initial part of the response curve for obtaining the diffusion time constant. The mathematical model that is generally used to analyse ZLC response curves is based on the following assumptions [87, 89, 92]: (1) equilibrium between sorbate concentration at the particle surface and in the surrounding gas at Henry’s law region, (2) perfect mixing of fluid surrounding the particles with negligible hold-up in the fluid phase in

comparison with the adsorbed phase hold-up, (3) the flow rate of the gas stream is sufficiently high, and the heat and mass transfer resistances can be eliminated, and (4) the temperature of the adsorption column is considered to be constant.

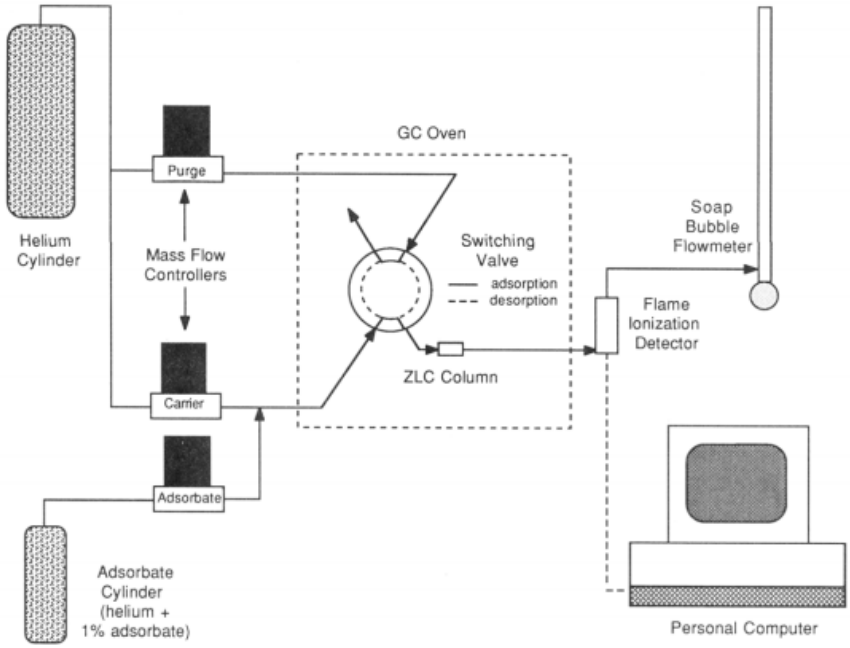

Figure 2-8. A typical schematic of ZLC set-up [88]**.**

Ruthven and Brandani [93] modified the ZLC model for the case in which surface barrier resistance is rate controlling. They compared the forms of the ZLC response for surface resistance and internal diffusion control. They showed that for linear or nearly linear systems, these two patterns of behaviour can be distinguished experimentally by examining the ratio of slope to intercept of the ZLC response plotted in log-linear coordinates. Ruthven and Vidoni [94] have addressed a more general situation in which both internal and surface resistances are important. They have extended the mathematical model for zero length column system to the situation in which the sorption kinetics are controlled by the combined effect of intraparticle diffusion and surface resistance to mass transfer. They have validated their new model by the experimental data for diffusion of ethane in DDR zeolite [94].

2.4.2 Models for adsorption kinetics

The adsorption of an adsorbate species from bulk gas phase in to a particle is normally described by a two-step process, transport through the film to the outer surface of the particle and diffusion into the particle. Depending on the dimensions of the adsorbent pores, structure

and process conditions, the mechanism of mass transport in porous solids may be governed by pore diffusion, surface diffusion, or an interfacial barrier resistance [51].

A number of mathematical models have been proposed to describe the adsorption dynamics in heterogeneous and bidisperse structured porous solids which have been widely used in adsorption processes [95, 96]. These models can be categorised as those that consider the transport in the micropores to be significant at the particle scale, and those that limited to transport locally to the microscale. In the work of Wakao and Smith [97], the particle scale diffusion of gases in both micropores and macropores have been considered assuming a random pore structure, with no account of adsorption effects. The assumption of negligible adsorption was subsequently relaxed by Schneider and Smith [98] who considered simultaneous gas and adsorbate diffusion in macropores and micropores respectively over the whole particle, while remaining at equilibrium with a linear isotherm. Such an approach assumes rapid mass transfer between the macropore and micropore phases, as well as high permeability in the micropores, comparable to that in the macropores. However, when the micropore permeability is significantly smaller than that of the macropores, the diffusion in the micropores will be locally restricted to a scale much smaller than the particle size. Models of the adsorption dynamics in this limit assume the adsorbent particles to be bidisperse, comprising agglomerates of microporous microparticle called grains in which local transport occurs in micropores, with the intergrain macropores providing the pathways for particle-scale gas phase transport [96, 99, 100].

The particle scale mass transport in bidisperse particles follows the balance equation [51, 96]

$$\varepsilon_m \frac{\partial C_m}{\partial t} + (1-\varepsilon_m)\frac{\partial \bar{C}_\mu}{\partial t} = -\frac{1}{R^a}\frac{\partial}{\partial R}\left(R^a N_m\right) \tag{2-29}$$

and for spherical microparticles, the microscale transport follows

$$\varepsilon_\mu \frac{\partial C_\mu}{\partial t} = \frac{1}{r^2}\frac{\partial}{\partial r}\left(r^2 D_{e\mu}\frac{\partial C_\mu}{\partial r}\right) \tag{2-30}$$

where a is the geometrical parameter of the particle and N_m the particle scale flux. In these equations ε_μ and ε_m are porosity of the microparticle and particle, respectively. $D_{e\mu}$ is a

concentration-dependent effective diffusivity in the microparticle scale which is often considered to follow Darken relation [96], C_m is the adsorptive concentration in the particle scale, C_μ is the adsorptive concentration in the microparticle scale, and $\bar{C}_\mu$ its mean value. It should be mentioned that r and R are the radial position in the microparticle and particle scales, respectively.

In the simplest case, when particle scale diffusion of the micropore adsorbate is insignificant, the particle scale flux, N_m, is expressed as

$$N_m = -D_{em}\frac{\partial C_m}{\partial R} \tag{2-31}$$

where D_{em} is the effective diffusivity in the particle scale. The boundary condition for equation (2-30) is the adsorption isotherm which correlates the concentration in the microparticle scale, and the particle scale concentration. This model was first proposed by Ruckenstein et al. [100] who showed good agreement with data when the diffusion of the adsorbed species is assumed to occur only over the small length scale of the individual microspheres. While the approach has found much support in the subsequent literature, in some studies of adsorption in activated carbon the microstructure has been divided into two types of independent micropore phases with negligible particle scale macropore resistance [101]. Subsequent work has seen modifications to the above approach to include a particle scale flux contribution from the micropores, following Barrer [102] as well as Karger [103], who propose the hopping of molecules between the microparticles through the macropore spaces. Do and co-workers [104-106] incorporated this flux through an empirical surface diffusion of the adsorbed phase by an additional term in the equation (2-31) as follow

$$N_m = -D_{em}\frac{\partial C_m}{\partial R} - D_s(1-\varepsilon_m)\frac{\partial \bar{C}_\mu}{\partial R} \tag{2-32}$$

in which D_s is the surface diffusivity. Bhatia and co-workers [107, 108] have considered a microparticle through-flux arising from the macropore concentration variation around the microparticle surface. The flux in this model is written as follows

$$N_m = -D_{em}\frac{\partial C_m}{\partial R} - (1-\varepsilon_m)\int_0^{\frac{\pi}{2}}\left(D_{e\mu}\frac{\partial \bar{C}_\mu}{\partial R}\right)_s 2\sin(\theta)\cos(\theta)d\theta \tag{2-33}$$

in which Θ represents the angular position of microparticle surface. The mass balance on microparticle scale in this model is expressed as

$$\varepsilon_{\mu}\frac{\partial \bar{C}_{\mu}}{\partial t}=\frac{1}{r^2}\frac{\partial}{\partial r}\left(r^2 D_{e\mu}\frac{\partial \bar{C}_{\mu}}{\partial r}\right)+\frac{1}{r^2\sin(\theta)}\frac{\partial}{\partial \theta}\left[D_{e\mu}\sin(\theta)\frac{\partial \bar{C}_{\mu}}{\partial \theta}\right] \qquad (2\text{-}34)$$

However the through flux in this model is found to be generally negligible [95], since the microparticle permeability is generally far smaller than that corresponding to the macroscale transport. Some studies have considered particle scale diffusion in the micropores with negligible transport resistance at the microscale with a nonlinear isotherm and finite mass exchange rate between macropores and micropores [108-110] on the basis of Schneider and Smith [98] approach. Fletcher and Thomas [110] have considered a particle scale diffusion of the adsorbate assuming that the microscale transport resistance for the adsorbate to be insignificant for activated carbon, and the microscale resistance comprises an incorporation barrier for the adsorbate. Ding et al. [108] have incorporated the adsorbent heterogeneity through a pore-width-related potential energy and accounted for the adsorbate non-ideality by using a heterogeneous vacancy solution theory (VST) of adsorption for activated carbon.

The mechanism of surface diffusion has also attracted much attention in the literature [111, 112], considering a dual resistance model with the presence of a surface barrier resistance caused by constrictions at pore mouths along with a diffusion mechanism. Several studies have viewed surface diffusion as hopping of migrating molecules between neighbouring adsorbing sites [113-118], or as continuously adsorbing into and evaporating from the microparticle units [119]. Liu and Ruthven [120] have shown that kinetic data for O_2, N_2 and Ar on carbon molecular sieve (CMS) are consistent with internal diffusion control whereas the data for CH_4 are consistent with surface barrier resistance control. They also found that CO_2 displayed a transition from surface barrier resistance at lower temperatures to diffusion control at higher temperatures. They suggested that the relative importance of the two resistances depended on the ratio of their time constants, and is affected by changes in temperature or pressure. Kapoor and Yang [121] proposed a parallel-path model (PPM) for surface diffusion on heterogeneous surface. In their model, the surface is regarded as consisting of a series of parallel paths in a way that each path has a uniform but different energy. They have further studied the influence of the connectivity among the energetic sites on overall sorption kinetics based on the effective medium approximation [111].

Rutherford and Do [122] found that micropore diffusion is rate limiting for CO_2 adsorption on Takeda 5A CMS, while Nguyen and Do [123] presented a dual Langmuir kinetic model to describe adsorption of O_2, Ar and N_2 on Takeda 3A. In their work, the adsorption kinetics is modelled by a series of two consecutive processes, in which the nonselective adsorption of molecules in meso- and super-micropores is followed by the movement of adsorbed molecules into small micropores through the poremouth barriers. In other works, Qinglin et al. [124, 125], and Wang and LeVan [126] have considered a surface barrier resistance in series with a micropore diffusion resistance for the diffusion of gases in CMS, with negligible direct contribution of micropores to the macroscale flux. Wang and LeVan [126] have recently developed a general mathematical model for frequency response methods with analytical solutions derived to consider a variety of mass transfer resistances acting independently or in combination for biporous adsorbents.

Significant interfacial barrier resistance is known to be present also in other microporous materials such as zeolites, as seen in both experiment and simulation. Through analysis of sorption experimental data on zeolites, Karger and co-workers have shown that a barrier resistance exists at the surface, in addition to resistance to diffusion within the crystal [127, 128], while in other work Zimmermann et al. [129-132] have demonstrated the presence of a surface barrier resistance by combining transition state theory and equilibrium molecular dynamics simulations.

Since there is a gap of knowledge on the adsorption kinetics and diffusion of gases in CDCs, studies on the transport of gases in such materials are essential. Chapters 3 and 4 of this thesis present investigations on the transport of gases in CDCs.

2.5 Water adsorption in carbon materials

The synthesis and design of adsorbents to increase hydrophobicity is crucial for gas separation processes as the presence of H_2O poses significant challenges in many different areas of technology [133]. There are many experimental and simulation studies of adsorption of water in carbon pores presented in the literature [134, 135]. However, while the adsorption in carbon pores has been studied extensively, the understanding regarding the adsorption of H_2O in carbon materials is still incomplete [136-138]. The presence of water can lead to complex adsorption behaviour and affect the efficiency of adsorption processes [133, 137]. It is generally believed that the combination of weak carbon-water dispersive attractions and

strong water-water associative interactions is responsible for the complex behaviour of water confined in carbonaceous pores [134, 135].

It is well-accepted that the adsorption of H_2O in nanoporous carbon is determined by both surface groups and the pore size. In an approach which was first proposed by Pierce and Smith [139] and further developed by Dubinin and Serpinsky [140, 141], it is assumed that H_2O adsorption in carbonaceous pores involves clustering around primary adsorption sites. In this approach, the adsorption of H_2O despite the hydrophobicity of the carbon surface is believed to be due to the presence of significant numbers of adsorption centres (for example oxygen-containing centres) which have high affinity for H_2O [136, 142, 143]. Figure 2-9 illustrates the adsorption of water in carbon pores [144].

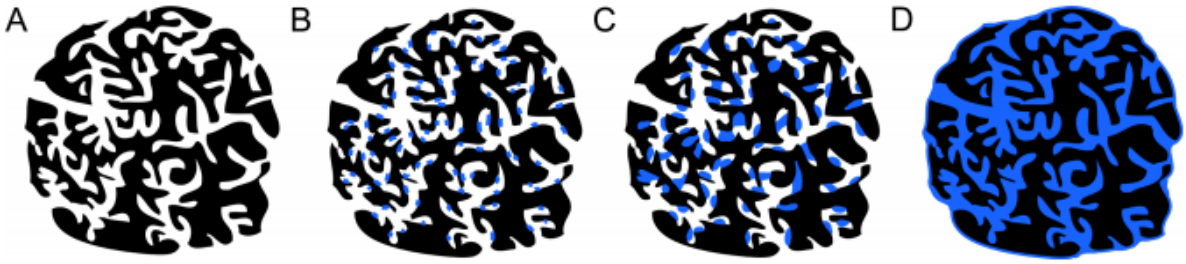

Figure 2-9. Water adsorption process in nanoporous carbon as a function of relative water vapor pressure: (A) no water adsorption at P/P0 = 0; (B) water is adsorbed on primary adsorption sites at low relative pressure (P/P0 < 0.3); (C) water clusters start to grow and cooperative adsorption takes place at medium to high relative pressure; and (D) nanopores are filled with water (P/P0 = 1) [144].

The initial H_2O molecules adsorbed on these centres act as nuclei for the growth of H_2O clusters due to hydrogen bonding [142, 143], and H_2O which has a very strong electrostatic intermolecular interactions compared to weak carbon-water dispersive interactions [145] grow into hydrogen-bonded clusters at primary active sites that are present on the carbon surface (surface groups) followed by the growth and coalescence of these clusters, leading to the bulk filling of the carbon pores [141, 146, 147].

The original Dubinin-Serpinsky (DS) equation which is still widely applied for the explanation of the mechanism of water adsorption on carbonaceous materials due to simplicity [134] is presented as

$$c_{\mu} = \frac{a_0 ch}{1 - ch} \tag{2-35}$$

where a_0 (mmol/g) is the surface concentration of the primary adsorption centres which can be used to distinguish carbons with different degrees of surface oxidation, h is the relative pressure (P/P_0), where P and P_0 are the equilibrium and saturation pressure respectively, c_{μ} (mmol/g) is the amount of adsorbed water at a specific P/P_0, and c (unit-less) is the ratio of the rate constants describing the kinetics of adsorption and desorption. The original DS-1 was improved assuming further adsorption causes the creation of water clusters at larger relative pressures and this process decreases the number of secondary adsorption sites, however the initial stages of water adsorption mechanism on carbonaceous material are similar to original Dubinin-Serpinsky (DS) model [134, 146].

Dubinin and Serpinsky has also presented the following equation

$$h = \frac{c_{\mu}}{c(a_0 + c_{\mu})(1 - kc_{\mu})} \tag{2-36}$$

where k (g/mmol) is a constant involved in decreasing active site concentration. Parameters c, a_0, and k are fitting parameters.

Barton et al. [146] presented an alternative modification of the DS isotherm model as:

$$h = \frac{1}{c(1 - kc_{\mu}(a_0 + c_{\mu}))} \tag{2-37}$$

In the derivation of the equations (2-36) and (2-37), the terms: $(1-kc_{\mu})$ and $(1-kc_{\mu}^2)$ are introduced to take into account the decrease in the number of adsorption sites with increasing adsorption. However, it is shown that these equations do not predict satisfactorily the final parts of water adsorption isotherms measured for largely microporous carbons [146, 148]. Subsequently, Barton et al. [148] have developed the following adsorption equation:

$$h = \frac{c_{\mu}}{ca_0 + cc_{\mu}(1 - \exp[-k^2(c_{\mu} - a_c)^2])} \tag{2-38}$$

Equation (2-38) is obtained by introducing the term (1 - exp[$-k^2(c_\mu - a_c)^2$]), and a fourth parameter, a_c. Barton et al. [146, 148] have suggested that the parameters k and a_c serve to trigger the start of the decline in adsorptive power, and k, as before, governs the rate of this decline with increasing adsorption.

Barton et al. [148] have used water adsorption data on different carbons to test their proposed equation, and the good fits were obtained as can be seen in Figure 2-10. They have shown that the values of a_c are all larger than those of a_s, however they have not assigned any physical meaning to a_c [134, 148, 149]. Gauden [149] suggests that this parameter (a_c) represents the total hypothetical number of adsorbed water molecules equal to or greater than a_s, needed to saturate all possible secondary and primary adsorption centres for the ideal arrangement of water molecules.

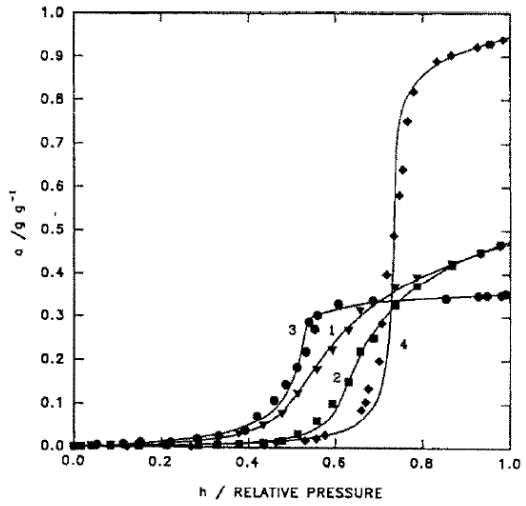

Figure 2-10. Comparison of the equation (2-38) to water adsorption isotherms (1) BPL AK, (2) BPL RED, (3) PVDC, (4) AX-21 [148]**.**

Based on the Dubinin-Serpinsky (DS) approach [140, 141] a number of semi-empirical water adsorption models have been presented in the literature providing fundamental information about the behaviour of H_2O in porous carbons [134]. Based on the adsorption of H_2O molecules on the active sites Talu and Muenier [150] have also developed a model assuming that at low loading the behaviour of the system is solely controlled by molecule to surface vertical interactions, and at intermediate loading where the inflection point of type V isotherms occurs, the adsorbed molecules form large clusters by association via hydrogen

bonding. The association theory of Talu and Muenier [150] is expressed by the following equations

$$P = \frac{H\psi}{1+K\psi}\exp(\frac{\psi}{a_m}) \tag{2-39}$$

where

$$\psi = \frac{-1+(1+4K\xi)^{1/2}}{2K} \tag{2-40}$$

$$\xi = \frac{a_m c_\mu}{a_m - c_\mu} \tag{2-41}$$

where H is the inverse of the Henry's law constant, K is related to the equilibrium constant for the cluster formation in micropores and a_m is the saturation capacity of the pore [150].

Talu and Meunier [150] have used water adsorption data on different carbons to test this theory, and good fits were obtained as can be seen in Figure 2-11. McCallum et al. [151] have successfully used this theory to describe the local water adsorption isotherms obtained from the computer simulation for the various pore widths. Mowla et al. [135] have also presented the results of comparison of this model with experimental data for different types of activated carbons.

Talu and Meunier [150] explains that their theory is not strictly a homogeneous surface model even though a single equation of state (Volmer EOS) is used. They state that in this theory the surface provides primary adsorption sites where the vertical interaction is a single value appearing in the Henry's law constant similar to homogeneous models in contrast to heterogeneous systems where the adsorption potential is a Boltzmann weighted statistical average. The clustering mechanism in the association theory also provides an infinite number of different energy sites for guest molecules. The energy released by adsorption of a molecule is the sum of two contributions: (i) The single vertical interaction value divided by the cluster size, and (ii) The energy of reaction. Since different size clusters each occupy a single site, the adsorption potential can take infinite values from the Henry's law value to zero [150].

Rutherford [152] has extended the CMMS theory which was originally developed by Malakhov and Volkov [153] to describe water adsorption isotherm in highly nanoporous

carbon adsorbents such as carbon molecular sieves. The CMMS model assumes adsorption of one water molecule per functional group followed by adsorption of two water molecules by hydrogen bonding. This configuration forms a triad of water molecules, which then allows secondary interactions. The CMMS model can describe the type IV and V water adsorption characteristics.

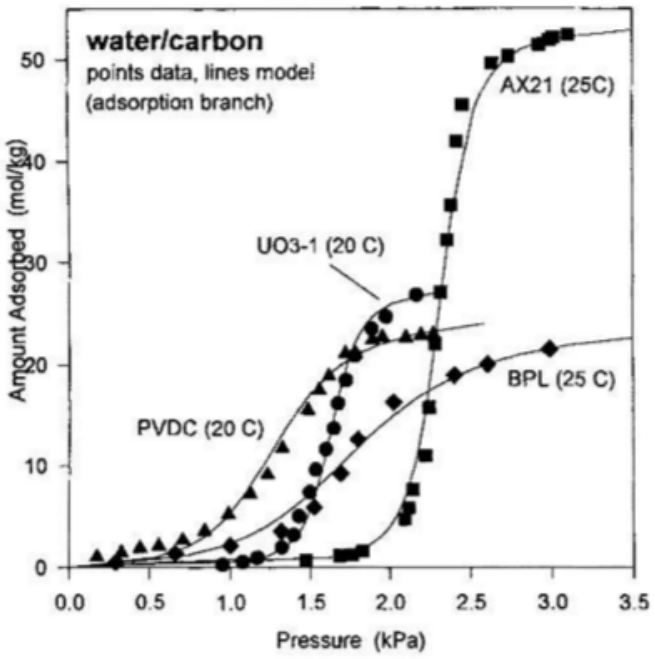

Figure 2-11. Application of the association theory of Talu and Muenier to data of water adsorption on different carbons [150]**.**

The CMMS model equation which is used to describe the water adsorption isotherm for samples with high concentrations of surface functional groups is presented as

$$C_{\mu} = \frac{a_0 b_{BET} h}{(1 - K_{as} h)(1 + b_L h)} + \frac{C_{\mu s} K_0 h}{(K_0 h + w_{l\sin g}^2)} \tag{2-42}$$

This model employs a BET-type equation to describe the adsorption contributions of the functional groups.

In order to use a Langmuir type equation to describe adsorption onto surface functional groups and samples which often exhibit type V isotherm, the CMMS model is presented as

$$C_{\mu} = \frac{a_0 b_L h}{(1 + b_L h)} + \frac{C_{\mu s} K_0 h}{(K_0 h + w_{l\sin g}^2)} \tag{2-43}$$

where

$$w_{l\sin g} = \frac{1}{2}(1 - K_1 h + \sqrt{(1 - K_1 h)^2 + 4K_0 h}) \quad (2\text{-}44)$$

in the above equations K_0 and K_1, are the equilibrium constants representing the interaction of water molecules with the functional group and with the side unit on the functional group, respectively, K_{as} is the constant of adsorption of the side associate, and b_{BET} and b_L are the BET and Langmuir affinity constant respectively.

Do and Do (DD) [154] have also developed a water adsorption isotherm equation assuming a two-stage mechanism, in which at the first stage, H_2O molecules are strongly bonded to the primary sites and form clusters via hydrogen bonds. They have explained that since a single H_2O molecule does not have sufficient dispersive force to adsorb inside the micropore, a cluster of five H_2O molecules (pentamer) is necessary to produce sufficient force for water to fill micropores. This model equation is expressed as

$$C_\mu = a_0 \frac{K_f \sum_{n=1} n h^n}{1 + K_f \sum_{n=1} h^n} + C_{\mu s} \frac{K_\mu \sum_{n=6} h^n}{K_\mu \sum_{n=6} h^n + \sum_{n=6} h^{n-5}} \quad (2\text{-}45)$$

where the definitions of a_0 and $C_{\mu s}$ are the same as previous models, K_f and K_μ, are the equilibrium rate constants for the chemisorption of water on functional groups and water filling of micropore respectively, and n is the average number of molecules in the fully developed water clusters on the surface functional groups.

Several modifications to the DD isotherm model [154] have been presented in the literature to describe water adsorption on carbon [142, 143, 155, 156]. Do et al. [142] have extended the DD model to describe the adsorption and desorption branches of water adsorption in activated carbon. Although this model can describe the different shapes of water adsorption isotherm in activated carbon, many physical parameters such as the size of water clusters and the equilibrium constant of water vapour in the micropores of activated carbon cannot be measured. Yao et al. [157] have developed a new model to calculate these parameters.

Laboratory experiments on a variety of hydrophobic carbons such as activated carbon fibres (ACFs) [158], some activated carbons [159] and carbide-derived carbons (CDCs) [21, 160] have shown that H_2O isotherms on these carbons are type V isotherm and strong H_2O

adsorption occurs at moderate relative pressures. Most of the experimental studies on adsorption of H_2O by microporous carbons have shown that the surface functional groups play the main role [140, 161-164], and some of these studies have investigated the role of surface groups by exposing carbon materials to controlled oxidative treatments [156, 164]. Computer simulations on H_2O adsorption have also shown the formation of clusters on primary adsorption centres, indicating the strong effect and predominant role of the primary surface groups in the enhancement of the H_2O adsorption [136, 151, 165-168]. The effect of several types of polar oxygen-containing sites (with different densities and local distributions) on the surface of the carbon has been investigated in a number of studies [151, 169, 170]. The presence and structure of water adsorbed in carbon micropores at ambient temperature have been investigated by different analysis such as X-ray diffraction [171], differential scanning calorimetry [172], and dielectric relaxation spectroscopy [172, 173].

2.6 Functionalization and surface modification of carbon materials

The treatment and functionalisation of carbonaceous surface is known as an effective method to control hydrophilicity/hydrophobicity and adsorption properties of carbon materials [174-176]. For example, increase in adsorption capacity [177], as well as an increase in conductivity and performance in super-capacitors [178] and batteries [179] have been reported based on targeted modification of surface chemistry. Oxygen [180], fluorine [181-183], nitrogen [184, 185], and sulphur [186, 187] functionalities are the most common among surface functional groups that have been found to enhance the performance and properties of carbon materials in various applications.

Fluorination has been shown as one of the most effective chemical methods to modify surface properties and control physical-chemical properties of various carbon materials due to the outstanding characteristics of the fluorine molecule. These characteristics include extreme reactivity, and the high electronegativity of the fluorine ion, which can lead to very strong bonds between fluorine and other materials [174, 175]. Ghimbeu et al. [188] have investigated the influence of material characteristics on fluorinated carbonaceous materials formed by exposure to molecular F_2 and atomic F released by XeF_2 decomposition, and suggest the fluorinated carbon is a good filter for hydrophobic pollutants due to the strong covalent bonding of fluorine. They also find a decrease in pore volume and specific surface area (SSA), with insignificant change in pore size distribution. Figure 2-12 shows the

nitrogen adsorption/desorption isotherms of their study on carbonaceous materials with different ordered textures, before and after different fluorination treatments.

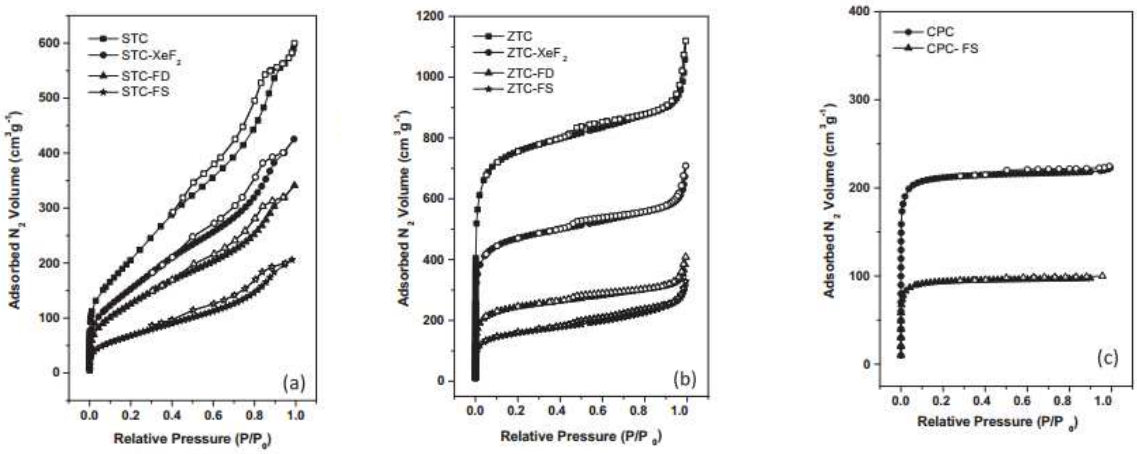

Figure 2-12. Nitrogen adsorption/desorption isotherms of carbonaceous materials with different ordered textures, microporous (CPC), mesoporous (STC), and micro/meso type (ZTC), before and after different fluorination treatments [188]**.**

Fluvio et al. [183] have demonstrated elemental fluorine-modified ordered carbonaceous materials to exhibit higher discharge potentials and power densities as well as faster reaction kinetics in primary lithium batteries, compared to commercial carbon fluorides. Jung et al. [189] and Im et al. [190] report fluorination of phenolic activated carbon and polyacrylonitrile-based activated carbon nanofibers to enhance electrochemical capacitance and CH_4 storage respectively. Leroux and Dubois [191] demonstrate improved performance of primary Li^+ ion batteries using ordered mesoporous carbonaceous materials having various amounts of fluorine, with tuning the fluorination temperature. Parmentier et al. [192] report large hysteresis and contradictory effects of the interaction of fluorinated carbonaceous materials with water, during water intrusion and adsorption/desorption measurements, with adsorption being lower on the adsorption branch, suggestive of hydrophobicity, but higher on the desorption branch as shown in Figure 2-13 suggestive of hydrophilicity.

Setoyama et. al [193], Lee et. al. [194], and Li et al. [195, 196] have shown that fluorination of activated carbon fibre (ACF) reduces N_2 adsorption and ethanol adsorption due to reduction in surface area, pore size, pore volume, and the surface energy [193, 194]. They demonstrate the level of fluorination to have an inverse relation with pore volume, surface area and mean pore width of the surface modified activate carbon fibers.

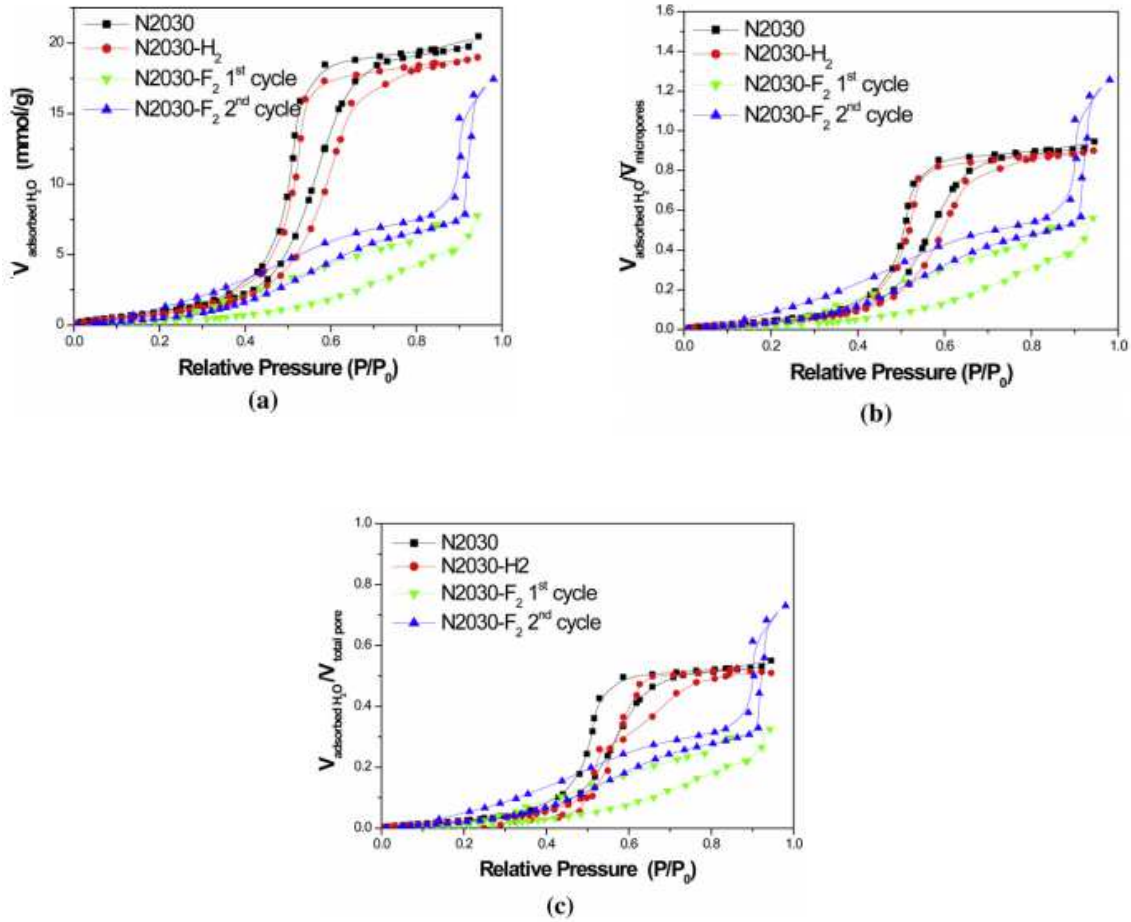

to the total pore volume

Figure 2-13. Water adsorption isotherms for N2030 (virgin), N2030-H2 (hydrogenated) and N2030-F2 (fluorine-doped) samples, (a) with a normal scale, (b) with a normalised scale with respect to the microporous volume and, (c) with a normalised scale with respect to the total pore volume [192].

In the literature, it has been reported that fluorine doped carbons form a variety of complex and highly versatile C–F bonds, in which the chemical and structural properties are influenced by either ionic or covalent bonding [175, 197]. It is shown that there are three main parameters which affect the fluorination of carbon materials [198]. The first of these is the level of graphitisation. More graphitized carbons require higher fluorination temperature. Graphitized carbons react with fluorine gas at temperature close or higher than 350°C and 600°C, forming covalent graphite fluorides of $(C_2F)_n$ and $(CF)_n$ structural types respectively

[198], whereas amorphous carbon with high fluorine content is obtained even at low temperature and even at room temperature [192]. A second variable affecting fluorination is the specific surface area. This affects the reactivity of carbons with F_2 gas, with higher specific surface area permitting lower fluorination temperature [192, 193]. Finally, surface curvature also affects fluorination, as it enhances reactivity of the carbon. Thus, fluorination temperature is also decreased when the carbon lattice exhibits curvature such as in fullerenes and nanotubes [198]. In this case fluorination is efficient at temperatures lower than 300°C [199, 200].

On the basis of simulations, Farmahini et al. [176] have recently investigated the effect of fluorine doping on hydrophobicity of SiCDCs, and the barriers for adsorption and diffusion of water vapor and CO_2 in the fluorinated and non-fluorinated structures. They have demonstrated an apparent dual effect of fluorination, showing that while fluorination generates more hydrophilic carbon surfaces, they actually act as more hydrophobic structures due to enhanced energy barriers in the disordered network of microporous carbon [176]. Although they report increase in adsorption energy and in water uptake for fluorine-doped carbon, they find that the increased adsorption is kinetically limited. They have demonstrated an increase in apparent hydrophobicity due to fluorination that is mediated by larger free energy barriers arising from stronger binding of fluid molecules inside the pore network. In their study for carbon dioxide, they have shown weakened solid-fluid binding energies in the fluorinated samples in which adsorption enthalpies and activation energy barriers are both decreased on fluorination.

Besides the works discussed above on carbon materials, there is little reported on fluorine doping and modifying the surface chemistry of CDCs, and investigations in this field is still an open issue. Chapters 5 and 6 of this thesis present a combination of characterization and experimental adsorption studies on fluorine doped CDCs.

2.7 References

[1] Presser V, Heon M, Gogotsi Y. Carbide-Derived Carbons–From Porous Networks to Nanotubes and Graphene. Adv Funct Mater. 2011;21(5):810-33.

[2] Yushin G, Dash R, Jagiello J, Fischer JE, Gogotsi Y. Carbide-Derived Carbons: Effect of Pore Size on Hydrogen Uptake and Heat of Adsorption. Adv Funct Mater. 2006;16(17):2288-93.

[3] Bonilla MR, Bae JS, Nguyen TX, Bhatia SK. Heat Treatment-Induced Structural Changes in SiC-Derived Carbons and their Impact on Gas Storage Potential. The Journal of Physical Chemistry C. 2010.

[4] Bhatia SK, Nguyen TX. Potential of silicon carbide-derived carbon for carbon capture. Ind Eng Chem Res. 2011;50(17):10380-3.

[5] Chmiola J, Yushin G, Gogotsi Y, Portet C, Simon P, Taberna PL. Anomalous increase in carbon capacitance at pore sizes less than 1 nanometer. Science. 2006;313(5794):1760.

[6] Welz S, McNallan MJ, Gogotsi Y. Carbon structures in silicon carbide derived carbon. Journal of materials processing technology. 2006;179(1):11-22.

[7] Wang J, Oschatz M, Biemelt T, Borchardt L, Senkovska I, Lohe MR, et al. Synthesis, characterization, and hydrogen storage capacities of hierarchical porous carbide derived carbon monolith. J Mater Chem. 2012;22(45):23893-9.

[8] Gogotsi Y, Nikitin A, Ye H, Zhou W, Fischer JE, Yi B, et al. Nanoporous carbide-derived carbon with tunable pore size. Nat Mater. 2003;2(9):591-4.

[9] Gogotsi Y, Dash RK, Yushin G, Yildirim T, Laudisio G, Fischer JE. Tailoring of nanoscale porosity in carbide-derived carbons for hydrogen storage. J Am Chem Soc. 2005;127(46):16006-7.

[10] Presser V, McDonough J, Yeon S-H, Gogotsi Y. Effect of pore size on carbon dioxide sorption by carbide derived carbon. Energy & Environmental Science. 2011;4(8):3059-66.

[11] Bae JS, Nguyen TX, Bhatia SK. Influence of synthesis conditions and heat treatment on the structure of Ti3SiC2-derived carbons. The Journal of Physical Chemistry C. 2009;114(2):1046-56.

[12] Nguyen TX, Bae JS, Bhatia SK. Characterization and adsorption modeling of silicon carbide-derived carbons. Langmuir. 2009;25(4):2121-32.

[13] Bae JS, Nguyen TX, Bhatia SK. Pore accessibility of Ti3SiC2-derived carbons. Carbon. 2014;68(Complete):531-41.

[14] Yushin G, Nikitin A, Gogotsi Y. Carbide derived carbon. In: Gogotsi Y, editor Nanomaterials Handbook, vol 3 CRC Press: Boca Raton,. 2006:239-82.

[15] Yushin GN, Hoffman EN, Nikitin A, Ye H, Barsoum MW, Gogotsi Y. Synthesis of nanoporous carbide-derived carbon by chlorination of titanium silicon carbide. Carbon. 2005;43(10):2075-82.

[16] Dimovski S, Nikitin A, Ye H, Gogotsi Y. Synthesis of graphite by chlorination of iron carbide at moderate temperatures. J Mater Chem. 2004;14(2):238-43.

[17] Danishevskii A, Mosina G, Smorgonskaya E, Gordeev S, Grechinskaya A, Jardin C, et al. Effect of preparation conditions on diamond cluster formation in bulk nanoporous carbon. Diamond Relat Mater. 2003;12(3):378-82.

[18] Gogotsi Y, Welz S, Ersoy DA, McNallan MJ. Conversion of silicon carbide to crystalline diamond-structured carbon at ambient pressure. Nature. 2001;411(6835):283-7.

[19] Zheng J, Ekström TC, Gordeev SK, Jacob M. Carbon with an onion-like structure obtained by chlorinating titanium carbide. J Mater Chem. 2000;10(5):1039-41.

[20] Kusunoki M, Suzuki T, Hirayama T, Shibata N, Kaneko K. A formation mechanism of carbon nanotube films on SiC (0001). Appl Phys Lett. 2000;77(4):531-3.

[21] Rose M, Kockrick E, Senkovska I, Kaskel S. High surface area carbide-derived carbon fibers produced by electrospinning of polycarbosilane precursors. Carbon. 2010;48(2):403-7.

[22] Gogotsi YG, Jeon ID, McNallan MJ. Carbon coatings on silicon carbide by reaction withchlorine-containing gases. J Mater Chem. 1997;7(9):1841-8.

[23] Nikitin A, Gogotsi, Y. Nanostructured Carbide-Derived Carbon (CDC). In: Nalwa HS, ed. Encyclopedia of Nanoscience and Nanotechnology: American Scientific Publishers: CA 2004, p. 553−74.

[24] Biscoe J, Warren B. An X-Ray Study of Carbon Black. J Appl Phys. 1942;13(6):364-71.

[25] Lozano-Castello D, Cazorla-Amoros D, Linares-Solano A, Oshida K, Miyazaki T, Kim Y, et al. Comparative characterization study of microporous carbons by HRTEM image analysis and gas adsorption. The Journal of Physical Chemistry B. 2005;109(31):15032-6.

[26] Webb PA, Orr C. Analytical Methods in Fine Particle Technology; 1997.

[27] Yang RT. Gas separation by adsorption processes: Butterworth-Heinemann; 2013.

[28] Rouquerol J, Rouquerol F, Llewellyn P, Maurin G, Sing KS. Adsorption by powders and porous solids: principles, methodology and applications: Academic press; 2013.

[29] Sircar S. Gibbsian Surface Excess for Gas Adsorption Revisited. Ind Eng Chem Res. 1999;38(10):3670-82.

[30] Sircar S. Measurement of Gibbsian surface excess. AIChE J. 2001;47(5):1169-76.

[31] Sudibandriyo M, Pan Z, Fitzgerald JE, Robinson Jr RL, Gasem KAM. Adsorption of methane, nitrogen, carbon dioxide, and their binary mixtures on dry activated carbon at 318.2 K and pressures up to 13.6 MPa. Langmuir. 2003;19(13):5323-31.

[32] Bae JS, Bhatia SK. High-pressure adsorption of methane and carbon dioxide on coal. Energy Fuels. 2006;20(6):2599-607.

[33] Keller J, Staudt R. Gas adsorption equilibria experimental method and adsorption isotherms: Springer; 2005.

[34] Van Ness H. Adsorption of Gases on Solids. Review of Role of Thermodynamics. Industrial & Engineering Chemistry Fundamentals. 1969;8(3):464-73.

[35] Myers AL. Gravimetric measurement of adsorption from binary gas mixtures. Pure Appl Chem. 1989;61(11):1949.

[36] Friederich RO, Mullins JC. Adsorption equilibria of binary hydrocarbon mixtures on homogeneous carbon black at 25 C. Industrial & Engineering Chemistry Fundamentals. 1972;11(4):439-45.

[37] Buss E. Gravimetric measurement of binary gas adsorption equilibria of methane--carbon dioxide mixtures on activated carbon. Gas separation & purification. 1995;9(3):189-97.

[38] Sing KS. Reporting physisorption data for gas/solid systems with special reference to the determination of surface area and porosity (Recommendations 1984). Pure Appl Chem. 1985;57(4):603-19.

[39] Sing K, Everett D, Haul R, Moscou L, Pierotti R, Rouquerol J, et al. Physical and biophysical chemistry division commission on colloid and surface chemistry including catalysis. Pure Appl Chem. 1985;57(4):603-19.

[40] Thommes M, Kaneko K, Neimark AV, Olivier JP, Rodriguez-Reinoso F, Rouquerol J, et al. Physisorption of gases, with special reference to the evaluation of surface area and pore size distribution (IUPAC Technical Report). Pure Appl Chem. 2015.

[41] Langmuir I. The adsorption of gases on plane surfaces of glass, mica and platinum. J Am Chem Soc. 1918;40(9):1361-403.

[42] Sips R. On the structure of a catalyst surface. The Journal of Chemical Physics. 1948;16(5):490-5.

[43] Malek A, Farooq S. Comparison of isotherm models for hydrocarbon adsorption on activated carbon. AIChE J. 1996;42(11):3191-201.

[44] Nitta T, Shigetomi T, KURO-OKA M, Katayama T. An adsorption isotherm of multi-site occupancy model for homogeneous surface. J Chem Eng Jpn. 1984;17(1):39-45.

[45] Sircar S, Rao M. Effect of adsorbate size on adsorption of gas mixtures on homogeneous adsorbents. AIChE J. 1999;45(12):2657-61.

[46] Staudt R, Dreisbach F, Keller J. Generalized Isotherms for Mono-and Multicomponent Adsorption. KLUWER INTERNATIONAL SERIES IN ENGINEERING AND COMPUTER SCIENCE. 1996:865-72.

[47] Giona M, Giustiniani M. Thermodynamics and kinetics of adsorption in the presence of geometric roughness. Separations Technology. 1996;6(2):99-110.

[48] Dreisbach F, Staudt R, Keller J. High pressure adsorption data of methane, nitrogen, carbon dioxide and their binary and ternary mixtures on activated carbon. Adsorption. 1999;5(3):215-27.

[49] Brunauer S, Emmett PH, Teller E. Adsorption of gases in multimolecular layers. J Am Chem Soc. 1938;60(2):309-19.

[50] Brunauer S, Emmett PH. The use of low temperature van der Waals adsorption isotherms in determining the surface areas of various adsorbents. J Am Chem Soc. 1937;59(12):2682-9.

[51] Ruthven DM. Principles of Adsorption and Adsorption Processes. 1984.

[52] Myers A, Prausnitz JM. Thermodynamics of mixed-gas adsorption. AIChE J. 1965;11(1):121-7.

[53] Richter E, Wilfried S, Myers AL. Effect of adsorption equation on prediction of multicomponent adsorption equilibria by the ideal adsorbed solution theory. Chem Eng Sci. 1989;44(8):1609-16.

[54] Cessford NF, Seaton NA, Düren T. Evaluation of ideal adsorbed solution theory as a tool for the design of metal–organic framework materials. Ind Eng Chem Res. 2012;51(13):4911-21.

[55] Murthi M, Snurr RQ. Effects of molecular siting and adsorbent heterogeneity on the ideality of adsorption equilibria. Langmuir. 2004;20(6):2489-97.

[56] Babarao R, Hu Z, Jiang J, Chempath S, Sandler SI. Storage and separation of CO2 and CH4 in silicalite, C168 schwarzite, and IRMOF-1: a comparative study from Monte Carlo simulation. Langmuir. 2007;23(2):659-66.

[57] Keskin S, Liu J, Johnson JK, Sholl DS. Testing the accuracy of correlations for multicomponent mass transport of adsorbed gases in metal− organic frameworks: Diffusion of H2/CH4 mixtures in CuBTC. Langmuir. 2008;24(15):8254-61.

[58] Bae Y-S, Mulfort KL, Frost H, Ryan P, Punnathanam S, Broadbelt LJ, et al. Separation of CO2 from CH4 using mixed-ligand metal− organic frameworks. Langmuir. 2008;24(16):8592-8.

[59] Liu B, Yang Q, Xue C, Zhong C, Chen B, Smit B. Enhanced Adsorption Selectivity of Hydrogen/Methane Mixtures in Metal− Organic Frameworks with Interpenetration: A Molecular Simulation Study. The Journal of Physical Chemistry C. 2008;112(26):9854-60.

[60] Yang Q, Xue C, Zhong C, Chen JF. Molecular simulation of separation of CO2 from flue gases in CU-BTC metal-organic framework. AIChE J. 2007;53(11):2832-40.

[61] Costa E, Sotelo J, Calleja G, Marron C. Adsorption of binary and ternary hydrocarbon gas mixtures on activated carbon: experimental determination and theoretical prediction of the ternary equilibrium data. AIChE J. 2004;27(1):5-12.

[62] Suwanayuen S, Danner RP. A gas adsorption isotherm equation based on vacancy solution theory. AIChE J. 1980;26(1):68-76.

[63] Ding L, Bhatia S. Application of heterogeneous vacancy solution theory to characterization of microporous solids. Carbon. 2001;39(14):2215-29.

[64] Hu X, Do DD. Comparing various multicomponent adsorption equilibrium models. AIChE J. 1995;41(6):1585-92.

[65] Valenzuela D, Myers A, Talu O, Zwiebel I. Adsorption of gas mixtures: effect of energetic heterogeneity. AIChE J. 1988;34(3):397-402.

[66] Wang K, Qiao S, Hu X. On the performance of HIAST and IAST in the prediction of multicomponent adsorption equilibria. Sep Purif Technol. 2000;20(2):243-9.

[67] Sircar S. Influence of adsorbate size and adsorbent heterogeneity of IAST. AIChE J. 1995;41(5):1135-45.

[68] Costa E, Sotelo J, Calleja G, Marron C. Adsorption of binary and ternary hydrocarbon gas mixtures on activated carbon: experimental determination and theoretical prediction of the ternary equilibrium data. AIChE J. 1981;27(1):5-12.

[69] Dubinin M. The potential theory of adsorption of gases and vapors for adsorbents with energetically nonuniform surfaces. Chem Rev (Washington, DC, U S). 1960;60(2):235-41.

[70] Dubinin M. Fundamentals of the theory of adsorption in micropores of carbon adsorbents: characteristics of their adsorption properties and microporous structures. Carbon. 1989;27(3):457-67.

[71] Shapiro AA, Stenby EH. Potential theory of multicomponent adsorption. J Colloid Interface Sci. 1998;201(2):146-57.

[72] Monsalvo MA, Shapiro AA. Modeling adsorption of binary and ternary mixtures on microporous media. Fluid Phase Equilib. 2007;254(1):91-100.

[73] Monsalvo MA, Shapiro AA. Study of high-pressure adsorption from supercritical fluids by the potential theory. Fluid Phase Equilib. 2009;283(1):56-64.

[74] Bjørner MG, Shapiro AA, Kontogeorgis GM. Potential theory of adsorption for associating mixtures: possibilities and limitations. Ind Eng Chem Res. 2013;52(7):2672-84.

[75] Kontogeorgis GM, Voutsas EC, Yakoumis IV, Tassios DP. An equation of state for associating fluids. Ind Eng Chem Res. 1996;35(11):4310-8.

[76] Evans R. The nature of the liquid-vapour interface and other topics in the statistical mechanics of non-uniform, classical fluids. Advances in Physics. 1979;28(2):143-200.

[77] Tarazona P. Free-energy density functional for hard spheres. Phys Rev A. 1985;31(4):2672.

[78] Ravikovitch PI, Haller GL, Neimark AV. Density functional theory model for calculating pore size distributions: pore structure of nanoporous catalysts. Adv Colloid Interface Sci. 1998;76:203-26.

[79] Do DD, Wang K. Dual diffusion and finite mass exchange model for adsorption kinetics in activated carbon. AIChE J. 1998;44(1):68-82.

[80] Bhatia SK. Density functional theory analysis of the influence of pore wall heterogeneity on adsorption in carbons. Langmuir. 2002;18(18):6845-56.

[81] Nguyen TX, Bhatia SK. Characterization of pore wall heterogeneity in nanoporous carbons using adsorption: the slit pore model revisited. The Journal of Physical Chemistry B. 2004;108(37):14032-42.

[82] Nguyen TX, Bhatia SK. Probing the pore wall structure of nanoporous carbons using adsorption. Langmuir. 2004;20(9):3532-5.

[83] Do DD. Adsorption analysis: equilibria and kinetics: Imperial College Press; 1998.

[84] Kärger J, Ruthven DM, Theodorou DN. Diffusion in nanoporous materials: John Wiley & Sons; 2012.

[85] Rees LVC, Shen D. Characterization of microporous sorbents by frequency-response methods. Gas separation & purification. 1993;7(2):83-9.

[86] Bülow M, Schlodder H, Rees L, Richards R. Molecular mobility of hydrocarbon ZSM5/silicalite systems studied by sorption uptake and frequency response methods. Stud Surf Sci Catal. 1986;28:579-86.

[87] Eic M, Ruthven DM. A new experimental technique for measurement of intracrystalline diffusivity. Zeolites. 1988;8(1):40-5.

[88] Hufton JR, Ruthven DM. Diffusion of light alkanes in silicalite studied by the zero length column method. Ind Eng Chem Res. 1993;32(10):2379-86.

[89] Brandani S, Ruthven DM. Analysis of ZLC desorption curves for gaseous systems. Adsorption. 1996;2(2):133-43.

[90] Loos JBWP, Verheijen PJT, Moulijn JA. Improved estimation of zeolite diffusion coefficients from zero-length column experiments. Chem Eng Sci. 2000;55(1):51-65.

[91] Brandani S, Ruthven DM. Moments analysis of the zero length column method. Ind Eng Chem Res. 1996;35(1):315-9.

[92] Qiao SZ, Bhatia SK. Diffusion of linear paraffins in nanoporous silica. Ind Eng Chem Res. 2005;44(16):6477-84.

[93] Ruthven D, Brandani F. ZLC response for systems with surface resistance control. Adsorption. 2005;11(1):31-4.

[94] Ruthven DM, Vidoni A. ZLC diffusion measurements: Combined effect of surface resistance and internal diffusion. Chem Eng Sci. 2011.

[95] Bhatia SK. Transport in bidisperse adsorbents: significance of the macroscopic adsorbate flux. Chem Eng Sci. 1997;52(8):1377-86.

[96] Kärger J, Ruthven DM. Diffusion in zeolites. Willey & Sons, New York. 1992.

[97] Wakao N, Smith JM. Diffusion in catalyst pellets. Chem Eng Sci. 1962;17(11):825-34.

[98] Schneider P, Smith JM. Chromatographic study of surface diffusion. AIChE J. 1968;14(6):886-95.

[99] Bhatia S. Transport in bidisperse adsorbents: significance of the macroscopic adsorbate flux. Chem Eng Sci. 1997;52(8):1377-86.

[100] Ruckenstein E, Vaidyanathan A, Youngquist G. Sorption by solids with bidisperse pore structures. Chem Eng Sci. 1971;26(9):1305-18.

[101] Seidel A, Gelbin D. Breakthrough curves for single solutes in beds of activated carbon with a broad pore-size distribution—I. Mathematical models of breakthrough curves in beds of activated carbon. Chem Eng Sci. 1986;41(3):541-8.

[102] Barrer RM. Flow into and through zeolite beds and compacts. Langmuir. 1987;3(3):309-15.

[103] Kärger J. Mass transfer through beds of zeolite crystallites and the paradox of the evaporation barrier. Langmuir. 1988;4(6):1289-92.

[104] Gray PG, Do DD. Adsorption and desorption of gaseous sorbates on a bidispersed particle with Freundlich isotherm: III. Contribution of surface diffusion to the sorption

dynamics of sulphur dioxide on activated carbon. Gas separation & purification. 1990;4(3):149-57.

[105] Hu X, Rao GN, Do DD. Effect of energy distribution on sorption kinetics in bidispersed particles. AIChE J. 1993;39(2):249-61.

[106] Do DD, Hu X. An energy-distributed model for adsorption kinetics in large heterogeneous microporous particles. Chem Eng Sci. 1993;48(11):2119-27.

[107] Bhatia SK, Gray PG, Do DD. Modelling of sorption of gaseous sorbates in bidispersed structured solids:: The concept of heterogeneity of the microphase. Gas separation & purification. 1991;5(1):49-55.

[108] Ding LP, Bhatia SK, Liu F. Kinetics of adsorption on activated carbon: application of heterogeneous vacancy solution theory. Chem Eng Sci. 2002;57(18):3909-28.

[109] Do D, Wang K. Dual diffusion and finite mass exchange model for adsorption kinetics in activated carbon. AIChE J. 1998;44(1):68-82.

[110] Fletcher AJ, Thomas KM. Adsorption and desorption kinetics of n-octane and n-nonane vapors on activated carbon. Langmuir. 1999;15(20):6908-14.

[111] Kapoor A, Yang RT. Surface diffusion on energetically heterogeneous surfaces--an effective medium approximation approach. Chem Eng Sci. 1990;45(11):3261-70.

[112] Kapoor A, Yang RT, Wong C. Surface diffusion. Catalysis Reviews—Science and Engineering. 1989;31(1-2):129-214.

[113] Higashi K, Ito H, Oishi J. Surface diffusion phenomena in gaseous diffusion. I. Surface diffusion of pure gas. Nippon Genshiryoku Gakkaishi (Japan). 1963;5.

[114] Smith RK, Metzner AB. Rates of surface migration of physically adsorbed gases. The Journal of Physical Chemistry. 1964;68(10):2741-7.

[115] Weaver JA, Metzner AB. The surface transport of adsorbed molecules. AIChE J. 1966;12(4):655-61.

[116] Yang RT, Fenn JB, Haller GL. Modification to the Higashi model for surface diffusion. AIChE J. 1973;19(5):1052-3.

[117] Thakur SC, Brown LF, Haller GL. Gas-adsorbate collisional effects and surface diffusion in porous materials. AIChE J. 1980;26(3):355-63.

[118] Thakur SC, Brown LF. Effects of gas-adsorbate momentum transfer on the movement of a mobile adsorbed phase over a uniform surface. AIChE J. 1983;29(4):696-8.

[119] Do DD. A model for surface diffusion of ethane and propane in activated carbon. Chem Eng Sci. 1996;51(17):4145-58.

[120] Liu H, Ruthven DM. Diffusion in carbon molecular sieves. Fundamentals of Adsorption: Springer 1996, p. 529-36.

[121] Kapoor A, Yang RT. Surface diffusion on energetically heterogeneous surfaces. AIChE J. 1989;35(10):1735-8.

[122] Rutherford S, Do D. Adsorption dynamics of carbon dioxide on a carbon molecular sieve 5A. Carbon. 2000;38(9):1339-50.

[123] Nguyen C, Do D. Dual Langmuir kinetic model for adsorption in carbon molecular sieve materials. Langmuir. 2000;16(4):1868-73.

[124] Qinglin H, Sundaram SM, Farooq S. Revisiting transport of gases in the micropores of carbon molecular sieves. Langmuir. 2003;19(2):393-405.

[125] Qinglin H, Farooq S, Karimi IA. Prediction of binary gas diffusion in carbon molecular sieves at high pressure. AIChE J. 2004;50(2):351-67.

[126] Wang Y, LeVan MD. Master curves for mass transfer in bidisperse adsorbents for pressure-swing and volume-swing frequency response methods. AIChE J. 2011;57(8):2054-69.

[127] Kärger J, Caro J. Interpretation and correlation of zeolitic diffusivities obtained from nuclear magnetic resonance and sorption experiments. Journal of the Chemical Society, Faraday Transactions 1: Physical Chemistry in Condensed Phases. 1977;73:1363-76.

[128] Kärger J, Pfeifer H. Nuclear magnetic resonance measurement of mass transfer in molecular sieve crystallites. J Chem Soc, Faraday Trans. 1991;87(13):1989-96.

[129] Zimmermann NE, Balaji SP, Keil FJ. Surface Barriers of Hydrocarbon Transport Triggered by Ideal Zeolite Structures. The Journal of Physical Chemistry C. 2012;116(5):3677-83.

[130] Zimmermann N, Smit B, Keil F. On the effects of the external surface on the equilibrium transport in zeolite crystals. The Journal of Physical Chemistry C. 2009;114(1):300-10.

[131] Zimmermann N, Jakobtorweihen S, Beerdsen E, Smit B, Keil F. In-depth study of the influence of host-framework flexibility on the diffusion of small gas molecules in one-dimensional zeolitic pore systems. The Journal of Physical Chemistry C. 2007;111(46):17370-81.

[132] Zimmermann NE, Haranczyk M, Sharma M, Liu B, Smit B, Keil FJ. Adsorption and diffusion in zeolites: the pitfall of isotypic crystal structures. Mol Simul. 2011;37(12):986-9.

[133] Webley PA. Adsorption technology for CO2 separation and capture: a perspective. Adsorption. 2014;20(2-3):225-31.

[134] Furmaniak S, Gauden PA, Terzyk AP, Rychlicki G. Water adsorption on carbons—Critical review of the most popular analytical approaches. Adv Colloid Interface Sci. 2008;137(2):82-143.

[135] Mowla D, Do D, Kaneko K. Adsorption of water vapor on activated carbon: a brief overview. Chem Phys Carbon. 2003;28:229-.

[136] Nguyen TX, Bhatia SK. How Water Adsorbs in Hydrophobic Nanospaces. The Journal of Physical Chemistry C. 2011;115(33):16606-12.

[137] Bhatia S, Nguyen T. Potential of silicon carbide-derived carbon for carbon capture. Ind Eng Chem Res. 2011;50(17):10380-3.

[138] Ohba T, Kanoh H, Kaneko K. Affinity transformation from hydrophilicity to hydrophobicity of water molecules on the basis of adsorption of water in graphitic nanopores. J Am Chem Soc. 2004;126(5):1560-2.

[139] Pierce C, Smith RN. The Adsorption–Desorption Hysteresis in Relation to Capillarity of Adsorbents. The Journal of Physical Chemistry. 1950;54(6):784-94.

[140] Dubinin M. Water vapor adsorption and the microporous structures of carbonaceous adsorbents. Carbon. 1980;18(5):355-64.

[141] Dubinin M, Serpinsky V. Isotherm equation for water vapor adsorption by microporous carbonaceous adsorbents. Carbon. 1981;19(5):402-3.

[142] Do D, Junpirom S, Do H. A new adsorption–desorption model for water adsorption in activated carbon. Carbon. 2009;47(6):1466-73.

[143] Horikawa T, Sekida T, Hayashi Ji, Katoh M, Do DD. A new adsorption–desorption model for water adsorption in porous carbons. Carbon. 2011;49(2):416-24.

[144] Wang H-J, Kleinhammes A, McNicholas TP, Liu J, Wu Y. Water adsorption in nanoporous carbon characterized by in situ NMR: measurements of pore size and pore size distribution. The Journal of Physical Chemistry C. 2014;118(16):8474-80.

[145] Rasaiah JC, Garde S, Hummer G. Water in nonpolar confinement: From nanotubes to proteins and beyond*. Annu Rev Phys Chem. 2008;59:713-40.

[146] Barton SS, Evans MJ, MacDonald JA. The adsorption of water vapor by porous carbon. Carbon. 1991;29(8):1099-105.

[147] Tao Y, Muramatsu H, Endo M, Kaneko K. Evidence of Water Adsorption in Hydrophobic Nanospaces of Highly Pure Double-Walled Carbon Nanotubes. J Am Chem Soc. 2010;132(4):1214-5.

[148] Barton S, Evans M, MacDonald J. An equation describing water vapour absorption on porous carbon. Carbon. 1992;30(1):123-4.

[149] Gauden PA. Does the Dubinin–Serpinsky theory adequately describe water adsorption on adsorbents with high-energy centers? J Colloid Interface Sci. 2005;282(2):249-60.

[150] Talu O, Meunier F. Adsorption of associating molecules in micropores and application to water on carbon. AIChE J. 1996;42(3):809-19.

[151] McCallum C, Bandosz T, McGrother S, Müller E, Gubbins K. A molecular model for adsorption of water on activated carbon: comparison of simulation and experiment. Langmuir. 1999;15(2):533-44.

[152] Rutherford S. Modeling water adsorption in carbon micropores: study of water in carbon molecular sieves. Langmuir. 2006;22(2):702-8.

[153] Malakhov A, Volkov V. Cooperative Multimolecular Sorption Equation: Application of an Alcohol-Poly (1-trimethylsilyl-1-propyne) System. POLYMER SCIENCE SERIES AC/C OF VYSOKOMOLEKULIARNYE SOEDINENIIA. 2000;42(10):1120-6.

[154] Do D, Do H. A model for water adsorption in activated carbon. Carbon. 2000;38(5):767-73.

[155] Neitsch M, Heschel W, Suckow M. Water vapor adsorption by activated carbon: a modification to the isotherm model of Do and Do. Carbon. 2001;39(9):1437-8.

[156] Horikawa T, Sakao N, Sekida T, Hayashi Ji, Do D, Katoh M. Preparation of nitrogen-doped porous carbon by ammonia gas treatment and the effects of N-doping on water adsorption. Carbon. 2012;50(5):1833-42.

[157] Yao X, Li L, Li H, He S, Liu Z, Ma W. A new model for calculating the adsorption equilibrium constant of water vapor in micropores of activated carbon. Computational Materials Science. 2014;89:137-41.

[158] Kimura T, Kanoh H, Kanda T, Ohkubo T, Hattori Y, Higaonna Y, et al. Cluster-associated filling of water in hydrophobic carbon micropores. The Journal of Physical Chemistry B. 2004;108(37):14043-8.

[159] Lodewyckx P. The effect of water uptake in ultramicropores on the adsorption of water vapour in activated carbon. Carbon. 2010;48(9):2549-53.

[160] Kockrick E, Schrage C, Borchardt L, Klein N, Rose M, Senkovska I, et al. Ordered mesoporous carbide derived carbons for high pressure gas storage. Carbon. 2010;48(6):1707-17.

[161] Gregg SJaS, K.S.W. Adsorption, Surface Area and Porosity. 1982.

[162] Bradley R, Rand B. On the physical adsorption of vapors by microporous carbons. J Colloid Interface Sci. 1995;169(1):168-76.

[163] Vartapetyan RS, Voloshchuk AbM. The mechanism of the adsorption of water molecules on carbon adsorbents. Russ Chem Rev. 1995;64(11):985.

[164] Alcañiz-Monge J, Linares-Solano A, Rand B. Water adsorption on activated carbons: study of water adsorption in micro-and mesopores. The Journal of Physical Chemistry B. 2001;105(33):7998-8006.

[165] Müller EA, Gubbins KE. Molecular simulation study of hydrophilic and hydrophobic behavior of activated carbon surfaces. Carbon. 1998;36(10):1433-8.

[166] Hummer G, Rasaiah JC, Noworyta JP. Water conduction through the hydrophobic channel of a carbon nanotube. Nature. 2001;414(6860):188-90.

[167] Slasli A, Jorge M, Stoeckli F, Seaton N. Water adsorption by activated carbons in relation to their microporous structure. Carbon. 2003;41(3):479-86.

[168] Striolo A, Chialvo AA, Cummings PT, Gubbins KE. Water adsorption in carbon-slit nanopores. Langmuir. 2003;19(20):8583-91.

[169] Jorge M, Schumacher C, Seaton NA. Simulation study of the effect of the chemical heterogeneity of activated carbon on water adsorption. Langmuir. 2002;18(24):9296-306.

[170] Brennan JK, Thomson KT, Gubbins KE. Adsorption of water in activated carbons: effects of pore blocking and connectivity. Langmuir. 2002;18(14):5438-47.

[171] Iiyama T, Nishikawa K, Suzuki T, Kaneko K. Study of the structure of a water molecular assembly in a hydrophobic nanospace at low temperature with in situ X-ray diffraction. Chem Phys Lett. 1997;274(1):152-8.

[172] Sliwinska-Bartkowiak M, Dudziak G, Sikorski R, Gras R, Gubbins K, Radhakrishnan R. Dielectric studies of freezing behavior in porous materials: Water and methanol in activated carbon fibres. Phys Chem Chem Phys. 2001;3(7):1179-84.

[173] Sanfelix PC, Holloway S, Kolasinski K, Darling G. The structure of water on the (0001) surface of graphite. Surf Sci. 2003;532:166-72.

[174] Lee Y-S. Syntheses and properties of fluorinated carbon materials. J Fluorine Chem. 2007;128(4):392-403.

[175] Touhara H, Okino F. Property control of carbon materials by fluorination. Carbon. 2000;38(2):241-67.

[176] Farmahini AH, Sholl DS, Bhatia SK. Fluorinated carbide-derived carbon: more hydrophilic, yet apparently more hydrophobic. J Am Chem Soc. 2015.

[177] Ghimbeu CM, Gadiou R, Dentzer J, Schwartz D, Vix-Guterl C. Influence of surface chemistry on the adsorption of oxygenated hydrocarbons on activated carbons. Langmuir. 2010;26(24):18824-33.

[178] Hulicova D, Yamashita J, Soneda Y, Hatori H, Kodama M. Supercapacitors prepared from melamine-based carbon. Chem Mater. 2005;17(5):1241-7.

[179] Song J, Xu T, Gordin ML, Zhu P, Lv D, Jiang YB, et al. Nitrogen-Doped Mesoporous Carbon Promoted Chemical Adsorption of Sulfur and Fabrication of High-Areal-Capacity Sulfur Cathode with Exceptional Cycling Stability for Lithium-Sulfur Batteries. Adv Funct Mater. 2014;24(9):1243-50.

[180] Vijayaraj M, Gadiou R, Anselme K, Ghimbeu C, Vix-Guterl C, Orikasa H, et al. The influence of surface chemistry and pore size on the adsorption of proteins on nanostructured carbon materials. Adv Funct Mater. 2010;20(15):2489-99.

[181] Sansotera M, Navarrini W, Resnati G, Metrangolo P, Famulari A, Bianchi CL, et al. Preparation and characterization of superhydrophobic conductive fluorinated carbon blacks. Carbon. 2010;48(15):4382-90.

[182] Nakajima T. Fluorine-carbon and Fluoride-carbon Materials: Marcel Dekker; 1994.

[183] Fulvio PF, Brown SS, Adcock J, Mayes RT, Guo B, Sun X-G, et al. Low-temperature fluorination of soft-templated mesoporous carbons for a high-power lithium/carbon fluoride battery. Chem Mater. 2011;23(20):4420-7.

[184] Raymundo-Piñero E, Cadek M, Beguin F. Tuning carbon materials for supercapacitors by direct pyrolysis of seaweeds. Adv Funct Mater. 2009;19(7):1032-9.

[185] Frackowiak E, Lota G, Machnikowski J, Vix-Guterl C, Béguin F. Optimisation of supercapacitors using carbons with controlled nanotexture and nitrogen content. Electrochim Acta. 2006;51(11):2209-14.

[186] Xia Y, Zhu Y, Tang Y. Preparation of sulfur-doped microporous carbons for the storage of hydrogen and carbon dioxide. Carbon. 2012;50(15):5543-53.

[187] Wohlgemuth S-A, White RJ, Willinger M-G, Titirici M-M, Antonietti M. A one-pot hydrothermal synthesis of sulfur and nitrogen doped carbon aerogels with enhanced electrocatalytic activity in the oxygen reduction reaction. Green Chem. 2012;14(5):1515-23.

[188] Ghimbeu CM, Guerin K, Dubois M, Hajjar-Garreau S, Vix-Guterl C. Insights on the reactivity of ordered porous carbons exposed to different fluorinating agents and conditions. Carbon. 2015;84:567-83.

[189] Jung M-J, Jeong E, Kim S, Lee SI, Yoo J-S, Lee Y-S. Fluorination effect of activated carbon electrodes on the electrochemical performance of electric double layer capacitors. J Fluorine Chem. 2011;132(12):1127-33.

[190] Im JS, Jung MJ, Lee Y-S. Effects of fluorination modification on pore size controlled electrospun activated carbon fibers for high capacity methane storage. J Colloid Interface Sci. 2009;339(1):31-5.

[191] Leroux F, Dubois M. Origin of the highly enhanced porosity of styryl LDH hybrid-type carbon replicas and study of a subsequent fluorination at low-temperature. J Mater Chem. 2006;16(46):4510-20.

[192] Parmentier J, Schlienger S, Dubois M, Disa E, Masin F, Centeno TA. Structural/textural properties and water reactivity of fluorinated activated carbons. Carbon. 2012;50(14):5135-47.

[193] Setoyama N, Li G, Kaneko K, Okino F, Ishikawa R, Kanda M, et al. Nitrogen adsorption on fluorinated activated carbon fiber. Adsorption. 1996;2(4):293-7.

[194] Lee YS, Kim YH, Hong JS, Suh JK, Cho GJ. The adsorption properties of surface modified activated carbon fibers for hydrogen storages. Catal Today. 2007;120(3):420-5.

[195] Li G, Kaneko K, Ozeki S, Okino F, Touhara H. Water rejective nature of fluorinated microporous carbon fibers. Langmuir. 1995;11(3):716-7.

[196] Li G, Kaneko K, Okino F, Touhara H, Ishikawa R, Kanda M. Adsorption behavior of polar molecules in fluorinated micropores. J Colloid Interface Sci. 1995;172(2):539-40.

[197] Panich A. Nuclear magnetic resonance study of fluorine–graphite intercalation compounds and graphite fluorides. Synth Met. 1999;100(2):169-85.

[198] Mar M, Ahmad Y, Dubois M, Guérin K, Batisse N, Hamwi A. Dual C F bonding in fluorinated exfoliated graphite. J Fluorine Chem. 2014.

[199] Banerjee S, Hemraj-Benny T, Wong SS. Covalent surface chemistry of single-walled carbon nanotubes. Adv Mater (Weinheim, Ger). 2005;17(1):17-29.

[200] Zhang W, Dubois M, Guérin K, Bonnet P, Kharbache H, Masin F, et al. Effect of curvature on C–F bonding in fluorinated carbons: from fullerene and derivatives to graphite. Phys Chem Chem Phys. 2010;12(6):1388-98.

Chapter 3 : Slow diffusion of methane in ultra-micropores of silicon carbide-derived carbon*

*Published in *Carbon*, Vol. 77, 560-576

We investigate macroscopic uptake kinetics of CH_4 in silicon carbide-derived carbon (SiC-DC). Ultra-microprosity in SiC-DC is found based on CO_2 adsorption at 273 K, but which has poor accessibility to Ar at 87 K. The adsorption kinetics of CH_4 is found to follow a bidisperse pore structure model, considering relatively rapid particle scale diffusion in large micropores, and a much slower local grain (or microparticle) scale diffusion in ultra-micropores. The grain scale activation energies are comparable with values for carbon molecular sieves, and consistent with values expected for the size range of the ultra-micropores, while the activation energies for transport in the larger particle scale micropores are comparable to those for conventional activated carbons. The particle scale diffusivities compare well with the results of equilibrium molecular dynamics simulations using a hybrid reverse Monte Carlo simulation constructed model of SiC-DC, with similar activation energy. On the other hand microscopic quasi-elastic neutron scattering measurements are found to probe only short-range barriers with lower activation energy. It is anticipated that ultra-micropores will not make a significant contribution to the transport in any membrane or adsorption-based process based on SiC-DC, due to the extremely slow transport in these ultra-micropores and their small pore volume.

3.1 Introduction

Carbide Derived Carbons (CDCs) [1], synthesised by the halogenation of metal carbides [1-3] are attracting increasing attention for potential application in gas separation and storage [4-9] and in electrochemical energy storage [1], owing to their ability to possess high surface area and tunable pore sizes, and their ease of synthesis from natural carbides. CDCs from different carbide precursors have been investigated by several groups [8, 10-15] using various techniques such as X-ray diffraction (XRD), transmission electron microscopy (TEM), Raman spectroscopy, and adsorption based characterization to understand the microstructural changes occurring during their preparation and post-synthesis treatment. Various kinds of CDCs have been explored by different research groups and specific surface areas of up to 3000 m^2g^{-1} [16] with small pore sizes have been reported [2-5, 14, 17-20]. These studies have shown CDCs to comprise a highly microporous structure, generally lacking macropores. On

the other hand conventional microporous activated carbons are known to possess a bidisperse structure, with macropores which provide the pathways enabling access to micropores in the particle interior [21, 22]. Surprisingly, evidence for a bidisperse structure for CDCs, even for purely nanoporous samples, has recently been obtained in this laboratory [15], with CO_2 adsorption at 273 K on Ti_3SiC_2 showing the presence of significant ultra-microporosity in the 0.33-0.37 nm pore size range. The existence of such ultra-microporosity in CDCs was previously unrecognized because ultra-micropores of this size are largely inaccessible to the most widely used characterization gases such as argon and nitrogen at low temperatures. Indeed, we have reported some inaccessibility of the pore space and internal structure to Ar at 87 K for nano-sized SiC-DC [5, 18] and Ti_3SiC_2-based CDCs [14].

Despite the intense efforts devoted to the characterization of CDCs, there has been no published report on the dynamics and the diffusion of gases in the internal structure of CDCs. A detailed investigation combining characterization and kinetic studies is therefore necessary to obtain a comprehensive understanding of the impact of pore structure and specifically the ultra-microporosity of CDC materials on adsorption behaviour. Such fundamental understanding of the transport of gases in the internal structure of CDCs exhibiting a bidisperse pore size distribution is very important for synthesizing advanced porous carbons for specific applications. We note that while ultra-micropores are usually defined as those smaller than 0.7 nm, we are particularly concerned here with those in the 0.32-0.37 nm range.

The uptake dynamics of gases in porous adsorbents has been a topic of considerable importance and significance in the field of gas adsorption, and extensive effort has been devoted to this in the literature [21, 22]. The adsorption of an adsorbate species from the bulk gas phase into a particle is normally described by a two-step process, involving transport through the film to the outer surface of the particle and diffusion into the particle. Depending on the dimensions of the adsorbent pores, structure and process conditions, the mechanism of mass transport in porous solids may be governed by pore diffusion, micropore diffusion (sometimes referred to as surface diffusion), or an interfacial barrier resistance.

Numerous mathematical models of adsorption dynamics in heterogeneous and bidisperse structured porous solids have been reported in the literature [23-27]. The various models can be loosely categorised as those that consider the transport in the micropores to be significant at the particle scale, and those that confine this transport locally to the microscale. Among the

earliest of the models is that of Wakao and Smith [28], which considers the particle scale diffusion of gases in both micropores and macropores, assuming a random pore structure, with no account of adsorption effects. This assumption of negligible adsorption was subsequently relaxed by Schneider and Smith [26], who considered simultaneous gas and adsorbate diffusion in macropores and micropores respectively over the whole particle, while remaining at equilibrium with a linear isotherm. Such an approach assumes rapid mass transfer between the macropore and micropore phases, as well as high permeability in the micropores, comparable to that in the macropores. However, when the micropore permeability is significantly smaller than that of the macropores, the diffusion in the micropores will be locally restricted to a scale much smaller than the particle size. Models of the adsorption dynamics in this limit assume the adsorbent particles to be bidisperse, comprising agglomerates of microporous microparticle called grains in which local transport occurs in micropores, with the inter-grain macropores providing the pathways for particle-scale gas phase transport [23-25]. This model was first proposed by Ruckenstein et al. [25] who showed good agreement with data when the diffusion of the adsorbed species is assumed to occur only over the small length scale of the individual microspheres. While the approach has found much support in the subsequent literature, in some studies of adsorption in activated carbon the microstructure has been divided into two types of independent micropore phases with negligible particle scale macropore resistance [29]. Subsequent work has seen modifications to the above approach to include a particle scale flux contribution from the micropores, following Barrer [30] as well as Karger [31], who propose the hopping of molecules between the microparticles through the macropore spaces. While Do and co-workers [32-34] incorporate this flux through an empirical surface diffusion of the adsorbed phase, Bhatia and co-workers [35, 36] consider a microparticle through-flux arising from the macropore concentration variation around the microparticle surface. However, this through flux is found to be generally negligible [23], since the microparticle permeability is generally far smaller than that corresponding to the macroscale transport. Subsequently, some studies have resurrected the Schneider and Smith [26] approach, considering particle scale diffusion in the micropores with negligible transport resistance at the microscale, but with a nonlinear isotherm and finite mass exchange rate between macropores and micropores [36-38]. In other work, Loughlin et al. [39], Qinglin et al. [40, 41] and Wang and LeVan [42] have considered a surface barrier resistance in series with a micropore diffusion resistance for the diffusion of

gases in carbon molecular sieves, with negligible direct contribution of micropores to the macroscale flux.

Apart from the development of the models, the detailed mechanism of surface diffusion has also attracted much attention in the literature [43, 44]. Several studies have viewed surface diffusion as hopping of migrating molecules between neighbouring adsorbing sites [45-50], or as continuously adsorbing into and evaporating from the microparticle units [51]. Kapoor and Yang [52] proposed a parallel-path model (PPM) for surface diffusion on heterogeneous surface. In their model, the surface is regarded as consisting of a series of parallel paths in a way that each path has a uniform but different energy. They have further studied the influence of the connectivity among the energetic sites on overall sorption kinetics based on the effective medium approximation [43].

Monte Carlo and molecular dynamics simulations methods have been also used to describe transport of gases in carbons [53-55]. Jepps et al. [53] have examined the transport of CH_4 in microporous carbon by performing equilibrium and nonequilibrium molecular dynamics simulations over a range of pore sizes and densities. They have shown density dependence of transport diffusion coefficient for CH_4 transport in carbon slit pores of different widths and two different trends in the variation of transport coefficient with pore density have been demonstrated. In small pores where fluid-solid interactions dominate, it is shown the transport coefficient decreases with increasing pore density while in the wider pores, the transport coefficient increases as the fluid density increases beyond the Henry's law regime, due to effects of fluid-fluid interaction. Strong dependence on the pore size of the relation between the transport coefficient and the density has been also shown by Nicholson [55] and recently by Bhatia et al. [54].

Here, we investigate methane uptake kinetics in silicon carbide-derived carbon using a volumetric method. It is shown this type of adsorbent has a bidisperse micropore distribution, with the microporosity comprising significant ultra-micropores. Based on the recent models reviewed above for activated carbon and other bidisperse structure porous adsorbents, the internal structure of SiC-DC is assumed to have ultra-microporous topologically connected networks in small independent domains called grains with larger micropores forming the inter-grain spaces. It is shown the kinetics of CH_4 adsorption is governed by two distinct diffusional resistances, arising from slow diffusion in the grain ultra-micropores and faster

diffusion in the larger particle scale micropores forming the intergrain pathways. We study the diffusion of methane in SiC-DC, comparing the macroscopic uptake kinetics data with self-diffusivities obtained from microscopic molecular dynamics (MD) simulations and quasi-elastic neutron scattering (QENS) measurements. In addition, we combine the characterization results obtained from structural analysis of SiC-DC, and the predictions of the experimental adsorption isotherm using our finite wall thickness model (FWT-NLDFT) approach [56], with the adsorption dynamics studies to gain understanding of the microstructure of the CDC.

3.2 Experimental section

3.2.1 Synthesis of SiC-DC1073

The SiC-DC samples used were synthesized in our laboratory by chlorine treatment of two different micrometer-sized SiC powders of nominal diameter 20 μm (Sigma Aldrich) and 1 μm (Alfa Aesar) at 1073 K. A known mass of SiC powder is initially subjected to ultra-high purity argon (BOC Gases, 99.999%) in a tube furnace and then a heating rate of 30 K/min is employed to raise the temperature of the furnace to 1073 K. Once the desired temperature is reached, the argon flow is replaced with ultra-high purity chlorine (BOC Gases, 99.9%) to begin the chlorine treatment. By-products such as silicon chloride ($SiCl_4$) vapor and the residual chlorine are captured in sodium hydroxide solution. After completion of reaction, the remaining carbon (CDC) is purged with argon flow at 1073 K for 30 min in the tube furnace, and then slowly cooled down to ambient temperature while purging. Further details of the procedure are available in an earlier publication from this laboratory [14].

3.2.2 Microscopic characterization of SiC-DC1073

The particle size distributions of SiC-DC samples are determined by an optical method based on light scattering analysis using a laser particle size analyser (Mastersizer 2000, Malvern Instruments, UK). The structural information on the SiC-DC1073 1 μm and 20 μm samples is obtained using a transmission electron microscope *(*JEOL 2100 at 200 Kv), and a field emission scanning electron microscope (JEOL-JSM-7100F) is used to observe the morphology of the SiC-DCs. XRD analysis of the SiC-DCs is performed using Cu Kα radiation (40 kV, 40 mA, l = 1.5418 Å) and a fixed slit mode over the 2θ range of 10-80°.

3.2.3 Volumetric adsorption and diffusion measurements

Volumetric adsorption measurements are conducted to measure excess adsorption isotherms [57, 58], as well as adsorption kinetics based on transient pressure changes during the adsorption step. Adsorption isotherm data of argon at 87 K and CO_2 at 273 K and CH_4 at six different temperatures (303-353 K) up to atmospheric pressure are measured volumetrically using a Micromeritics ASAP2020 adsorption analyser. Pore structure analysis of the synthesized SiC-DC samples is performed by interpretation of argon adsorption isotherm data at 87 K using non-local density functional theory (NLDFT) with the Finite Wall Thickness (FWT) model [56]. The pore volume distribution and surface area of the SiC-DCs is also obtained from the CO_2 adsorption isotherm at 273 K, using the in-built DFT2 (NLDFT) program from Micromeritics. High pressure adsorption of CH_4 is also carried out volumetrically using a Micromeritics HPVA sorption system at temperatures of 313 K, and 333 K for a range of pressure up to 5 MPa.

The uptake kinetics of CH_4 on the SiC-DC samples has been experimentally measured at the same time when the CH_4 adsorption equilibrium data are collected at six different temperatures (303-353 K) up to atmospheric pressure, using the volumetric Micromeritics ASAP2020. In the first stage of each experiment, samples are degassed at 623 K for a period of 12 hours. The degassed sample cell is transferred to the adsorption port where the sample is initially evacuated and then dosed with helium gas to determine the dead volume of the sample cell. The sample is eventually evacuated and dosed with CH_4 in small pressure steps (pressure steps were less than 0.1 mmHg), and the transient gas pressure signal from the pressure transducer is recorded for each pressure step. Isothermal conditions are maintained during all experiments using an insulated Dewar flask. The degas procedure is repeated for 4 hours on the same sample between measurements at different temperatures. It should be noted that volumetric technique has an inherent issue corresponding to the valve dynamics and the zero time pressure measurements. At time $t=0^-$ the inlet valve in the volumetric apparatus opens to dose the fixed amount of gas in the sample cell and the pressure is recorded and at time $t=0^+$ the valve closes which results in slight increase in the cell pressure. This effect which is caused due to valve dynamics is often merged together in the adsorption value at zero time resulting errors. This effect can be ignored if the diffusion is slow, however for the fast diffusion systems this could lead to incorrect results. In our work, the zero time

correction was done by theoretically calculating the zero time pressure by mass balance rather than the reading obtained from the pressure transducer.

3.3 Mathematical modeling

3.3.1 Adsorption isotherm

The isotherm equation for description of adsorption equilibrium is crucial for the successful representation of adsorption kinetics. In this work, based on the bidisperse pore size distribution of SiC-DC, and the presence of ultra-micropores, the experimental isotherm data are analysed using a proposed dual Henry-Langmuir mode isotherm equation to describe single component adsorption equilibrium on SiC-DC. The Henry-Langmuir isotherm equation is represented mathematically as follows

$$C_a(P) = \frac{C_{\mu m} K_L C_{be}}{1 + K_L C_{be}} + K_H C_{be} \tag{3-1}$$

where $C_a(P)$ is the total sorption per unit particle volume at bulk concentration C_{be}, $C_{\mu m}$ is the micropore capacity per unit particle volume, K_L is the Langmuirian affinity constant, and K_H is the Henry constant. The affinity coefficient and Henry constant have an exponential dependence on inverse temperature, following

$$K_H = A_h \exp\left(\frac{-\Delta H_h}{RT}\right) \tag{3-2}$$

$$K_L = A_\ell \exp\left(\frac{-\Delta H_\ell}{RT}\right) \tag{3-3}$$

where ΔH_ℓ and ΔH_h represent the adsorption enthalpies for the Langmuir and Henry modes respectively.

3.3.2 Adsorption kinetics

We have applied several transport models to match the transient adsorption data obtained in the volumetric adsorption apparatus, and obtain diffusion parameters from the fitting.

3.3.2.1 Unipore model

The first model we have applied assumes a unipore structure pervading the entire CDC particle, with no microscale or external mass transfer resistance. Further, since each step in

the experiment involves only a small bulk pressure change in the sample chamber, the concentration of the bulk gas surrounding the particle, and therefore the interfacial concentration of adsorbate in equilibrium with this bulk gas, is assumed constant during the transient phase after introduction of the adsorptive dose in the sample cell. In this case, the resistance to diffusion is entirely at the particle scale, and assuming spherical particles of radius R_P, the transport model follows

$$\frac{\partial C_a}{\partial t} = \frac{1}{R^2}\frac{\partial}{\partial R}\left(D_a R^2 \frac{\partial C_a}{\partial R^2} \right) \tag{3-4}$$

with boundary conditions $\partial C_a / \partial R = 0$ at $R = 0$, and $C_a = C_{af}$ at $R = R_p$, with initial condition $C_a(0, R) = C_{ao}$. Here C_{af} is the adsorbed amount in equilibrium with the surrounding bulk gas, and the intra-particle diffusion coefficient, D_a, is assumed constant in view of the small external pressure change. This coefficient has an embedded factor of tortuosity. Considering heat and mass transfer resistances to be negligible, and the sample temperature to remain constant, the analytical solution of the above model provides

$$\frac{M_t(t)}{M_\infty} = 1 - \frac{6}{\pi^2}\sum_{n=1}^{\infty}\frac{1}{n^2}\exp\left(-\frac{n^2\pi^2 D_a t}{R_P{}^2}\right) \tag{3-5}$$

where $M_t(t)$ is the total uptake of adsorbate in the spherical particle at time t, and M_∞ is the final amount adsorbed at long time.

3.3.2.2 Unipore model with non-linear isotherm

In the above model, there are two main assumptions involved in the formulation: (i) the surrounding bulk gas phase concentration (or pressure) in the sample chamber is constant, and (ii) the intra-particle transport coefficient is constant since the change in bulk pressure is small. The latter assumption is satisfied even when the change in adsorbed amount is finite, if the isotherm is linear, as follows from the Darken equation: $D_a(C_a) = D_{ao}\, d\ln(C_b)/d\ln(C_a)$. Here we consider another model in which the first of these assumptions is relaxed, and the bulk gas concentration is allowed to vary during a pressure step. Further, we assume that adsorption equilibrium is attained at the particle surface following a Langmuirian isotherm (a simplification compared to the actual isotherm that we subsequently fitted - the combined Henry-Langmuir model in Eq. (3-1)). In this case, Eq. (3-4) has the interfacial boundary

condition $C_a(t,R_p)=I(C_b(t))$, where $I(C_b)$ represents the Langmuir isotherm with $C_b(t)$ being the bulk gas concentration. To account for the variation of bulk concentration with time, the adsorptive mass balance equation in the gas phase provides:

$$V_{ex}\frac{dC_b}{dt}=-3D_a(C_a(R_P))\frac{m}{R_P\rho_P}\left(\frac{\partial C_a}{\partial R}\right)\Bigg|_{R=R_P} \tag{3-6}$$

in which V_{ex} is the external volume in the sample cell, m is the mass of adsorbent and ρ_P is the particle density. The transient uptake in this model is obtained as

$$M_t(t)=\frac{M_w V_{ex}\left(C_{bo}-C_b(t)\right)}{m} \tag{3-7}$$

where M_w is the gas molecular weight and C_{bo} is the initial bulk gas concentration in the sample chamber.

3.3.2.3 Bipore diffusion model

Given the evidence of ultra-microporosity in Ti_3SiC_2-derived carbon [15] and, as will be seen here, also in SiC-DC, we consider a third model based on the assumption of a bidisperse structure; this comprises two kinds of pores: the ultra-micropores ranging from 3.3-3.7 Å and larger micropores. In ultra-micropores, the overlapping of the potential energy field due to the solid leads to an enhanced potential field in favour of adsorption. In comparison, there is relatively much less adsorption in larger micropores, and these are viewed as the pathways through which the adsorptive diffuses from the bulk phase into the ultra-micropores. It is assumed that ultra-micropores have topologically connected networks in small independent microparticles called grains, with the larger micropores forming the inter-grain space as the pathways.

The particle scale mass transport in such bidisperse particles follows the balance equation [23, 25]

$$\varepsilon_m\frac{\partial C_m}{\partial t}+\varepsilon_\mu(1-\varepsilon_m)\frac{\partial \bar{C}_\mu}{\partial t}=-\frac{1}{R^2}\frac{\partial}{\partial R}\left(R^2N_m\right) \tag{3-8}$$

and for spherical grains (microparticles) the microscale transport follows

$$\frac{\partial C_\mu}{\partial t} = \frac{1}{r^2}\frac{\partial}{\partial r}\left(r^2 D_\mu(C_\mu)\frac{\partial C_\mu}{\partial r} \right) \tag{3-9}$$

where ε_μ is the microporosity of the grains, and ε_m the inter-grain (micro)porosity of the particle, respectively. C_m is the adsorptive concentration in the particle scale micropores, C_μ is the adsorbed phase concentration in the grain scale ultra-micropores, and $\bar{C}_\mu$ its mean value, given by

$$\bar{C}_\mu(t) = \frac{3}{r_g^3}\int_0^{r_g} r^2 C_\mu(t,r)dr \tag{3-10}$$

Further, $D_\mu(C_\mu)$ is a concentration-dependent ultra-micropore diffusivity (with an embedded tortuosity factor), assumed to follow the Darken relation $D_\mu(C_\mu) = D_{\mu o} d\ln(C_{be})/d\ln(C_\mu)$, where C_{be} is the equilibrium pseudo-bulk gas concentration corresponding to adsorbate concentration C_μ. The effect of pore size heterogeneity on the concentration-dependence of this microscale transport coefficient was examined by Bhatia [27], considering a random pore network, showing the choice of isotherm model and the heterogeneity to have significant influence.

In the simplest case, when particle scale diffusion of the micropore adsorbate is insignificant, the particle scale flux, N_m, is expressed as

$$N_m = -\varepsilon_m D_m \frac{\partial C_m}{\partial R} \tag{3-11}$$

where D_m is the effective macropore diffusivity. The fast mass transfer boundary condition for Eq. (3-9) implies that the adsorbed phase concentration at the microparticle surface, $C_\mu(t,r_g)$, and the local concentration in the larger surrounding particle-scale micropores are in equilibrium. Following the dual Henry-Langmuir isotherm in Eq. (3-1), it is assumed that the Langmuirian part of this isotherm corresponds to the adsorption in the grains or microparticles, and the Henry law part corresponds to the larger pores permitting diffusion at the particle scale. Assuming an ideal bulk gas phase, the adsorbate concentration in the ultra-micropores follows

$$\varepsilon_\mu(1-\varepsilon_m)C_\mu = \frac{C_{\mu m}K_L C_{be}}{1+K_L C_{be}} \tag{3-12}$$

while the adsorbed concentration in the larger particle scale pores follows

$$\varepsilon_m C_m = K_H C_{be} \tag{3-13}$$

Here C_{be} is the local pseudo-bulk gas equilibrium concentration. Eqs. (12) and (13) combine to provide the interfacial boundary condition for Eq. (3-9)

$$C_\mu(t,R,r_g) = \frac{\varepsilon_m C_{\mu m}K_L C_m(t,R)}{\varepsilon_\mu(1-\varepsilon_m)K_H[1+K_L\varepsilon_m C_m(t,R)/K_H]} \tag{3-14}$$

while $\partial C_\mu / \partial r = 0$ at $r = 0$. Similarly, Eq. (3-8) has the boundary conditions $\partial C_m / \partial R = 0$ at $R = 0$, and $C_m(t,R_P) = K_H R_g T C_b(t)/\varepsilon_m$, where the bulk gas concentration $C_b(t)$ follows

$$V_{ex}\frac{dC_b}{dt} = -3\varepsilon_m D_m \frac{m}{R_P\rho_P}\left(\frac{\partial C_m}{\partial R}\right)\Bigg|_{R=R_P} \tag{3-15}$$

which is similar to Eq. (3-6). Following the Darken relation, the effective ultra-micropore diffusivity in the grains has the loading dependence

$$D_\mu(C_\mu) = \frac{D_{\mu o}C_{\mu m}}{(C_{\mu m}-\varepsilon_\mu(1-\varepsilon_m)C_\mu)} \tag{3-16}$$

based on the Langmuirian isotherm in Eq. (3-12), where $D_{\mu o}$ is the mobility. The effective particle scale diffusivity D_{em} is readily seen to be loading-independent based on the isotherm in Eq. (3-13). The time dependent total uptake for this model is obtained as before using Eq. (3-7).

3.4 Results and discussion

3.4.1 Structural characterization

3.4.1.1 Morphology and particle size of synthesized SiC-DC1073

Figure 3-1 illustrates the Scanning Electron Microscopy (SEM) micrograph of both SiC-DC 1 µm and 20 µm, showing individual particles.

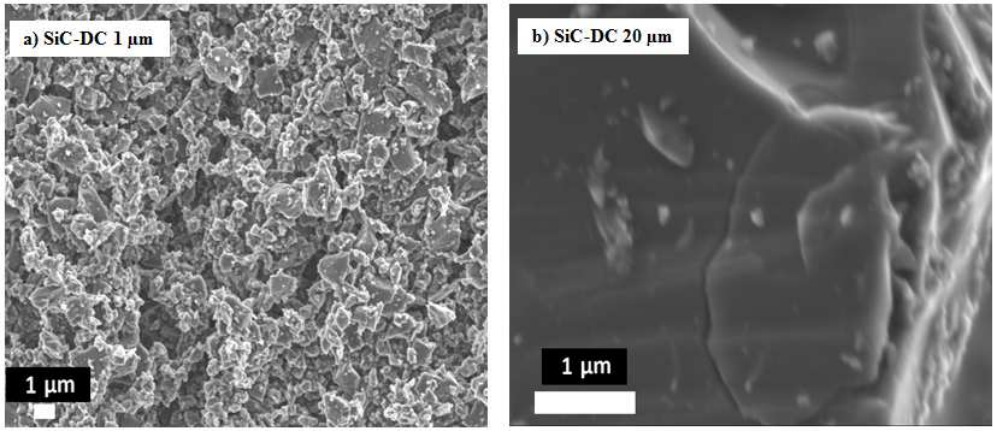

Figure 3-1. SEM images of SiC-DC1073 particles of nominal size (a) 1 µm, and (b) 20 µm.

A higher tendency of agglomeration for the 1 µm particles compared to 20 µm sample is evident. Figure 3-1 also suggests that the primary particles of the sample of nominal size 1 µm are significantly smaller. Cracks are also visible on the surface of the particles which can potentially affect the kinetic uptake data of CH_4 adsorption, and enhance interfacial mass transfer. Figure 3-2 illustrates the particle size distribution of SiC-DC1073 1 µm and 20 µm particles and their precursors, obtained using the Malvern Mastersizer laser sizing instrument. It is seen that the particle size of the synthesized SiC-DC is close to its precursor, and chlorine treatment does not have a significant effect on the particle size distribution of the samples, which remain nearly unchanged after the synthesis process. Figure 3-2 also shows a small modal size of about 0.6 µm diameter for the particles of nominal size 1 µm, consistent with the observation of smaller primary particle size based on the micrographs in Figure 3-1.

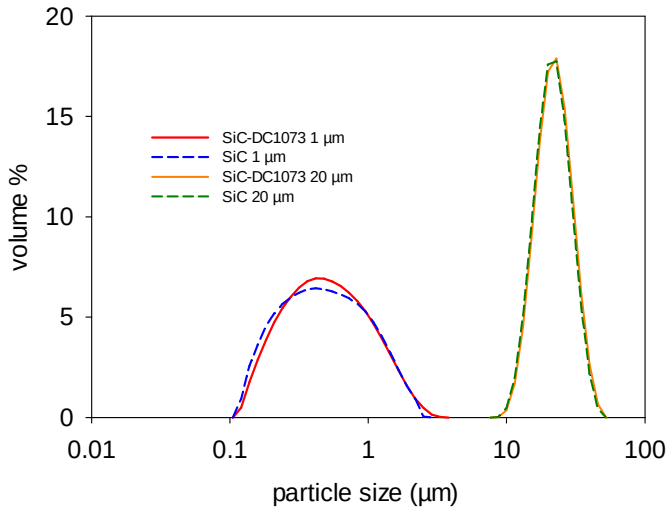

Figure 3-2. Particle size distribution curves for SiC-DC samples and their precursors.

3.4.1.2 High resolution transmission electron microscopy

The structure of the synthesized SiC-DC samples was also investigated using high resolution transmission microscopy (HRTEM). The HRTEM image of SiC-DCs in Figure 3-3 reveals a predominantly amorphous structure in the core of the samples, as is it to be expected. On the other hand, these TEM images also reveal the existence of grains inside the structure of the synthesized SiC-DC samples. The size of grains observed in these images are roughly in the range of 35-45 nm and 25-35 nm for SiC-DC1073 1 µm and 20 µm samples respectively. Some degree of graphitization in an outer shell CDC samples has been reported in the literature [14, 18], and this is found to increase as the synthesis temperature increases. While such increased graphitization does appear to occur on the surface of the grains in Figure 3-3, the extent does seem lower than that observed for nanosized SiC-DC in the literature [18]. SiC-DCs generally remain amorphous up to chlorine treatment temperature of 1473 K [4], however at 1073 K and higher temperatures, a slight increase of graphite ordering has been reported [3, 5]. A slightly more ordered structure is found in SiC-DC1073 1 µm compared to 20 µm, consistent with XRD patterns presented below.

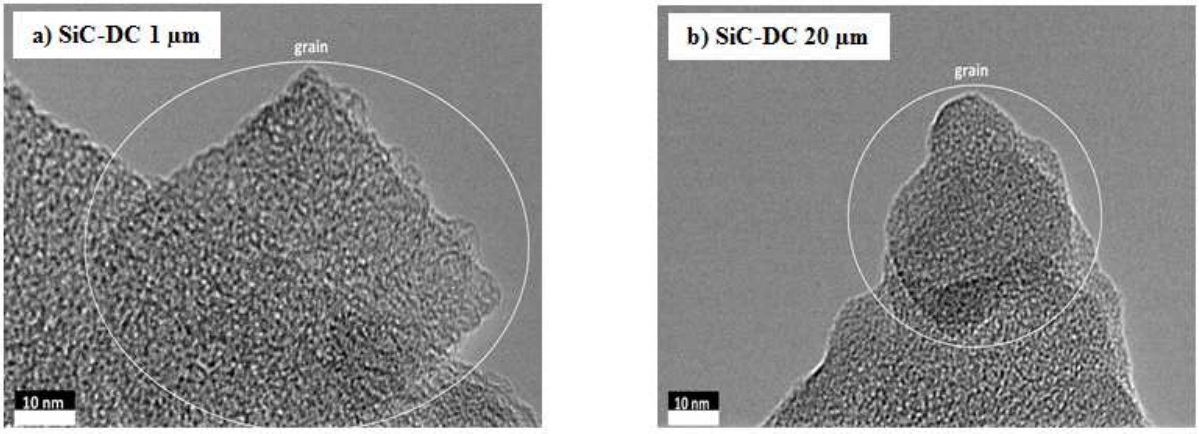

Figure 3-3. High resolution TEM images of SiC-DC1073 particles of nominal size (a) 1 µm, and (b) 20 µm.

3.4.1.3 X-ray diffraction

The structure of the synthesized SiC-DCs has been characterized using X-ray diffraction (XRD). Figure 3-4 shows the XRD patterns of the both SiC-DC samples synthesized from 1 µm and 20 µm SiC precursors. The SiC-DC1073 1 µm and 20 µm samples exhibit a graphite peak at 25.9-25.12° and weak peak at about 43.6° and 43.4°, corresponding to the (002) and

(004) reflections respectively. The *d*-spacings calculated from (002) peaks are 3.43 and 3.54 Å based on Bragg's law. The broad (002) reflection between the scattering angle 15–30º in the XRD pattern of SiC-DC samples, which is related to the interlayer spacing between two graphitic sheets is indicative of the poor degree of graphitization and highly amorphous nature of the SiC-DC. It is well known that mainly amorphous carbon is involved in the structural organization of CDCs [59]. The growth of a small sharp (002) peak of the SiC-DC 1 µm sample in comparison with SiC-DC 20 µm reveals that the 1 µm sample has better stacking of carbon sheets. However, this small graphitization degree may not necessarily lead to an increase in pore accessibility for argon and CO_2 in the highly amorphous structure of SiC-DC because of the presence of structural distortions arising from folding and twisting of the sheets known to occur in disordered activated carbons.

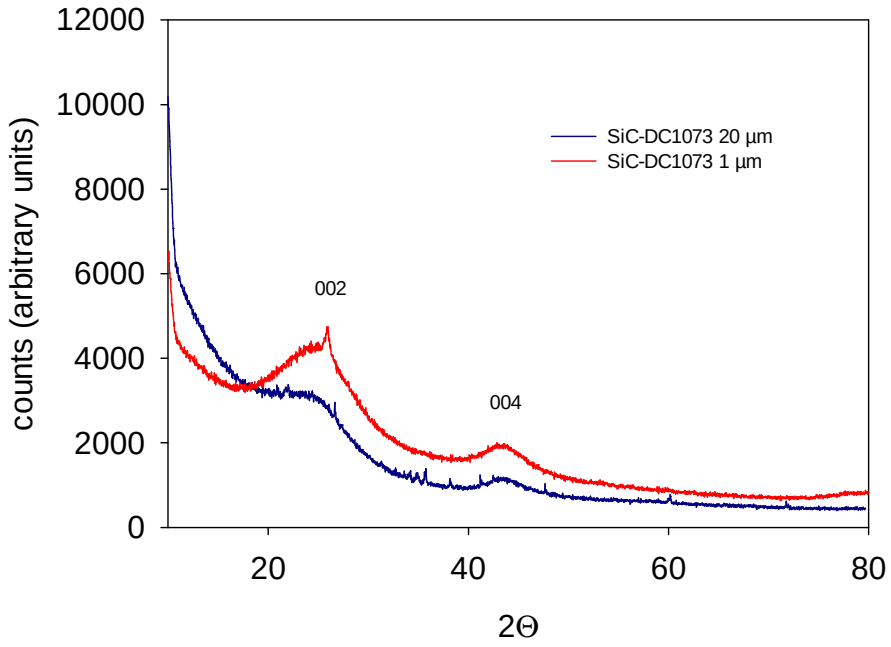

Figure 3-4. XRD patterns of SiC-DC1073 particles of nominal size 1 µm and 20 µm.

3.4.1.4 Pore structure characterization

The helium skeletal density of the SiC-DC samples is measured using a Helium Pycnometer (Micromeritics Accupyc 1330). The helium densities for the 1 µm and 20 µm samples are 2.52 and 2.28 (g/cm^3) respectively. The helium densities for both samples are close to the density of graphite (2.27 g/cm^3). Figure 3-5 compares the argon adsorption isotherms of the both SiC-DC1073 1 µm and 20 µm at 87 K. The argon adsorption isotherms on these samples

are of a typical type I isotherm for microporous materials. Both samples exhibit relatively similar argon adsorption isotherms at 87 K, indicating that these samples should have similar pore structure as can be also seen in HRTEM images presented in Figure 3-3. The SiC-DC1073 1 μm sample shows larger adsorbed amount of argon at 87 K up to relative pressures of 0.001. This higher adsorbed amount of argon for SiC-DC1073 1 μm is indicative of larger pore volume of small pores.

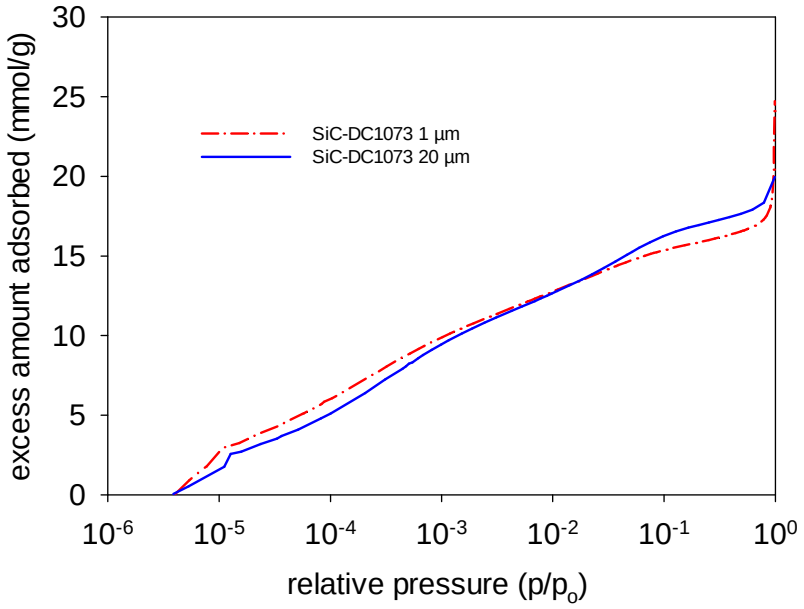

Figure 3-5. Experimental argon adsorption isotherm for 1 μm and 20 μm SiC-DC1073 particles.

In order to study the pore structure of the samples, the argon adsorption isotherms are interpreted using NLDFT with the finite wall thickness (FWT) model [56]. Figure 3-6 shows the PSD of SiC-DC samples prepared from SiC of different particle size distribution at 1073 K. The obtained surface area of the SiC-DC1073 1 μm and 20 μm samples using the FWT-NLDFT model are 1507.5 and 1452.1 (m^2/g) respectively, while the pore volumes are 0.52 cm^3/g and 0.51 cm^3/g respectively. These values are slightly lower than those obtained using nanosized SiC [5], where pore volume of about 0.6 cm^3/g has been reported, and may reflect a small degree of shrinkage due to some graphitisation of the micrometer-sized samples during their necessarily longer chlorine treatment period. Based on the pore volumes and skeletal densities it is estimated that a reduction in pore volume from 0.6 cm^3/g to 0.51 cm^3/g corresponds to only about 3-4% reduction in particle radius, too small to accurately measure

by the laser sizing method. This is made further difficult by the tendency of the carbon particles to cluster and agglomerate, particularly for the 1 µm sample, which skews the distribution towards larger sizes. Although the agglomerates are largely broken down by ultrasonification in our system, some clusters may remain or reform during the measurement procedure.

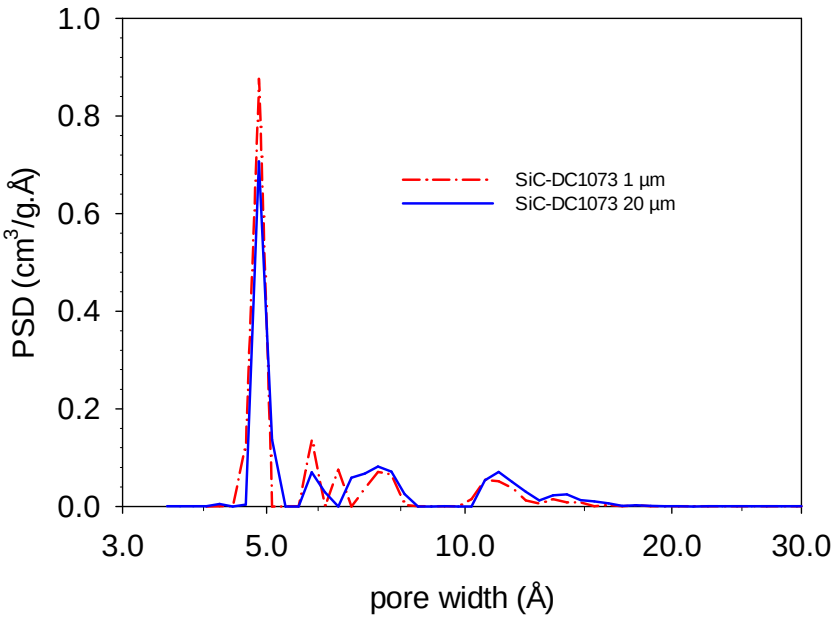

Figure 3-6. Comparison of the PSD of the SiC-DC1073 samples prepared from precursors with different particle size distributions. The PSD is obtained by the interpretation of argon adsorption at 87 K using FWT model.

3.4.2 Predictions of CO_2 and CH_4 adsorption isotherms

The structural data (pore size and pore wall thickness distributions) obtained from interpreting experimental sub-atmospheric adsorption isotherms of argon at 87 K are used to predict the low pressure CO_2 isotherm and high pressure adsorption isotherms of CH_4 in the synthesized SiC-DC1073. A detailed description of the FWT-NLDFT approach, considering a slit pore size distribution (PSD) and a wall thickness distribution (PWTD), interaction potential models and related parameters, can be found elsewhere [18, 56].

3.4.2.1 CO_2 adsorption at 273 K

The sub-atmospheric pressure CO_2 adsorption isotherm at 273 K for SiC-DC1073 1 µm is predicted using the FWT model and the comparison between the Ar PSD-based predictions

(excess theoretical adsorption isotherm) and the experimental data is shown in Figure 3-7. For the predictions, the microstructure of the investigated SiC-DC samples is assumed to be rigid under this low pressure condition. CO_2 is treated as an effective Lennard-Jones (LJ) sphere for which the LJ parameters for the CO_2-CO_2 interactions are taken from elsewhere [60]. The Lennard-Jones carbon-carbon interaction parameters are taken to be similar to Steel's values for graphite: σ_c = 3.4 Å and ε_c/k_B = 28 K. The generalized Lorentz-Berthelot combing rule is used to determine the LJ fluid-carbon (CO_2-C) interaction. For this low pressure CO_2 adsorption, the binary parameter value of k_{cf} = 0 is used since the one-center assumption for CO_2 molecules is suitable at sub-atmospheric pressures [18]. It can be observed that the FWT model provides reasonably good agreement between the excess theoretical and experimental adsorption isotherm for the synthesized sample, indicating good approximation of the slit-pore model for even very disordered carbons such as the SiC-DC. This has been also shown to satisfactorily predict the sub-atmospheric CO_2 isotherm of nano-sized SiC-DC in previous work of this laboratory [18]. The under-prediction which is observed at very low pressure indicates a pore accessibility problem for argon at 87 K at low pressures, and that the synthesized SiC-DC has lower pore accessibility for argon at 87 K compared to CO_2 at 273 K. This is because of relatively lower diffusivity of argon at 87 K in the pore structure of SiC-DC, and a pore entry barrier in the narrowest pores [61]. With increase in pressure, however, the barrier appears to be overcome, as the CO_2 adsorption is more accurately predicted in this region.

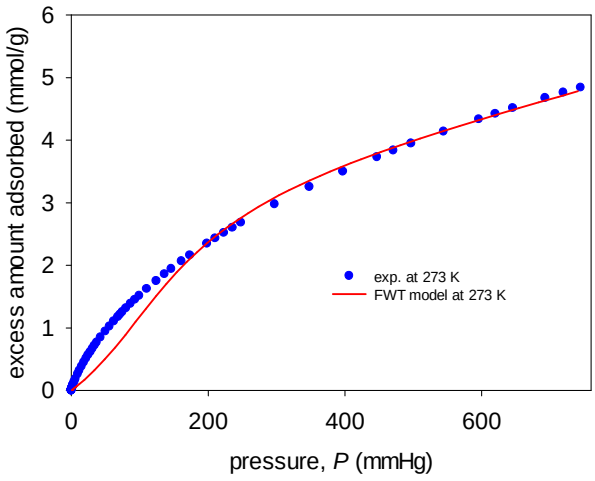

Figure 3-7. Predicted and experimental sub atmospheric adsorption isotherms of CO_2 at 273 K on 1 µm SiC-DC1073 particles.

The experimental sub-atmospheric CO_2 adsorption isotherm data is also analysed using the Micromeritics DFT2 NLDFT program to obtain the pore size distribution. The presence of a narrow ultra-microporosity in the range of 3.3–3.8 Å is suggested by Figure 3-8 for both 1 µm and 20 µm samples, with that for the 1 µm samplebeing more prominent than for the 20 µm sample. Since CO_2 at 273 K cannot fill micropores larger than 9 Å at pressures less than 760 mmHg, the pore volume and surface area obtained under these conditions are indicative of the micropore volume in pores smaller than 9 Å in width.

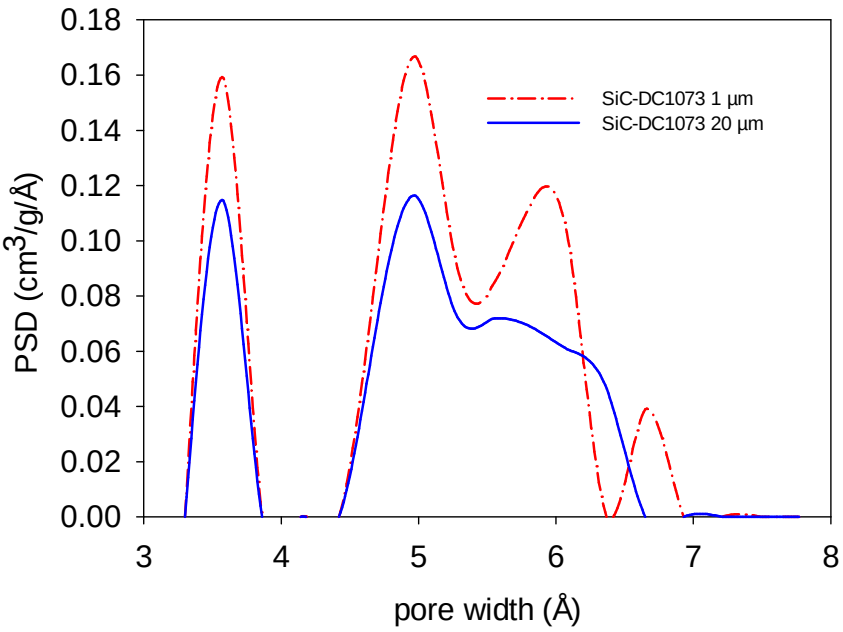

Figure 3-8. Pore size distribution obtained from CO_2 adsorption at 273 K using non-local density functional theory for SiC-DC1073 particles of nominal size 1 and 20 µm.

It is evident that most of the ultra-microporosity peak in the PSD obtained from the CO_2 isotherm at 273 K is not present in the PSD obtained from argon at 87 K, which is an indication of a possible pore accessibility problem for argon at 87 K in SiC-DC1073. A similar trend has been also shown for the Ti_3SiC_2 based CDCs in recent work from this group [15]. Since CO_2 has a smaller critical size (3.3 Å) compared to argon (3.4 Å) and because the molecular kinetic energy at the temperature of the CO_2 adsorption of 273 K is higher than that at the argon adsorption temperature of 87 K [15, 24], CO_2 at 273 K shows better accessibility in ultra-micropores than argon at 87. It can be seen that SiC-DC1073 20 µm shows lower ultra-microporsity, possibly due to the more amorphous and disordered structure

of 20 µm samples as shown in HRTEM and XRD analysis. The slightly lower graphitization degree of SiC-DC1073 20 µm compared to 1 µm may lead to the formation of highly constricted pore mouths and decrease the pore accessibility of CO_2. The surface areas for the 1 µm and 20 µm samples obtained from CO_2 adsorption are 1960 and 1730 (m^2/g) with micropore volumes (< 9 Å) of 0.237 and 0.174 (cm^3/g) respectively. Apart from Ti_3SiC_2-derived carbons [15], the existence of ultra-microporosity in CDCs has been recently shown in work from this laboratory also through SANS-based characterization of various CDCs and conventional activated carbons [62], as well as hybrid reverse Monte Carlo (HRMC) simulations of SiC-DC [63]. Presser et al. [64] have also presented a study on the effect of CDC micropore size on low pressure CO_2 sorption. They reported high CO_2 sorption capacity of up to 7.1 mmol/g for CDC at 273 K and ambient pressure, but did not uncover the ultra-microposity.

3.4.2.2 High pressure CH_4 adsorption at 273 K

The FWT-NLDFT model is used to predict high pressure methane adsorption using PSD and PWTD obtained from argon adsorption. Figure 3-9 compares the excess theoretical high pressure adsorbed quantities of methane at 313 and 333 K in SiC-DC1073 1 µm predicted by the FWT-NLDFT model with the experimental data. For these predictions, all the LJ parameters for CH_4-CH_4 and CH_4-C interactions are taken from the previous work from this laboratory [18]. As can be seen, the FWT model predictions are in good agreement with experimental high pressure adsorption isotherms of CH_4 in the SiC-DC1073 1 µm samples, although a very slight over-prediction for the CH_4 adsorption isotherm is observed. Nguyen et. al [18] have also report some over-prediction of the CH_4 isotherms by the FWT-NLDFT model for their CDC, both at 313 K and 333 K, using the PSD based on Ar adsorption at 87 K. While these authors attributed the overprediction to difference in accessibility between Ar, having critical pore diameter of 3.4 Å, and CH_4, which has a critical pore diameter of 3.6 Å, this explanation would appear inconsistent with the match at the lower temperature of 313 K in Figure 3-9. Nevertheless, the overprediction even at 333 K seen here is rather small, within 3-5%, and likely due to sample-dependent variations. Thus, while Ar at 87 K would appear to have slightly lower accessibility to the ultra-micropores as compared to CO_2, it may have similar accessibility as methane at 313 K and 333 K for this CDC sample.

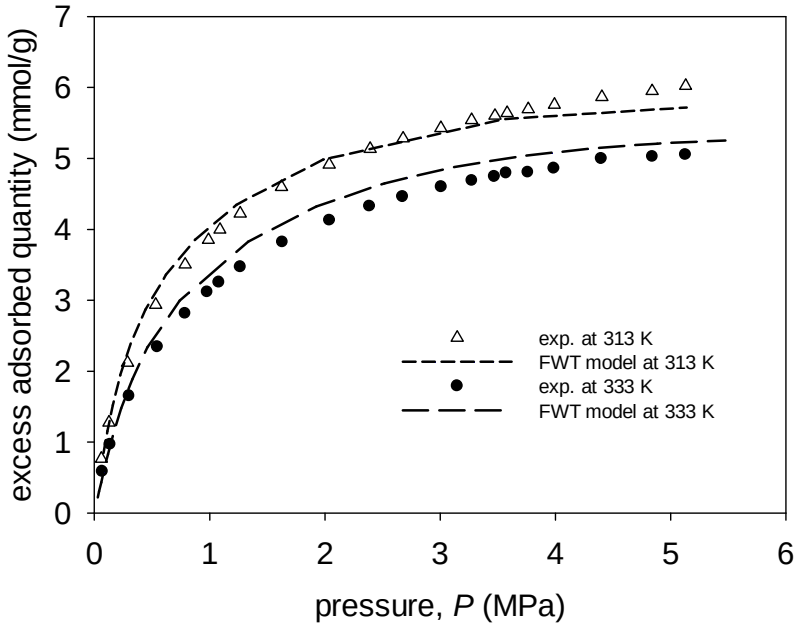

Figure 3-9. Comparison between high pressure adsorption isotherms of CH_4 in SiC-DC1073 particles of nominal size 1µm at 313 K and 333 K predicted by the FWT model and corresponding experimental data.

3.4.3 Low pressure CH_4 adsorption equilibrium and kinetics

The dual Henry-Langmuir isotherm model was applied to the adsorption equilibrium data of CH_4 on SiC-DC1073 1 µm and 20 µm at temperature range of 303-353 K up to atmospheric pressure. The fit of the Henry-Langmuir isotherm to the experimental adsorption isotherm data (excess amount adsorbed per unit particle volume) is shown in Figure 3-10, in which the micropore capacity ($C_{\mu m}$) is held constant over the six temperatures. Under the sub-atmospheric pressure conditions the bulk density is sufficiently small that the difference between absolute and excess isotherms is insignificant. It is evident that the Henry-Langmuir isotherm can adequately fit the data over the pressure range shown. The evaluated parameters from the dual Henry-Langmuir isotherm are presented in Table 3-1. The dual Henry-Langmuir isotherm is attributed to the pore size heterogeneity of the adsorbent, with the Langmuir part related to ultra-micrpores in the grains, and the Henry part to the larger micropores in the particle providing access pathways into the particle interior and to the ultra-micropores. The ultra- micropore capacity of the SiC-DC1073 1 µm and 20 µm samples obtained from fitting the dual Henry-Langmuir isotherm is 1.37 and 1.17 mmol/cc of particle volume respectively.

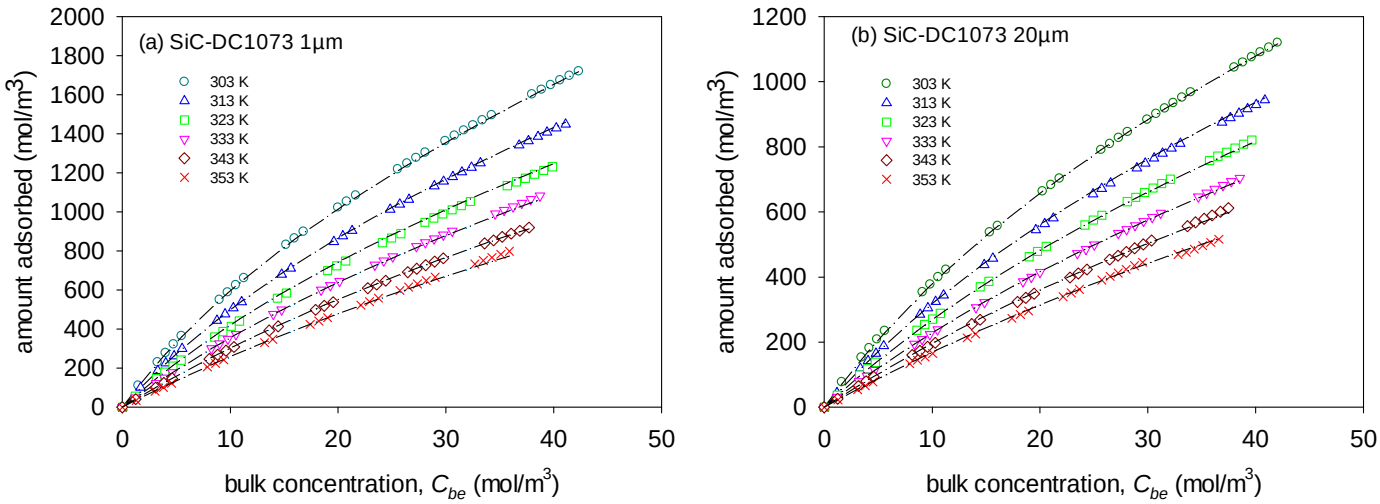

Figure 3-10. Fits of low pressure methane adsorption isotherm for SiC-DC1073 particles of nominal size (a) 1 µm, and (b) 20 µm at 303-353 K with Langmuir-Henry isotherm model.

Based on the molecular area of 17.3 $Å^2$ of CH_4, and the measured skeletal densities and pore volumes, these ultra-micropore capacities lead to estimates of the ultra-micropore volume of 0.046 and 0.04 cc/g for the 1 µm and 20 µm samples respectively, assuming a single layer of CH_4 molecules in ultra-micropores having mean size of 3.5 Å. These values are in remarkably good agreement with the ultra-micropore volumes obtained from the PSDs based on the 273 K CO_2 adsorption isotherms for the 1 µm and 20 µm samples, of 0.044 cc/g and 0.032 cc/g respectively, and may reflect some accessibility of the ultra-micropores to CH_4 at 313 K and above in the time frame of the experiment. On the other hand Ar at 87 K may have slightly lower accessibility to the ultra-micropores, evident in the PSDs in Figure 3-6, with the ultra-micropores probably being filled at higher than equilibrium pressures. The pore volumes of the two samples may therefore be marginally higher than the values of 0.52 cc/g and 0.51 cc/g, for the 1 µm and 20 µm samples respectively, obtained using Ar adsorption, depending on the filling attained for the ultra-nicropores. The parameters in Table 3-1, obtained from the fitting of the Henry-Langmuir isotherm to experimental equilibrium data, are used in the proposed bipore model to extract the diffusivities in larger micropores and ultra-micropores.

Table 3-1. Isotherm parameters for CH_4 on SiC-DC1073 particles of nominal size 1 µm and 20 µm.

adsorbent	$C_{\mu m}$ (mol/m^3)	$A_\ell \times 10^5$ (m^3/mol)	A_h (dimensionless)	$-\Delta H_\ell$ (kJ/mol)	$-\Delta H_h$ (kJ/mol)
SiC-DC 1 µm	1365.26	4.20	0.0327	17.28	16.22
SiC-DC 20 µm	1165.34	4.48	0.0193	16.37	16.03

3.4.3.1 Comparison of diffusion models

Subsequent to the interpretation of the adsorption equilibrium, the transport models presented in Section 3.3.2 were applied to the uptake kinetics data of CH_4 on the two adsorbents at different temperatures to understand the diffusion mechanism inside the synthesized SiC-DC particles and extract the CH_4 diffusion coefficients. In solving the models Eq. (3-9) were discretised using finite differences and converted to ODEs, which were solved together with the bulk phase balance Eqs. (3-6) and (3-15) in MATLAB using a stiff system solver. A least square minimisation method implemented in MATLAB was used to fit the model solution to the experimental fractional uptake data. The fitting parameters were the effective diffusivity in the particle scale micropores, D_m, and the ratio $D_{\mu o}/r_g^2$ which represents the inverse of the diffusional time scale in the grains. The typical kinetic uptake curves of CH_4 on both SiC-DC samples and the comparison of the models are plotted in Figure 3-11. It is clear that the first two models, which assume a single diffusion mechanism over the particle scale, cannot fit the data, which has a rapid initial uptake. Nearly 60% of the uptake is complete in the first second itself, and occurs too rapidly for the system to capture this dynamics. This suggests a diffusion mechanism involving at least two time scales. Further, in the experimental approach used in this study, the gas concentration is not constant but decreases with time due to finite volume of the bulk gas phase which is depleted as adsorption occurs in the SiC-DC. Consequently, the simple model in Eq (3-5) [65], which assumes a constant bulk gas concentration besides having only one diffusion mechanism, provides the least satisfactory fit of the measured data, while the bipore model fits the experimental CH_4 uptake data reasonably well compared to other alternative micropore diffusion models. Although as much as 60% of the uptake is complete by the first experimental point, the remaining part of the dynamics still captures the dynamics of both the particle and grain scale transport processes, with better data fits compared to the purely particle scale diffusion models.

Experiments with different amount of mass of adsorbent were conducted to investigate the effect of mass of sample on the diffusion uptake curves, and showed no effect of sample mass in the 0.3-0.75 g range. Thus, the results are free of heat and mass transfer resistances related to the sample pile.

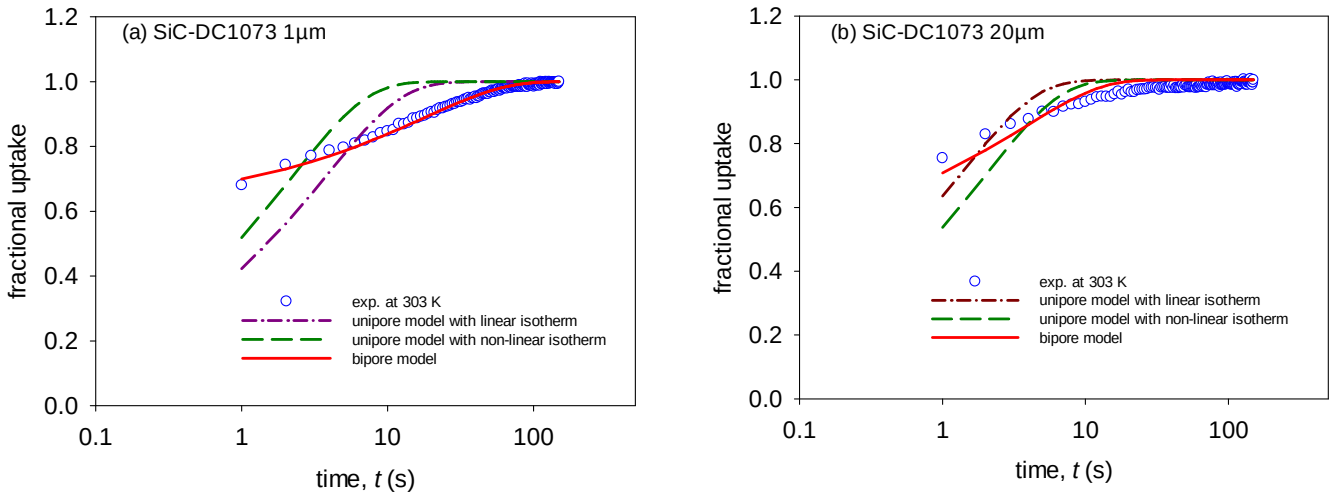

Figure 3-11. Comparison of different models for diffusion of CH_4 in SiC-DC1073 particles of nominal size (a) 1 µm, and (b) 20 µm (0.3 g), Symbols: experimental data; lines: models fit.

From Figure 3-11 it is evident that sorption equilibrium is reached faster for the larger particle size of nominal diameter 20 µm. The equilibration times are around 20 s for the largest and about 40 s for the smallest particle size fraction. This cannot be explained by the pore size distribution effects alone, as the particle scale micropores in the two samples have similar distributions (PSDs), as seen in Figure 3-6. This suggests that the two samples are structurally different, with the smaller particle size sample providing larger barriers to intra-particle and/or intra-grain transport due to internal constrictions and structural distortions arising from twisting and folding of the underlying graphene sheets, which cannot be captured by the slit pore models behind the PSDs in Figure 3-6. Such distortions of the sheets are indeed evident from the hybrid reverse Monte Carlo simulation-based atomistic structures of the SiC-DC [63]. Differences in structure evolution between different particle size samples during chlorine treatment may be expected, since the partial pressures of the chlorine and metal chloride at the reaction interface during chlorine treatment will be strongly particle size dependent. Smaller particles will have higher chlorine partial pressures and lower metal

chloride patrial pressures at the carbide/carbon interface, and more rapid diffusion through the developing porous structure, and therefore faster chlorination rate. The faster chlorination may be expected to lead to greater structural distortions. Further, since the different particle size samples originated from different manufacturers they may be expected to have different trace impurities, which could also influence the structural development during chlorine treatment.

3.4.3.2 Effect of the temperature on effective diffusivities

The CH_4 transient uptake curves of both samples at different temperatures are given in Figure 3-12 for pressure of 400 mmHg. The symbols represent experimental data and lines are theoretical fitting results.

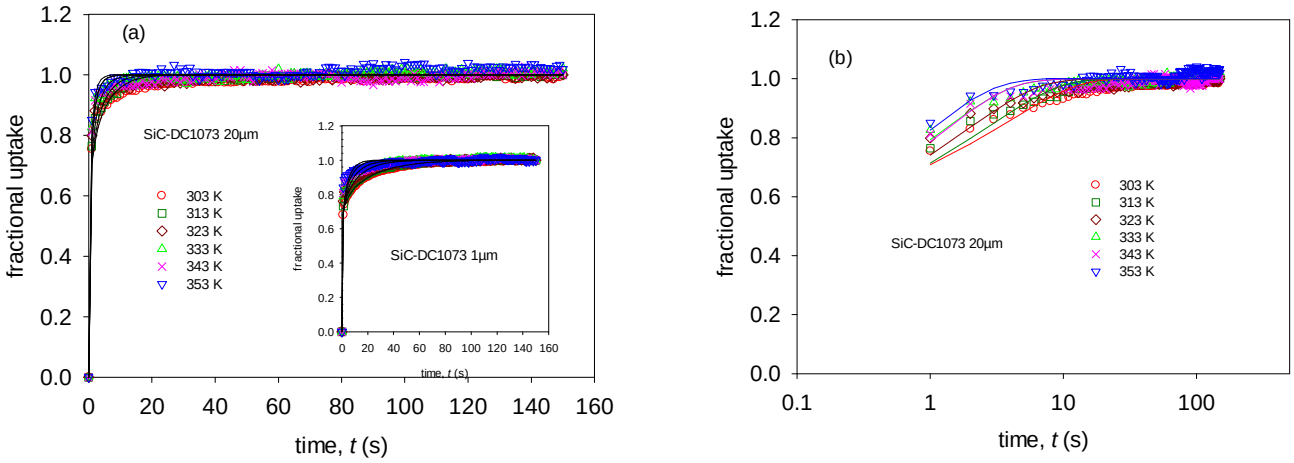

Figure 3-12. Effect of temperature and model fits for SiC-DC1073 particles of nominal size (a) 20 µm and 1 µm (inset) at pressure of 400 mmHg, and (b) model fits in semi-log coordinates for SiC-DC1073 20 µm, Symbols: experimental data; lines: model fit.

A strong temperature dependence of the diffusion uptake curves and time required to reach equilibrium is evident. Parameter values obtained by fitting experimental data and corresponding diffusivities are listed in Table 3-2, showing the diffusivity increasing with increasing temperature, in both the large micropores and the grain scale ultra-micropores, but at different rates. Thus, while the particle scale diffusivity increases by a factor of about 2.5 over the temperature range of 303-353 K, the grain scale diffusivity increases by a factor of over 6-10; this is indicative of higher activation energy in the ultra-micropores in comparison

to the larger grain-scale micropores, as is to be expected. These activation energies will be subsequently discussed; nevertheless, from the extent of the increase it is clear that the transport in both modes has an underlying activated diffusion mechanism, consistent with the microporous nature of the associated porosity.

Table 3-2. Diffusion parameters of CH_4 in SiC-DC1073 particles of nominal size 1 μm and 20 μm at different temperatures and pressure of 400 mmHg, mass of sample: 0.3g.

adsorbent	temperature (K)	$D_m \times 10^9$ (m^2/s)	$D_{\mu o}/r_g^2$ (s^{-1})	activation energy based on CH_4 diffusion in grain scale (kJ/mol)
SiC-DC1073 1 μm	303	3.6	0.0020	42.57
	313	4.9	0.0042	
	323	5.5	0.0067	
	333	6.2	0.0103	
	343	7.2	0.0141	
	353	9.5	0.0250	
SiC-DC1073 20 μm	303	4.6	0.0112	31.74
	313	6.8	0.0166	
	323	7.4	0.0260	
	333	8.4	0.0438	
	343	9.5	0.0466	
	353	11.3	0.0651	

From the magnitudes of the values of $D_{\mu o}/r_g^2$ in Table 3-2, and the grain sizes of about 40 nm and 30 nm for the 1 μm and 20 μm particles respectively, it is estimated that the value of $D_{\mu o}$ is extremely small, and of the order of 10^{-17} m^2/s for CH_4 in the ultra-micropores in SiC-DC. In comparison the diffusion coefficient in the larger particle scale micropores is of the order of 10^{-9} m^2/s, which is in the usual range for carbon micropores. From a practical viewpoint therefore adsorption and transport in the ultra-micropores is unlikely to make a significant contribution to any membrane or adsorptive separation process using SiC-DC, not only due to slow diffusion in the ultra-micropores, but also due to their small pore volume.

3.4.3.3 Effect of pressure on effective diffusivities

Experiments on the sorption of pure CH_4 were conducted at different pressures, over small pressure steps covering the pressure range of 400-700 mmHg and at temperature of 313 K. As shown in Figure 3-13, the uptake curves for CH_4 show a very slight decrease in rate with

increase in pressure. The bipore model is applied to extract the diffusivity values for both SiC-DC1073 samples. The results are presented in Table 3-3 and Figure 3-13a and b.

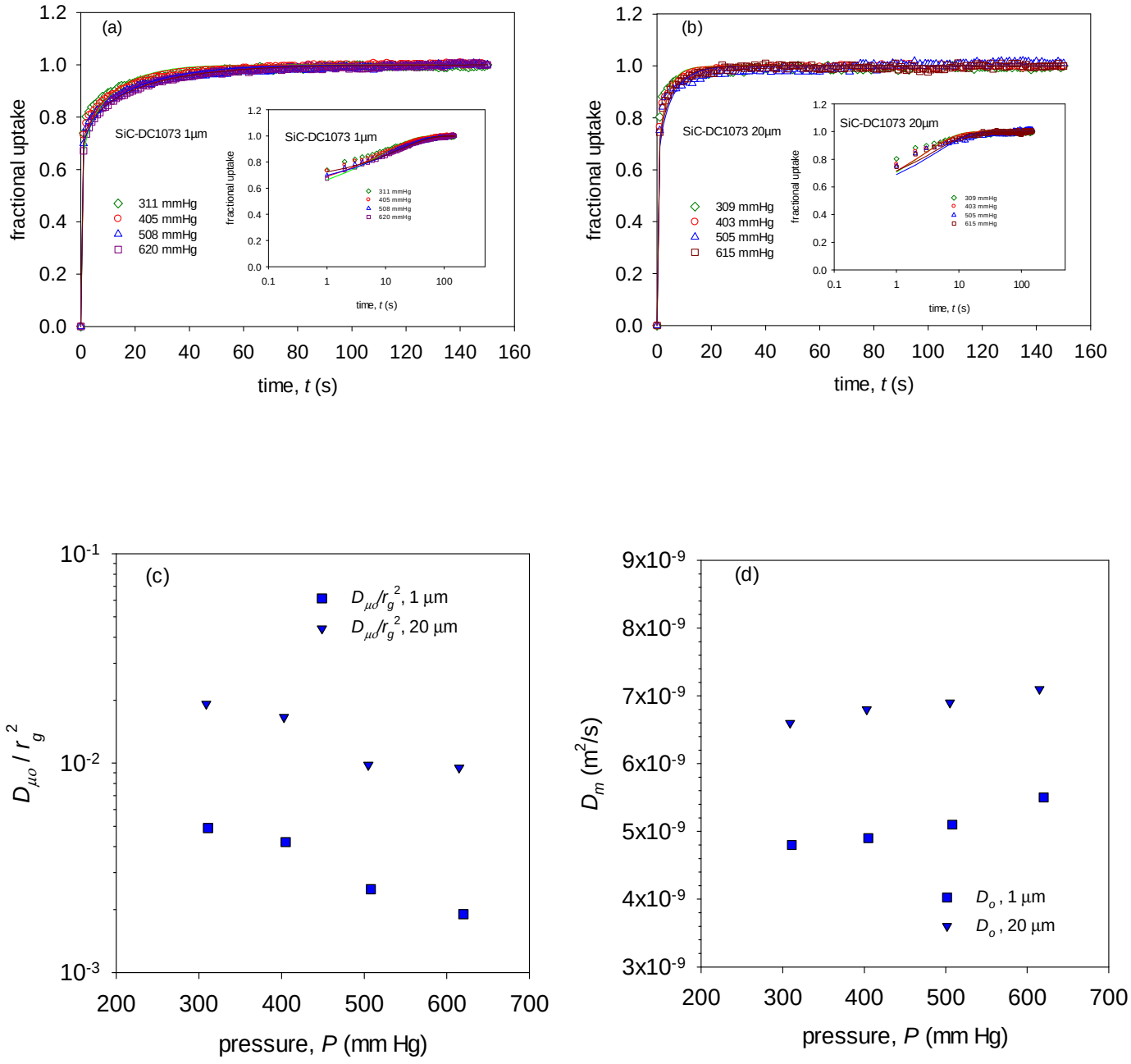

Figure 3-13. Effect of pressure on CH_4 uptake curves for SiC-DC1073 particles of nominal size (a) 1 µm, and (b) 20 µm, and on diffusivities in (c) grain-scale ultra-micropores, and (d) particle scale micropores, at 313 K.

Table 3-3. Diffusion parameters of CH_4 on SiC-DC1073 particles of nominal size 1 µm and 20 µm at different pressures and temperature of 40 °C, mass of sample: 0.3g.

adsorbent	pressure (mmHg)	$D_m \times 10^9$ ($m^2.s^{-1}$)	$D_{\mu o}/r_g^2$ (s^{-1})
SiC-DC1073 1 µm	311	4.8	0.0049
	405	4.9	0.0042
	508	5.1	0.0025
	620	5.5	0.0019
SiC-DC1073 20 µm	309	6.6	0.0192
	403	6.8	0.0166
	505	6.9	0.0098
	615	7.1	0.0095

As can be seen, the particle scale diffusivities, D_m, in the larger micropores show only a slight increase with increase in pressure and are nearly constant, while the diffusivities in ultra-micropores, $D_{\mu o}$, decrease with increasing pressure. These results are consistent with literature results based on simulations of the loading-dependence of the methane diffusivity in carbon slit pores at various pore sizes. Nicholson has shown strong pore size dependence of the relation between the CH_4 diffusivity and loading through simulation studies in graphite micropores [55]. Decrease in methane diffusivity with increasing loading in very narrow pores has been observed in molecular dynamics simulations of transport in slit pores carbons [53], and in single-walled carbon nanotubes [54]. It is shown that at low loadings, corresponding to the Henry's law region, the diffusivities remain nearly constant with increasing loading, but two different trends in the variation of diffusion coefficients with loading beyond the Henry's law regime can be observed. In very small pores (≤ 1 nm) the diffusion coefficient decreases with increasing loading, while in wider pores, the diffusion coefficients increases as the loading increases beyond the Henry's law regime [53]. The difference in behaviour arises because of the increasing contribution of viscous flow with increase in loading in large pores where multilayers can form. On the other hand in narrow pores fluid-solid interactions dominate, and increase in loading causes mutual interference between fluid molecules with negligible viscous contribution, and this reduces the diffusivity with increase in loading.

3.4.3.4 Comparison with molecular dynamics simulation

In recent work from this laboratory the atomistic structure of SiC-DC has been obtained using hybrid reverse Monte Carlo (HRMC) simulation [63], and this structure has been used by us as a platform for predicting diffusion coefficients using equilibrium molecular dynamics (EMD) simulations [66]. Here we use these simulation results to validate the particle scale transport model and resulting transport coefficients, and since the details are provided elsewhere [66] we only briefly outline the simulation method here. The simulations were performed over a wide range of temperatures from 150 K to 1000 K, using the LAMMPS simulation package [67], with an all atom model of CH_4 with partial charges, in which translational and rotational degrees of freedom of rigid bodies were both thermostated using the Nose-Hoover algorithm detailed in the literature [68-71]. A potential cut-off distance of 18 Å was used, and a standard Ewald formulation used for electrostatic interactions. A Verlet time integrator was used with time step equal to 1 fs, and MD simulations were run for at least 18 ns in the production phase so that displacement of the center of mass of the molecules was greater than the size of the unit cell (40 Å). To calculate self-diffusivity of CH_4, mean-squared displacements (MSDs) of the center of mass of the molecules were collected in the Fickian regime, in which log-log dependence of MSD with time is linear. Self-diffusivity was then obtained using the well-known Einstein equation:

$$D_s = \frac{1}{2Nd}\lim_{t\to\infty}\frac{1}{t}\langle\sum_{i=1}^{N}\left|r_i(t)-r_i(0)\right|^2\rangle \tag{3-17}$$

where $r_i(t)$ is the center of mass position vector of molecule *i* at time *t*, *N* is the number of molecules and *d* is dimensionality of the system. At infinite dilution case the self-diffusion coefficient approaches the collective diffusivity and may be compared to that obtained from the macroscopic uptake experiments reported here.

Here, the low density uptake-based particle scale diffusion data in Table 3-2 are compared with the results of EMD simulations [66] at very low loading (~ 0.027 mmol/g) and microscopic quasi-elastic neutron scattering (QENS) measurements [66]. The uptake-based diffusivities correspond to about 400 mm bulk pressure and, as seen from the results in Table 3-3, are unaffected by pressure at the low corresponding uptake. The QENS experiments were carried out using the time-of-flight spectrometer IN6, at the Institut Laue-Langevin (ILL). The details of QENS experiments on SiC-DC 20 µm samples are presented in our

recent publication elsewhere [66]. Figure 3-14 compares the temperature dependence of the particle scale diffusion coefficients obtained from uptake kinetics with self-diffusivities obtained from molecular dynamics simulation and QENS measurements at low density.

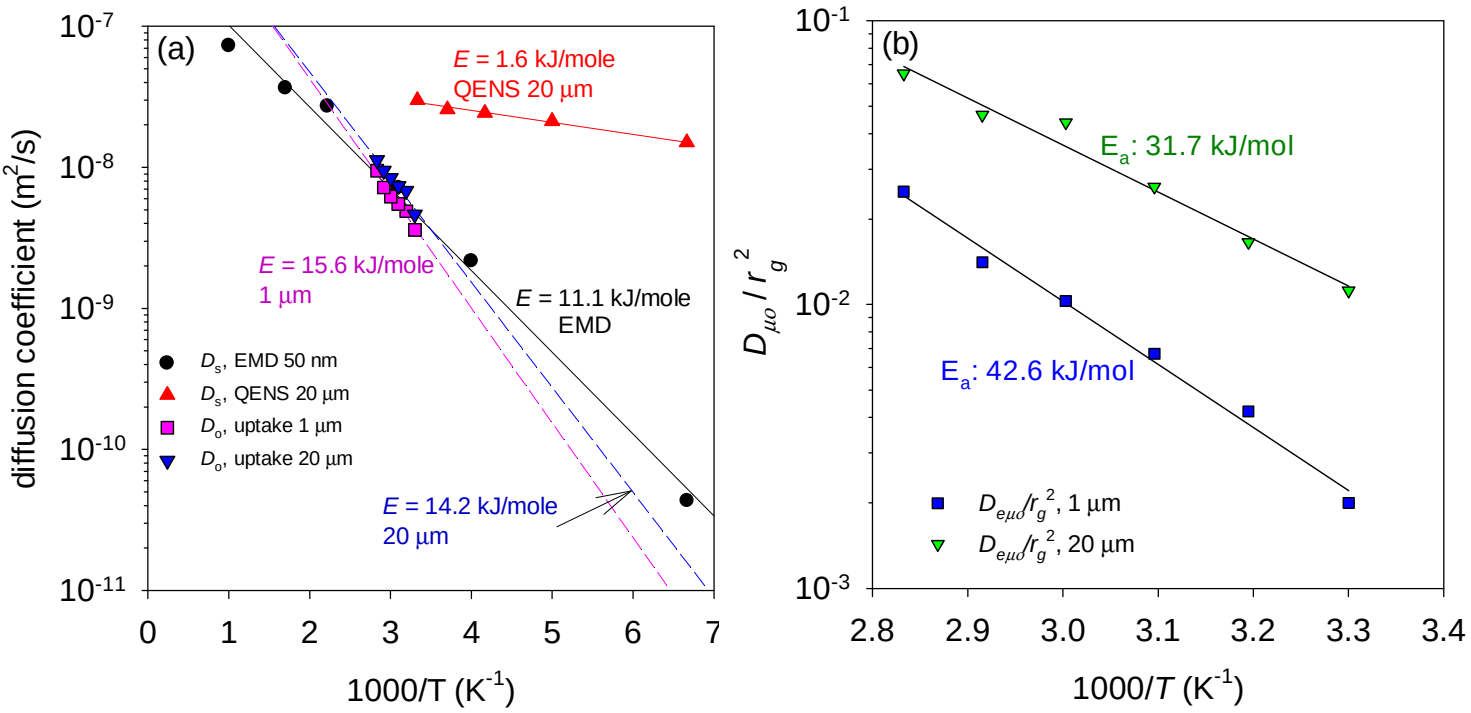

Figure 3-14. Temperature dependence of (a) CH_4 diffusivities obtained from bipore model, simulation and QENS measurement [66], and (b) $D_{\mu o}/r_g^2$ in grain-scale ultra-micropores.

As seen in Figure 3-14, there is excellent agreement between the particle scale diffusion coefficients with the predictions of the molecular dynamics simulation, while the QENS-based diffusion coefficients are as much as one order of magnitude larger. Since long-range diffusion of fluid molecules is considerably retarded by internal barriers arising from structural constrictions and disorder, macroscopic diffusivities are almost always several orders of magnitude smaller than microscopic diffusivities, usually measured by molecular dynamics simulation or QENS experiments, which probe much smaller length scales [72-75]. Interestingly, our MD results show very good agreement with the measured particle scale diffusion coefficients, which is remarkable considering that the simulations are based on a structure derived purely from neutron scattering measurements, and not using adsorption data. This agreement not only supports the present model, but also shows that the slow ultra-micropore diffusion is not captured by MD. This is readily rationalised based on the low

values of $D_{\mu o}/r_g^2$ in Tables 3-2 and 3-3, which suggest extremely low values of $D_{\mu o}$, of the order of 10^{-17} m^2/s, based on the grain sizes estimated using HRTEM as discussed in Section 3.4.1.2. Such small diffusivities will lead to immeasurably small displacements in the time scale of an MD simulation. We further note here that the scattering measurements on which the HRMC structure is based were made with 50 nm sized SiC particles [63], while the current study has used larger particles. The agreement is still excellent, despite the precursor particle differences, suggesting that the CDC structure is only weakly dependent on particle size.

3.4.3.5 Activation energy and adsorption isosteric heat

The activation energies corresponding to the particle and grain scale diffusion of CH_4 on the SiC-DC samples were derived from the slopes of the Arrhenius plots (Figure 3-14). The magnitude of the activation energy at low loading, corresponding to a pressure of about 400 kJ/mole, for the different particle size of SiC-DC 1 µm and 20 µm samples in the larger micropores is 15.6 and 14.2 kJ/mol respectively, while the grain scale ultra-micropores CH_4 show higher activation energies of 42.6 and 31.7 kJ/mol respectively. The activation energy obtained from the grain scale diffusion is almost twice the heat of adsorption value presented below. These values are significantly larger than the activation energy for micropore diffusion of methane molecules in microporous carbon of 11.7 kJ/mole found by Prasetyo et al. [76]. On the other hand they are close to the activation energy of 40 kJ/mole for CH_4 diffusion in Takeda 3 Å carbon molecular sieve found by Rutherford et al. [77], and slightly smaller than the activation energy of 50 kJ/mole for methane transport in a different carbon molecular sieve determined by Reid and Thomas [78]. The large activation energies obtained from the CH_4 diffusivity in the grains suggests the presence of constrictions and internal pore-mouth barriers that affect the entry of CH_4 molecules into the ultra-micropores. In support it is noted that based on the variation of fluid solid interaction potential energy with pore size Rutherford et al. [77] estimate an effective aperture size of 0.32 nm, for the activation barrier of 40 kJ/mole found by them for methane diffusion in Takeda 3 Å carbon molecular sieve. The lower activation energy of 31.7 kJ/mole found here for the 20 µm sample would correspond to only a very slightly larger aperture width. This is consistent with the pore size range of 0.33-0.37 nm found here for the ultra-micropores in the grains, depicted Figure 3-8, providing strong support for the present model. A further noteworthy

result in support is that the lower activation energies of 15.6 and 14.2 kJ/mol found here for the larger particle-scale micropores, are close to the value of 11.7 kJ/mole found by Prasetyo et al. [76], suggesting that these pores are of a similar size range as the micropores in traditional activated carbon. This is indeed evident from the PSDs in Figure 3-6, showing the pore size range to be similar to that of many commercial activated carbons [36, 60]. The very slightly higher activation energy in the larger micropores, of 15.6 and 14.2 kJ/mol, in comparison to that obtained from simulation, of 11.1 kJ/mol, seen in Figure 3-14, does indicate the possibility of some structural constrictions and internal barriers that affect macroscopic transport, but are not captured at the small length scale of simulation (~10 nm). We note here that a slightly lower activation energy from simulation, of about 7.05 kJ/mole, has been reported in our recent article [66], but that is for a pressure of 400 mmHg and corresponds to the higher loading of about 1.2 mmol/g, close to that used in the QENS experiments, somewhat beyond the infinite dilution region.

The isosteric heat of adsorption is also important when adsorbents are considered for potential adsorption processes. The amount of heat released from an adsorption process could have an adverse effect on the adsorption capacities of the components which can result in a loss of the adsorbent capacity. The contributions to isosteric heats of adsorption at zero loading, ΔH, from the Langmuir and Henry Law parts of the isotherms may be obtained, following

$$-\Delta H = RT^2 \frac{d\ln(P)}{dT} \tag{3-18}$$

where P is pressure. Figure 3-15 depicts the respective equilibrium constants calculated from fitting of the dual Langmuir-Henry equation to CH_4 experimental isotherm data for both SiC-DCs. The values of the heats of adsorption, lying in the range of 18-20 kJ/mole, are in the usual range for methane adsorption in microporous carbons of 17-20 kJ/mole [79]. Interestingly, both the ultra-micropores and the larger particle scale micropores have nearly similar heats, which at first appeared surprising. However, this is readily reconciled with the variation of interaction energy of CH_4, and the resulting heat of adsorption, with carbon slit pore size, estimated by Rutherford et al. [77] and replotted in the inset in Figure 3-15(a). At the narrow pore width of the ultra-micropores of about 0.35 nm (Figure 3-8) CH_4 is in the region of the curve to the left of the minimum, and the theoretically estimated isosteric heat is

about 22 kJ/mole. This is in very good agreement with the experimental results in Figure 3-15(a), given the high sensitivity of the heat with pore size in this region.

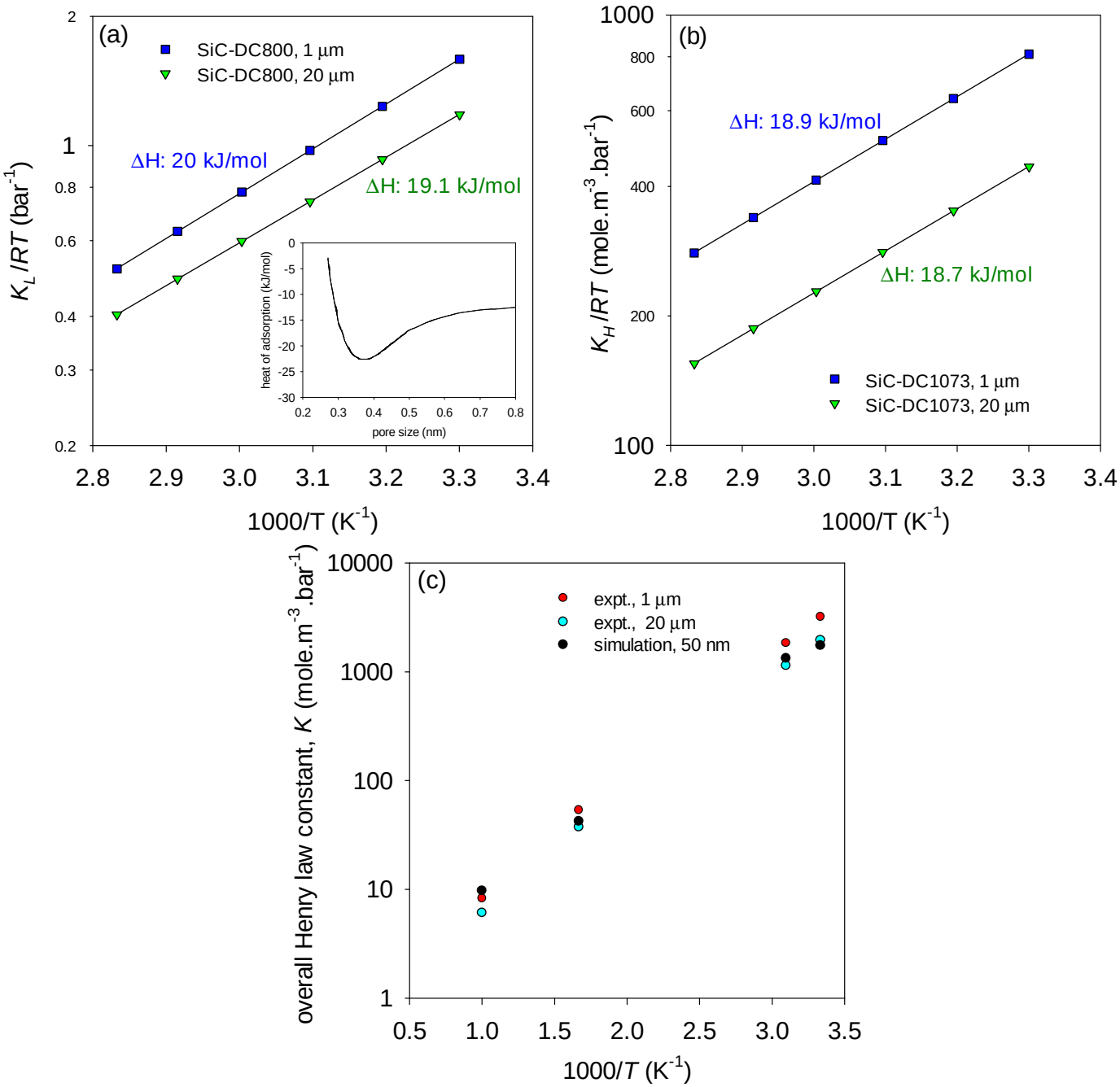

Figure 3-15. Temperature variation of calculated (a) Langmuir, and (b) Henry law mode equilibrium constants, obtained from the dual Langmuir-Henry model in SiC-DC1073 particles of nominal size 1 µm and 20 µm. The inset in (a) depicts the variation in isosteric heat with pore size, theoretically estimated by Rutherford et al. [77]. (c) Comparison of overall Henry law constant from dual mode isotherm with that from grand canonical Monte Carlo simulation [66].

On the other hand, for the pore width of about 0.48 nm for the larger particle scale micropores, corresponding to the first peak of the pore size distributions in Figures 3-6 and 3-8, the inset of Figure 3-15(a) shows CH_4 to now be in the part of the curve to the right of the minimum, with an isosteric heat of about 17.9 kJ/mole, also in very good agreement with the experimental results. Figure 3-15(c) compares the overall Henry constants from grand canonical Monte Carlo simulation [66] and the present measurements. The experimental values are estimated using the low loading limit of the dual Henry-Langmuir model in Eqs (3-1)-(3-3), and the constants in Table 3-1. Very good agreement is observed between the experimental results and the simulation, providing cross-validation.

Regarding the assumption of isothermal conditions in the kinetics models, it should be mentioned that the maximum energy release per unit mass of carbon equals the product of the specific heat of carbon (C_p=0.71 J/g°C) and the maximum possible temperature rise. If we assume that this energy is not dissipated and is accumulated in the sample, and by considering the amount adsorbed of methane roughly around 0.02 mmol/g, in a given step, then the maximum temperature rise would be only around 0.5°C, for the heat of adsorption of about 18 kJ/mol for CH_4. Nevertheless, most of this energy is expected to be dissipated, justifying our assumption of isothermality.

Regarding the issue of the valve dynamics in the volumetric measurement technique [80] that is used in our work, it should be mentioned that we have also conducted a blank run and monitored the pressure signals. The time of the disturbances induced due to the valve dynamics was less than one second as it is shown in Figure 3-16.

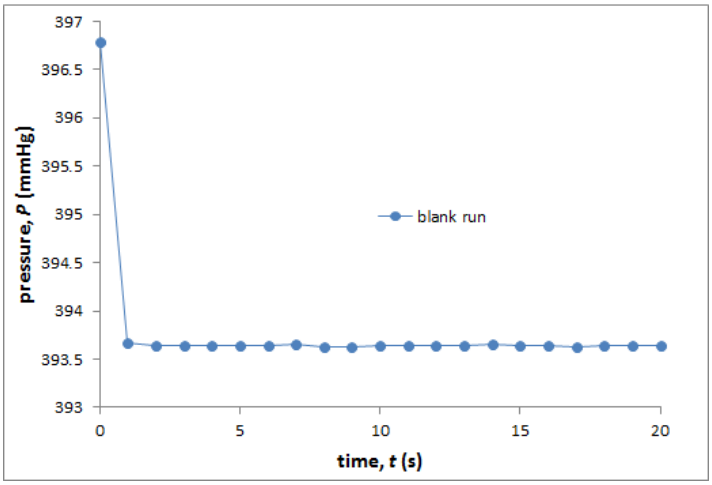

Figure 3-16 Pressure response in blank run in the experimental kinetics measurements

3.5 Conclusions

We have characterized the microstructure of micrometer-sized SiC-DC samples synthesized at 1073 K, investigating both solid structure and pore structure, using different characterization techniques such as SEM, TEM, XRD, helium density and adsorption. The HRTEM analysis showed the existence of grains in the amorphous structure of SiC-DC particles, while CO_2 adsorption at 273 K indicates the presence of significant ultra-microporosity not observed in characterisations based on Ar adsorption at 87 K. The FWT-NLDFT model with PSD obtained from argon adsorption at 87 K is used to predict experimental sub-atmospheric CO_2 adsorption at 273 K and high pressure CH_4 adsorption at 313 and 333 K. All the experimental data are reasonably well predicted by the FWT-NLDFT model, however, under-prediction is observed at very low pressure for sub-atmospheric CO_2 adsorption at 273 K indicating a pore accessibility problem for argon at 87 K.

The presence of both ultra-microporosity and grains in SiC-DC particles suggests that this ultra-microporosity exists locally in the grains, and a bidisperse structure model is proposed here for this CDC, comprising grain scale ultra-micropores and larger particle scale micopores. A dual Langmuir-Henry adsorption isotherm has been found to fit data for CH_4 adsorption isotherms on SiC-DC at different temperatures very well, consistent with this bididpserse structure model. This model is also found to correlate experimental data for transient uptake kinetics of CH_4 in SiC-DC, more satisfactorily than alternative micropore diffusion models involving only one diffusional length scale. The activation energy for the diffusion of CH_4 in the grains is comparable to that for carbon molecular sieves, in agreement with our model considering the grains to be ultra-microporous.

A comparison of macroscopic uptake-based data with simulation results and QENS measurement data shows remarkable agreement between simulation dynamics and the uptake-based diffusivities. The difference between the activation energies obtained from simulation and QENS with that from macroscopic uptake, suggests that there are some structural constrictions and internal barriers, which are not captured by the simulation or the QENS measurement.

3.6 References

[1] Presser V, Heon M, and Gogotsi Y, Carbide-Derived Carbons–From Porous Networks to Nanotubes and Graphene. Adv Funct Mater, 2011; **21**(5):810-833.

[2] Gogotsi Y, Nikitin A, Ye H, Zhou W, Fischer JE, Yi B. Nanoporous carbide-derived carbon with tunable pore size. Nat Mater 2003;2(9):591-4.

[3] Yushin GN, Hoffman EN, Nikitin A, Ye H, Barsoum MW, Gogotsi Y. Synthesis of nanoporous carbide-derived carbon by chlorination of titanium silicon carbide. Carbon 2005;43(10):2075-82.

[4] Yushin G, Dash R, Jagiello J, Fischer JE, Gogotsi Y. Carbide-Derived Carbons: Effect of Pore Size on Hydrogen Uptake and Heat of Adsorption. Adv Funct Mater 2006;16(17):2288-93.

[5] Bonilla MR, Bae JS, Nguyen TX, Bhatia SK. Heat Treatment-Induced Structural Changes in SiC-Derived Carbons and their Impact on Gas Storage Potential. J Phys Chem C 2010;114(39):16562-75.

[6] Bhatia SK, Nguyen TX. Potential of silicon carbide-derived carbon for carbon capture. Ind Eng Chem Res 2011;50(17):10380-3.

[7] Chmiola J, Yushin G, Gogotsi Y, Portet C, Simon P, Taberna PL. Anomalous increase in carbon capacitance at pore sizes less than 1 nanometer. Sci 2006;313(5794):1760.

[8] Welz S, McNallan MJ, Gogotsi Y, Carbon structures in silicon carbide derived carbon. J Mater Process Technol 2006;179(1):11-22.

[9] Wang J, Oschatz M, Biemelt T, Borchardt L, Senkovska I, Lohe MR. Synthesis, characterization, and hydrogen storage capacities of hierarchical porous carbide derived carbon monolith. J Mater Chem 2012;22(45):23893-9.

[10] Pérez CR, Yeon SH, Ségalini J, Presser V, Taberna PL, Simon P. Structure and Electrochemical Performance of Carbide-Derived Carbon Nanopowders. Adv Funct Mater 2013;23(8):1081-9.

[11] Dash R, Chmiola J, Yushin G, Gogotsi Y, Laudisio G, Singer J. Titanium carbide derived nanoporous carbon for energy-related applications Carbon 2006;44(12):2489-97.

[12] Gogotsi Y, Dash RK, Yushin G, Yildirim T, Laudisio G, Fischer JE. Tailoring of nanoscale porosity in carbide-derived carbons for hydrogen storage. J Amer Chem Soc 2005;127(46):16006-7.

[13] Zheng J, Ekström TC, Gordeev SK, Jacob M. Carbon with an onion-like structure obtained by chlorinating titanium carbide. J Mater Chem 2000;10(5):1039-41.

[14] Bae JS, Nguyen TX, Bhatia SK. Influence of synthesis conditions and heat treatment on the structure of Ti3SiC2-derived carbons. J Phys Chem C 2009;114(2):1046-56.

[15] Bae JS, Nguyen TX, Bhatia SK. Pore accessibility of Ti3SiC2-derived carbons. Carbon 2014;68:531-41.

[16] Rose M, Kockrick E, Senkovska I, Kaskel S. High surface area carbide-derived carbon fibers produced by electrospinning of polycarbosilane precursors. Carbon, 2010;**48**(2):403-407.

[17] Gogotsi YG, Jeon ID, McNallan MJ. Carbon coatings on silicon carbide by reaction withchlorine-containing gases. J Mater Chem 1997;7(9):1841-8.

[18] Nguyen TX, Bae JS, Bhatia SK. Characterization and adsorption modeling of silicon carbide-derived carbons. Langmuir 2009;25(4):2121-32.

[19] Gogotsi Y, Welz S, Ersoy DA, McNallan MJ. Conversion of silicon carbide to crystalline diamond-structured carbon at ambient pressure. Nature 2001;411(6835):283-7.

[20] Nikitin A, Gogotsi Y. Nanostructured Carbide-Derived Carbon (CDC). In: Nalwa HS, ed. Encyclopedia of Nanoscience and Nanotechnology: Amer Sci Publishers: CA 2004 p. 553−74.

[21] Do DD. Adsorption analysis: equilibria and kinetics: Imperial College Press; 1998.

[22] Kärger J, Ruthven DM, Theodorou DN. Diffusion in nanoporous materials: John Wiley & Sons; 2012.

[23] Bhatia SK. Transport in bidisperse adsorbents: significance of the macroscopic adsorbate flux. Chem Eng Sci 1997;52(8):1377-86.

[24] Kärger J, Ruthven DM. Diffusion in zeolites. Willey & Sons, New York. 1992.

[25] Ruckenstein E, Vaidyanathan AS, Youngquist GR. Sorption by solids with bidisperse pore structures. Chem Eng Sci 1971;26(9):1305-18.

[26] Schneider P, Smith JM, Chromatographic study of surface diffusion. AIChE J 1968;14(6):886-95.

[27] Bhatia SK. Transport of adsorbates in microporous solids: arbitrary isotherm. Proceedings of the Royal Society of London Series A: Math Phys Sci 1994;446(1926):15-37.

[28] Wakao N, Smith JM. Diffusion in catalyst pellets. Chem Eng Sci 1962;17(11):825-34.

[29] Seidel A, Gelbin D. Breakthrough curves for single solutes in beds of activated carbon with a broad pore-size distribution—I. Mathematical models of breakthrough curves in beds of activated carbon. Chem Eng Sci 1986;41(3):541-8.

[30] Barrer RM. Flow into and through zeolite beds and compacts. Langmuir 1987;3(3):309-15.

[31] Kärger J. Mass transfer through beds of zeolite crystallites and the paradox of the evaporation barrier. Langmuir 1988;4(6):1289-92.

[32] Gray PG, Do DD. Adsorption and desorption of gaseous sorbates on a bidispersed particle with Freundlich isotherm: III. Contribution of surface diffusion to the sorption dynamics of sulphur dioxide on activated carbon. Gas Sep Purif 1990;4(3):149-57.

[33] Hu X, Rao GN, Do DD. Effect of energy distribution on sorption kinetics in bidispersed particles. AIChE J 1993;39(2):249-61.

[34] Do DD, Hu X. An energy-distributed model for adsorption kinetics in large heterogeneous microporous particles. Chem Eng Sci 1993;48(11):2119-27.

[35] Bhatia SK, Gray PG, Do DD. Modelling of sorption of gaseous sorbates in bidispersed structured solids:: The concept of heterogeneity of the microphase. Gas Sep Purif 1991;5(1):49-55.

[36] Ding LP, Bhatia SK, Liu F. Kinetics of adsorption on activated carbon: application of heterogeneous vacancy solution theory. Chem Eng Sci 2002;57(18):3909-28.

[37] Do DD, Wang K. Dual diffusion and finite mass exchange model for adsorption kinetics in activated carbon. AIChE J 1998;44(1):68-82.

[38] Fletcher AJ, Thomas KM. Adsorption and desorption kinetics of n-octane and n-nonane vapors on activated carbon. Langmuir 1999;15(20):6908-14.

[39] Loughlin KF, Hassan MM, Fatehi AI, Zahur M. Rate and equilibrium sorption parameters for nitrogen and methane on carbon molecular sieve. Gas Sep Purif 1993;7(4):264-73.

[40] Qinglin H, Farooq S, Karimi IA. Prediction of binary gas diffusion in carbon molecular sieves at high pressure. AIChE J 2004;50(2):351-67.

[41] Qinglin H, Sundaram SM, Farooq S. Revisiting transport of gases in the micropores of carbon molecular sieves. Langmuir 2003;19(2):393-405.

[42] Wang Y, LeVan MD. Master curves for mass transfer in bidisperse adsorbents for pressure-swing and volume-swing frequency response methods. AIChE J 2011;57(8):2054-69.

[43] Kapoor A, Yang RT. Surface diffusion on energetically heterogeneous surfaces--an effective medium approximation approach. Chem Eng Sci 1990;45(11):3261-70.

[44] Kapoor A, Yang RT, Wong C. Surface diffusion. Cat Rev - Sci Eng 1989;31(1-2):129-214.

[45] Higashi K, Ito H, Oishi J. Surface diffusion phenomena in gaseous diffusion. I. Surface diffusion of pure gas. Nippon Genshiryoku Gakkaishi (Japan). 1963;5.

[46] Smith RK, Metzner AB. Rates of surface migration of physically adsorbed gases. J Phys Chem 1964;68(10):2741-7.

[47] Weaver JA, Metzner AB. The surface transport of adsorbed molecules. AIChE J 1966;12(4):655-61.

[48] Yang RT, Fenn JB, Haller GL. Modification to the Higashi model for surface diffusion. AIChE J 1973;19(5):1052-3.

[49] Thakur SC, Brown LF, Haller GL. Gas-adsorbate collisional effects and surface diffusion in porous materials. AIChE J 1980;26(3):355-63.

[50] Thakur SC, Brown LF. Effects of gas-adsorbate momentum transfer on the movement of a mobile adsorbed phase over a uniform surface. AIChE J 1983;29(4):696-8.

[51] Do DD. A model for surface diffusion of ethane and propane in activated carbon. Chem Eng Sci 1996;51(17):4145-58.

[52] Kapoor A, Yang RT. Surface diffusion on energetically heterogeneous surfaces. AIChE J 1989;35(10):1735-8.

[53] Jepps OG, Bhatia SK, Searles DJ. Modeling molecular transport in slit pores. J Chem Phys 2004;120:5396.

[54] Bhatia SK, Chen H, Sholl DS. Comparisons of diffusive and viscous contributions to transport coefficients of light gases in single-walled carbon nanotubes. Mol Simul 2005;31(9):643-9.

[55] Nicholson D. Simulation studies of methane transport in model graphite micropores. Carbon 1998;36(10):1511-23.

[56] Nguyen TX, Bhatia SK. Probing the pore wall structure of nanoporous carbons using adsorption. Langmuir 2004;20(9):3532-5.

[57] Sircar S. Gibbsian Surface Excess for Gas Adsorption Revisited. Ind Eng Chem Res 1999;38(10):3670-82.

[58] Sircar S. Measurement of Gibbsian surface excess. AIChE J 2001;47(5):1169-76.

[59] Jänes A, Thomberg T, Lust E. Synthesis and characterisation of nanoporous carbide-derived carbon by chlorination of vanadium carbide. Carbon 2007;45(14):2717-22.

[60] Nguyen TX, Bhatia SK, Nicholson D. Prediction of high-pressure adsorption equilibrium of supercritical gases using density functional theory. Langmuir 2005;21(7):3187-97.

[61] Nguyen TX, Bhatia SK. Kinetic restriction of simple gases in porous carbons: transition-state theory study. Langmuir 2008;24(1):146-54.

[62] Nguyen TX, Bhatia SK. Characterization of accessible and inaccessible pores in microporous carbons by a combination of adsorption and small angle neutron scattering. Carbon 2012;50(8):3045-54.

[63] Farmahini AH, Opletal G, Bhatia SK. Hybrid Reverse Monte Carlo Modeling of Silicon Carbide-Derived Nanoporous Carbon. J Phys Chem C 2013;117(27):14081-94.

[64] Presser V, McDonough J, Yeon SH, Gogotsi Y. Effect of pore size on carbon dioxide sorption by carbide derived carbon. Energy Environ Sci 2011; **4**(8): 3059-3066.

[65] Crank J. The mathematics of diffusion. Clarendon, Oxford. 1975:71.

[66] Farmahini AH, Shahtalebi A, Jobic H, Bhatia SK. Influence of Structural Heterogeneity on Diffusion of CH_4 and CO_2 in Silicon Carbide-Derived Nanoporous Carbon. J Phys Chem C, 2014, in press.

[67] Plimpton S. Fast parallel algorithms for short-range molecular dynamics. J Comput Phys, 1995; **117**(1): 1-19.

[68] Hoover WG. Canonical dynamics: equilibrium phase-space distributions. Phys Rev A, 1985; **31**(3): 1695-7.

[69] Martyna GJ, Tuckerman ME, Tobias DJ, Klein ML. Explicit reversible integrators for extended systems dynamics. Molecular Physics, 1996;**87**(5):1117-1157.

[70] Martyna GJ, Klein ML, Tuckerman M. Nosé–Hoover chains: The canonical ensemble via continuous dynamics. J Chem Phys, 1992;**97**(4):2635-2643.

[71] Kamberaj H, Low R, Neal M. Time reversible and symplectic integrators for molecular dynamics simulations of rigid molecules. J Chem Phys, 2005;**122**(22):224114.

[72] Jobic H. Molecular dynamics of n-pentane in NaX zeolite studied by quasi-elastic neutron scattering. Phys Chem Chem Phys, 1999;**1**(4):525-530.

[73] Jobic H, Schmidt W, Krause CB, Karger J. PFG NMR and QENS diffusion study of N-Alkane homologues in MFI-type zeolites. Microporous Mesoporous Mater, 2006;**90**(1):299-306.

[74] Feldhoff A, Caro J, Jobic H, Ollivier J, Krause CB, Galvosas P, Karger J. Intracrystalline transport resistances in nanoporous zeolite X. ChemPhysChem, 2009;**10**(14):2429-2433.

[75] Jobic H, Theodorou DN. Quasi-elastic neutron scattering and molecular dynamics simulation as complementary techniques for studying diffusion in zeolites. Microporous Mesoporous Mater, 2007;**102**(1):21-50.

[76] Prasetyo I, Do DD. Adsorption rate of methane and carbon dioxide on activated carbon by the semi-batch constant molar flow rate method. Chem Eng Sci 1998;53(19):3459-67.

[77] Rutherford SW, Nguyen C, Coons JE, Do D.D. Characterization of carbon molecular sieves using methane and carbon dioxide as adsorptive probes. Langmuir 2003;19(20):8335-42.

[78] Reid CR, Thomas KM. Adsorption kinetics and size exclusion properties of probe molecules for the selective porosity in a carbon molecular sieve used for air separation. J Phys Chem B 2001;105(43):10619-29.

[79] Düren T, Sarkisov L, Yaghi OM, Snurr RQ. Langmuir 2004; 20 (7):2683-2689.

[80] Brandani S. Analysis of the piezometric method for the study of diffusion in microporous solids: isothermal case. Adsorption 1998;4(1):17-24.

Chapter 4 : Barriers to diffusion of CO_2 in microporous carbon derived from silicon carbide[*]

[*]Published in *Carbon*, Vol. 88, 1-15

We investigate the adsorption equilibrium and uptake kinetics of CO_2 in nanoporous silicon carbide-derived carbon (SiC-DC) experimentally, as well as by simulation through Grand Canonical Monte Carlo (GCMC) and equilibrium molecular dynamics (EMD) simulations using a hybrid reverse Monte Carlo (HRMC) simulation-based atomistic structural model of the carbon. The kinetics is best explained when a grain surface barrier resistance mechanism is incorporated in a bidisperse pore structure model, considering particle scale diffusion in large micropores and a local grain scale diffusion in ultra-micropores. Good agreement is found between simulated and experimental isotherms; however, experimental particle scale diffusivities are almost two orders of magnitude smaller than those obtained from EMD, suggesting the presence of long range barriers for CO_2 not captured by the HRMC model structure. These barriers lead to about two orders of magnitude reduction in the particle-scale diffusivity of CO_2 compared to CH_4. On the other hand activation barriers for grain scale diffusion of CO_2 are comparable to those for CH_4 in the SiC-DC, and in carbon molecular sieves, consistent with the ultra-microporous nature of the grains. The activation barrier for interfacial mass transfer coefficient at the grain surface is also consistent with values for carbon molecular sieves.

4.1 Introduction

The large anthropogenic greenhouse gas (GHG) emissions and their impact on global climate is one of the primary environmental issues and concerns facing modern society. Among GHGs, carbon dioxide (CO_2) emission from fossil fuel combustion in power plants has the largest contribution to global warming effects and climate change potential. This has stimulated the development of a number of carbon mitigation technologies, in the effort to stabilize atmospheric CO_2 at a level that could minimize the impact on the global climate. Among the various technological options, the capture and storage of CO_2 from combustion flue gases is currently the subject of extensive attention worldwide, with numerous proposed alternatives. Of these, membrane separation and the selective adsorption of CO_2 on porous adsorbent solids offers environmentally friendly technology, which is also economical. Many possible solids have been investigated for CO_2 adsorption including metal organic

frameworks (MOFs), zeolites, activated carbons, carbon nanotubes (CNTs), and carbide-derived carbons (CDCs). The synthesis techniques have allowed the pore size of adsorbent solids such as CDCs [1] to be engineered and tailored to suit a wide range of applications. It has been demonstrated that CDCs possess unique properties and are promising for gas adsorption and storage applications due to their narrow pore size distribution and large pore volume [1-3].

The synthesis of CDCs by etching metals from a carbide precursor using chemical extraction, halogenation, hydrothermal and vacuum decomposition methods have been well discussed in the literature [1,4-7]. In our laboratory, CDCs synthesized by chlorination have been characterized in detail using a battery of techniques such as gas adsorption, high resolution transmission electron microscopy (HRTEM), helium pycnometery, Raman spectroscopy and small angle neutron scattering (SANS) [2-3,8-9]. The experimental characterization results of the SiC-DC1073 (silicon carbide-derived carbon prepared by chlorination at 1073 K) from X-ray diffraction (XRD) and HRTEM have demonstrated a highly disordered nanoporous structure, which is partially inaccessible to some gases [2,3]. Recently, evidence for bidisperse structure of CDCs, even for purely nanoporous samples, has been reported in our laboratory [2]; with CO_2 adsorption at 273 K on SiC-DC and Ti_3SiC_2-DC, showing that highly nanoporous SiC-DCs comprise two kinds of pores, ultra-micropores having size in the range of 0.33-0.37 nm inside small independent grains (or microparticles) and larger particle scale micropores. Here, we refer to the 0.33-0.37 nm pores as ultra-micropores, although it is common to use this term more generally for pores smaller than 0.7 nm. Argon adsorption has been employed for the characterization of CDCs and their pore size distribution, however ultra-micropores pose difficulty for this technique because the ultra-micropores are largely inaccessible to argon at low temperatures. Carbon dioxide adsorption at 273 K has shown promise as a means for the characterization of ultra-micropores in carbide-derived carbons and offers the advantage of probing pore sizes of several angstroms. It has been demonstrated that in SiC-DCs with no macropores, the large micropores provide pathways and access to the ultra-micropores inside the grains [2]. Thus, the large micropores form the voids generated from the agglomeration of carbon grains which contain the ultra-micropores.

A detailed investigation of the kinetics of CH_4 uptake in SiC-DC has been presented in our recent publication [2]. We have obtained grain scale activation energies for CH_4 diffusion

very close to values for carbon molecular sieve (CMS), consistent with the presence of ultra-microporosity in the grains. The uptake dynamics of gases in CMS has been also a topic of considerable importance and significance in the field of gas adsorption, and numerous mathematical models of adsorption dynamics have been proposed in the literature for these materials, which are known to possess a bidisperse structure with distinguishable macropore and micropore resistances to the transport of adsorbates [10-11]. The diffusion mechanism of gases in these materials has been usually explained by a dual resistance model with the presence of a surface barrier resistance caused by constrictions at pore mouths along with a diffusion mechanism. Liu and Ruthven [12] have shown that kinetic data for O_2, N_2 and Ar on CMS are consistent with internal diffusion control whereas the data for CH_4 are consistent with surface barrier resistance control. They also found that CO_2 displayed a transition from surface barrier resistance at lower temperatures to diffusion control at higher temperatures. They suggested that the relative importance of the two resistances depended on the ratio of their time constants, and is affected by changes in temperature or pressure. Rutherford and Do [13] found that micropore diffusion is rate limiting for CO_2 adsorption on Takeda 5A CMS, while Nguyen and Do [14] presented a dual Langmuir kinetic model to describe adsorption of O_2, Ar and N_2 on Takeda 3A. In their work, the adsorption kinetics is modelled by a series of two consecutive processes, in which the nonselective adsorption of molecules in meso- and super-micropores is followed by the movement of adsorbed molecules into small micropores through the pore mouth barriers. In other works, Qinglin et al. [15-16], and Wang and LeVan [17] have considered a surface barrier resistance in series with a micropore diffusion resistance for the diffusion of gases in CMS, with negligible direct contribution of micropores to the macroscale flux. Significant interfacial barrier resistance is known to be present also in other microporous materials such as zeolites, as seen in both experiment and simulation. Through analysis of sorption experimental data on zeolites, Karger and co-workers have shown that a barrier resistance exists at the surface, in addition to resistance to diffusion within the crystal [18-19], while in other work Zimmermann et al. [20-23] have demonstrated the presence of a surface barrier resistance by combining transition state theory and equilibrium molecular dynamics simulations.

In our recent work investigating the diffusion mechanism of CH_4 [2], we have proposed a bipore transport model based on the assumption of a bidisperse structure, following evidence of ultra-microporosity in SiC-DC and Ti_3SiC_2-DC [2-3]. Adsorption in large micropores is

relatively weak, and these are viewed as the pathways through which the adsorptive diffuses from the bulk phase into the ultra-micropores. On the other hand, in ultra-micropores, the overlapping of the potential energy field due to the solid leads to an enhanced potential field leading to stronger adsorption. It was shown that the kinetics of CH_4 adsorption is governed by two distinct diffusional resistances, arising from slow diffusion in the grain ultra-micropores and faster diffusion in the larger particle scale micropores forming the intergrain pathways [2]. Some accessibility problems of gases have also been reported for Ti_3SiC_2-DCs and SiC-DCs [2-3,9]. The accessibility of a molecule to the pore space depends on the molecular dimension relative to the size of the pores as well as temperature and pressure. The energy barriers affecting accessibility are either due to narrow pore entries near strong binding sites [3], or due to the flexibility of the pore space [24-25]. Such barriers may be overcome by sufficiently high molecular kinetic energy [26]. At a given temperature, some pore spaces may remain inaccessible until a sufficiently high driving force, such as resulting from an increase in pressure, promotes molecular entry. The presence of such accessibility issues in CDCs suggests that interfacial barriers may be significant and require consideration in the analysis of uptake kinetics data for CDC particles.

From a theoretical viewpoint Monte Carlo and molecular dynamics (MD) simulations can be used to provide prediction of adsorption and diffusion of gases in disordered microporous materials, based on the use of realistic adsorbent model structures [27-30]. Our recent work on the diffusion of CH_4 in the internal structure of SiC-DC[2], compared predictions from MD simulations with diffusivities from quasi-elastic neutron scattering (QENS) measurements and with macroscopic uptake-based CH_4 transport coefficients [2,27], finding remarkable agreement between MD simulation results and the uptake-based diffusivities of CH_4 in SiC-DC at low uptake. From the comparison between the activation energies obtained from MD simulation and QENS with that from macroscopic uptake kinetics, it was concluded that there were some internal barriers which were not captured in the QENS experiments.

We investigate here the diffusion of CO_2 in disordered microporous SiC-DC at various temperatures and loading, using a volumetric technique. Experimental adsorption uptake kinetics and equilibrium data for CO_2 are obtained using small pressure steps, and the dependence of the uptake kinetics on loading and temperature interpreted using a bipore model incorporating a grain surface barrier resistance. In addition, isotherm predictions

obtained by grand canonical Monte Carlo (GCMC) simulation, and CO_2 self-diffusivities obtained from molecular dynamics simulation, using the atomistic model of disordered microporous SiC-DC developed in our laboratory [30], are compared with those from the experimental low pressure CO_2 data. The results obtained support presence of significant surface barrier resistance mechanism for the diffusion of CO_2 in the synthesized SiC-DCs, possibly related to structural constrictions and large entry barriers near the grain surface.

4.2 Experimental section

The SiC-DC1073 samples employed in this work have been synthesized by chlorination at 1073 K of two different micron-sized SiC precursor powders of nominal diameter 1μm and 20μm, provided by Alfa Aesar and Sigma Aldrich respectively. The particle size distribution of synthesized SiC-DCs and their precursors, obtained by laser sizing, is shown elsewhere [2]. For chlorination, ultra-high purity chlorine (BOC Gases, 99.9%) and ultra-high purity argon are used as reactive and purging gases respectively at 1073 K. The synthesized SiC-DC samples were characterized using helium pycnometery, high resolution transmission electron microscopy (HRTEM), X-ray diffraction, Scanning Electron Microscopy (SEM), and low temperature argon and CO_2 adsorption measurements. The pore size distribution (PSD) of the samples, obtained using argon (87 K) and CO_2 (273 K) adsorption measurements, using a Micromeritics ASAP 2020 analyser, are depicted in Figure 4-1.

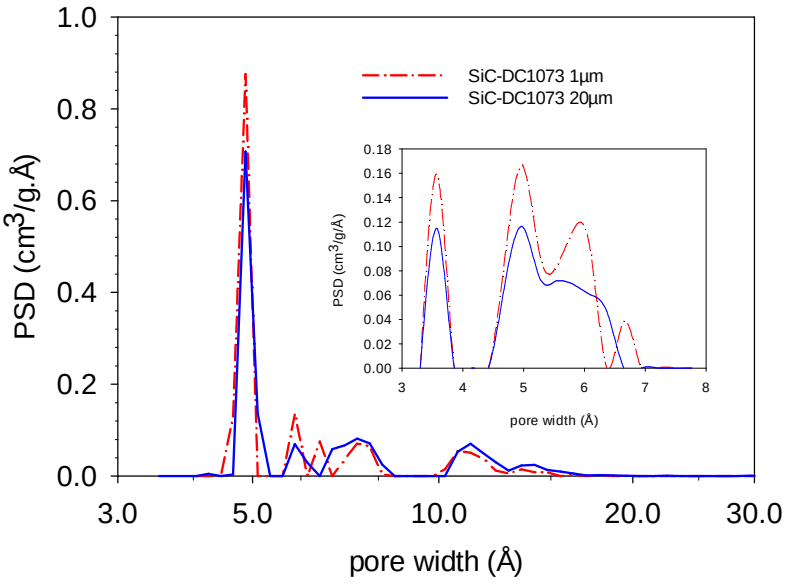

Figure 4-1. Argon and CO_2 (inset) based PSD of the SiC-DC1073 samples [2].

The sample preparation procedure and the structural characterization of the synthesized SiC-DCs are presented and discussed in detail in our previous publication [2]. The size of grains observed in the HRTEM images were reported in the range of 35-45 nm and 25-35 nm for SiC-DC1073 1µm and 20µm respectively [2]. The surface area of the SiC-DC1073 1µm and 20µm samples are reported [2] as 1508 and 1452 (m^2/g) respectively by argon adsorption at 87 K using the Finite Wall Thickness Density Functional Theory (FWT-DFT) model developed in our laboratory [31]. The pore volumes of the SiC-DC1073 1µm and 20µm samples are estimated as 0.52 cm^3/g and 0.51 cm^3/g respectively [2].

Adsorption equilibrium and kinetic data of CO_2 were obtained volumetrically using the Micromeritics ASAP 2020 adsorption analyser. A detailed description of the experimental measurement procedure is given elsewhere [2]. The adsorption isotherms were obtained at five different temperatures (303-343 K) and gas pressures up to atmospheric. Temperature control was achieved using an insulated Dewar flask with a circulating jacket connected to a thermostated water bath. In each measurement, the SiC-DC samples were firstly prepared by degassing at 623 K for 12 h. CO_2 adsorption is subsequently conducted by dosing in small pressure steps. For each pressure step, the temporal variation of pressure is recorded and converted into the transient adsorbed amount as a function of time. The final amount adsorbed at the last pressure point in a given step shows the amount adsorbed at equilibrium at that pressure. Degassing of the sample is repeated between measurements for 4 h.

4.3 Simulation

For interpretation of the experimental CO_2 isotherms and kinetics, we performed molecular simulations of adsorption of carbon dioxide on SiC-DC at different temperatures using grand canonical Monte Carlo (GCMC) and equilibrium molecular dynamics (EMD) simulations. For performing the simulations, we used the atomistic model of SiC-DC1073 K recently obtained in our laboratory [30] based on the experimental structure factor data from neutron scattering, using the Hybrid Reverse Monte Carlo (HRMC) simulation technique [28,30,32-33]. It is termed the HRMC model of SiC-DC throughout this work. Nanoporous SiC-DC synthesized by the chlorination of 50 nm size βSiC particles at 1073 K was used in the neutron scattering experiments [30]. The HRMC model of disordered SiC-DC provides a 40 Å cubic unit cell comprising 3052 carbon atoms. The simulations performed for this study have made use of all-atom molecular models and force field parameters; these and details of

the modelling technique, as well as validation procedure of the HRMC constructed model, are presented elsewhere [27,30]. We performed GCMC simulations of adsorption of CO_2 in the constructed HRMC model at 303, 323 and 343 K. In this study, sub-atmospheric equilibrium adsorption isotherms of carbon dioxide were computed sampling 50 million Monte Carlo configurations at each pressure point. A rigid carbon dioxide model possessing three distinct Lennard-Jones and Coulombic sites was used [30, 34], with model parameters given in Table 4-1.

Table 4-1. Molecular models and interaction parameters employed for GCMC simulation of adsorption isotherms [30, 34].

		fluid-fluid interactions		solid-fluid interactions		molecular model			
fluid molecule	atom	σ_{ff} (Å)	ε_{ff}/k_B (K)	ε_{cf} (Å)	ε_{cf}/k_B (K)	X(Å)	Y(Å)	Z(Å)	Charge (e)
CO_2	C	2.82	28.68	3.112	32.36	0.000	0.000	0.000	+0.664
	O	3.03	82.00	3.215	54.71	0.000	0.000	±1.162	-0.332

The self-diffusivity of CO_2 in the HRMC-based SiC-DC atomistic structure was obtained using EMD simulations in the canonical (NVT) ensemble, performed over a wide range of temperatures from 150 K to 1000 K. The LAMMPS simulation package [35] was used, with translational and rotational degrees of freedom of rigid bodies both thermostated using the Nosé-Hoover algorithm with chains, following Hoover [36] and Martyna et al. [37-38]. A Verlet time integrator was used with time step equal to 1 fs, and the damping constant of the thermostat was taken to be 5 fs or 10 fs depending on the thermodynamic conditions of the system. Short-range intermolecular interactions were modelled using the 12-6 Lennard-Jones potential with a cut-off distance of 18 Å, while a standard Ewald formalism was employed for electrostatic interactions with cut-off distance of 18 Å. MD simulations were run for at least 18 ns in the production phase, so that displacement of the centre of mass of the molecules was greater than the size of the unit cell (40 Å). The details of the simulation method are provided in our recent publication [27]. To calculate self-diffusivity of CO_2, mean-squared displacements (MSDs) of the centre of mass of the molecules were collected in the Fickian regime, in which dependence of MSD with time is linear. Self-diffusivity was then obtained using the Einstein equation:

$$D_s = \frac{1}{2Nd}\lim_{t\to\infty}\frac{1}{t}\langle\sum_{i=1}^{N}\left|r_i(t)-r_i(0)\right|^2\rangle \tag{4-1}$$

where $r_i(t)$ is center of mass position vector of molecule *i* at time *t*, *N* is number of molecules and *d* is dimensionality of the system.

4.4 Model

4.4.1 Isotherm representation

There are various fundamental and empirical isotherm equations available in the literature to describe adsorption equilibria [39], crucial for the successful representation of adsorption kinetics. Here, a dual Henry-Langmuir isotherm equation based on the bidisperse pore size distribution of SiC-DC is used to correlate the single component CO_2 adsorption on SiC-DC and obtain equilibrium constants. The dual Henry-Langmuir isotherm is related to the pore size heterogeneity of the adsorbent, with the Langmuir part corresponding to the ultra-micropores in domains termed grains, and the Henry part to the larger micropores in the particle providing access pathways into the particle interior and to the ultra-micropores. The relevant equation corresponding to this isotherm model is

$$C_a(P) = \frac{C_{\mu m}K_L C_{be}}{1+K_L C_{be}} + K_H C_{be} \tag{4-2}$$

where $C_a(P)$ and C_{be} are total adsorbed amount per unit particle volume and bulk concentration respectively, $C_{\mu m}$ is micropore capacity per unit particle volume, K_L is the Langmuirian constant, and K_H is the Henry constant. The Langmuirian and Henry constants have an exponential dependence on inverse temperature, following

$$K_L = A_\ell \exp\left(\frac{-\Delta H_\ell}{RT}\right) \tag{4-3}$$

$$K_H = A_h \exp\left(\frac{-\Delta H_h}{RT}\right) \tag{4-4}$$

where ΔH_ℓ is adsorption enthalpy for the Langmuirian part and ΔH_h is adsorption enthalpy for the Henry Law part, corresponding to the grain scale ultra-micropores and larger particle scale micropores respectively.

4.4.2 Uptake kinetics

To determine kinetic parameters from the experimental data of CO_2 on SiC-DC, an appropriate model is necessary. In our previous work [2], we investigated CH_4 diffusion in SiC-DC, and showed that the diffusion mechanism involves two time scales, comprising relatively rapid particle scale diffusion in the large micropores, and a much slower local grain scale diffusion in the ultra-micropores, in a bidisperse structure. Here, we found that the bipore model considered in our earlier work did not fit the experimental uptake data of CO_2 satisfactorily, and the data reflected the presence of a third time scale. Consequently, we have augmented this model with a local barrier resistance on the surface of the grains. Thus, a three-resistance model is used for CO_2 uptake kinetics, comprising barrier resistance at the grain surface and ultra-micropore diffusional resistance in the grain interior, along with micropore diffusional resistance at the particle scale.

In this model, according to Eq. (4-2), it is considered that the Langmuirian part of the isotherm corresponds to the adsorption in the grains, and the Henry law part corresponds to the diffusion at the particle scale in the larger micropores. Based on these assumptions, the adsorbed concentration in the ultra-micropores follows

$$\varepsilon_\mu(1-\varepsilon_m)C_\mu = \frac{C_{\mu m}K_L C_{\mu be}}{1+K_L C_{\mu be}} \tag{4-5}$$

and the adsorbate concentration in the particle scale pores follows

$$\varepsilon_m C_m = K_H C_{mbe} \tag{4-6}$$

where ε_μ is microporosity of the grains, ε_m is inter-grain porosity of the particle, C_μ is adsorbed phase concentration in the grain scale ultra-micropores, C_m is adsorbate concentration in the particle scale micropores, and $C_{\mu be}$ and C_{mbe} are local pseudo-bulk gas equilibrium concentrations corresponding to the adsorbate at the grain and particle scales respectively.

For modelling the kinetics, we consider bidisperse SiC-DC spherical particles of radius R_p, comprising spherical ultra-microporous grains of radius r_g. Following the assumptions discussed above, we consider a third resistance corresponding to an interfacial barrier at the grain surface, besides the resistances to diffusion at the particle and grain scales. The particle scale mass balance equation takes the form

$$\varepsilon_m \frac{\partial C_m}{\partial t} = -\frac{1}{R^2}\frac{\partial}{\partial R}\left(R^2 N_m\right) - \frac{3k_m}{r_g}[C_{mbe}(t,R) - C_{\mu be}(t,R,r_g)] \tag{4-7}$$

in which k_m is the interfacial mass transfer coefficient at the grain surface, and N_m is particle scale flux due to the larger sample spanning micropores. This particle scale flux is expressed as

$$N_m = -\varepsilon_m D_m \frac{\partial C_m}{\partial R} \tag{4-8}$$

where D_m is the diffusivity in the particle scale micropores. Eq. (4-7) has the symmetry boundary condition at the centre, $\partial C_m / \partial R = 0$ at $R = 0$, and the surface boundary condition, $C_m(t,R_P) = K_H C_b(t)/\varepsilon_m$, where the bulk gas concentration $C_b(t)$ follows the material balance

$$V_{ex}\frac{dC_b}{dt} = -\frac{3m\varepsilon_m D_m}{R_P \rho_P}\left(\frac{\partial C_m}{\partial R}\right)\Bigg|_{R=R_P} \tag{4-9}$$

in which V_{ex} is external volume in the sample cell, m is mass of adsorbent and ρ_P is particle density. For the spherical grains (microparticles) at any position in the particle, the microscale transport follows

$$\frac{\partial C_\mu}{\partial t} = \frac{1}{r^2}\frac{\partial}{\partial r}\left(r^2 D_\mu(C_\mu)\frac{\partial C_\mu}{\partial r}\right) \tag{4-10}$$

Eq. (4-10) has the symmetry boundary condition $\partial C_\mu / \partial r = 0$ at $r = 0$, and the interfacial flux balance boundary condition

$$D_{\mu}(C_{\mu})\varepsilon_{\mu}(1-\varepsilon_m)\left(\frac{\partial C_{\mu}}{\partial r}\right)_{r_g} = k_m[C_{mbe}(t,R)-C_{\mu be}(t,R,r_g)] \tag{4-11}$$

at the grain surface ($r = r_g$). Following the Darken relation, the effective ultra-micropore diffusivity in the grains has the loading dependence

$$D_{\mu}(C_{\mu}) = \frac{D_{\mu o}C_{\mu m}}{(C_{\mu m}-\varepsilon_{\mu}(1-\varepsilon_m)C_{\mu})} \tag{4-12}$$

based on the Langmuirian isotherm in Eq. (4-5), where $D_{\mu o}$ is the mobility. The transient total uptake can be written as

$$M_t(t) = \frac{M_w V_{ex}\left(C_{bo}-C_b(t)\right)}{m} \tag{4-13}$$

in which M_w is gas molecular weight and C_{bo} is initial bulk gas concentration in the sample chamber.

In order to extract transport parameters from experimental uptake curves and confirm the gas transport mechanism in SiC-DC1073, the above model equations were solved numerically. Eqs (4-7) and (4-10) were discretised using finite differences and converted to ordinary differential equations (ODEs), which were solved together with the bulk phase balance Eq. (4-9). The entire sets of equations were coded in MATLAB and solved using a stiff system solver to obtain the concentration profile. A least square minimisation method implemented in MATLAB was used to fit the model solution to the experimental fractional uptake data. The fitting parameters were the effective diffusivity in the particle scale micropores, D_m, barrier mass-transfer coefficient, k_m, and the ratio $D_{\mu o}/r_g^2$ which represents the inverse of the diffusional time scale in the grains.

4.5 Results and discussion

4.5.1 Adsorption equilibrium

Experimental adsorption equilibrium data (excess amount adsorbed per unit particle volume) of CO_2 on the synthesized SiC-DC1073 obtained at five different temperatures (303-343 K)

are presented in Figure 4-2. The difference between the absolute and excess amount adsorbed in sub-atmospheric experiments is not significant due to the sufficiently small bulk density. The low pressure CO_2 adsorption isotherm indicates much greater uptake and stronger adsorption of CO_2 in SiC-DC samples, compared to CH_4 that has been reported in our previous work [2]. CO_2 uptake up to 3.2 and 2.3 mmol/g were obtained at 303 K and pressure about 760 mmHg for SiC-DC 1µm and 20µm samples respectively, which is significantly higher than the adsorption capacity of CH_4 uptake which was about 1.5 mmol/g and 1.0 mmol/g at 303 K and 760 mmHg for SiC-DC 1µm and 20µm samples respectively. Generally, CO_2 has a higher uptake capacity and is more strongly adsorbed than CH_4, particularly in carbons, and these results are in accord with simulations for idealised slit pores [40].

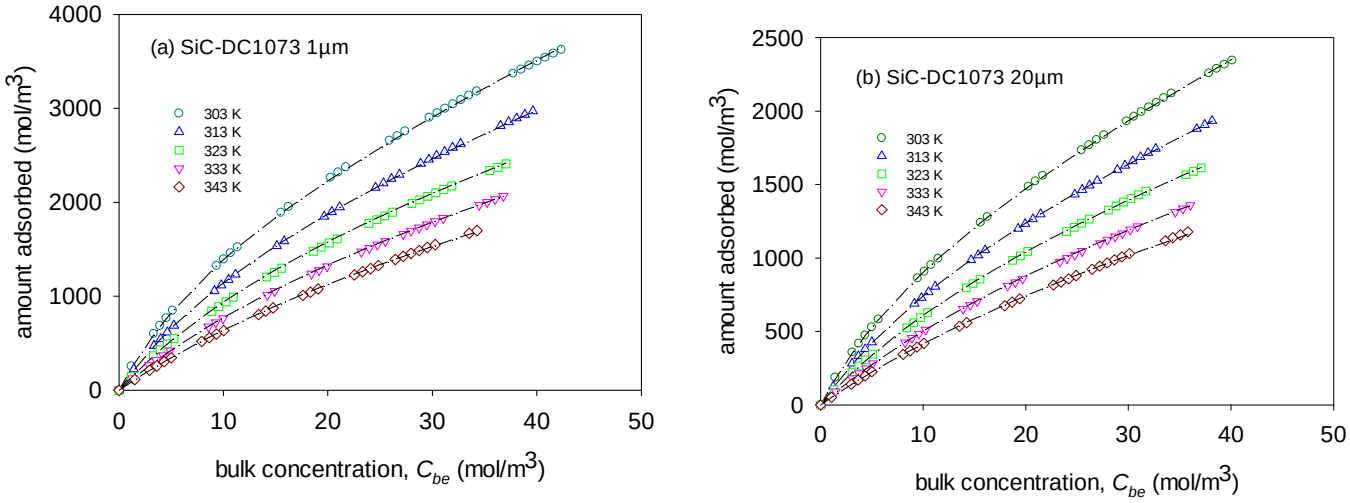

Figure 4-2. Fits of low pressure CO_2 adsorption isotherm for SiC-DC1073 particles of nominal size (a) 1 µm, and (b) 20 µm at 303-343 K with dual Langmuir-Henry isotherm model.

The dual Henry-Langmuir isotherm model in Eq. (4-2) was used here to correlate the adsorption isotherms of CO_2 on SiC-DC1073 1µm and 20µm over the temperature range of 303-343 K. The model has been applied successfully to describe CO_2 adsorption on SiC-DC1073. As can be seen in Figure 4-2 the Henry-Langmuir isotherm model fitted the experimental adsorption isotherm quite well within the entire pressure and temperature range considered in this study. The solid lines in the figure represent the dual Henry-Langmuir model using the optimized equation parameters, whose values are listed in Table 4-2. This

isotherm model has been previously applied to describe CH_4 adsorption in SiC-DC [2], considering bimodal pore size distribution. The ultra- micropore capacity of the SiC-DC1073 1µm and 20µm samples obtained from the fit of the dual Henry-Langmuir isotherm model to the experimental data is 2.01 mmol/cm^3 and 1.35 mmol/cm^3 of particle volume respectively. The parameters obtained from the fitting of the Henry-Langmuir isotherm to experimental equilibrium data, are used here in the proposed kinetics model to extract CO_2 diffusion coefficients in larger micropores, ultra-micropores, and surface barrier mass-transfer coefficients.

Table 4-2. Isotherm parameters for CO_2 on SiC-DC1073 particles of nominal size 1 µm and 20 µm.

adsorbent	$C_{\mu m}$ (mol/m^3)	$A_\ell \times 10^6$ (m^3/mol)	A_h (dimensionless)	$-\Delta H_\ell$ (kJ/mol)	$-\Delta H_h$ (kJ/mol)
SiC-DC 1 µm	2013.99	7.94	0.0294	23.23	18.72
SiC-DC 20 µm	1347.55	8.01	0.0263	22.95	18.03

4.5.2 CO_2 adsorption kinetics

During measurement of single-component equilibrium adsorption isotherms of CO_2 in SiC-DC1073 in the ASAP 2020, the transient pressure variation in the system was recorded after introduction of a small pre-set dose of adsorptive. The uptake-time relation was then determined from this pressure variation. A typical transient uptake of CO_2 on SiC-DC 1µm, obtained at 400 mmHg and 313 K, and that of CH_4 at the same conditions [2], is depicted in Figure 4-3(a). The bipore model, considering only grain and particle scale diffusion resistances but no interfacial barrier resistance, used in our previous work for CH_4 adsorption kinetics [2], was applied here also for CO_2. Figure 4-3(a) also illustrates the fit of the bipore model to both CO_2 and CH_4 uptake kinetics data. The symbols represent experimental data, and solid lines the bipore model fitting results. As can be seen in this figure, while the bipore model fits CH_4 experimental uptake data reasonably well, it cannot fit CO_2 uptake data on SiC-DC1073 1µm. This comparison between model and experiment reveals the middle part of the experimental uptake to proceed somewhat slower than the model prediction, with the initial response, governed by rapid diffusion in the large particle scale micropores, and later part controlled by slow grain scale diffusion, being closer. This suggests the presence of a third time scale corresponding to the early part of the grain scale transport process, which

most likely corresponds to a barrier resistance at the ultra-micropore mouths at the grain surface. The surface barrier resistance in SiC-DCs may occur due to pore mouth constrictions and structural distortions near the grain surface.

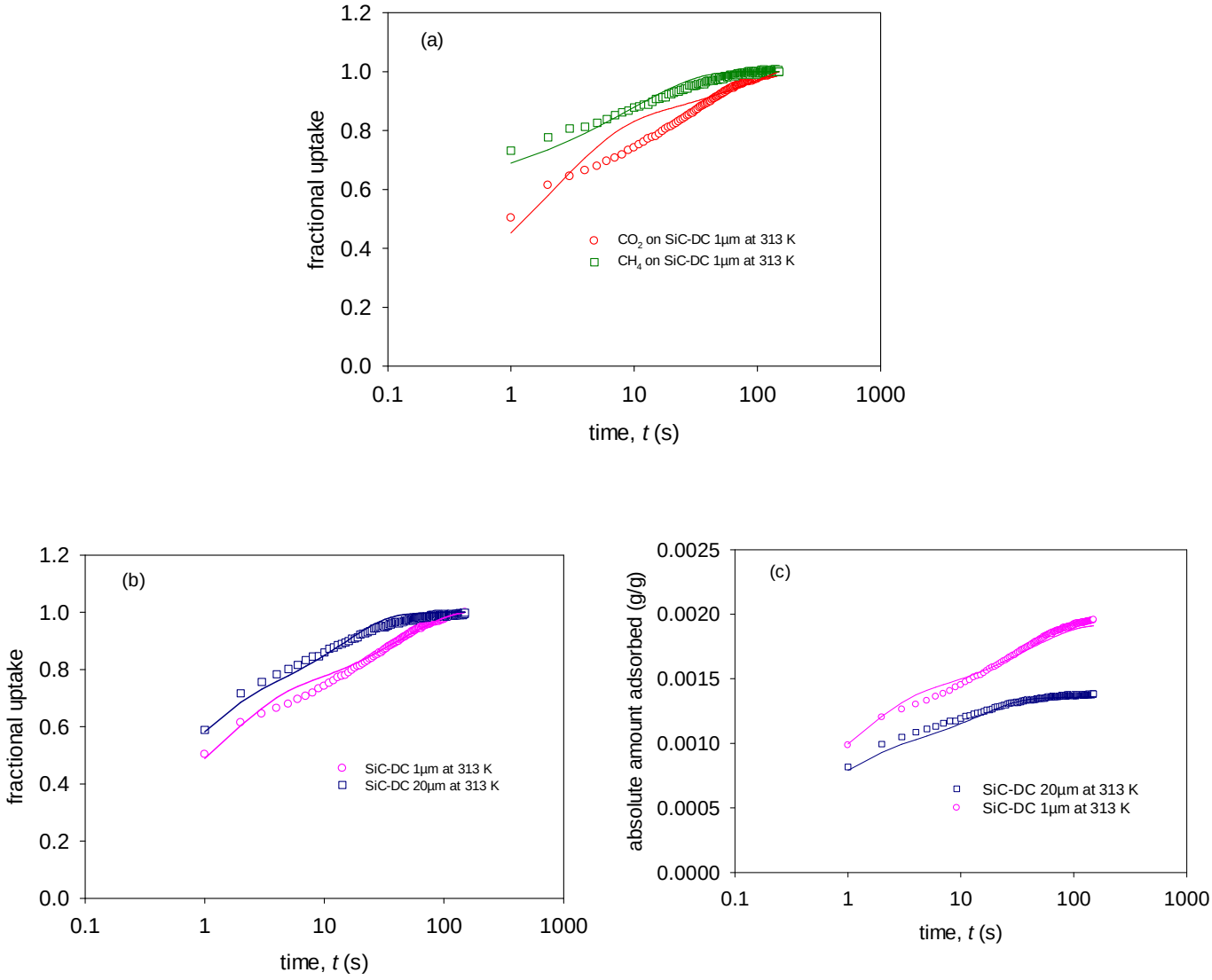

Figure 4-3. (a) Kinetic uptake curves of CO_2 and CH_4 in SiC-DC1073 1µm particles at 313 K and corresponding model fits using bipore model [2], and (b and c) kinetic uptake curves of CO_2 in SiC-DC1073 particles of nominal size 1µm, and 20µm (0.3g) at 313 K and corresponding model fits using bipore model with interfacial resistance on grain surface: (b) fractional, and (c) absolute amount adsorbed. Symbols: experimental data; lines: model fit.

In order to evaluate the model proposed above and to understand the transport mechanism, the model equations were applied to the experimental CO_2 kinetic data. Figures 4-3(b) and 4-3(c) depict the fit of the proposed model with the experimental CO_2 uptake kinetics data, both

as fractional and as absolute adsorption. It can be seen from Figures 4-3(b) and 4-3(c) that the model provides satisfactory fit of the measured CO_2 uptake for both SiC-DC1073 1µm and 20µm samples. For CO_2 uptake, the adsorbed amount reaches equilibrium in less than 50 s for SiC-DC 20µm at 313 K, while it takes more than 80 s to reach equilibrium for SiC-DC 1µm. In the case of CH_4, equilibrium was attained in less than 60 sec for SiC-DC 1µm [2], showing faster adsorption kinetics for CH_4 as compared to CO_2. In both cases, although about 40-50 percent of the uptake is completed by the first experimental point, the remaining part of the dynamics still captures the dynamics of both the particle and grain scale transport processes.

As a metric of the quality of model predictions, the error of the fit of the experimental data was estimated. The relative standard deviation of the fit of fractional adsorption was in the range of 1-2.5 percent, while the maximum relative error was in the range of 4-8 percent, for the 1 µm and 20 µm particles over the range of temperatures investigated. We note that while there is considerable improvement in the model fit on introducing the interfacial resistance on the grain surface in the present work, there is still a small amount of discrepancy in the mid-range of the uptake. This is attributed to the effect of structural heterogeneity on the transport, which is not captured through the single overall grain scale diffusivity used in the present model. The presence of a pore size distribution (Figure 4-1) implies a distribution of diffusion coefficients and energy barriers. While consideration of such distributions can improve the fit [41], it will entail additional parameter fitting which we have preferred to avoid here.

From Figure 4-3 it is evident that sorption equilibrium is reached faster for the larger particle size of nominal diameter 20 µm. This cannot be explained by the pore size distribution effects alone, as the particle scale micropores in the two samples have similar distributions (PSDs), as seen in Figure 4-1. This suggests that the two samples are structurally different, with the smaller particle size sample providing larger barriers to intra-particle and/or intra-grain transport due to internal constrictions and structural distortions arising from twisting and folding of the underlying graphene sheets, which cannot be captured by the slit pore models underlying the PSDs. Such distortions of the sheets are evident from the hybrid reverse Monte Carlo simulation-based atomistic structures of the SiC-DC [30]. Differences in structural evolution between different particle size samples during chlorine treatment may be expected, since the partial pressures of the chlorine and metal chloride at the reaction

interface during chlorine treatment will be strongly particle size dependent. Smaller particles will have higher chlorine partial pressures and lower metal chloride patrial pressures at the carbide/carbon interface, and more rapid diffusion through the developing porous structure, and therefore faster chlorination rate. The faster chlorination may be expected to lead to greater structural distortions. Further, since the precursors for the different particle size samples originated from different manufacturers they may be expected to have different trace impurities, which could also influence the structural development during chlorine treatment.

Experiments with different amount of mass of adsorbent were also conducted to investigate the effect of sample mass on the uptake curves. The CO_2 uptake curves for two different amounts of SiC-DC1073 1µm (0.1g and 0.3g) at 303 K and pressure of around 400 mmHg showed independence to sample mass. Thus, it can be assumed that the results are free of heat and mass transfer resistances related to the sample pile.

4.5.3 Molecular simulation of adsorption equilibrium and kinetics

GCMC simulations were performed for carbon dioxide up to atmospheric pressure and at temperature of 303, 323, and 343 K, and the results compared with the sub-atmospheric experimental CO_2 adsorption isotherms. Figure 4-4 depicts the comparison of the predicted CO_2 adsorption isotherms with the experimental results for SiC-DC 1µm. It can be seen that there is excellent agreement between simulation isotherm and experimental adsorption isotherms of SiC-DC1073 1µm indicating that our HRMC model is able to provide accurate predictions of the experimental CO_2 adsorption isotherm data.

To theoretically investigate dynamics of CO_2 in the amorphous structure of SiC-DC, equilibrium molecular dynamics simulations were also performed. The temperature dependence of self-diffusivities of CO_2 was studied by tracing spatial positions of molecular configurations over time trajectories from multiple MD simulations. Starting from initial configurations obtained using GCMC, MD simulations were performed at various temperatures between 150 K and 1000 K and self-diffusion coefficients were determined using Eq. (4-1). The results for the self-diffusivity of CO_2 at these temperatures, obtained for low density, i.e. infinite dilution, are shown in Figure 4-5(a), comparing their temperature dependence with that of the uptake-based particle scale diffusion coefficients obtained from the volumetric experiments at low pressure (400 mm Hg). We note that fundamentally self- and collective diffusivities should be equal at low density for which fluid-solid interactions

are dominant, prompting this comparison between the low density experimental results and simulations.

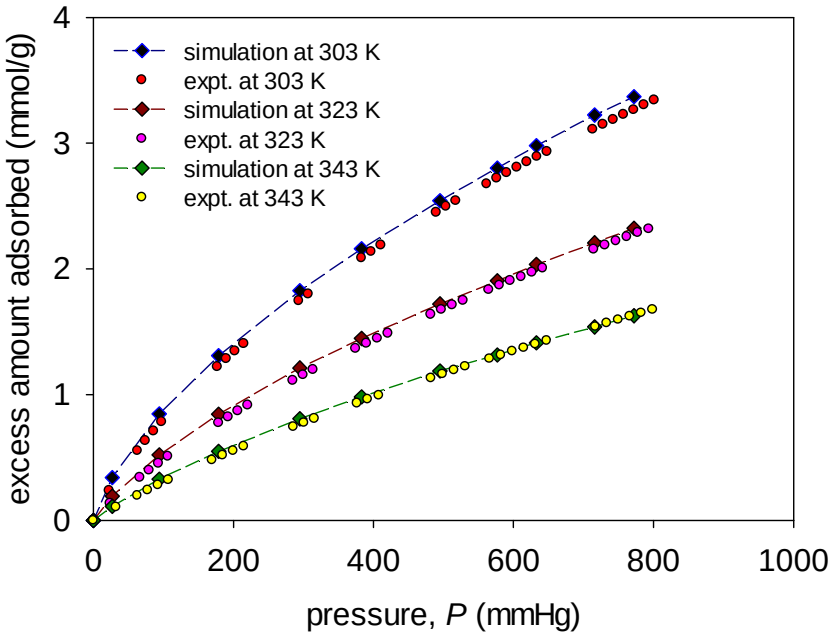

Figure 4-4. Comparison of simulation isotherms and experimental sub-atmospheric adsorption of CO_2 on 1µm SiC-DC1073.

As can be seen in Figure 4-5(a), the predictions of the molecular dynamics simulation are as much as two orders of magnitude larger than the particle scale diffusion coefficients, while in our previous work [2] we observed excellent agreement between the results of CH_4 uptake kinetics measurements obtained by the volumetric technique with the molecular dynamics simulation results. Further, the low density experimental activation energy for CO_2, of about 26 kJ/mole, is over 10 kJ/mole larger than that from EMD simulations, of about 15.2 kJ/mole. Similarly large, several orders of magnitude, differences between macroscopically determined transport coefficients and those from MD simulation and microscopic measurements are commonly reported in the literature [42-45], and are generally attributed to the presence of structural constrictions and barriers affecting long range transport [46]. Thus, the discrepancy between the microscopic EMD simulations and the macroscopic uptake experiments observed here is indicative of defects providing long range transport barriers for CO_2 that are not captured in the HRMC structural model.

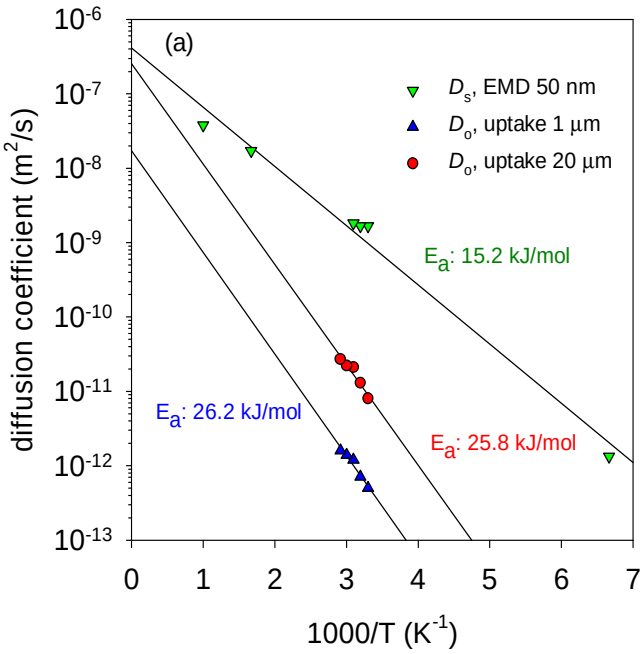

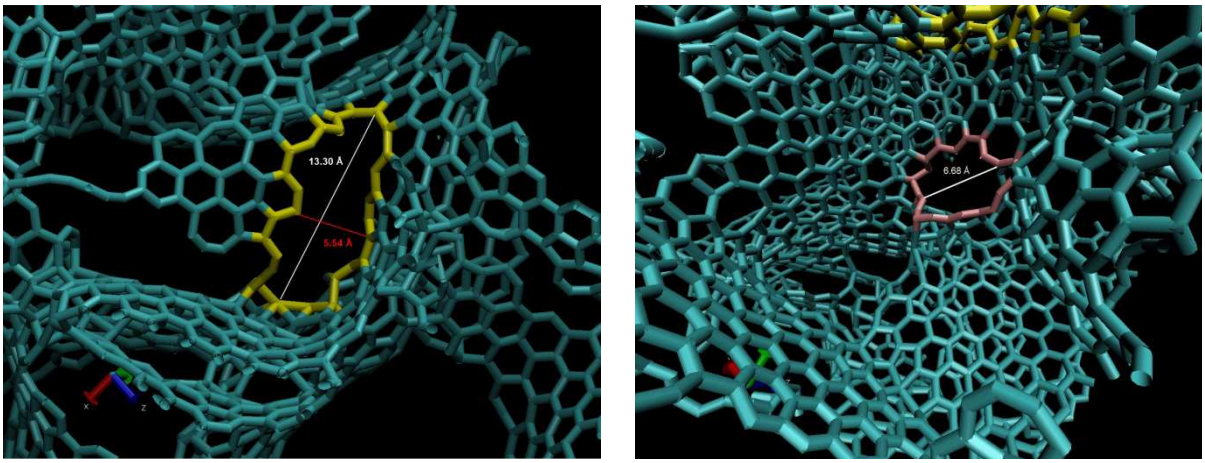

(b) **(c)**

Figure 4-5. (a) Comparison of temperature dependence of particle scale micropore diffusivities of CO_2 obtained from model and from simulation, and geometry of two different pore entries in SiC-DC structure based on HRMC model [27], (b) entry A, and (c) entry B having contrasting energy barriers for CO_2 and CH_4. (b and c) reprinted with permission from Farmahini et al. [27]. Copyright © 2014 American Chemical Society.

While we did not observe such differences between simulation and macroscopic measurements for CH_4 in our recent work, the difference for CO_2 is not surprising given its much greater sensitivity of its transmission energy barrier to differences in the pore mouth size and surrounding structure reported by us elsewhere [27]. Thus, for two different pore entries depicted in Figures 4-5(b) and 4-5(c) [27], based on the HRMC model, the greater

steric hindrance (i.e. repulsion) for CH_4 for pore entry A was found to dominate and lead to a larger barrier for this molecule (36.5 kJ/mole) compared to CO_2 (23 kJ/mole) since at this pore entry the surrounding pore body structure has low density of carbon and therefore weak binding; however, the barrier for CO_2 for pore entry B was seen to be much larger (137 kJ/mol for CO_2 and 75.5 kJ/mol for CH_4), since the surrounding pore body carbon density is high for this pore mouth, leading to strong binding and dominance of dispersive interactions [27].

4.5.4 Effect of temperature on transport parameters

The fractional and absolute kinetic uptake curves of CO_2 for diffusion on SiC-DC at different temperatures are depicted in Figures 4-6(a) and 4-6(b) respectively, for pressure of 400 mmHg, showing good agreement between experimental data and model fit, and strong dependence of the uptake on temperature.

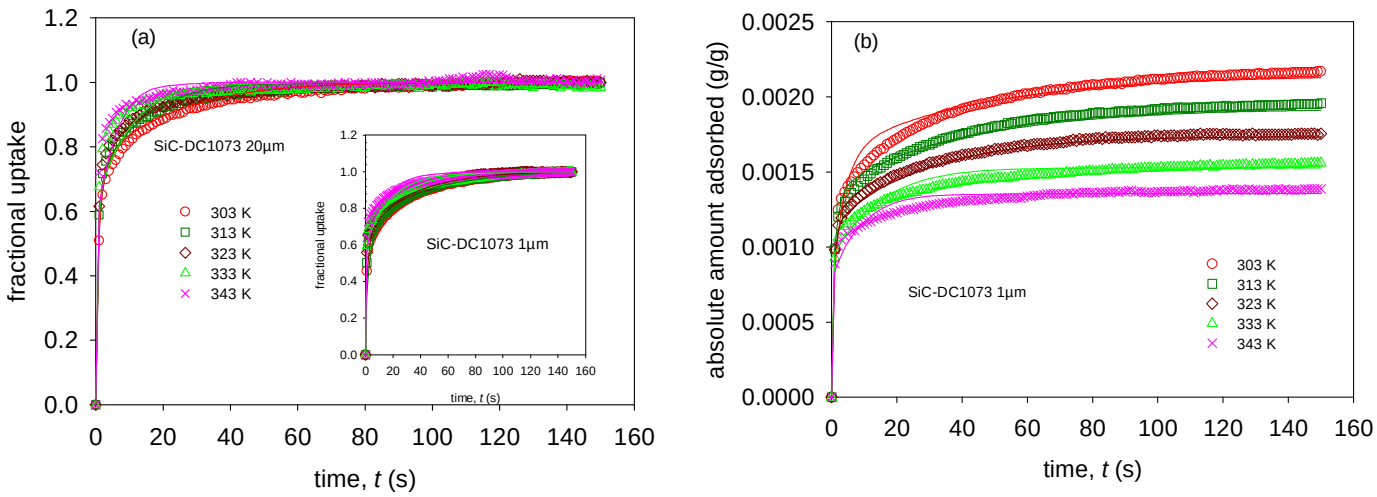

Figure 4-6. Effect of temperature and model fits on (a) CO_2 kinetic fractional uptake curves of SiC-DC1073 particles of nominal size 20µm and 1µm (inset), and (b) comparison of model predictions and absolute amount adsorbed kinetic uptake curves for 1µm samples at pressure of 400 mmHg, Symbols: experimental data; lines: model fit.

The fitted transport parameters of CO_2 in SiC-DC at different temperatures are presented in Figures 4-5(a), 4-7(a) and 4-7(b), showing the diffusivities to increase with increasing temperature, in both the large micropores and the grain scale ultra-micropores, as expected. The higher rate of increase of grain scale diffusivities is indicative of higher activation energy in the ultra-micropores in comparison to the particle scale micropores.

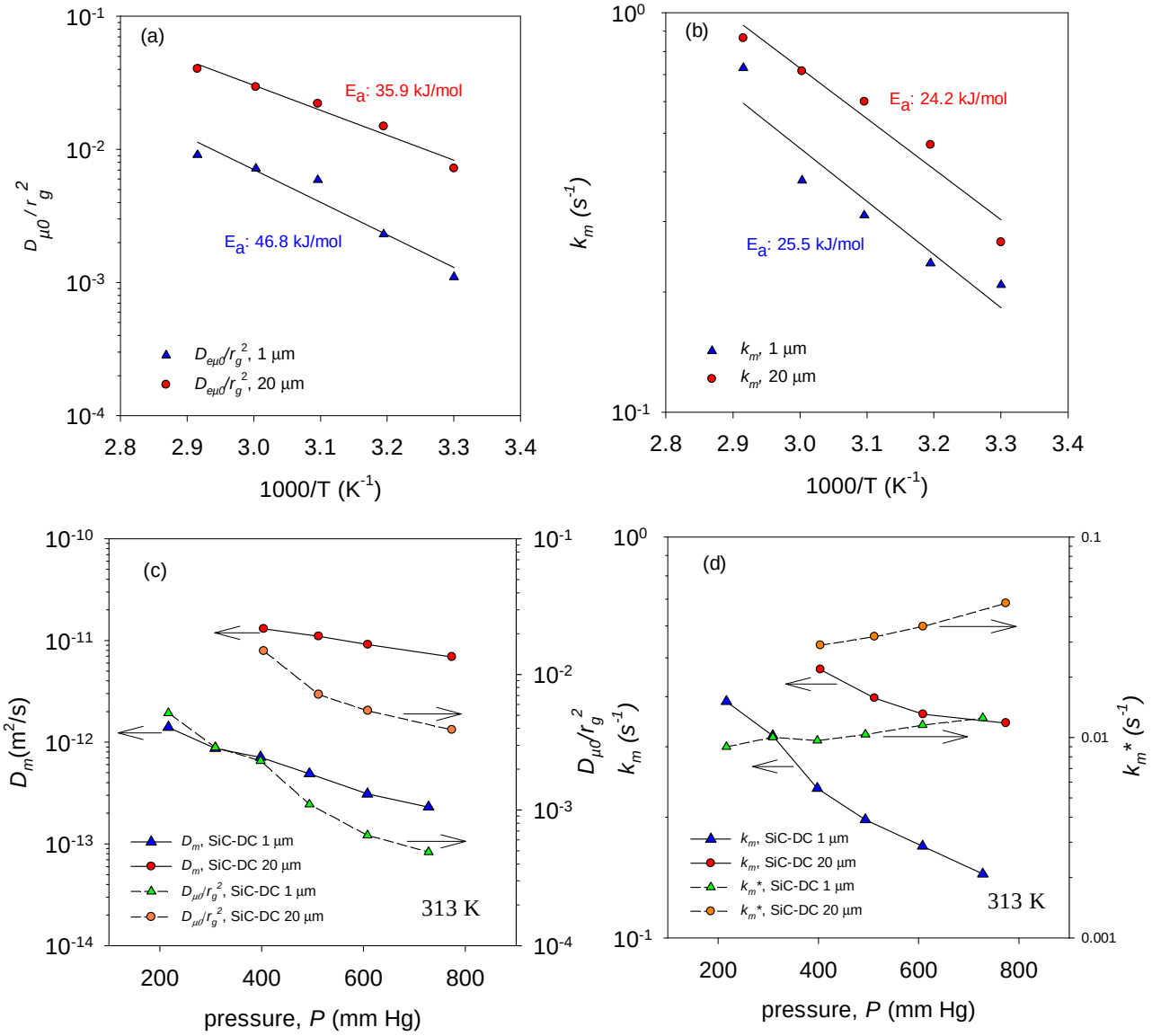

Figure 4-7. Temperature dependence of (a) scaled CO_2 diffusivities, $D_{\mu o}/r_g^2$, in grain-scale ultra-micropores, and (b) interfacial mass transfer coefficients at grain surface, and effect of pressure at 313 K on diffusivities in (c) particle scale micropores and grain-scale ultra-micropores, and on (d) barrier mass-transfer coefficients.

Considering the grain size of about 30 nm for the SiC-DC particles, it is estimated that the values of $D_{\mu o}$ to be in the order of 10^{-18} m^2/s for the CO_2 diffusion in the grain scale ultra-micropores. The magnitudes of the values of $D_{\mu o}/r_g^2$ as shown in Figure 4-7(a) are smaller than those obtained for CH_4 presented in our recent work [2]. As for CH_4 adsorption, it can be concluded that the adsorption and transport in the ultra-micropores will not make a significant contribution to the transport in any adsorption-based process based on SiC-DC, due to the extremely slow diffusion in these ultra-micropores and their small pore volume.

The grain-scale ultra-micropores of SiC-DC1073 1 µm and 20 µm show higher CO_2 activation energies of 46.8 and 35.9 kJ/mol respectively. These grain scale activation energies are significantly larger than the activation energy for micropore diffusion of CO_2 in microporous carbon of 13.8 kJ/mol reported by Prasetyo et al. [47]. Rutherford et al. [48] have also reported activation energy of 16 kJ/mol for CO_2 diffusion in Takeda 3 Å carbon molecular sieve. However, the activation energies for the grain-scale diffusion of CO_2 are comparable to those for CH_4 found in our recent study [2], and to the values for CH_4 in carbon molecular sieve reported by Rutherford et al. [48]. The larger activation energies of CO_2 in the ultra-micropores of grains of SiC-DC compared to the activation energies reported for CMS suggest the presence of narrower pores and constrictions and internal pore-mouth barriers that affect the entry of CO_2 molecules into the ultra-micropores.

The particle scale diffusivity values of the order of about 10^{-11} m^2/s obtained in this study (Figure 4-5(a)) appear to be two orders of magnitude smaller than the CH_4 particle scale diffusivities reported in the previous work [2]. These values are also around two orders of magnitudes smaller than the diffusivity values obtained from EMD simulation discussed above. The smaller values of diffusivities for CO_2 compared to CH_4 can be explained by the use of Transition State Theory (TST) [26,49-50] based on the differences between the particle scale activation energies of CO_2 and CH_4, assuming that diffusion is controlled by pore mouth barriers. For the different SiC-DC samples of 1 µm and 20 µm nominal particle size, the magnitude of the activation energies in the larger micropores, corresponding to pressure of about 400 mmHg, are 26.2 and 25.8 kJ/mol respectively. The particle scale activation energies of CH_4 for SiC-DC1073 1 µm and 20 µm samples reported by us [2] are 15.6 and 14.2 kJ/mol respectively, which indicates that particle scale activation energies for CO_2 are about 10 kJ/mol higher than those for CH_4. According to transition state theory, the relation between CO_2 and CH_4 diffusivities will follow

$$\frac{D_{CO_2}}{D_{CH_4}} = \sqrt{\frac{M_{CH_4}}{M_{CO_2}}}\, e^{-(E_{CO_2}-E_{CH_4})/R_gT} \tag{4-14}$$

assuming entropic differences between the dividing surface and pore are similar for CO_2 and CH_4. Here R_g is the ideal gas constant, M_{CH4} and M_{CO2} are the molecular weights, and E_{CH4} and E_{CO2} are the activation energies. CO_2 and CH_4 particle scale diffusivity values obtained for SiC-DC1073 20 µm in this and our recent [2] study are in the order of 10^{-11} and 10^{-9} m^2/s

respectively. Based on Eq. (4-14), and the activation energy difference of about 10 kJ/mole, we estimate a diffusivity ratio of about 69 at the mean temperature of 323 K in this study, which is broadly consistent with the experimental ratio.

The comparison of the activation energy values obtained from the uptake experiment and simulation indicates the presence of additional barriers not captured by the HRMC model. It should be also noted that the activation energies obtained for CO_2 are higher than the activation energy of CH_4 reported in our previous work [2]. As seen in Figure 4-7(b) the activation energies of the barrier mass-transfer coefficients are about 25.5 kJ/mole and 24.2 kJ/mol for SiC-DC1073 1µm and 20 µm respectively, œmparable to the activation energies of the barrier coefficients reported by Qinglin et al. [15], of 30.3kJ/mol for the adsorption of CO_2 on Takeda CMS, providing support for our consideration of the interfacial barrier resistance.

4.5.5 Effect of loading on transport parameters

In Figure 4-7(c) and (d), showing the variation of diffusion parameters with pseudo-bulk pressure (as a substitute for loading), it may be seen that diffusivity in larger micropores, ultra-micropores and the interfacial mass transfer coefficient decreases monotonically with increasing loading. The effect of loading on the diffusion in ultra-micropores is strong, and for the ultra-micropores this observation is consistent with the results presented in our previous work for CH_4 [2]. Such decrease of the collective diffusion coefficient with increase in loading in narrow pores has been reported also in molecular dynamics simulations for CH_4 in carbon slit pores up to 0.66 nm open pore width [51], and in (10,10) carbon nanotubes having centre to centre diameter of 1.36 nm (open pore diameter of 1.02 nm) [52], and is due to the strong fluid-solid interactions in such pores. When fluid-solid interaction is dominant, increase in loading enhances mutual interference of molecules through inter-molecular collisions without significant increase in the viscous contribution, which leads to decrease in collective diffusivity. Such decrease in collective diffusivity has been reported also for CO_2 in $AlPO_4$-5, having open pore diameter of 0.73 nm, from QENS experiments and MD simulations [46].

In our previous work [2], the particle scale diffusivity of CH_4 showed a slight increase with increase in pressure and loading, while in the present work for CO_2 a slight decrease is instead seen. Such behaviour is most likely due to the strong fluid-solid interaction for CO_2 in

the larger particle scale micropores, evident also from the relatively high magnitude of the heat of adsorption of CO_2 compared to CH_4, to be subsequently discussed. In further support of this, we note that while the collective diffusivity of CH_4 in carbon slits having open pore width 1.06 nm increases with increase in loading [51], the stronger fluid-solid interaction in carbon nanotubes of comparable open pore size of 1.02 nm diameter leads to decrease in the collective diffusivity with increase in loading [52].

Qinglin et al. [15] have shown the extracted barrier resistance coefficients for carbon molecular sieves have strong dependence on concentration. They have reported the barrier resistance coefficients to increase with loading. They have found that for carbon dioxide the concentration dependence of the barrier coefficient is stronger than that for the micropore diffusivity. Similarly, Giesy and LeVan [53] have reported that barrier coefficients for oxygen, nitrogen, and argon in carbon molecular sieves increase with increasing pressure. On the other hand, Reid and Thomas [54] have reported that for a given temperature, the barrier coefficient for Pyridine reaches a maximum at $P/P^0 \sim 0.25$, and at higher concentration the barrier coefficient decreases with increasing loading. They have also shown that at this relative pressure, a Fickian-diffusion mechanism is followed at higher adsorption temperatures, when diffusion through the barrier is fast compared with diffusion along the pores. Here, we have observed that for a given temperature (at 313 K) as shown in Figure 4-7(d), the barrier coefficients decrease with increasing loading. This decrease in barrier coefficients with increase in loading for CO_2 on SiC-DC is essentially due to the different mass transfer driving force ($[C_{mbe}\text{-}C_{\mu be}]$) in our model, as opposed to that ($\varepsilon_\mu(1-\varepsilon_m)$ $[C_\mu(C_{mbe})\text{-}C_\mu]$) in the literature models referred to above [15,53-54]. Based on the Langmuir isotherm used for the micropore adsorbate in Eq. (4-5), it is readily seen that

$$\varepsilon_\mu(1-\varepsilon_m)[C_\mu(C_{mbe})-C_\mu]=\frac{K_L C_{\mu m}}{(1+K_L C_{mbe})(1+K_L C_{\mu be})}[C_{mbe}-C_{\mu be}] \tag{4-15}$$

so that the mass transfer coefficient, k_m^*, based on the driving force ($\varepsilon_\mu(1-\varepsilon_m)[C_\mu(C_{mbe})\text{-}C_\mu]$) is related to the present mass transfer coefficient, k_m, by

$$k_m^*=\frac{(1+K_L C_{mbe})(1+K_L C_{\mu be})}{K_L C_{\mu m}}k_m \tag{4-16}$$

which explains why k_m^* can increase with increase in loading. Figure 4-7(d) depicts the variation of k_m^* with pressure, estimated from Eq. (4-16), showing an increase with increase in loading for both 1µm and 20 µm samples, with similar slopes.

4.5.6 Heat of adsorption

The isosteric heat of adsorption is a measure of the interactions between adsorbate molecules with the adsorbent atoms, and provides useful information about the energetic heterogeneity of the solid surface. It can be estimated from isotherms using the Van 't Hoff relation

$$-\Delta H = R_g T^2 \left(\frac{\partial \ln P}{\partial T} \right)_{n_a} \tag{4-17}$$

where ΔH (kJ mol^{-1}) is isosteric heat of adsorption, P is pressure (kPa), T is temperature, R_g is gas constant, and n_a is adsorption amount (mmol g^{-1}). The plots of the variation of heat of adsorption for CO_2 and also CH_4 as a function of loading are shown in Figure 4-8(a). It can be seen that the isosteric heats of both CO_2 and CH_4 do not remain constant but decrease with increasing loading, an indication of energetic heterogeneity of the adsorbent surface. The isosteric heat of adsorption was also obtained from GCMC simulation using the HRMC-based structural model, computed using the fluctuation formula

$$Q^{st} = R_g T - \frac{\langle NU \rangle - \langle N \rangle \langle U \rangle}{\langle N^2 \rangle - \langle N \rangle^2} \tag{4-18}$$

where N refers to the number of molecules, U is the energy and $\langle \cdot \rangle$ indicates the average over the simulation run. Heterogeneity of SiC-DC structure is also evident in our simulation results of the isosteric heat of adsorption, as it also decreases with increasing loading as shown in Figure 4-8(a). This decrease is because the favourable adsorption sites are occupied progressively as loading increases, therefore adsorption process becomes less exothermic with increase in loading. It can be seen there is good agreement between the heat of adsorption obtained from the experiments and that obtained from the simulation. The small difference between the two may largely be attributed to minor differences in the structure of the smaller SiC-DC particles (50 nm nominal size) used in obtaining the scattering data on which the HRMC simulation is based, compared to the 1 µm and 20 µm particles synthesised for this study.

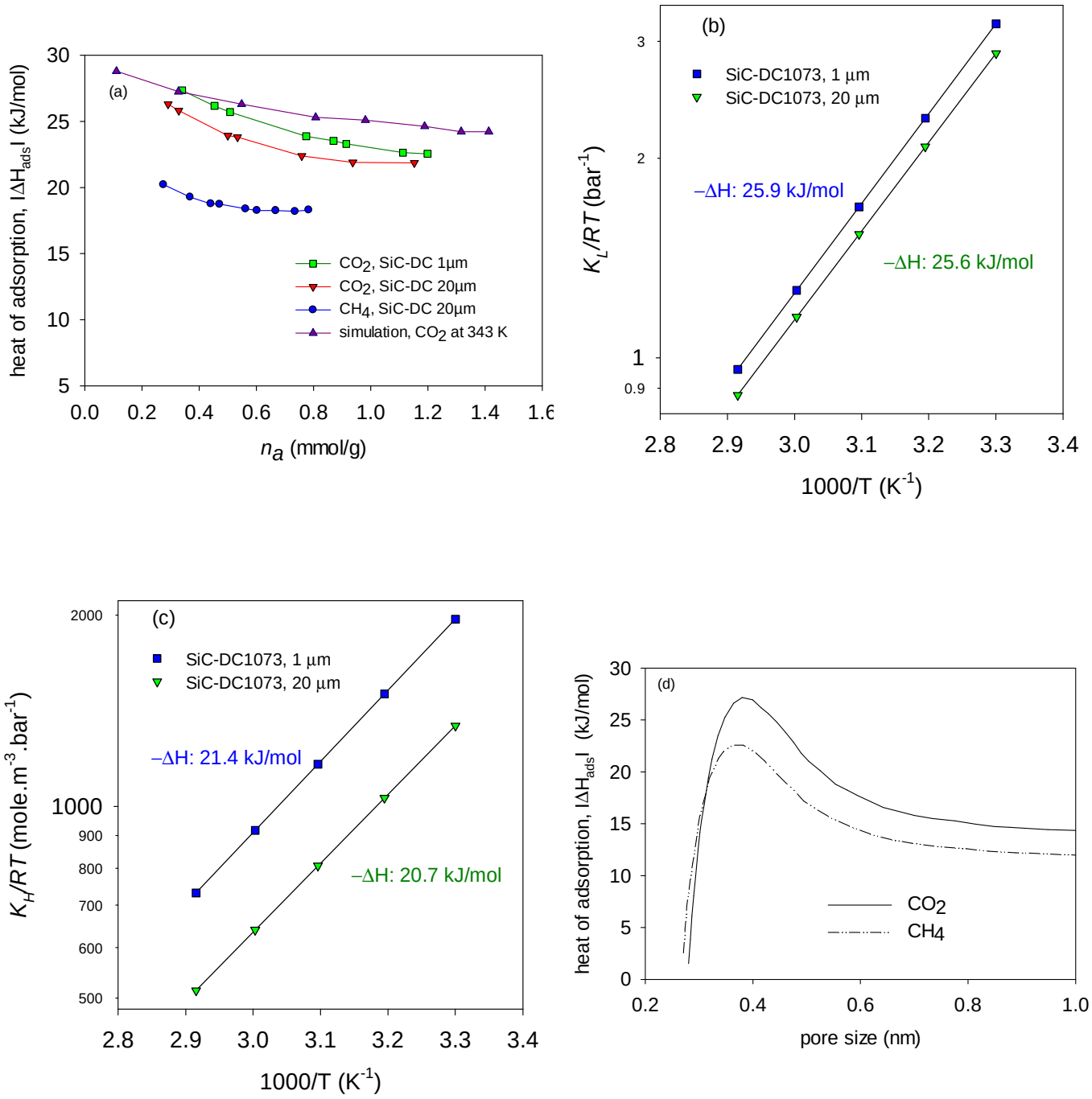

Figure 4-8. (a) Isosteric heat of adsorption as a function of loading for CO_2 and CH_4 obtained from experiment and simulation at 343 K. Temperature variation of (b) fitted Langmuir, (c) fitted Henry law mode equilibrium constants, obtained from the dual Langmuir-Henry model in SiC-DC1073 particles of nominal size 1 µm and 20 µm, and (d) variation of isosteric heat with pore size, theoretically estimated by Rutherford et al. [48].

Figure 4-8(b) and (c) depict enthalpies of adsorption, ΔH, obtained from the Langmuirian and Henry Law parts of the isotherms and the respective equilibrium constants calculated from fitting of the dual Langmuir-Henry equation to CO_2 experimental isotherm data, for SiC-DC1073 1µm and 20 µm. The values of the heats of adsorption are in the range of 21-26 kJ/mol, and are in the usual range for CO_2 adsorption in microporous carbons. The adsorption enthalpy obtained from the Langmuirian part of the isotherm, which is related to adsorption in the ultra-microporous grains, compare reasonably well with the heat of adsorption of CO_2 measured in a molecular sieving carbon, of 28.4 kJ/mol, reported by Reid and Thomas [55], and 30 kJ/mol reported by Rutherford et al. [48]. In both grain scale ultra-micropores and particle scale micropores, the adsorption enthalpies for CO_2 are higher than those obtained from CH_4. This observation is also consistent with the results reported by Rutherford et al. [48] for the variation of heat of adsorption for CO_2 and CH_4 with carbon slit pore size, depicted in Figure 4-8(d). This figure shows that the absolute value for the CO_2 and CH_4 heat of adsorption will reach a maximum followed by a decrease as pores of larger dimensions are filled, and at larger pore sizes the heat of adsorption of both CO_2 and CH_4 reaches a constant value. The maximum absolute values for the heats of adsorption in this figure are 27.5 and 22.5 kJ/mol for CO_2 and CH_4, respectively. These values compare well with the measured values for CO_2 and CH_4 presented in our work calculated from the isotherm data. As can be seen in Figure 4-8(d), for the pore width of about 0.48 nm for the particle scale micropores, corresponding to the first peak of the pore size distributions of the synthesized SiC-DC samples, CO_2 is in the right region of the maximum, and the theoretically isosteric heat is estimated about 22 kJ/mol, while at the narrow pore width of the ultra-micropores of about 0.35 nm corresponding to the first peak of the CO_2 pore size distribution of the SiC-DC samples, CO_2 is in the left region of the maximum with an isosteric heat of about 26 kJ/mol. These values are in good agreement with the corresponding experimental estimates in Figure 4-8(c) and (b) respectively, supporting our use of the dual Henry-Langmuir isotherm.

Figure 4-8(a) and (d) demonstrate stronger binding of CO_2 in the nanoscale pores of the SiC-DC, with both experiment and simulation showing higher heat of adsorption for CO_2. It is this stronger binding that is responsible for the larger adsorption of CO_2, as well as its higher energy barrier discussed earlier, as stronger binding enhances the energy barrier to be crossed when moving between sites.

Regarding the assumption of isothermal conditions in the kinetics models, based on the explanation presented in Chapter 3, and by considering the amount adsorbed of CO_2 per step roughly around 0.04 mmol/g, with heat of adsorption of 25 kJ/mol, then if we assume that the energy is not dissipated and is accumulated in the sample, the maximum temperature rise would be only around 1.4°C. In reality much of the heat released would be dissipated and the actual temperature rise will be much smaller, justifying our assumption of isothermality.

4.6 Summary and conclusions

Our equilibrium adsorption data for CO_2 on SiC-DC at different temperatures, and up to atmospheric pressure, are well fitted by a dual Henry-Langmuir isotherm model. It is found that GCMC simulations using a representative atomistic HRMC model of the SiC-DC provides accurate predictions for CO_2 adsorption equilibrium over a wide range of temperatures up to atmospheric pressure. We have found that isosteric heats of adsorption obtained from simulation for CO_2 are also in very good agreement with those obtained from fits of experimental isotherm data.

Adsorption kinetics of CO_2 has been studied at different temperature over a wide range of loading, and interpreted by a bidisperse structure model assuming that ultra-micropores have topologically connected networks in small independent grains, with the larger micropores forming the inter-granular space as particle-scale pathways. It is found that the adsorption kinetics is strongly influenced by a barrier resistance at the grain surface where entry into the ultra-microporosity occurs. Thus, uptake of CO_2 in the bidisperse pore structure of SiC-DC samples occurs through a rapid diffusion in the large particle-scale micropores, in which a Henry law isotherm holds, and a combination of barrier resistance at the grain surface and diffusional resistance in the grain interior with a Langmuirian isotherm. It is shown that the proposed model is able to capture uptake curve results in the entire range covered in this study. The extracted micropore and ultra-micropore transport parameters, and barrier mass transfer coefficients, have strong dependence on temperature and loading, and follow Arrhenius law in the studied temperature range. The activation energy for diffusion of CO_2 in the grains, of about 36-47 kJ/mole is comparable to that for CH_4 [2], and to literature results for carbon molecular sieves [48], in agreement with our model considering the grains to be ultra-microporous. Activation energies for the interfacial mass transfer of CO_2 at the grain

surface are about 25 kJ/mole and also consistent with literature results for the interfacial barrier in carbon molecular sieves [15].

We have also investigated self-diffusion of carbon dioxide in the HRMC model of SiC-DC over a wide range of temperatures using equilibrium molecular dynamics simulations. A comparison of our simulation results with experimental macroscopic uptake-based data reveals that MD-based diffusivities are as much as two orders of magnitude larger than the particle scale diffusion coefficients. From the difference between the activation energies obtained from the kinetic uptake measurements and MD simulations, it is concluded that there are some internal barriers and structural constrictions which are not captured by MD simulation. Such discrepancy is not found for CH_4, and is largely due to the stronger dispersive interactions and higher sensitivity of the barriers for CO_2 to small inaccuracies in the HRMC structure. These long range barriers for CO_2 are also responsible for the particle scale diffusivity of CO_2 being about two orders of magnitude smaller than that of CH_4.

4.7 References

[1] Presser V, Heon M, Gogotsi Y. Carbide-Derived Carbons–from Porous Networks to Nanotubes and Graphene. Adv. Funct. Mater 2011; 21(5):810-833.

[2] Shahtalebi A, Farmahini AH, Shukla P, Bhatia SK. Slow Diffusion of Methane in Ultra-Micropores of Silicon Carbide-Derived Carbon. Carbon 2014; 77:560-576.

[3] Nguyen TX, Bae JS, Bhatia SK. Characterization and Adsorption Modeling of Silicon Carbide-Derived Carbons. Langmuir 2009; 25(4):2121-2132.

[4] Becker P, Glenk F, Kormann M, Popovska N, Etzold BJ. Chlorination of Titanium Carbide for the Processing of Nanoporous Carbon: A Kinetic Study. Chem. Eng. J. 2010; 159(1):236-241.

[5] Gogotsi YG, Yoshimura M. Formation of Carbon Films on Carbides under Hydrothermal Conditions. Nature (London) 1994; 367: 628-630.

[6] Sutter P. Epitaxial Graphene: How Silicon Leaves the Scene. Nat. Mater. 2009; 8(3):171-172.

[7] Dash R, Chmiola J, Yushin G, Gogotsi Y, Laudisio G, Singer J, Fischer J, Kucheyev S. Titanium Carbide Derived Nanoporous Carbon for Energy-Related Applications. Carbon 2006; 44(12):2489-2497.

[8] Nguyen TX, Bhatia SK. Characterization of Accessible and Inaccessible Pores in Microporous Carbons by a Combination of Adsorption and Small Angle Neutron Scattering. Carbon 2012; 50(8):3045-3054.

[9] Bonilla MR, Bae JS, Nguyen TX, Bhatia SK. Heat Treatment-Induced Structural Changes in SiC-Derived Carbons and Their Impact on Gas Storage Potential. J. Phys. Chem. C 2010; 114:16562-16575.

[10] Loughlin KF, Hassan MM, Fatehi AI, Zahur M. Rate and Equilibrium Sorption Parameters for Nitrogen and Methane on Carbon Molecular Sieve. Gas Sep. Purif. 1993; 7(4):264-273.

[11] Rynders RM, Rao M, Sircar S. Isotope Exchange Technique for Measurement of Gas Adsorption Equilibria and Kinetics. AIChE J. 1997; 43(10):2456-2470.

[12] Liu H, Ruthven DM. Diffusion in Carbon Molecular Sieves. In Fundamentals of Adsorption, Springer 1996; p. 529-536.

[13] Rutherford S, Do D. Adsorption Dynamics of Carbon Dioxide on a Carbon Molecular Sieve 5a. Carbon 2000; 38(9):1339-1350.

[14] Nguyen C, Do D. Dual Langmuir Kinetic Model for Adsorption in Carbon Molecular Sieve Materials. Langmuir 2000; 16(4):1868-1873.

[15] Qinglin H, Sundaram SM, Farooq S. Revisiting Transport of Gases in the Micropores of Carbon Molecular Sieves. Langmuir 2003; 19(2):393-405.

[16] Qinglin H, Farooq S, Karimi IA. Prediction of Binary Gas Diffusion in Carbon Molecular Sieves at High Pressure. AIChE J 2004; 50(2):351-367.

[17] Wang Y, LeVan MD. Master Curves for Mass Transfer in Bidisperse Adsorbents for Pressure-Swing and Volume-Swing Frequency Response Methods. AIChE J 2011; 57(8):2054-2069.

[18] Kärger J, Caro J. Interpretation and Correlation of Zeolitic Diffusivities Obtained from Nuclear Magnetic Resonance and Sorption Experiments. J. Chem. Soc., Faraday Trans. 1 1977; 73:1363-1376.

[19] Kärger J, Pfeifer H. Nuclear Magnetic Resonance Measurement of Mass Transfer in Molecular Sieve Crystallites. J. Chem. Soc., Faraday Trans. 1991; 87(13):1989-1996.

[20] Zimmermann NE, Balaji SP, Keil FJ. Surface Barriers of Hydrocarbon Transport Triggered by Ideal Zeolite Structures. J. Phys. Chem. C 2012; 116(5):3677-3683.

[21] Zimmermann N, Smit B, Keil F. On the Effects of the External Surface on the Equilibrium Transport in Zeolite Crystals. J. Phys. Chem. C 2009; 114(1):300-310.

[22] Zimmermann N, Jakobtorweihen S, Beerdsen E, Smit B, Keil F. In-Depth Study of the Influence of Host-Framework Flexibility on the Diffusion of Small Gas Molecules in One-Dimensional Zeolitic Pore Systems. J. Phys. Chem. C 2007; 111(46):17370-17381.

[23] Zimmermann NE, Haranczyk M, Sharma M, Liu B, Smit B, Keil FJ. Adsorption and Diffusion in Zeolites: The Pitfall of Isotypic Crystal Structures. Mol. Simul. 2011; 37(12):986-989.

[24] Shang J, Li G, Singh R, Gu Q, Nairn KM, Bastow TJ, Medhekar N, Doherty CM, Hill AJ, Liu JZ. Discriminative Separation of Gases by a "Molecular Trapdoor" Mechanism in Chabazite Zeolites. J. Am. Chem. Soc. 2012; 134(46):19246-19253.

[25] Shimomura S, Higuchi M, Matsuda R, Yoneda K, Hijikata Y, Kubota Y, Mita Y, Kim J, Takata M, Kitagawa S. Selective Sorption of Oxygen and Nitric Oxide by an Electron-Donating Flexible Porous Coordination Polymer. Nat. Chem. 2010; 2(8):633-637.

[26] Nguyen TX, Bhatia SK. Determination of Pore Accessibility in Disordered Nanoporous Materials. J. Phys. Chem. C 2007; 111(5):2212-2222.

[27] Farmahini AH, Shahtalebi A, Jobic H, Bhatia SK. Influence of Structural Heterogeneity on Diffusion of CH_4 and CO_2 in Silicon Carbide-Derived Nanoporous Carbon. J. Phys. Chem. C 2014; 118:11784-11798

[28] Nguyen T, Bhatia S, Jain S, Gubbins K. Structure of Saccharose-Based Carbon and Transport of Confined Fluids: Hybrid Reverse Monte Carlo Reconstruction and Simulation Studies. Mol. Simul. 2006; 32(7):567-577.

[29] Moore JD, Palmer JC, Liu YC, Roussel TJ, Brennan JK, Gubbins KE. Adsorption and Diffusion of Argon Confined in Ordered and Disordered Microporous Carbons. Appl. Surf. Sci. 2010; 256(17):5131-5136.

[30] Farmahini AH, Opletal G, Bhatia SK. Hybrid Reverse Monte Carlo Modeling of Silicon Carbide-Derived Nanoporous Carbon. J. Phys. Chem. C 2013; 117:14081−14094.

[31] Nguyen TX, Bhatia SK. Characterization of Pore Wall Heterogeneity in Nanoporous Carbons Using Adsorption: The Slit Pore Model Revisited. J. Phys. Chem. B 2004; 108(37):14032-14042.

[32] Opletal G, Petersen T, O'Malley B, Snook I, McCulloch DG, Marks NA, Yarovsky I. Hybrid Approach for Generating Realistic Amorphous Carbon Structure Using Metropolis and Reverse Monte Carlo. Mol. Simul. 2002; 28:927-938.

[33] Jain SK, Pellenq RJM, Pikunic JP, Gubbins KE. Molecular Modeling of Porous Carbons Using the Hybrid Reverse Monte Carlo Method. Langmuir 2006; 22(24):9942-9948.

[34] Vishnyakov A, Ravikovitch PI, Neimark AV. Molecular level models for CO_2 sorption in nanopores. Langmuir 1999; 15(25):8736-42

[35] Plimpton S. Fast Parallel Algorithms for Short-Range Molecular Dynamics. J. Comput. Phys. 1995; 117(1):1-19.

[36] Hoover WG. Canonical Dynamics: Equilibrium Phase-Space Distributions. Phys. Rev. A. 1985; 31(3):1695.

[37] Martyna GJ, Klein ML, Tuckerman M. Nosé–Hoover Chains: The Canonical Ensemble Via Continuous Dynamics. J. Chem. Phys. 1992; 97(4):2635-2643.

[38] Martyna GJ, Tuckerman ME, Tobias DJ, Klein ML. Explicit Reversible Integrators for Extended Systems Dynamics. Mol. Phys. 1996; 87(5):1117-1157.

[39] Do DD. Adsorption Analysis: Equilibria and Kinetics; Imperial College Press; 1998.

[40] Kurniawan Y, Bhatia SK, Rudolph V. Simulation of Binary Mixture Adsorption of Methane and CO_2 at Supercritical Conditions in Carbons. AIChE J. 2006; 52(3):957-967.

[41] Ding LP, Bhatia SK, Liu F. Kinetics of adsorption on activated carbon: application of heterogeneous vacancy solution theory. Chem Eng Sci 2002;57(18):3909-3928.

[42] Jobic H. Molecular Dynamics of N-Pentane in Nax Zeolite Studied by Quasi-Elastic Neutron Scattering. Phys. Chem. Chem. Phys. 1999; 1(4):525-530.

[43] Jobic H, Schmidt W, Krause CB, Kärger J. PFG NMR and QENS Diffusion Study of n-Alkane Homologues in MFI-Type Zeolites. Microporous Mesoporous Mater. 2006; 90(1):299-306.

[44] Jobic H, Theodorou DN. Quasi-Elastic Neutron Scattering and Molecular Dynamics Simulation as Complementary Techniques for Studying Diffusion in Zeolites. Microporous Mesoporous Mater. 2007; 102(1):21-50.

[45] Feldhoff A, Caro J, Jobic H, Ollivier J, Krause CB, Galvosas P, Kärger J. Intracrystalline Transport Resistances in Nanoporous Zeolite X. ChemPhysChem 2009; 10(14):2429-2433.

[46] Rives Sb, Jobic H, Beale A, Maurin G. Diffusion of CH_4, CO_2, and Their Mixtures in $AlPO_4$-5 Investigated by Qens Experiments and Md Simulations. J. Phys. Chem. C 2013; 117(26):13530-13539.

[47] Prasetyo I, Do D. Adsorption Rate of Methane and Carbon Dioxide on Activated Carbon by the Semi-Batch Constant Molar Flow Rate Method. Chem. Eng. Sci. 1998; 53(19):3459-3467.

[48] Rutherford SW, Nguyen C, Coons JE, Do DD. Characterization of Carbon Molecular Sieves Using Methane and Carbon Dioxide as Adsorptive Probes. Langmuir 2003; 19(20):8335-8342.

[49] Chandler D. Statistical Mechanics of Isomerization Ddynamics in Liquids and the Transition State Approximation. J. Chem. Phys. 1978; 68(6):2959-2970.

[50] Voter AF, Doll JD. Dynamical Corrections to Transition State Theory for Multistate Systems: Surface Self-Diffusion in the Rare-Event Regime. J. Chem. Phys. 2005; 82:80-92.

[51] Jepps OG, Bhatia SK, Searles DJ. Modeling Molecular Transport in Slit Pores. J. Chem. Phys. 2004; 120:5396-5406.

[52] Bhatia SK, Chen H, Sholl DS. Comparisons of Diffusive and Viscous Contributions to Transport Coefficients of Light Gases in Single-Walled Carbon Nanotubes. Mol. Simul. 2005; 31(9):643-649.

[53] Giesy TJ, LeVan MD. Mass Transfer Rates of Oxygen, Nitrogen, and Argon in Carbon Molecular Sieves Determined by Pressure-Swing Frequency Response. Chem. Eng. Sci. 2013; 90;250-257.

[54] Reid C, Thomas K. Adsorption Kinetics and Size Exclusion Properties of Probe Molecules for the Selective Porosity in a Carbon Molecular Sieve Used for Air Separation. J. Phys. Chem. B 2001; 105(43):10619-10629.

[55] Reid C, Thomas K. Adsorption of Gases on a Carbon Molecular Sieve Used for Air Separation: Linear Adsorptives as Probes for Kinetic Selectivity. Langmuir 1999; 15(9):3206-3218.

Chapter 5 : Effect of fluorine doping on structure and CO_2 adsorption in silicon carbide-derived carbon*

*Published in *Carbon*, Vol. 96, 565-577

We investigate the effect of fluorine-functionalisation of nanoporous silicon carbide-derived carbon (SiCDC), on its structural as well as adsorption properties, with the aim of assessing its suitability for CO_2 capture. The morphology and structure of samples fluorinated to three different F/C ratios are characterized by several analysis techniques, as well as gas adsorption. Fluorination is seen to have a stabilising effect on SiCDC, and stronger C–F bonds are formed at high levels of fluorination. Further, increasing fluorination level leads to a decrease of specific surface area and total pore volume, consistent with recent simulation results from this laboratory. Fluorination has little effect on the ultra-microporosity at low levels of fluorination, but leads to significant decrease at high levels of fluorination. Sub-atmospheric pressure CO_2 adsorption kinetics is interpreted using a bidisperse pore structure model, considering particle scale diffusion in large micropores and local grain scale diffusion with an interfacial barrier in ultra-micropores. The comparison of the CO_2 uptake-time curves for the fluorinated and non-fluorinated samples shows slightly slower uptake with increasing fluorination level, largely due to decrease in pore volume and surface area. The isosteric heat of adsorption and activation energy barriers both decrease mildly with increased level of fluorination.

5.1 Introduction

The functionalisation and surface modification of carbons is an area of much current interest, due to its relevance to the engineering of their hydrophilic/hydrophobic and adsorption properties. For example, increase in adsorption capacity [1], as well as an increase in conductivity and performance in supercapacitors [2] and batteries [3] has been reported based on targeted modification of surface chemistry. Oxygen [4], fluorine [5-7], nitrogen [8, 9], and sulphur [10, 11] functionalities are the most common among surface functional groups that have been found to enhance the performance and properties of carbon materials in various applications.

Fluorination has been shown as one of the most effective chemical methods to modify surface properties and control physical-chemical properties of various carbon materials due to the

outstanding characteristics of the fluorine molecule. These characteristics include extreme reactivity, and the high electronegativity of the fluorine ion, which can lead to very strong bonds between fluorine and other materials [12, 13]. Ghimbeu et al. [14], who investigated the influence of material characteristics on fluorinated carbonaceous materials formed by exposure to molecular F_2 and atomic F released by XeF_2 decomposition, suggest fluorinated carbon to be a good filter for hydrophobic pollutants due to strong covalent bonding of fluorine. They also find a decrease in pore volume and specific surface area, with insignificant change in pore size distribution. Jung et al. [15] and Im et al. [16] report fluorination of phenolic activated carbon and polyacrylonitrile-based activated carbon nanofibers to enhance electrochemical capacitance and CH_4 storage respectively, due to the high electronegativity of the surface fluorine. Leroux and Dubois [17] demonstrate improved performance of primary Li^+ ion batteries using ordered mesoporous carbonaceous materials having various amounts of fluorine, with tuning the fluorination temperature. Parmentier et al. [18] report large hysteresis and contradictory effects of the interaction of fluorinated carbonaceous materials with water, during water intrusion and adsorption/desorption measurements, with adsorption being lower on the adsorption branch, suggestive of hydrophobicity, but higher on the desorption branch, suggestive of hydrophilicity. Setoyama et. al [19], Lee et. al. [20], and Li et al. [21, 22] have shown that fluorination of activated carbon fibre (ACF) reduces N_2 adsorption and ethanol adsorption due to reduction in surface area, pore size, and pore volume [19, 20] and the surface energy [19]. They demonstrate the level of fluorination to have an inverse relation with pore volume, surface area and mean pore width of the surface modified activate carbon fibres [20].

In the literature, it has been reported that fluorine doped carbons form a variety of complex and highly versatile C–F bonds, in which the chemical and structural properties are influenced by either ionic or covalent bonding [13, 23]. It is shown that there are three main parameters which affect the fluorination of carbon materials [24]. The first of these is the level of graphitisation, with more graphitized carbons requiring higher fluorination temperature, while amorphous carbon can attain high fluorine content at low and even room temperature [18]. A second variable affecting fluorination is the specific surface area, with higher specific surface area permitting lower fluorination temperature [18, 19], and finally surface curvature also affects fluorination, as it enhances reactivity of the carbon [25, 26].

Chapter 5. Effect of fluorine doping on structure and CO_2 adsorption in silicon carbide-derived carbon

Besides the work on conventional carbon materials, discussed above, there is little reported on fluorine doping and modifying the surface chemistry of CDCs. To the best of our knowledge there is no experimental report investigating the effect of fluorine doping of microporous carbons on CO_2 adsorption with the aim of assessing their suitability for carbon capture. On the basis of simulations, Bhatia and Nguyen [27] have shown CDCs are potential candidates as adsorbents for CO_2 capture. CDCs synthesized from inorganic precursors have no polar functional groups and are composed of purely covalently bonded carbon compared to conventional carbon materials which are made from natural precursors [27]. Such carbons are hydrophobic in nature, preventing water adsorption depending on their structure. Increased hydrophobicity of CDCs and their water-repelling nature can provide good characteristics for CO_2 capture, while H_2O has an unfavourable interaction with CO_2. Farmahini et al. [28] have theoretically investigated the effect of fluorine doping on hydrophobicity of nanoporous SiCDC, and the differences in barriers for adsorption and diffusion of water vapor and CO_2 between the fluorinated and non-fluorinated structures. In their simulation study, they have shown weakened solid-fluid binding energies for CO_2 in the fluorinated samples, in which adsorption enthalpies are decreased on fluorination, with small change in activation energy barriers.

A detailed investigation combining characterization and experimental adsorption studies has been performed here to obtain a comprehensive understanding of the adsorption properties, microstructure of fluorine doped CDCs and the nature and the strength of the C-F bonds of the fluorinated CDCs. Such fundamental understanding of the internal structure of the fluorine doped CDCs and their adsorption behaviour is essential for the preparation of the advanced porous carbons for specific applications. Virgin and fluorinated SiCDCs have been characterized by a variety of microscopic techniques as well as gas adsorption, to investigate their pore structure and adsorption properties. A detailed description of the experimental measurement procedure is given in our previous published works [29, 30], in which we have shown that SiCDCs have a bidisperse micropore distribution, with the microporosity comprising significant ultra-micropores (0.32–0.37 nm) and larger micropores forming the inter-grain spaces [29-31]. Here, it has been shown that the bimodal micropore size distribution is preserved after the fluorination of the SiCDC samples. Experimental adsorption uptake kinetics data for CO_2 on virgin and fluorinated samples are interpreted using the bipore model incorporating a grain surface barrier resistance presented in our

previous work [30]. The results support the presence of surface barrier resistance for the diffusion of CO_2 in both the virgin and fluorinated samples, indicating the presence of structural constrictions and large entry barriers near the grain surface of fluorinated samples.

5.2 Experimental

5.2.1 Sample synthesis

SiCDCs were produced in our laboratory by chlorination of commercial micron-sized SiC β-phase, 99.8% powder at 1073 K provided by Alfa Aesar. Chlorination was conducted on SiC powder using ultrahigh purity chlorine (BOC Gases, 99.9%) and ultrahigh purity argon (BOC Gases, 99.999%) as reactive and purging gases, respectively. A heating rate of 30 K/min was employed to increase the temperature of the tube furnace to 1073 K. For CDC synthesis, we adopted the CDC preparation procedure described by us in detail elsewhere [29].

5.2.2 Fluorination conditions

The fluorination of SiCDCs were conducted by solid-gas reaction at three different conditions named LF (Low Fluorination, 10 min F_2/N_2), MF (Medium Fluorination, 20 min F_2/N_2) and HF (High Fluorination, 60 min F_2/N_2) which refers to 10 min, 20 min and 60 min of fluorination respectively. Prior to fluorination, each sample was outgassed overnight under primary vacuum at 120 °C in order to eliminate physisorbed molecules on the carbon surface or entrapped in the porosity. Subsequently, the oven temperature was cooled to room temperature, and mixed gaseous atmosphere having various F/N_2 ratios was applied for the required duration. Gaseous molecular fluorine, supplied by Solvay Fluor, having purity 98–99% V/V, with maximum 0.5% V/V HF and other gases, primarily O_2/N_2 at approximately 0.5% V/V, and a passivated nickel reactor (coated with NiF_2) was used for fluorination of the SiCDC. Once the fluorination at room temperature was complete, pure nitrogen purge was used to replace the residual molecular fluorine. The corresponding reaction is as follows: $C + (x/2)F_2 = CF_x$. The ratio of the fluorine atoms to carbon atoms (F/C) was also obtained using an Escalab 220iXL X-ray photoelectron spectrometer. The measurements showed F/C atomic ratio of 0.062, 0.087, and 0.307 for LF, MF and HF samples respectively. The X-ray photoelectron spectroscopy survey spectrum for the virgin and fluorinated samples is shown in Figure S5-1 of the Supplementary Data.

It is noted that fluorination was conducted in the laboratory at Institut de Chimie de Clermont-Ferrand, Université Blaise Pascal, France.

5.2.3 Physico-chemical characterization

The atomistic structure of the virgin and fluorinated SiCDCs was analyzed from high-resolution TEM micrographs obtained using a JEOL 1010 transmission electron microscope at 100 kV. The selected-area electron diffraction (SAED) pattern of the samples was examined using a TECNAI F20 FEG transmission electron microscope at 200 kV.

Fourier transform infrared (FTIR) spectroscopy in the frequency range from 400 to 4000 cm^{-1} was also used to underline the different C–F bonds. Thermogravimetric analysis (TGA) experiments were carried out using a Shimadzu TGA-50 instrument, in order to evaluate the thermal stability of the fluorinated carbon. Measurements were made in air at a heating rate of 2 °C/min from room temperature to 600 °C using about 10 mg of sample (accuracy of 0.001 mg).

5.2.4 Argon adsorption

The experimental Ar adsorption and desorption isotherms were measured with a volumetric adsorption apparatus (Micromeritics ASAP2020) at 87 K. The samples were degassed in vacuum at 473 K prior to the analysis. The specific surface areas (SSA) of the virgin and fluorinated samples were obtained with the Brunauer–Emmett–Teller (BET) method for $0.01< P/P_0 < 0.05$, as recommended by Kaneko et al. [32] for microporous materials. The pore size distribution (PSD) of the synthesized SiCDC and fluorinated samples was determined by interpretation of argon adsorption isotherm data using non-local density functional theory (NLDFT) with the Finite Wall Thickness (FWT) model [33-35]. Due to the limited validity of these methods for the fluorinated samples, complementary analysis of the isotherms were performed by the Dubinin–Raduschkevitch (DR) equation, and the micropore volume and surface area of the samples were obtained using the DR plots.

5.2.5 CO_2 adsorption

CO_2 adsorption isotherms of the samples were also measured using the Micromeritics ASAP 2020 instrument at different temperatures. Prior to each adsorption experiment, the samples were degassed at 473 K. After the samples were cooled down, the degassed sample cell was transferred to the adsorption port of the analysis section of the instrument and adsorption

isotherm measurements were conducted. The pore volume and surface area, and the pore size distributions of both virgin and fluorinated samples were also obtained from the CO_2 adsorption isotherm at 273 K using the in-built DFT2 (NLDFT) program from Micromeritics. The Dubinin–Raduschkevitch method was also used to obtain the textural parameters of the samples from CO_2 adsorption isotherm. The uptake kinetics of CO_2 on both virgin and fluorinated samples was experimentally measured at 303-333 K up to atmospheric pressure, using the Micromeritics ASAP2020. In this experimental procedure, the transient gas pressure signals from the pressure transducer are recorded for each pressure step. Isothermal conditions are maintained during all experiments using an insulated Dewar flask.

5.3 Results and discussion

Prior to gas sorption and CO_2 measurements, the structural characterization, properties and the nature of the C–F bonding of the samples were first investigated, using the different techniques indicated above. The structural characterization of the samples provides insight into the obtained argon and CO_2 adsorption isotherms of the samples.

5.3.1 Structural characterizations of the fluorinated CDCs

5.3.1.1 HRTEM

The HRTEM images of the virgin and the fluorinated samples are shown in Figure S5-2 of the Supplementary Data, as are the corresponding SAED patterns. The HRTEM images are indicative of the highly amorphous nature and highly disordered microstructure of the virgin and the fluorinated samples. The amorphous structure is also in agreement with the diffuse rings shown in the SAED patterns for the virgin and fluorinated samples. A slight increase of graphite ordering in MF sample can be observed in HRTEM images. In the literature, the degree of graphitization of CDC samples has been reported to increase with synthesis temperature [36, 37]. The extent of graphitization observed in these micron-sized samples is lower than that of nano-sized SiCDC samples prepared at the same temperature [37]. It is reported that SiCDCs generally remain amorphous up to very high synthesis temperatures [38]. Compared with the virgin sample, no significant change in morphology of the fluorinated samples is observed with HRTEM even after high level of fluorination.

5.3.1.2 FTIR analysis

Fourier transform infrared (FTIR) spectroscopy was also used to underline the different kinds of C–F bonds. Figure 5-1a shows the FT-IR transmittance spectra of the virgin and fluorinated CDC samples for different levels of fluorination. As seen in Figure 5-1, FTIR confirms the formation of C-F bonds in all fluorinated samples. The 1608 cm^{-1} band for virgin sample is related to the aromatic C=C stretching vibration. In the SiCDC-LF, SiCDC-MF and SiCDC-HF samples this band increased to 1625 cm^{-1}, 1662 cm^{-1} and 1671 cm^{-1}, respectively [39]. The vibration band at the higher wave number is related to the stronger chemical bonding. The bands at 1016 cm^{-1} in the LF sample, 1052 cm^{-1} in the MF sample, and 1083 cm^{-1} in the HF sample correspond to the semi-ionic C-F bonds [12]. It can be seen that the intensity of the C-F bonding has increased significantly. The band at 1717 cm^{-1} in the LF sample corresponds to the C-CF_2 stretch [40]. This peak is shifted to 1746 cm^{-1} in the MF sample, and almost disappears in the HF sample.

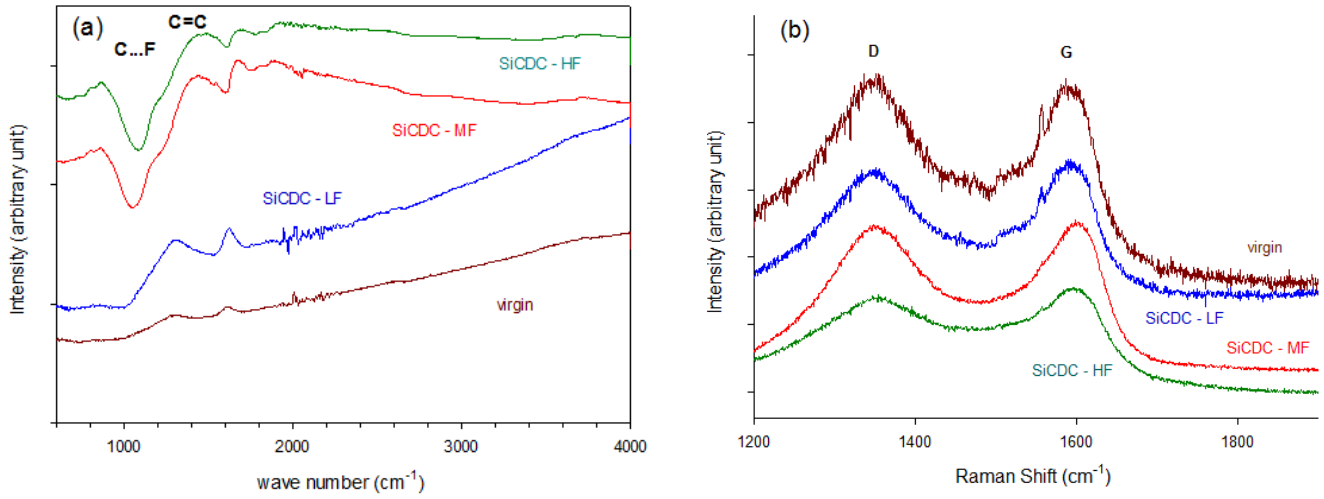

Figure 5-1. (a) FT-IR spectroscopy for virgin and fluorinated samples, and (b) Raman spectra of virgin and fluorinated samples.

5.3.1.3 Raman spectra

Figure 5-1b depicts Raman spectra of the virgin and fluorinated samples. For all samples, it can be seen that there are two: the characteristic disorder (D) band near 1347–1358 cm^{-1} and the graphite (G) band at 1585–1597 cm^{-1}. The intensity ratio of *D* and *G* bands was determined as the peak height ratio between the *D* and *G* bands of Raman spectra in Figure 5-

1b. The *I*(D)/*I*(G) ratio for the virgin, LF, MF and HF samples are 2.18, 1.89, 1.74, and 2.36 respectively, which shows that the intensity ratio of D and G bands decreases with the sample fluorination and goes through a minimum and then increases with high duration of fluorination. The increase in ordering and graphitisation degree by fluorination (which likely also saturates some defects such as dangling bonds) is also consistent with HRTEM observations for MF sample. The Raman spectra of all samples imply that the obtained SiCDC and the fluorinated samples have a predominantly amorphous structure.

5.3.1.4 Thermogravimetric analysis

Thermogravimetric analyses (TGA) curves of the virgin and fluorinated samples are shown in Figure 5-2, where Figure 5-2a shows the weight loss as a function of temperature from 30°C to 600°C and Figure 5-2b shows the corresponding derivative curves. The TGA curve of the virgin sample shows water desorption about 100°C. The virgin sample shows a significant amount of adsorbed moisture compared to the fluorinated samples. This is probably due to the exposure of the virgin sample to the ambient air for a large amount of time as it was prepared in the laboratory in Australia and sent to the collaborating laboratory in France.

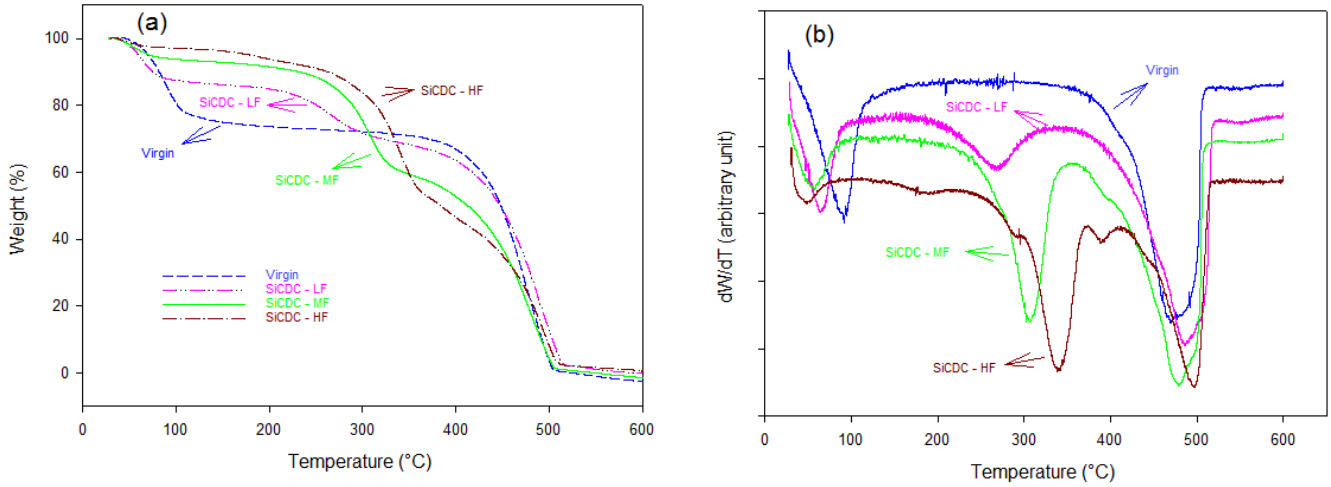

Figure 5-2. (a) Integral, and (b) derivative TGA curves for virgin and fluorinated samples.

The results show that in the fluorinated samples less water is trapped, and for which lower desorption occurs at temperature below 70°C. This decrease of adsorbed water in the fluorinated samples is consistent with increased hydrophobicity. For the fluorinated samples, the main decomposition process at around 300°C, and corresponds to C-F decomposition.

The TGA derivative curve indicates that the higher the level of fluorination the higher the C-F bond strength, based on a higher decomposition temperature of C-F; thus higher fluorination levels result in more stable C–F bonds. It can be also noticed that the higher the fluorination level, the more numerous are the C-F bonding sites that decompose. Thus, the HF sample has 4 sites, decomposing at 180, 300, 340 and 380 °C as seen in Figure 5-2b. With increasing duration of fluorination, more stable bonds are formed, such as those decomposing at 380°C. Some weak C–F bonds, decomposing at 180 °C are also formed over the longer duration of the HF fluorination, and likely arise at low energy sites of the virgin carbon.

At higher TGA temperatures the oxidation of carbon into CO_2occurs, and the temperature for this increases with fluorination. Thus, fluorination appears to have a stabilising effect, with the oxidation temperature increasing from about 480 to 500°C from virgin to HF samples, and the onset of the oxidation peak occurring at higher temperature with increasing level of fluorination.

5.3.2 Argon adsorption at 87 K

Argon adsorption/desorption isotherms of the virgin and fluorinated samples are shown in Figure 5-3a. There are six kinds of adsorption isotherms categorized in IUPAC classification, and each indicates a distinct pore structure. The Ar adsorption isotherms of both virgin and fluorinated samples are classified as type I, showing a sharp increase in the adsorbed argon volume at low relative pressures. Most of the pore volume of the samples is filled at very low relative pressures (<0.05), indicative of highly microporous nature of the samples.

It can be seen in Figure 5-3a that as the level of fluorination increases, the amount of argon adsorbed gradually decreased from the virgin sample to the HF sample. A small increase in the amount adsorbed at high pressures (P/P_0 > 0.9) for the both virgin and fluorinated samples is also observed. The low level fluorinated sample (LF) shows larger adsorbed amount of argon at 87 K compared to high level fluorinated sample at very low relative pressures. This higher adsorbed amount of argon for LF sample compared to MF and HF samples is indicative of larger volume of small micropores. Argon desorption curves for all samples are also depicted in Figure 5-3a, showing lack of hysteresis for both virgin and fluorinated samples, at least above P/P_0 of about 10^{-3}.

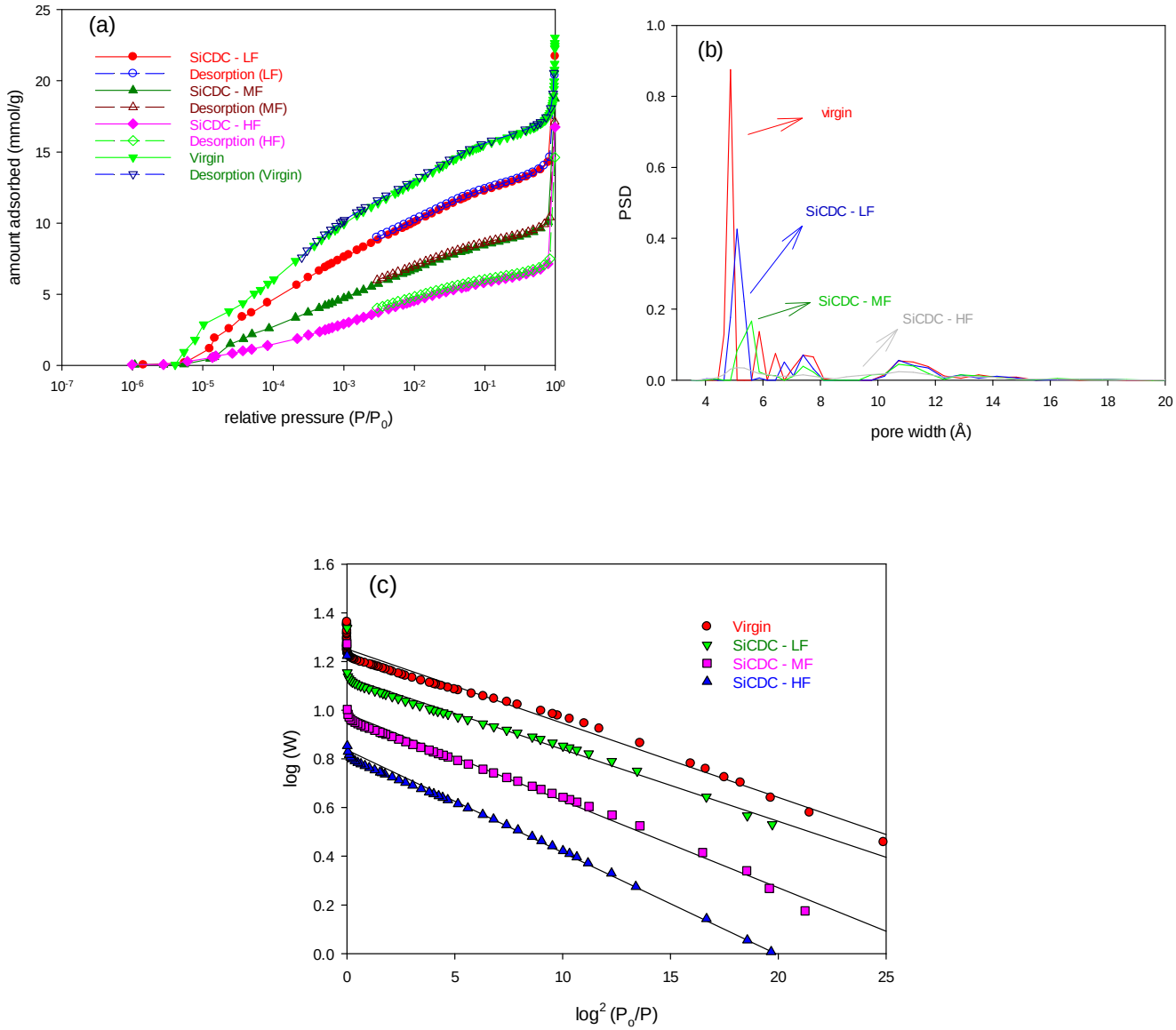

Figure 5-3. (a) Argon adsorption/desorption isotherm at 87 K, (b) DFT pore size distributions (PSDs), and (c) DR plots from argon adsorption isotherm, for virgin and fluorinated samples.

As one of the pore characteristic parameters, pore size distribution (PSD) influences the adsorption equilibrium and gas transport, and was investigated here using non-local density functional theory (NLDFT) with the Finite Wall Thickness (FWT) model [33-34]. The corresponding pore size distributions (PSDs) of all samples obtained from FWT-NLDFT are shown in Figure 5-3b. It can be seen that all samples primarily possess micropores having widths below 1.5 nm, and the presence of larger pores is negligible. As illustrated in Figure 5-3b, before fluorine treatment, the pore size is distributed in the range of 0.4-1.5 nm, and after fluorination, the microporous nature of the untreated sample is roughly preserved.

However, it can be seen that when the SiCDCs are fluorinated, the range of the pore size distribution gradually narrows from the virgin sample to the highly fluorinated SiCDC, and the fluorination of SiCDCs reduces the micropore volume. It is seen that the peak at ~4.9 Å in the virgin sample shifts toward larger values, as the fluorination level increases.

The fluorinated samples also show a significant decrease in the height of the peaks in the PSD curves by the fluorination process, suggesting decrease in the microporosity. In Table 5-1 a continual decrease of pore volume on increasing fluorination level can be observed. The fluorinated samples have a range of 400-1120 m^2/g for specific surface area, and a pore volume range of 0.16–0.37 cm^3/g showing significant decrease with increasing fluorination level. Similar behaviour has been also reported in the literature [19-21, 41, 42]. Table 5-1, also summarizes surface area of the samples obtained by BET, and show similar trend for the samples. It should be mentioned that any change in the structure of the fluorinated samples is due to the presence of F atoms on the surface which reduces pore volume and surface area, and to some extent due to structural relaxation on bonding with fluorine. However it is not due to thermal effects as the fluorination of virgin SiCDC occurred at room temperature, while the virgin sample had already annealed at the synthesis temperature of 1073 K at which the virgin SiCDC was prepared. As a result, structural changes similar to those from post-treatment by gases such as Ar or N_2, which is normally carried out at high temperatures, cannot arise from the fluorination.

Table 5-1. Textural parameters obtained by BET and DFT model.

Sample	S_{BET} (m^2/g)	DFT (from Ar isotherm)		DFT2 (from CO_2 isotherm)	
		Pore volume (cm^3/g)	Surface area (m^2/g)	Pore volume (cm^3/g)	Surface area (m^2/g)
virgin	1230.62	0.519	1527.3	0.236	1955
LF	981.30	0.367	1118.5	0.205	1754
MF	674.69	0.241	642.4	0.172	1402
HF	464.34	0.164	401.9	0.091	854

Since the DFT model is not accurate for the fluorinated samples due to the presence of fluorine (whose interaction is not considered in the existing models), the textural properties of the untreated SiCDC and fluorinated samples are further evaluated by the Dubinin–Radushkevich (DR) equation, which can be written as follows

$$\log W = \log W_0 - (RT / \beta E_0)^2 \log^2 (P_0 / P) \tag{5-1}$$

Here, W_0 (cm^3/g STP) is the "micropore capacity" and E_0 (kJ/mol) is the characteristic adsorption energy related to the micropore structure. R and T are the universal gas constant and adsorption temperature respectively, and β is an affinity coefficient which depends on the strength of surface molecule interaction. In the present study, we have used the affinity coefficient β(argon) of 0.267 [43].

The micropore surface area (MSA) of the samples can be also determined, following:

$$\text{MSA} = \frac{\sigma \times W_0 \times \text{Avogadro's number}}{\text{volume of 1 g mol of gas at STP}} \tag{5-2}$$

where σ is the molecular cross sectional area of the gas (nm^2), which for Ar is 0.142 nm^2, and the "total micropore volume" V_0 (cm^3/g) is defined as follows

$$V_0 = W_0 \times \rho_c \tag{5-3}$$

where ρ_c is the density conversion factor (cm^3 liquid/cm^3 STP) of the adsorptive. The density conversion factor used here for argon is 0.00128 (cm^3 liquid/cm^3 STP). The textural properties of the samples obtained from this method are presented in Table 5-2.

The average micropore width, L_0 of the locally slit-shaped micropores can be also estimated from the E_0 value by the Dubinin–Stoeckli (DS) relation (results shown in Table 5-2). Several forms of the DS relation are known [44-46]. Here we used the following equation [46]:

$$L_0(nm) = \frac{10.8}{(E_0 - 11.4)} \tag{5-4}$$

where E_0 (kJ/mol) is the characteristics energy expressed in Dubinin-Radushkevich equation [46]. Eq. (5-4) reflects the average pore size of the actual micropore distribution. From Table 5-2, it can be seen that fluorination reduces the micropore volume consistent with the results obtained from DFT method. The reduction of the micropore volume with fluorination could be attributable to the blocking of micropores by the C-F bondings.

Table 5-2. Textural parameters obtained from Ar adsorption interpreted by the Dubinin–Radushkevich (DR) equation.

Sample	Micropore capacity (mmol/g)	Characteristic energy (kJ/mol)	L_0 (nm)	Micropore volume (cm^3/g)	Micropore surface area (m^2/g)
virgin	17.84	23.65	0.88	0.51	1526
LF	13.63	24.02	0.86	0.39	1166
MF	9.67	21.84	1.03	0.28	827
HF	6.86	20.14	1.23	0.20	586

The DR plots obtained from Ar adsorption isotherms are presented in Figure 5-3c. The slopes of the DR plots for the virgin and LF samples are close to each other; suggesting that the adsorption energy and the average slit-width, L_0 (nm) for the LF sample do not significantly change by fluorination. For the MF and HF samples, the slopes of the DR plots are larger than the virgin and LF samples, suggesting higher average slit-width, L_0 (nm) for the MF and HF samples. It can be seen that for both virgin and fluorinated samples, the values of the surface area and pore volume obtained from the DR equation are close to the values obtained by the DFT method and show similar trend. The decrease of pore volume, and specific surface area of the SiCDCs on fluorination is also consistent with simulation results reported elsewhere [28].

5.3.3 CO_2 adsorption and kinetics

We have also investigated the equilibrium uptake of CO_2 in all fluorinated SiCDCs, and have compared the results with those for the virgin sample, to investigate the effect of fluorination on adsorption of CO_2. Sub-atmospheric adsorption of CO_2 was conducted at different temperatures volumetrically. As depicted in Figure 5-4a the virgin sample exhibits a

relatively high CO_2 adsorption capacity at 273 K. The main reason for the high performance in CO_2 adsorption is related to the high porosity of samples, characterized by their large specific surface area and pore volume. However, in Figure 5-4b, it can be seen that fluorination decreases adsorption of CO_2, even at the lowest level of fluorination, which could be related to the smaller total specific surface area and reduction in micropores after fluorination. This behavior was also observed by simulation and is reported elsewhere [28].

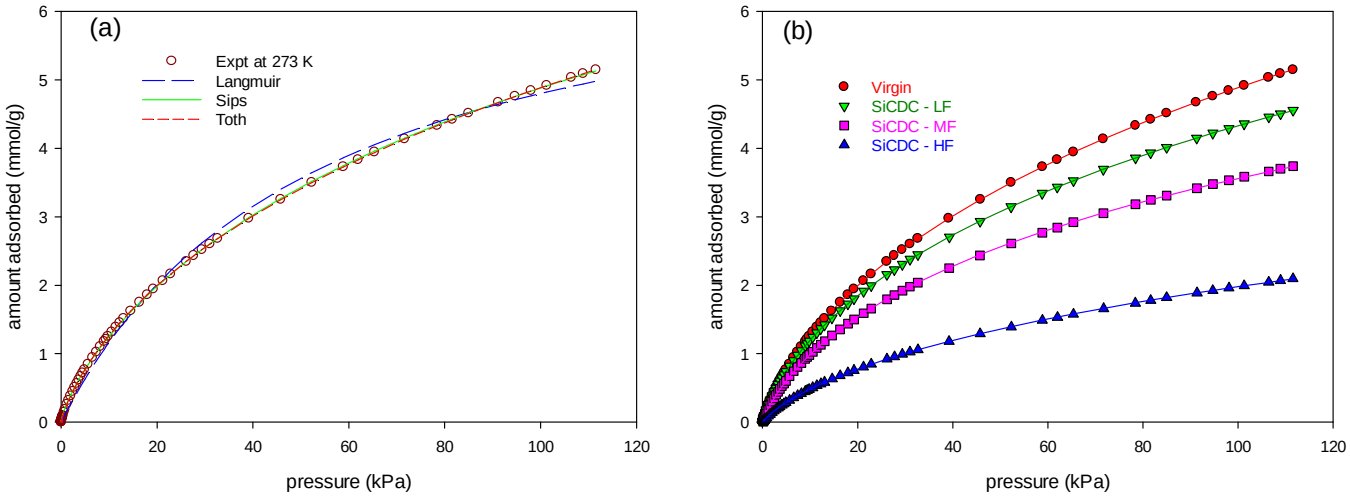

Figure 5-4. (a) Experimental sub-atmospheric adsorption isotherms of CO_2 at 273 K on the virgin sample, and fits of Langmuir, Sips, and Toth models (lines), and (b) experimental sub-atmospheric adsorption isotherms of CO_2 at 273 K on virgin and fluorinated samples, lines are Toth model fits.

We have fitted the Langmuir, Sips, and Toth adsorption isotherm models to the experimental CO_2 adsorption equilibrium data of virgin and fluorinated samples at 273 K. These models are expressed as follows [47, 48]

$$\text{Langmuir:}\quad q = \frac{q_m bP}{1+bP} \tag{5-5}$$

$$\text{Sips:}\quad q = \frac{q_m (bP)^n}{1+(bP)^n} \tag{5-6}$$

$$\text{Toth:}\quad q = \frac{q_m bP}{\left[1+(bP)^t\right]^{1/t}} \tag{5-7}$$

In these models q is the adsorbed amount, P is the equilibrium pressure, q_m and b are the adsorption capacity and equilibrium constant. Further n and t are the isotherm parameters of the Sips and Toth models respectively, and characterise heterogeneity. Fit of the these three isotherm models (Eqs. 5-5, 5-6, 5-7) shows that the Toth equation is the most successful for both virgin and fluorinated samples under these experimental conditions. The comparison of these three models on the fitting of the CO_2 equilibrium data for the virgin sample is shown in Figure 5-4a, and the fitted parameters are listed in Table 5-3. The parameter t, in Toth model is usually less than unity, and is similar for all samples, suggesting that they have similar degree of heterogeneity.

Table 5-3. Isotherm parameters estimated for CO_2 for different isotherm models.

isotherm models	parameters	Virgin	SiCDC - LF	SiCDC - MF	SiCDC - HF
Langmuir	q_m (mmol/g)	7.35	6.21	5.08	3.12
	b (1/kPa)	0.0188	0.0216	0.0221	0.0165
Sips	q_m (mmol/g)	12.51	10.87	7.70	5.32
	b (1/kPa)	0.0055	0.0057	0.0082	0.0051
	n	0.7596	0.7329	0.7719	0.7767
Toth	q_m (mmol/g)	31.64	27.18	14.31	13.44
	b (1/kPa)	0.0116	0.0155	0.0179	0.0090
	t	0.3568	0.3386	0.4164	0.3719

The pore size distribution of the samples based on interpreting the CO_2 adsorption data by the Micromeritics DFT2 NLDFT program is presented in Figure 5-5a. The pore volume and specific surface area of the samples are indicative of the micropore volume in pores smaller than 9 Å in width, since CO_2 at 273 K cannot fill larger pores at sub-atmospheric pressures. As seen in Table 5-1 the surface areas are somewhat larger than those from Ar adsorption indicative of some inaccessibility of Ar possibly due to ultramicropores. In our recent works [29, 30, 49] the existence of ultra-microporosity in SiCDCs has been shown and discussed. The presence of ultra-microporosity in CDCs are also shown in other works from this group

through SANS-based characterization of various CDCs and conventional activated carbons [50], as well as hybrid reverse Monte Carlo (HRMC) simulations of SiCDC [51]. The smallest pores corresponding to the first peak represent ultra-micropores, and hence are of a distinctly smaller size range than the main micropores. This has been found for other CDCs as well in our laboratory [29, 30, 49], and the ultra-microporous nature has been confirmed by our findings that the activation energy for diffusion in these pores corresponds to high values (40-50 kJ/mol) known for carbon molecular sieves [29, 30]. As seen in Figure 5-5a, ultra-microporosity (<3.7 Å) is present in the PSD obtained from the CO_2 isotherm at 273 K for all samples, but not present in the PSD obtained from argon at 87 K, an indication of a pore accessibility problem for argon at 87 K.

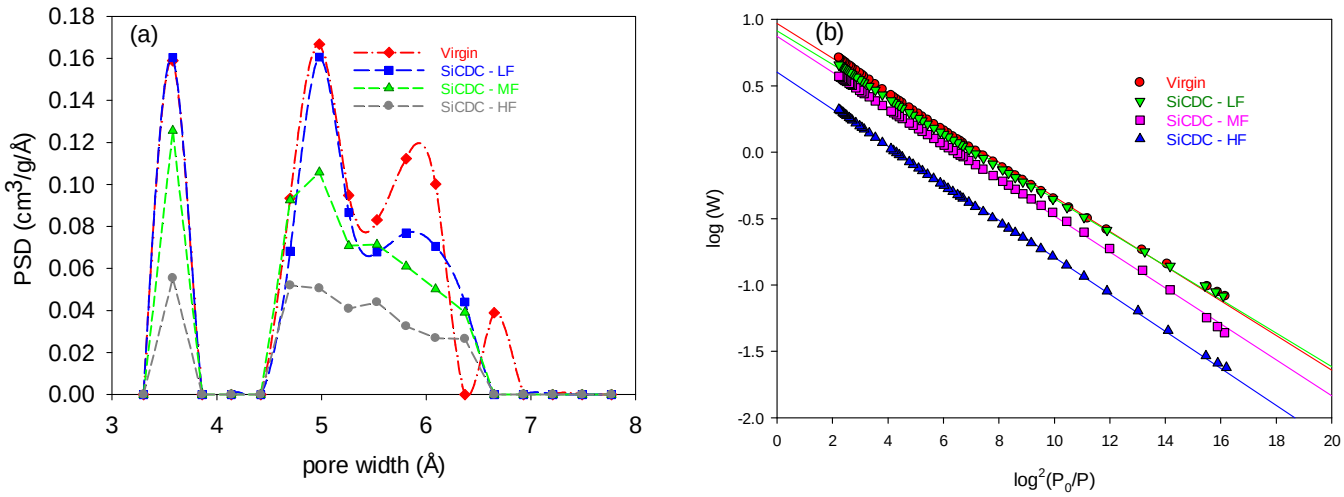

Figure 5-5. (a) DFT Pore size distributions, and (b) DR plots, for virgin and fluorinated SiCDCs obtained from CO_2 adsorption at 273 K.

All samples have the presence of the ultramicropore peak at ~3.5 Å with reduction in the volume in the MF and HF samples. It is seen that the peak at ~6.8 Å in the virgin sample is substantially lost in the fluorinated samples, which indicates fluorination lowers the pore volume of the larger micropores, as seen in Table 5-1. This behaviour is also consistent with some published experimental characterization data for fluorinated activated carbons [18, 21] showing reduction of pore volume on fluorination. The fluorination of the samples may destroy large micropores and also blocks (or narrows) micropores by fluorine-functional groups which formed in the fluorination process. In Section 5.3.1 it was demonstrated that the surface chemistry, and porosity of SiCDCs are affected by the fluorination. These factors

exhibit a strong connection with the CO_2 adsorption ability for fluorinated SiCDCs, as shown in Figure 5-4b and 5-5a, in which the observed CO_2 adsorption capacity of SiCDCs decreases at higher fluorination conditions with the decrease in the surface area and the porosity.

The usefulness of carbon dioxide in characterizing the microporous structure of carbonaceous adsorbents with the Dubinin–Radushkevich (DR) is also very well established [52, 53]. Here, we have also determined the micropore capacity W_0 and E_0 of CO_2 from the DR plots (Figure 5-5b). The DR parameters are also shown in Table 5-4. For CO_2 we have used the affinity coefficient $\beta(CO_2)$ of 0.461 [54, 55], the density conversion factor (cm^3 liquid/cm^3 STP) of 0.00183, and the molecular cross sectional area of 0.17 nm^2 in Eqs 5-1, 5-2, 5-3 to obtain the structural parameters of the samples by this method. The data obtained from DR method using CO_2 adsorption isotherms also suggests that the pore volume and specific surface area of the pores for the fluorinated samples decrease with increasing level of fluorination.

Table 5-4. Textural parameters obtained from interpretation of CO_2 adsorption by the Dubinin–Radushkevich (DR) equation.

Sample	Micropore capacity (mmol/g)	Characteristic energy (kJ/mol)	Micropore volume (cm^3/g)	Micropore surface area (m^2/g)
virgin	9.31	20.69	0.382	953.57
LF	8.19	21.03	0.336	838.27
MF	7.45	20.32	0.306	763.34
HF	4.02	20.02	0.165	411.56

In order to investigate the effect of F atoms, we have plotted the surface area and pore volume-normalised isotherms of CO_2 at 273 K. Figure 5-6a and 5-6b show that the normalised isotherms differ from each other, with the medium and high F doping reducing the adsorption more than that for low F. This indicates that interaction of CO_2 with F atoms leads to reduced adsorption at low pressures. However, the maximum capacity (fitted using Toth model) shows a linear correlation with surface area and pore volume (insets of Figure 5-6a and 5-6b), suggesting that F atoms do not significantly affect the CO_2 capacity at high pressures, at which CO_2-CO_2 interactions must dominate.

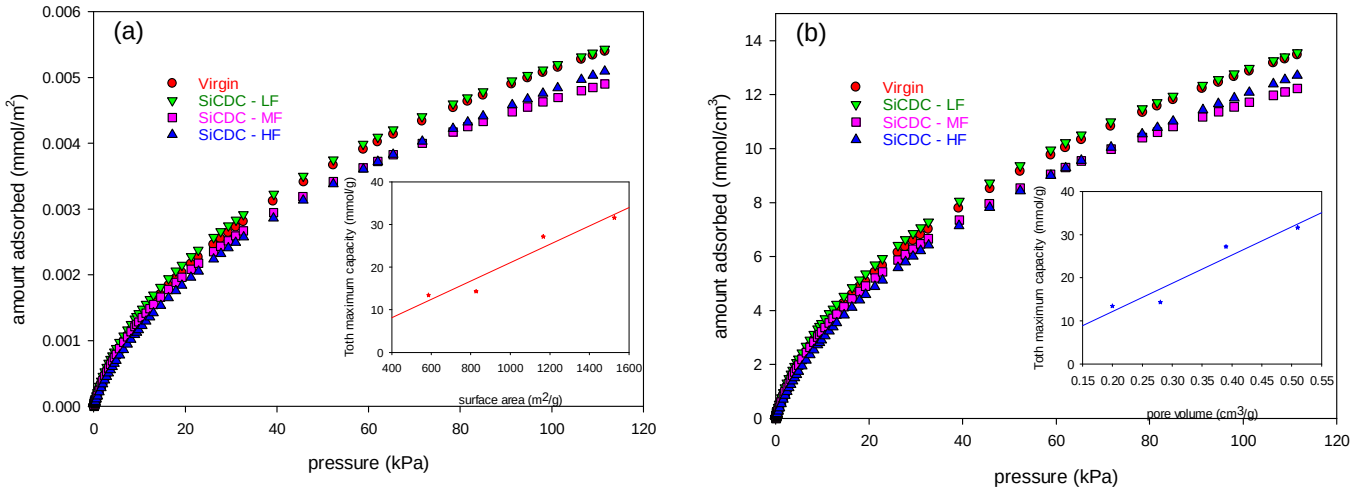

Figure 5-6. Experimental sub-atmospheric isotherms of CO_2 at 273 K normalised by (a) surface area, and (b) pore volume on virgin and fluorinated samples. Insets in (a) and (b) represent the correlation of maximum capacity with surface area and pore volume respectively.

The transient pressure variation during the measurement of equilibrium adsorption isotherms of CO_2 at 303-333 K in virgin and fluorinated samples has been also measured. The uptake-time relation was then determined from the pressure variation. In our previous works, we have investigated CH_4 and CO_2 diffusion in SiCDCs, and showed that the diffusion mechanism involves two time scales, comprising relatively rapid particle scale diffusion in the large micropores, and a much slower local grain scale diffusion in the ultra-micropores, in a bidisperse structure [29, 30]. The dual Henry-Langmuir isotherm model (Eqn (a) in the Appendix) was used here to correlate the adsorption isotherms of CO_2 on virgin and fluorinated samples over the temperature range of 303-333 K. The model has been applied successfully to describe CO_2 adsorption on virgin and fluorinated samples. As can be seen in Figure 5-7 the Henry-Langmuir isotherm model fitted the experimental adsorption isotherm quite well within the entire pressure and temperature range considered in this work. The solid lines in the figure represent the dual Henry-Langmuir model using the optimized equation parameters, whose values are listed in Table 5-5.

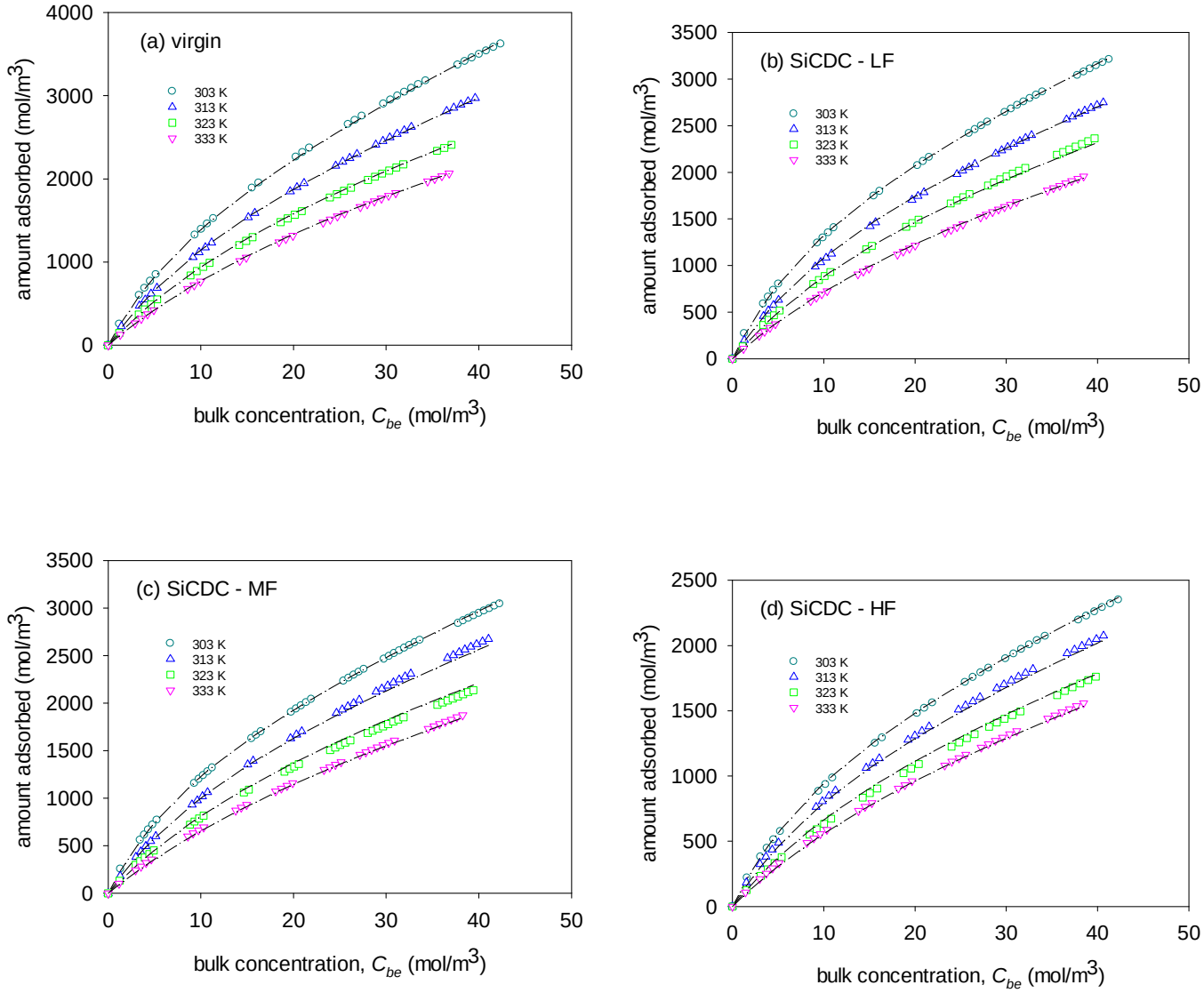

Figure 5-7. Fits of low pressure CO_2 adsorption isotherm for (a) virgin, (b) SiCDC – LF, (c) SiCDC – MF and (d) SiCDC – HF at 303– 333 K with dual Langmuir–Henry isotherm model.

The fractional kinetic uptake curves of CO_2 on both virgin and fluorinated samples obtained at 313 K is depicted in Figure 5-8a for pressure of 400 mmHg. The absolute kinetic uptake curves for the same conditions are also presented in the inset of the Figure 5-8a. The comparison between the uptake-time curves for both virgin and fluorinated samples reveals that the fractional uptake curves for virgin and low fluorinated samples are almost overlapping, however the high fluorinated sample's uptake curve proceeds somewhat slower than the other samples which indicates reduction in diffusivity with increasing fluorination

level. Consequently faster CO_2 adsorption kinetics for samples with lower level of fluorination is expected.

Table 5-5. Dual Langmuir–Henry model isotherm parameters for CO_2 on virgin and fluorinated SiCDCs.

adsorbent	$C_{\mu m}$ (mol/m^3)	$A_\ell \times 10^6$ (m^3/mol)	A_h (dimensionless)	$-\Delta H_\ell$ (kJ/mol)	$-\Delta H_h$ (kJ/mol)
virgin	2013.99	7.94	0.0294	23.23	18.72
SiCDC - LF	2010.73	3.79	0.0264	25.14	18.65
SiCDC - MF	1810.94	4.13	0.0822	25.02	15.54
SiCDC - HF	1409.79	6.27	0.1610	23.93	13.18

In order to estimate the diffusion parameters the model equations proposed in our recent work [30], and presented in the Supporting Data were applied to the experimental CO_2 kinetic data. Figure 5-8a depicts the fit of the model with the experimental CO_2 uptake kinetics data, both as fractional and as absolute (inset) adsorption. As seen from Figure 5-8a the model provides satisfactory fit of the measured CO_2 uptake for both virgin and fluorinated samples. The small discrepancy in the mid-range of the uptake can be attributed to the effect of structural heterogeneity on the transport, which is not captured through the single overall grain scale diffusivity used in the model. Consideration of the pore size distribution (Figure 5-3b) and a distribution of diffusion coefficients and energy barriers can improve the fit [30, 56], however it will require additional fitting parameters which have been avoided in this work.

The extracted micropore, ultra-micropore transport parameters, and barrier mass transfer coefficients for the virgin and fluorinated samples and the corresponding activation energies derived from the slopes of the Arrhenius plots are presented in Figure 5-8(b-d). It can be seen that the magnitude of the particle scale and grain scale activation energies are decreased on fluorination. The grain scale activation energies in all samples are significantly larger than the activation energy for micropore diffusion of CO_2 in microporous carbon reported by Prasetyo et al. [57], and the activation energy of 16 kJ/mol for CO_2 diffusion in Takeda 3A° carbon molecular sieve reported by Rutherford et al. [58].

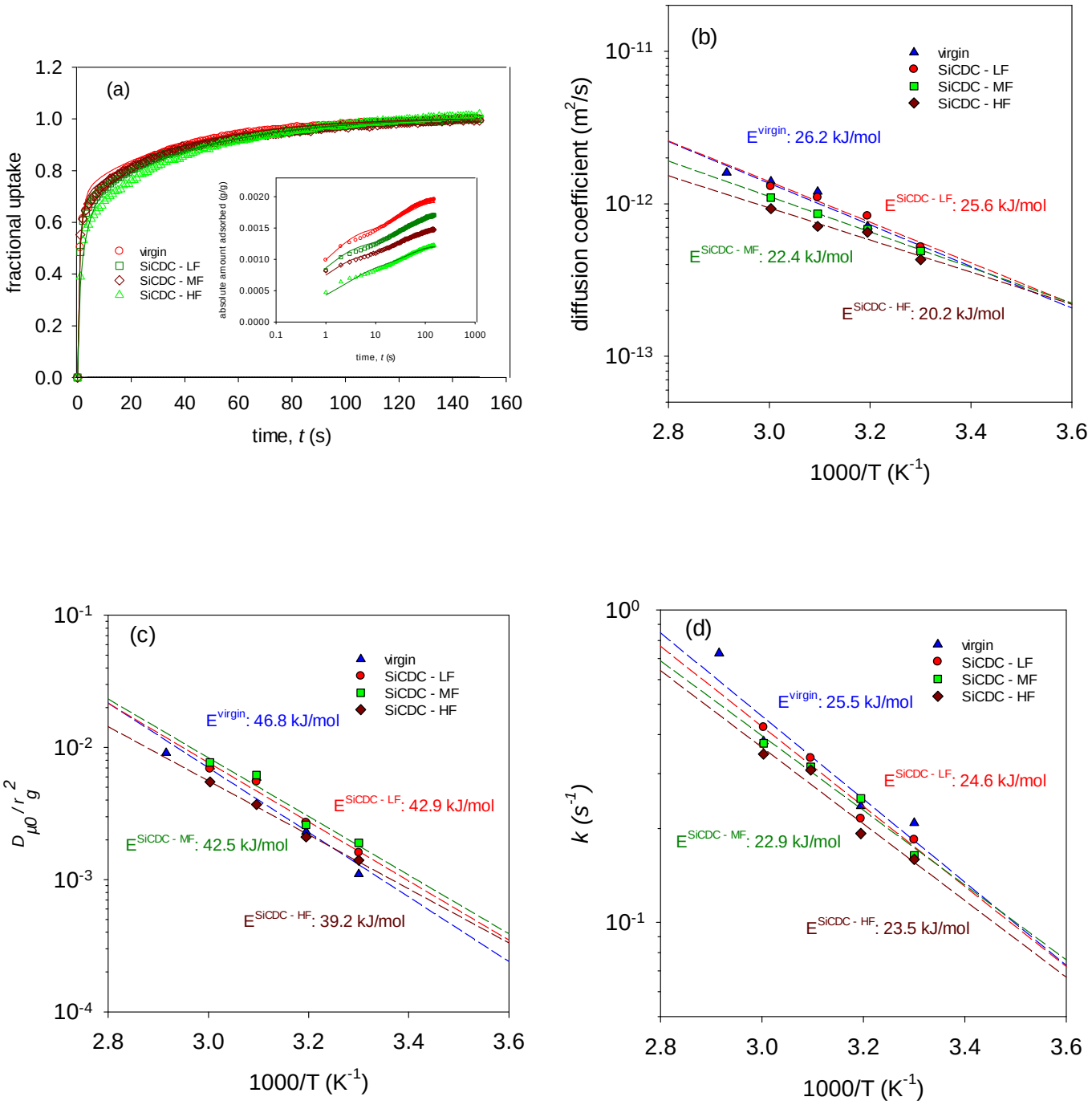

Figure 5-8. (a) CO_2 fractional kinetic uptake curves for virgin and fluorinated SiCDCs and their corresponding absolute amount adsorbed kinetic uptake curves (inset) at 313 K and pressure of around 400 mmHg, and temperature dependence of (b) CO_2 diffusivities in particle scale micropores obtained from the model, (c) $D_{\mu o}/r_g^2$ in grain-scale ultra-micropores, and (d) interfacial mass transfer coefficient at grain surface.

The larger activation energies of CO_2 in the ultra-micropores of grains of virgin and fluorinated samples compared to the activation energies reported for CMS suggest the presence of narrower pores and constrictions and internal pore-mouth barriers that affect the entry of CO_2 molecules into the ultramicropores. Due to the extremely slow diffusion in the ultra-micropores and their small pore volume, it can be concluded that the adsorption and transport in the ultra-micropores will not make a significant contribution to the transport. As seen in Figure 5-8d the activation energies of the barrier mass-transfer coefficients are in the range of 22.9-25.5 kJ/mol for the virgin and fluorinated samples, comparable to the activation energies of the barrier coefficients reported by Qinglin et al. [59], of 30.3 kJ/mol for the adsorption of CO_2 on Takeda CMS.

The isosteric heat of adsorption at zero loading, ΔH, from the Langmuir and Henry Law parts of the isotherms can be obtained based on the following equation

$$-\Delta H = RT^2 \frac{d\ln(P)}{dT} \tag{5-8}$$

where P is pressure. Figure 5-9(a-b) depict enthalpies of adsorption obtained from the Henry and Langmuirian Law parts of the isotherms and the respective equilibrium constants calculated from fitting of the dual Langmuir–Henry equation to CO_2 experimental isotherm data for the virgin and fluorinated samples. The values of the heats of adsorption are in the usual range for CO_2 adsorption in microporous carbons. The adsorption enthalpy obtained from the Henry part of the isotherm, which is related to adsorption in the particle scale, reduces with increasing the level of fluorination, however the adsorption enthalpy obtained from the Langmuirian part of the isotherm is almost constant and is in reasonable agreement with the heat of adsorption of CO_2 measured in a molecular sieving carbon reported by Reid and Thomas [60] of 28.4 kJ/mol, and Rutherford et al. [58] of 30 kJ/mol.

5.3.4 Comparison with simulation

In recent work from this group [28], atomistic models of fluorine-doped SiCDC at three different levels of fluorination (having F/C atomic ratios of 0.019, 0.053 and 0.1) have been developed based on a hybrid reverse Monte Carlo (HRMC) constructed model of SiCDC [51].

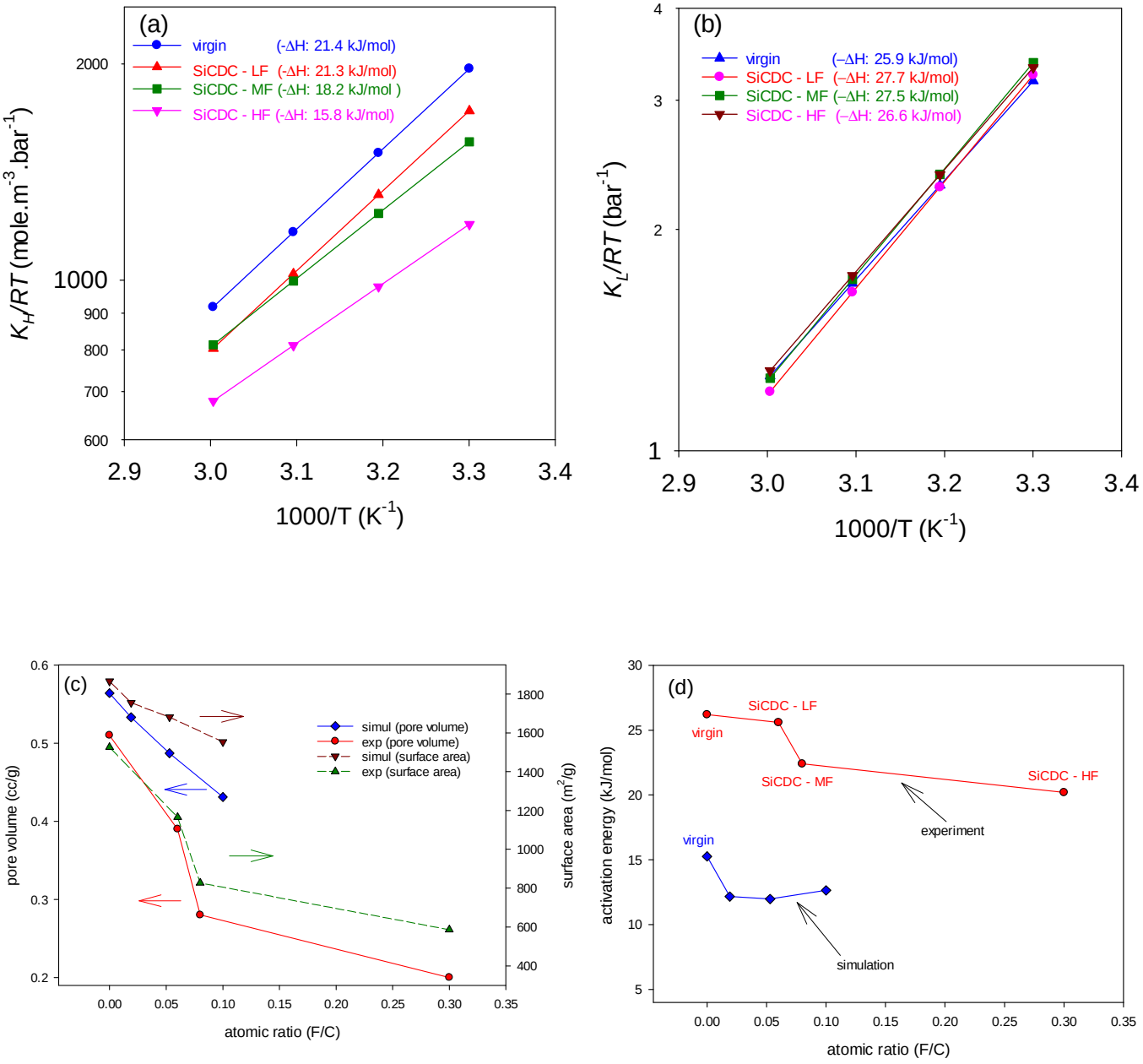

Figure 5-9. Temperature variation of (a) fitted Henry, and (b) fitted Langmuir mode equilibrium constants, obtained from the dual Langmuir–Henry model; and (c) variation of pore volume and surface area obtained from experimental Ar adsorption and simulation with fluorination level (F/C atomic ratio) for the virgin and fluorinated samples, and (d) variation of activation energies with fluorination level for experiment and simulation.

The later HRMC simulation-based model of SiCDC has shown good performance against a wide range of structural characterization, equilibrium and experimental kinetic uptake data for different gases [31]. The details of the atomistic models of fluorine-doped SiCDCs are

provided elsewhere [28]. Here we compare these simulation results with our experimental findings. In simulation studies the pore size distributions (PSDs) of the fluorinated models have shown a trend of pore volume reduction for pores in the range of 8-12 Å. The formation of large pores at ~14 Å and increase in mean pore diameter, despite reduction in pore volume in low level fluorinated SiCDCs have been observed in simulation. However this trend has not been seen for highly fluorinated structures [28]. In Figure 5-9c the variation of pore volume and surface area obtained from experimental argon adsorption and simulation with fluorination level (F/C atomic ratio) for the virgin and fluorinated samples is shown. As can be seen in this figure both experiment and simulation shows similar decreasing trends for the variation of pore volume and surface area with fluorination level. Nevertheless, the experimental values of pore volume and surface area are considerably lower than those predicted by the simulations, suggesting that the siting of the fluorine in the simulation differs from that attained in the experiment.

In simulation it is observed that fluorination decreases the sub-atmospheric adsorption isotherms of CO_2 at 273 K considerably even at the lowest level of fluorination [28]. It is shown that the reduction in CO_2 adsorption is attributed to the weakening of the solid-fluid interactions due to the reduction in high energy sites on fluorinated samples. Fluorination reduces the strength of the solid-fluid binding interactions for carbon dioxide, and many of the high energy adsorption sites for CO_2 adsorption are lost in the fluorinated models [28]. This effect is similar to that deduced here from Figures 5-4 and 5-6, supporting our conclusions regarding the effect of interactions with fluorine at low pressure.

The dynamics of CO_2 in the both virgin and fluorinated samples have been also investigated theoretically by equilibrium molecular dynamics (EMD) simulations. The details of the simulation method are provided elsewhere [28]. Figure 5-9d compares the variation of activation energies with fluorination level (F/C atomic ratio) from experiments with that for the fluorine-doped and virgin SiCDC atomistic models obtained from simulation. As shown in this figure, fluorination reduces the activation energies for CO_2, for both the experiment and simulation, supporting our findings. In a DFT study Wu et al. [61] have also shown that fluorine modified porous graphene has a smaller energy barrier for CO_2 diffusion compared to the non-fluorinated graphene. However, in Figure 5-9d it can be seen that the experimental activation energies of virgin and fluorinated samples are somewhat larger than those from

simulations. The higher activation energies obtained from the experimental measurements in comparison to those from simulation indicates the presence of additional barriers not captured by the HRMC model [31]. Such difference between transport coefficient obtained from experiment and simulation have been also reported and discussed in our previous works [30, 31], and is indicative of the presence of uncharacterised structural constrictions and defects influencing long range transport barriers. Similar discrepancy between macroscopically determined transport coefficients and microscopic measurements are also reported in the literature [62-66].

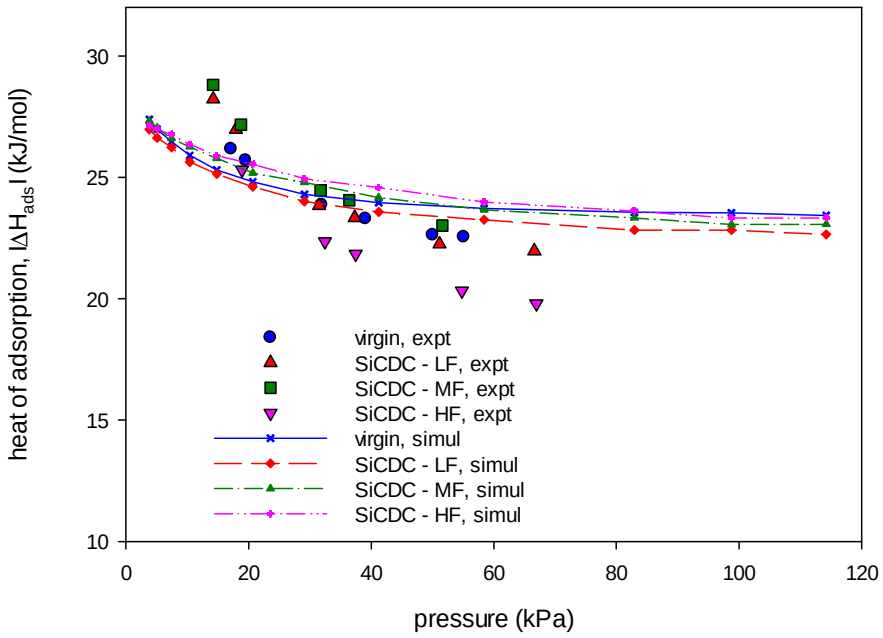

Figure 5-10. Isosteric heat of adsorption as a function of pressure for CO_2, obtained from experiment and simulation.

Figure 5-10 compares the experimental variation of isosteric heat of adsorption, with that reported from simulation using the HRMC structure [28]. It can be seen that the isosteric heat of CO_2 does not remain constant and decrease with increasing pressure at low to moderate pressures for both experiment and simulation, an indication of energetic heterogeneity in both cases. The decrease of the heat on pressure increase indicates reduction of strongly adsorbing sites on fluorinated samples, and progressive occupation of lower energy adsorption sites as pressure increases. While the trends are quite similar, the quantitative differences between the heat of adsorption obtained from the experiments and those obtained from simulation are

likely due to differences in the siting of the fluorine in the simulation compared to that realised in the experiment; this leads to structural differences in the simulation-based and experimental fluorinated carbons.

5.4 Conclusions

We have characterized the microstructure of fluorinated SiCDCs, investigating their solid structure and pore structures, using different characterization techniques. The HRTEM/ SAED images showed highly amorphous nature of the virgin and fluorinated SiCDCs. The Raman spectra of all samples also confirmed that the virgin SiCDCs and fluorinated samples have a predominantly amorphous structure with medium fluorinated sample to have fewer structural defects. The formation of C–F bonds in all fluorinated samples was seen in FTIR spectroscopy. The TGA analysis indicates higher levels of fluorination leads to more stable C–F bonds. It is shown that fluorination does not collapse the microstructure of the fluorinated SiCDCs significantly. From the PSD based on the argon adsorption, it is observed that increasing the level of fluorination for SiCDCs narrows the range of the pore size distribution. It is shown that fluorination of the SiCDCs has little effect on the ultra-microporosity of the low fluorinated sample, while higher levels of fluorination decrease the ultra-microporosity of SiCDCs significantly.

The decreases of pore volume, and surface area on fluorination is in agreement with simulation studies. Comparison of the experimental adsorption isotherms and kinetic uptake of CO_2 in fluorinated SiCDC with virgin SiCDC shows that fluorination gives rise to reduction of equilibrium uptake and cause slower CO_2 adsorption kinetics in agreement with simulation. We have shown that adsorption enthalpies obtained from fits of experimental isotherm data for CO_2 and the activation energy barriers for CO_2 diffusion decrease with increasing the level of fluorination.

5.5 Supplementary data

5.5.1 Isotherm model

The dual Henry-Langmuir isotherm equation based on the bidisperse pore size distribution of SiCDC presented in our previous work [30] is used to correlate the single component CO_2 adsorption on the samples. In the dual Henry-Langmuir isotherm the Langmuir part corresponds to the ultra-micropores in grains, and the Henry part to the larger micropores in the particle. The isotherm is

$$C_a(P) = \frac{C_{\mu m} K_L C_{be}}{1 + K_L C_{be}} + K_H C_{be} \tag{a}$$

where $C_a(P)$ and C_{be} are total adsorbed amount per unit particle volume and bulk concentration respectively, $C_{\mu m}$ is micropore capacity per unit particle volume, K_L is the Langmuirian constant, and K_H is the Henry constant. The Langmuirian and Henry constants have an exponential dependence on inverse temperature, following

$$K_L = A_\ell \exp\left(\frac{-\Delta H_\ell}{RT}\right) \tag{b}$$

$$K_H = A_h \exp\left(\frac{-\Delta H_h}{RT}\right) \tag{c}$$

where ΔH_ℓ is adsorption enthalpy for the Langmuirian part and ΔH_h is adsorption enthalpy for the Henry Law part, corresponding to the grain scale ultra-micropores and larger particle scale micropores respectively.

5.5.2 Uptake kinetics

The adsorbed concentration in the ultra-micropores follows

$$\varepsilon_\mu (1 - \varepsilon_m) C_\mu = \frac{C_{\mu m} K_L C_{\mu be}}{1 + K_L C_{\mu be}} \tag{d}$$

and the adsorbate concentration in the particle scale pores follows

$$\varepsilon_m C_m = K_H C_{mbe} \tag{e}$$

where ε_μ is microporosity of the grains, ε_m is inter-grain porosity of the particle, C_μ is adsorbed phase concentration in the grain scale ultra-micropores, C_m is adsorbate concentration in the particle scale micropores, and $C_{\mu be}$ and C_{mbe} are local pseudo-bulk gas equilibrium concentrations corresponding to the adsorbate at the grain and particle scales respectively.

The particle scale mass balance equation has the following form

$$\varepsilon_m \frac{\partial C_m}{\partial t} = -\frac{1}{R^2}\frac{\partial}{\partial R}\left(R^2 N_m\right) - \frac{3k_m}{r_g}[C_{mbe}(t,R) - C_{\mu be}(t,R,r_g)] \tag{f}$$

in which k_m is the interfacial mass transfer coefficient at the grain surface, and N_m is particle scale flux due to the larger sample spanning micropores. It is assumed that the bidisperse SiC-DC spherical particles of radius R_p, comprise spherical ultra-microporous grains of radius r_g.

This particle scale flux is expressed as

$$N_m = -\varepsilon_m D_m \frac{\partial C_m}{\partial R} \tag{g}$$

where D_m is the diffusivity in the particle scale micropores. Eq (g) has the symmetry boundary condition at the centre, $\partial C_m / \partial R = 0$ at $R = 0$, and the surface boundary condition, $C_m(t,R_P) = K_H C_b(t)/\varepsilon_m$, where the bulk gas concentration $C_b(t)$ follows the material balance

$$V_{ex}\frac{dC_b}{dt} = -\frac{3m\varepsilon_m D_m}{R_P \rho_P}\left(\frac{\partial C_m}{\partial R}\right)\Bigg|_{R=R_P} \tag{h}$$

in which V_{ex} is external volume in the sample cell, m is mass of adsorbent and ρ_P is particle density. For the spherical grains at any position in the particle, the microscale transport follows

$$\frac{\partial C_\mu}{\partial t} = \frac{1}{r^2}\frac{\partial}{\partial r}\left(r^2 D_\mu(C_\mu)\frac{\partial C_\mu}{\partial r}\right) \tag{i}$$

Eq (i) has the symmetry boundary condition $\partial C_\mu / \partial r = 0$ at $r = 0$, and the interfacial flux balance boundary condition

$$D_\mu(C_\mu)\varepsilon_\mu(1-\varepsilon_m)\left(\frac{\partial C_\mu}{\partial r}\right)_{r_g} = k_m[C_{mbe}(t,R) - C_{\mu be}(t,R,r_g)] \quad \text{(j)}$$

at the grain surface ($r = r_g$). The transient total uptake is obtained from

$$M_t(t) = \frac{M_w V_{ex}\left(C_{bo} - C_b(t)\right)}{m} \quad \text{(k)}$$

in which M_w is gas molecular weight and C_{bo} is the initial bulk gas concentration in the sample chamber.

5.5.3 X-ray photoelectron spectroscopy survey spectrum

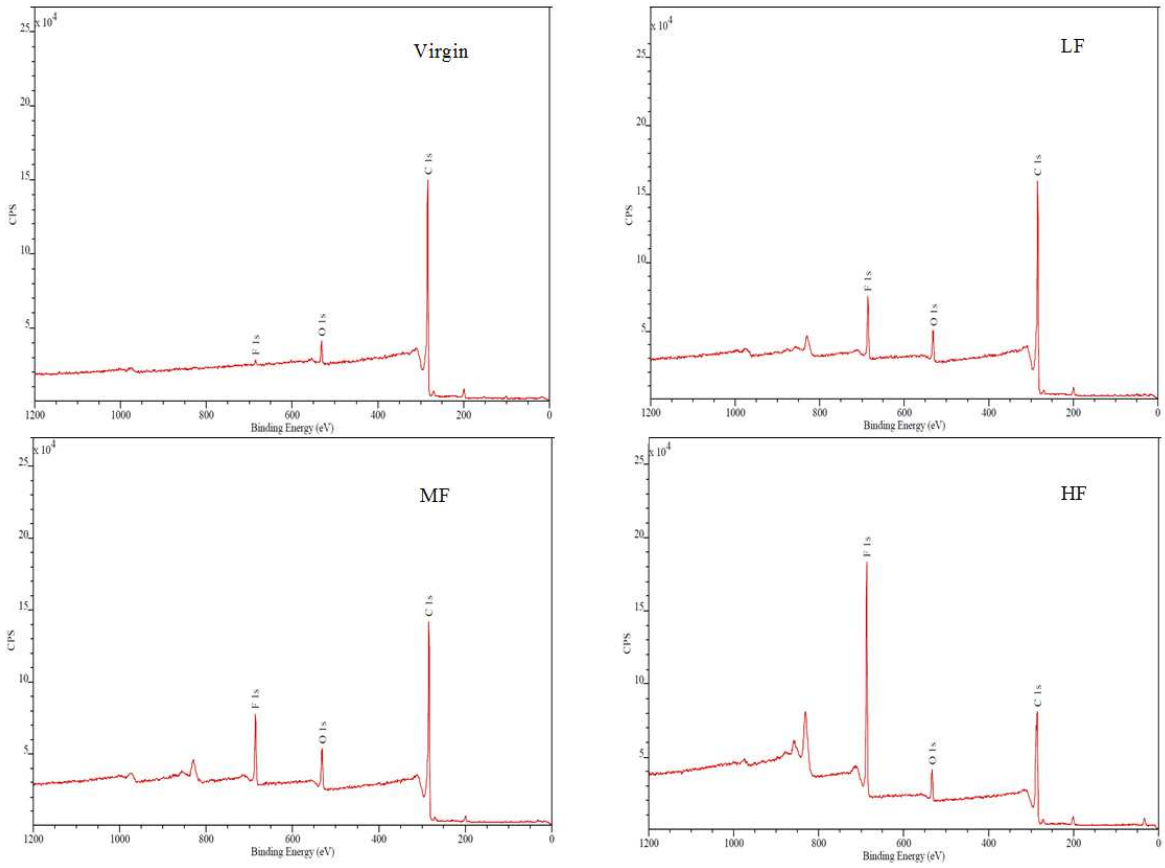

Figure S5-1. The X-ray photoelectron spectroscopy survey spectrum for the virgin and fluorinated samples.

5.5.4 HRTEM images and SAED of the virgin and the fluorinated samples

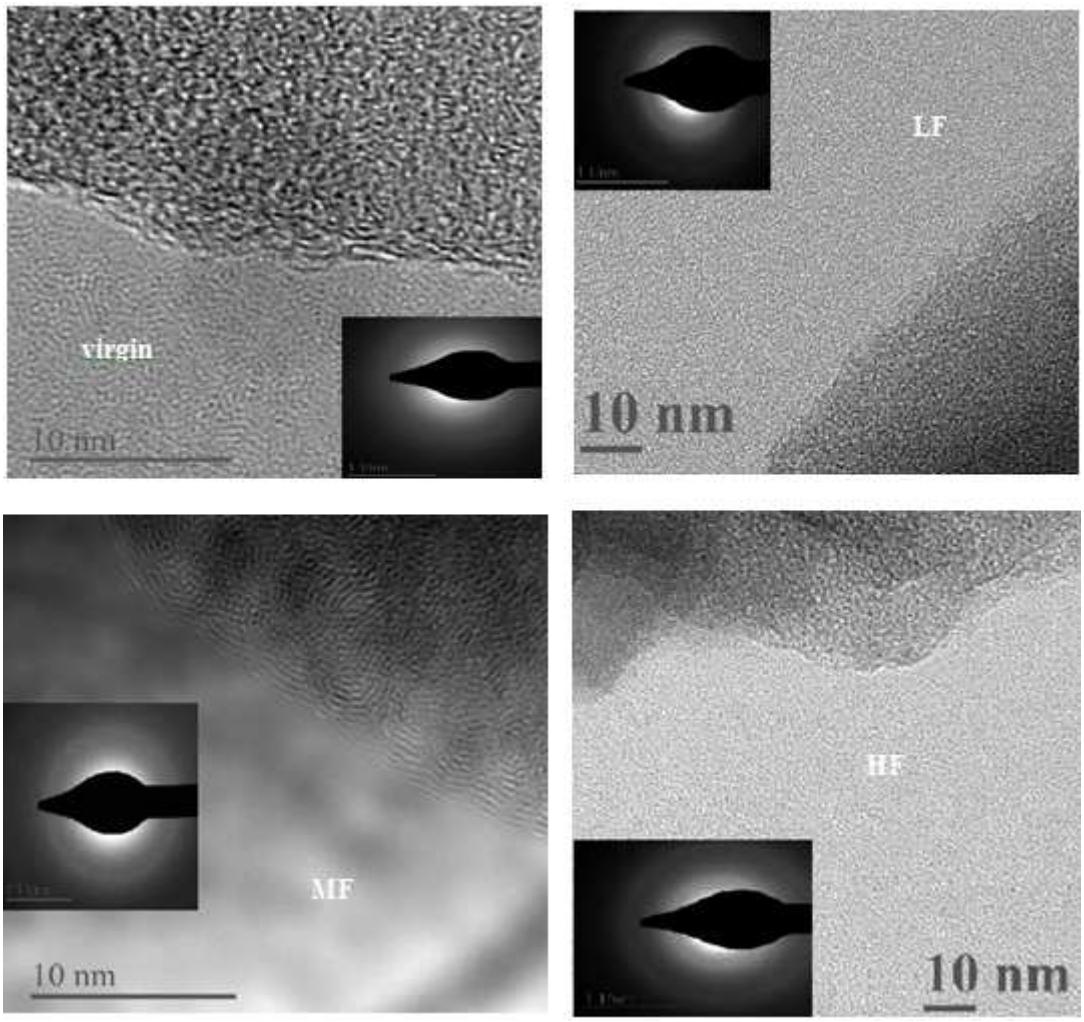

Figure S5-2. HRTEM images and SAED of the virgin and the fluorinated samples.

5.6 References

[1] Ghimbeu CM, Gadiou R, Dentzer J, Schwartz D, Vix-Guterl C. Influence of surface chemistry on the adsorption of oxygenated hydrocarbons on activated carbons. Langmuir 2010;26(24):18824-33.

[2] Hulicova D, Yamashita J, Soneda Y, Hatori H, Kodama M. Supercapacitors prepared from melamine-based carbon. Chem Mater 2005;17(5):1241-7.

[3] Song J, Xu T, Gordin ML, Zhu P, Lv D, Jiang YB, et al. Nitrogen-Doped Mesoporous Carbon Promoted Chemical Adsorption of Sulfur and Fabrication of High-Areal-Capacity Sulfur Cathode with Exceptional Cycling Stability for Lithium-Sulfur Batteries. Adv Funct Mater 2014;24(9):1243-50.

[4] Vijayaraj M, Gadiou R, Anselme K, Ghimbeu C, Vix-Guterl C, Orikasa H, et al. The influence of surface chemistry and pore size on the adsorption of proteins on nanostructured carbon materials. Adv Funct Mater 2010;20(15):2489-99.

[5] Sansotera M, Navarrini W, Resnati G, Metrangolo P, Famulari A, Bianchi CL, et al. Preparation and characterization of superhydrophobic conductive fluorinated carbon blacks. Carbon 2010;48(15):4382-90.

[6] Nakajima T. Fluorine-carbon and Fluoride-carbon Materials: Marcel Dekker; 1994.

[7] Fulvio PF, Brown SS, Adcock J, Mayes RT, Guo B, Sun X-G, et al. Low-temperature fluorination of soft-templated mesoporous carbons for a high-power lithium/carbon fluoride battery. Chem Mater 2011;23(20):4420-7.

[8] Raymundo-Piñero E, Cadek M, Beguin F. Tuning carbon materials for supercapacitors by direct pyrolysis of seaweeds. Adv Funct Mater 2009;19(7):1032-9.

[9] Frackowiak E, Lota G, Machnikowski J, Vix-Guterl C, Béguin F. Optimisation of supercapacitors using carbons with controlled nanotexture and nitrogen content. Electrochim Acta 2006;51(11):2209-14.

[10] Xia Y, Zhu Y, Tang Y. Preparation of sulfur-doped microporous carbons for the storage of hydrogen and carbon dioxide. Carbon 2012;50(15):5543-53.

[11] Wohlgemuth S-A, White RJ, Willinger M-G, Titirici M-M, Antonietti M. A one-pot hydrothermal synthesis of sulfur and nitrogen doped carbon aerogels with enhanced electrocatalytic activity in the oxygen reduction reaction. Green Chem 2012;14(5):1515-23.

[12] Lee Y-S. Syntheses and properties of fluorinated carbon materials. J Fluorine Chem 2007;128(4):392-403.

[13] Touhara H, Okino F. Property control of carbon materials by fluorination. Carbon 2000;38(2):241-67.

[14] Ghimbeu CM, Guerin K, Dubois M, Hajjar-Garreau S, Vix-Guterl C. Insights on the reactivity of ordered porous carbons exposed to different fluorinating agents and conditions. Carbon 2015;84:567-83.

[15] Jung M-J, Jeong E, Kim S, Lee SI, Yoo J-S, Lee Y-S. Fluorination effect of activated carbon electrodes on the electrochemical performance of electric double layer capacitors. J Fluorine Chem 2011;132(12):1127-33.

[16] Im JS, Jung MJ, Lee Y-S. Effects of fluorination modification on pore size controlled electrospun activated carbon fibers for high capacity methane storage. J Colloid Interface Sci 2009;339(1):31-5.

[17] Leroux F, Dubois M. Origin of the highly enhanced porosity of styryl LDH hybrid-type carbon replicas and study of a subsequent fluorination at low-temperature. J Mater Chem 2006;16(46):4510-20.

[18] Parmentier J, Schlienger S, Dubois M, Disa E, Masin F, Centeno TA. Structural/textural properties and water reactivity of fluorinated activated carbons. Carbon 2012;50(14):5135-47.

[19] Setoyama N, Li G, Kaneko K, Okino F, Ishikawa R, Kanda M, et al. Nitrogen adsorption on fluorinated activated carbon fiber. Adsorption 1996;2(4):293-7.

[20] Lee YS, Kim YH, Hong JS, Suh JK, Cho GJ. The adsorption properties of surface modified activated carbon fibers for hydrogen storages. Catal Today 2007;120(3):420-5.

[21] Li G, Kaneko K, Ozeki S, Okino F, Touhara H. Water rejective nature of fluorinated microporous carbon fibers. Langmuir 1995;11(3):716-7.

[22] Li G, Kaneko K, Okino F, Touhara H, Ishikawa R, Kanda M. Adsorption behavior of polar molecules in fluorinated micropores. J Colloid Interface Sci 1995;172(2):539-40.

[23] Panich A. Nuclear magnetic resonance study of fluorine–graphite intercalation compounds and graphite fluorides. Synth Met 1999;100(2):169-85.

[24] Mar M, Ahmad Y, Dubois M, Guérin K, Batisse N, Hamwi A. Dual C F bonding in fluorinated exfoliated graphite. J Fluorine Chem 2014;174:36-41.

[25] Banerjee S, Hemraj-Benny T, Wong SS. Covalent surface chemistry of single-walled carbon nanotubes. Adv Mater (Weinheim, Ger) 2005;17(1):17-29.

[26] Zhang W, Dubois M, Guérin K, Bonnet P, Kharbache H, Masin F, et al. Effect of curvature on C–F bonding in fluorinated carbons: from fullerene and derivatives to graphite. Phys Chem Chem Phys 2010;12(6):1388-98.

[27] Bhatia S, Nguyen T. Potential of silicon carbide-derived carbon for carbon capture. Ind Eng Chem Res 2011;50(17):10380-3.

[28] Farmahini AH, Sholl DS, Bhatia SK. Fluorinated carbide-derived carbon: more hydrophilic, yet apparently more hydrophobic. J Am Chem Soc 2015;137: 5969-5979.

[29] Shahtalebi A, Farmahini AH, Shukla P, Bhatia SK. Slow diffusion of methane in ultra-micropores of silicon carbide-derived carbon. Carbon 2014;77:560-76.

[30] Shahtalebi A, Shukla P, Farmahini AH, Bhatia SK. Barriers to diffusion of CO 2 in microporous carbon derived from silicon carbide. Carbon 2015;88:1-15.

[31] Farmahini AH, Shahtalebi, A., Jobic, H., Bhatia, S.K. Influence of Structural Heterogeneity on Diffusion of CH_4 and CO_2 in Silicon Carbide-Derived Nanoporous Carbon. J Phys Chem C 2014;118:11784−11798.

[32] Kaneko K, Ishii C. Superhigh surface area determination of microporous solids. Colloids Surf 1992;67:203-12.

[33] Nguyen TX, Bhatia SK. Characterization of pore wall heterogeneity in nanoporous carbons using adsorption: the slit pore model revisited. J Phys Chem B 2004;108(37):14032-42.

[34] Nguyen TX, Bhatia SK. Probing the pore wall structure of nanoporous carbons using adsorption. Langmuir 2004;20(9):3532-5.

[35] Bhatia SK. Density functional theory analysis of the influence of pore wall heterogeneity on adsorption in carbons. Langmuir 2002;18(18):6845-56.

[36] Bae JS, Nguyen TX, Bhatia SK. Influence of synthesis conditions and heat treatment on the structure of Ti_3SiC_2-derived carbons. J Phys Chem C 2009;114(2):1046-56.

[37] Nguyen TX, Bae JS, Bhatia SK. Characterization and adsorption modeling of silicon carbide-derived carbons. Langmuir 2009;25(4):2121-32.

[38] Yushin G, Dash R, Jagiello J, Fischer JE, Gogotsi Y. Carbide-Derived Carbons: Effect of Pore Size on Hydrogen Uptake and Heat of Adsorption. Adv Funct Mater 2006;16(17):2288-93.

[39] Gong P, Wang Z, Wang J, Wang H, Li Z, Fan Z, et al. One-pot sonochemical preparation of fluorographene and selective tuning of its fluorine coverage. J Mater Chem 2012;22(33):16950-6.

[40] Li L, Zi F, Zheng Y. The characterization of fluorocarbon films on NiTi alloy by magnetron sputtering. Appl Surf Sci 2008;255(2):432-4.

[41] Del Cul G, Trowbridge L, Toth L, Fiedor J. Some investigations of the reaction of activated charcoal with fluorine and uranium hexafluoride. J Fluorine Chem 2000;101(1):137-48.

[42] Cronce D, Mansour A, Brown R, Beard B. SeF_4 and SF_4 Fluorination of BPL activated carbon surfaces. Carbon 1997;35(4):483-95.

[43] Dubinin M. Adsorption in micropores. J Colloid Interface Sci 1967;23(4):487-99.

[44] Sun J. Pore size distribution model derived from a modified DR equation and simulated pore filling for nitrogen adsorption at 77 K. Carbon 2002;40(7):1051-62.

[45] Mangun CL, Benak KR, Economy J, Foster KL. Surface chemistry, pore sizes and adsorption properties of activated carbon fibers and precursors treated with ammonia. Carbon 2001;39(12):1809-20.

[46] Stoeckli F, Slasli A, Hugi-Cleary D, Guillot A. The characterization of microporosity in carbons with molecular sieve effects. Microporous Mesoporous Mater 2002;51(3):197-202.

[47] Do DD. Adsorption analysis: equilibria and kinetics: Imperial College Press; 1998.

[48] Toth J. Isotherm equations for monolayer adsorption of gases on heterogeneous solid surfaces. Fundamentals of Adsorption 1984:657-65.

[49] Bae JS, Nguyen TX, Bhatia SK. Pore accessibility of Ti3SiC2-derived carbons. Carbon 2014;68:531-41.

[50] Nguyen TX, Bhatia SK. Characterization of accessible and inaccessible pores in microporous carbons by a combination of adsorption and small angle neutron scattering. Carbon 2012;50(8):3045-54.

[51] Farmahini AH, Opletal G, Bhatia SK. Hybrid Reverse Monte Carlo Modeling of Silicon Carbide-Derived Nanoporous Carbon. J Phys Chem C 2013; 117, 14081−14094.

[52] Garrido J, Linares-Solano A, Martin-Martinez J, Molina-Sabio M, Rodriguez-Reinoso F, Torregrosa R. Use of nitrogen vs. carbon dioxide in the characterization of activated carbons. Langmuir 1987;3(1):76-81.

[53] Guillot A, Stoeckli F. Reference isotherm for high pressure adsorption of CO 2 by carbons at 273 K. Carbon 2001;39(13):2059-64.

[54] Carrasco-Marin F, López-Ramón M, Moreno-Castilla C. Applicability of the Dubinin-Radushkevich equation to carbon dioxide adsorption on activated carbons. Langmuir 1993; 9(11):2758-60.

[55] Ismail I. Microporosity of a Graphitized Rayon Fabric Oxidized in Air. Carbon 1991; 29(1):119-22.

[56] Ding LP, Bhatia SK, Liu F. Kinetics of adsorption on activated carbon: application of heterogeneous vacancy solution theory. Chem Eng Sci 2002;57(18):3909-28.

[57] Prasetyo I, Do DD. Adsorption rate of methane and carbon dioxide on activated carbon by the semi-batch constant molar flow rate method. Chem Eng Sci 1998; 53(19):3459-67.

[58] Rutherford SW, Nguyen C, Coons JE, Do DD. Characterization of carbon molecular sieves using methane and carbon dioxide as adsorptive probes. Langmuir 2003;19(20):8335-42.

[59] Qinglin H, Sundaram SM, Farooq S. Revisiting transport of gases in the micropores of carbon molecular sieves. Langmuir 2003;19(2):393-405.

[60] Reid C, Thomas K. Adsorption of gases on a carbon molecular sieve used for air separation: linear adsorptives as probes for kinetic selectivity. Langmuir 1999;15(9):3206-18.

[61] Wu T, Xue Q. Fluorine-modified porous graphene as membrane for CO2/N2 separation: molecular dynamic and first-principles simulations. J Phys Chem C 2014;**118**(14):7369-7376.

[62] Rives Sb, Jobic H, Beale A, Maurin G. Diffusion of CH4, CO2, and Their Mixtures in AlPO4-5 Investigated by QENS Experiments and MD Simulations. J Phys Chem C 2013;117(26):13530-9.

[63] Jobic H. Molecular dynamics of n-pentane in NaX zeolite studied by quasi-elastic neutron scattering. Phys Chem Chem Phys 1999;1(4):525-30.

[64] Jobic H, Schmidt W, Krause CB, Kärger J. PFG NMR and QENS diffusion study of n-alkane homologues in MFI-type zeolites. Microporous Mesoporous Mater 2006;90(1):299-306.

[65] Jobic H, Theodorou DN. Quasi-elastic neutron scattering and molecular dynamics simulation as complementary techniques for studying diffusion in zeolites. Microporous Mesoporous Mater 2007;102(1):21-50.

[66] Feldhoff A, Caro J, Jobic H, Ollivier J, Krause CB, Galvosas P, et al. Intracrystalline transport resistances in nanoporous zeolite X. ChemPhysChem 2009;10(14):2429-33.

Chapter 6 : Water adsorption in fluorinated silicon carbide-derived microporous carbon

We investigate the effect of fluorine doping on hydrophobicity/hydrophilicity of microporous silicon carbide-derived carbon (SiCDC), exploring the water vapor adsorption in virgin and fluorinated samples. By the application of different semi-empirical models to the experimental water adsorption isotherms of fluorinated and non-fluorinated samples, we have analysed the effect of fluorine-doping on the adsorption mechanism. The surface chemistry of the virgin and fluorinated samples are characterized by X-ray photoelectron spectroscopy and ^{19}F nuclear magnetic resonance analysis techniques. Besides the different textural features such as surface area and pore size distribution, the virgin and fluorinated SiCDCs present distinct surface chemistries in terms of the nature and quantity of the C-F bonds. The comparison of the characterization results of the samples with model parameters is used as the methodology to understand the water adsorption mechanism in virgin and fluorinated SiCDCs. We demonstrate that with increasing the level of fluorination the hydrophobic character of the low and medium fluorinated SiCDC samples remains almost constant while the highly fluorine-doped SiCDC is less hydrophobic. We identify a pore accessibility problem for argon in the fluorine-doped SiCDCs, demonstrating that fluorine functionalisation blocks the carbon pores for the nonpolar argon molecules while allowing polar H_2O molecules to grow into clusters and migrate into the internal volume of the micropores. The findings of this study should aid understanding of the water adsorption mechanism in microporous carbons.

6.1 Introduction

The synthesis and design of adsorbents to increase hydrophobicity is crucial for industrial applications since H_2O is ubiquitous in most environments and its presence poses significant challenges in many different areas of technology such as gas separation. While gas adsorption in carbon pores has been studied extensively, our understanding regarding the adsorption of H_2O in carbon materials is still incomplete [1-4]. The presence of H_2O can lead to complex adsorption behaviour and affect the efficiency of CO_2 capture by adsorption [2, 5], as it hampers the CO_2 adsorption.

Water adsorption on microporous carbons usually has a steep uptake with a clear hysteresis at medium or high relative pressures. McBain et al. [6] associated water uptake with capillary

condensation, while in another approach, first proposed by Pierce and Smith [7] and further developed by Dubinin and Serpinsky (DS) [8, 9], it is assumed that H_2O adsorption in carbonaceous pores involves clustering around primary adsorption centres. In this phenomenological model, the adsorption of H_2O, despite the hydrophobicity of the carbon surface is believed to be due to the presence of significant numbers of adsorption centres (for example oxygen-containing centres) which have high affinity for H_2O [1, 4, 10]. The initial H_2O molecules adsorbed on these centres act as nuclei for the formation of H_2O clusters [4, 10], leading to the growth of larger hydrogen-bonded clusters. These clusters eventually connect, either along the surface or across the pore, and the bulk filling of the carbon pores occurs [9, 11, 12].

Most of the experimental studies on adsorption of H_2O by microporous carbons have shown that surface functional groups play the main role [8, 13-16], and some of these studies have investigated the role of surface groups by exposing carbon materials to controlled oxidative treatments [16, 17]. Computer simulations on H_2O adsorption have also shown the formation of clusters on primary adsorption centres, indicating the strong effect and predominant role of primary surface groups in the enhancement of the H_2O adsorption [1, 18-22]. The effect of several types of polar oxygen-containing sites (with different densities and local distributions) on the surface of the carbon has been investigated in a number of studies [19, 23, 24]. The presence and structure of water adsorbed in carbon micropores at ambient temperature have been investigated by different techniques such as X-ray diffraction [25], differential scanning calorimetry [26], and dielectric relaxation spectroscopy [26, 27]. Iiyama et al. [25] have applied an in situ X-ray diffraction technique to water confined in carbonaceous micropores showing solid-like structure for water molecular assembly at 303 K based on electron radial distribution function analysis.

Laboratory experiments on a variety of hydrophobic carbons such as activated carbon fibres (ACFs) [28], some activated carbons [29] and carbide-derived carbons (CDCs) [30, 31] have shown that H_2O isotherms on these carbons are of type V based on the IUPAC classification, and strong H_2O adsorption occurs at moderate relative pressures. Based on the DS approach [8, 9] a number of semi-empirical water adsorption models have been presented in the literature providing fundamental information about the behaviour of H_2O in porous carbons [32]. Barton et al. [11, 33] have developed equations using some empirical corrections to fit

the shapes of the isotherms and describe the experimental water adsorption on carbon. Gauden [34] has investigated the mechanism of water adsorption on carbonaceous adsorbents with high energy centres using the DS approach and the equations formulated by Barton et al. [11, 33], explaining that these models provide adequate descriptions of water adsorption isotherms only for carbons having a low concentration of primary adsorption sites. Based on the adsorption of H_2O molecules on the active sites Talu and Muenier [35] have also developed a model assuming that at low loading the behaviour of the system is solely controlled by molecule to surface vertical interactions, and at intermediate loading where the inflection point of type V isotherms occurs, the adsorbed molecules form large clusters by association via hydrogen bonding. Do and Do (DD) [36] have developed a water adsorption isotherm equation assuming a two-stage mechanism, in which at the first stage, H_2O molecules are strongly bonded to the primary sites and form clusters via hydrogen bonds. They have explained that since a single H_2O molecule does not have sufficient dispersive force to adsorb inside the micropore, a cluster of five H_2O molecules (pentamer) is necessary to produce sufficient force for water to fill micropores. Several modifications to the DD isotherm model [36] have been presented in the literature to describe water adsorption on carbon [4, 10, 17, 37]. Although the model proposed by Do et al. [4] can describe the different shapes of water adsorption isotherm in activated carbon, many physical parameters such as the size of water clusters and the equilibrium constant of water vapour in the micropores of activated carbon cannot be measured. Yao et al. [38] have developed a new model to calculate these parameters.

The doping of carbonaceous materials with heteroelements is known as an effective method to induce modifications of their hydrophilicity/hydrophobicity and water adsorption behaviour [39-43], for example the fluorine-doped carbonaceous materials have been considered as a new class of materials that may exhibit promising characteristics and properties that make them attractive not only for gas adsorption processes but also for other applications such as in supercapacitors and batteries [44-47]. In a simulation study, Farmahini et al. [41] have recently investigated the effect of fluorination on hydrophobic/hydrophilic characteristics of microporous SiCDC. They have illustrated that fluorination generates more hydrophilic carbon surfaces however they effectively act as more hydrophobic structures due to increased energy barriers resulting from the stronger adsorption. However there is no experimental report on the effect of fluorine doping on hydrophobicity/hydrophilicity of

CDCs, although studies with activated carbons have been reported [48, 49]. In our previous experimental work [50] we have studied the effect of fluorine-functionalisation of silicon carbide-derived carbon (SiCDC) on its structure as well as CO_2 adsorption. The present work contributes to the understanding of the effect of fluorination of microporous SiCDC on experimental water adsorption, to enable tuning of the hydrophobic/hydrophilic characteristics SiCDCs. The textural properties of the virgin and fluorinated samples were evaluated by Ar and CO_2 adsorption, and the surface chemistry (i.e. C–F bond nature and its quantity) is determined by ^{19}F nuclear magnetic resonance (NMR), and X-ray photoelectron spectroscopy (XPS) analysis. In order to study the interactions of H_2O with fluorine doped atoms contributing as functional groups, we apply a number of semi-empirical isotherm models whose relevance to microporous CDCs is not reported in the literature.

6.2 Methodology

6.2.1 SiCDC synthesis and fluorine doping

SiCDCs were prepared in our laboratory by chlorination of commercial micron-sized SiC powders provided by Alfa Aesar as described previously in detail in our previous work [51]. The temperature that was used for the SiCDC synthesis was 1073 K. Three different fluorine-doped SiCDCs denoted LF (Low Fluorinated), MF (Medium Fluorinated), and HF (High Fluorinated) were prepared by solid-gas reaction for a fluorination time of 10 min, 20 min and 60 min respectively. Before fluorination the samples were initially outgassed overnight in the oven under primary vacuum at 393 K in order to eliminate physisorbed molecules on the carbon surface or entrapped in the pores. A passivated nickel reactor covered with NiF_2 is used for the fluorination of SiCDC. After outgassing, the oven temperature was cooled to the room temperature, and the samples were subjected to the mixed gaseous atmosphere having various F/N_2 ratios for the required duration. Gaseous molecular fluorine purchased from Solvay Fluor (purity 98–99% V/V with HF maximum 0.5% V/V and other gases, primarily O_2/N_2 at approximately 0.5% V/V) was used in the fluorination method. Once the fluorination was completed, nitrogen purge started to replace the residual molecular fluorine. A detailed study of the effect of fluorine-functionalisation of silicon carbide-derived carbon on its structure and morphologies as well as CO_2 adsorption has been presented in our recent publication [50]. Different techniques including high-resolution TEM, Fourier transform infrared (FTIR), Raman spectroscopy, and Thermogravimetric analysis (TGA) techniques

were used for the structural characterization of virgin and fluorinated samples in our previous work [50]. In the previous work we have presented the Ar adsorption isotherms at 87 K and CO_2 adsorption at 273 K. For each sample, the textural properties including surface area, pore volumes, and pore size distributions, were extracted from the experimental Ar and CO_2 isotherms by applying the appropriate density functional theory (DFT) algorithms and Dubinin-Radushkevich (DR) equations. Table 6-1 provides some of these sample characterization data.

It is noted that fluorination was conducted in the laboratory at Institut de Chimie de Clermont-Ferrand, Université Blaise Pascal, France.

Table 6-1. Textural characteristics of virgin and fluorinated samples obtained using DFT [50].

Sample	Argon		CO_2	
	Pore volume (cm^3/g)	Surface area (m^2/g)	Pore volume (cm^3/g)	Surface area (m^2/g)
virgin	0.519	1527.3	0.236	1955
LF	0.367	1118.5	0.205	1754
MF	0.241	642.4	0.172	1402
HF	0.164	401.9	0.091	854

6.2.2 X-ray photoelectron spectroscopy (XPS)

The X-ray Photoelectron Spectroscopy (XPS) analysis was performed with a VG Scientific Escalab 220iXL X-ray photoelectron spectrometer equipped with a monochromatized AlKα (1253.6eV) source. Some details on the XPS are also presented in our previous work [50]. The survey spectra were used to determine the atomic content of carbon, oxygen and fluorine on the material surface. The data analysis was done using Casa XPS software.

6.2.3 NMR experiments

NMR experiments were performed at room temperature using a Bruker Avance spectrometer with working frequency of 282.2 MHz for ^{19}F. A magic-angle spinning (MAS) probe (Bruker) operating with a 4 mm rotor was used. For MAS spectra, a simple sequence was performed with a single $\pi/2$ pulse length of 4.0 µs. ^{19}F chemical shifts were referenced to CF_3COOH.

6.2.4 Water adsorption experiments

The experimental water adsorption and desorption isotherms at 303 K were obtained using a volumetric adsorption apparatus (Micromeritics ASAP2020). The samples were degassed at 473 K prior to the analysis. After the samples were cooled to ambient temperature, the degassed sample cell was transferred to the adsorption port of the analysis section of the instrument and isotherm measurements were conducted.

6.2.5 Water adsorption isotherm models

Here, we report the application of the Dubinin-Serpinsky (DS) equation [9], the equation proposed by Barton et al. [11, 33], and the model proposed by Talu and Meunier [35] to the water adsorption isotherms measured for virgin and fluorinated SiCDC samples. Following is a brief description of these models and equations.

The DS equation is still widely applied for the explanation of the mechanism of water adsorption on carbonaceous materials due to its simplicity [32] while considering the key mechanism of water clustering around primary surface groups. The original DS which applies only up to the relative pressures where the upswing of the isotherm begins, is presented as

DS-1: $$c_\mu = \frac{a_0 ch}{1 - ch} \tag{6-1}$$

where a_0 (mmol/g) is the surface concentration of the primary adsorption centres (i.e., hydrophilic functional groups), h is the relative pressure (P/P_0), where P and P_0 are the equilibrium and saturation pressure respectively, c_μ (mmol/g) is the amount of adsorbed water at a specific P/P_0, and c (unit-less) is the ratio of the rate constants describing the kinetics of adsorption and desorption. DS-1 is improved assuming further adsorption causes the creation of water clusters at larger relative pressures and this process decreases the number of secondary adsorption sites, however the initial stages of water adsorption mechanism on the carbonaceous material are similar to DS-1 model [11, 32]. This model denoted as DS-2, is implicit in form, following

DS-2: $$h = \frac{c_\mu}{c(a_0 + c_\mu)(1 - kc_\mu)} \tag{6-2}$$

where k (g/mmol) is a constant involved in decreasing active site concentration. This parameter represents the loss of the secondary adsorption sites. Parameters c, a_0, and k are fitting parameters. In the derivation of the above equation, the term $(1-kc_\mu)$ is introduced to take into account the decrease in the number of adsorption sites with increasing adsorption. However, it is shown that the DS-2 equation does not predict satisfactorily the final parts of water adsorption isotherms measured for largely microporous carbons [11, 33]. Subsequently, Barton et al. [33] proposed the empirical isotherm

$$\text{BEM:} \qquad h = \frac{c_\mu}{ca_0 + cc_\mu(1-\exp[-k^2(c_\mu - a_c)^2])} \tag{6-3}$$

which appears to perform better than DS-2 model. The BEM equation is obtained by introducing the term $(1 - \exp[-k^2(c_\mu - a_c)^2])$, and a fourth parameter, a_c. Barton et al. [11, 33] have suggested that the parameters k and a_c serve to trigger the start of the decline in adsorptive power, and k governs the rate of this decline with increasing adsorption. Barton et al. [33] have shown that the values of a_c are all larger than those of saturation adsorption, a_s, at p/p_0=1, not assigning any physical meaning to a_c [32, 33]. Gauden [34] suggests that this parameter (a_c) represents the total hypothetical number of adsorbed water molecules equal to or greater than a_s, needed to saturate all possible secondary and primary adsorption centres for the ideal arrangement of water molecules.

In this work we have also applied the proposed model by Talu and Meunier [35] to the water adsorption isotherms measured for virgin and fluorine-doped SiCDC samples to investigate the water adsorption mechanism. Talu and Meunier [35] have suggested a semi-empirical model based on the association theory of water molecules in micropores which considers the creation of clusters of water molecules on the adsorbent surface. This model is expressed by the equations

$$\text{Talu-Meunier:} \qquad P = \frac{H_0\psi}{1+K\psi}\exp\left(\frac{\psi}{N_m}\right) \tag{6-4}$$

where

$$\psi = \frac{-1+(1+4K\xi)^{1/2}}{2K} \tag{6-5}$$

$$\xi = \frac{N_m N}{N_m - N} \tag{6-6}$$

where H_0 is the inverse of the Henry's law constant, K is a parameter related to the equilibrium constant for the cluster formation in micropores, N_m is the saturation capacity of the pore, and N is the amount of adsorbed water in the unit of mmol/g at pressure P [35]. Talu and Meunier [35] state that their association theory is not strictly a homogeneous surface model even though a single equation of state (Volmer EOS) is used. However they explain that in this theory the surface provides primary adsorption sites where the vertical interaction is a single value appearing in the Henry's law constant similar to homogeneous models, in contrast to heterogeneous systems where the adsorption potential is a Boltzmann weighted statistical average. The clustering mechanism in the association theory provides an infinite number of different energy sites for guest molecules. The energy released by adsorption of a molecule is the sum of two contributions: (i) The single vertical interaction value divided by the cluster size, and (ii) The energy of reaction. Since different size clusters each occupy a single site, the adsorption potential can take infinite values from the Henry's law value to zero [35]. Talu and Meunier [35] have used water adsorption on activated carbon to test this theory and have reported good fits. McCallum et al. [19] have successfully used this theory to describe the local water adsorption isotherms obtained from the computer simulation for various pore widths. Mowla et al. [52] have also presented the results of comparison of this model with experimental data for different types of activated carbons.

6.3 Results and discussion

6.3.1 Surface chemistry and physicochemical characterization

Understanding the hydrophobicity/hydrophilicity of fluorine-doped carbons requires fundamental knowledge of the nature and the amount of surface functional groups, as these will influence the interactions with the molecules. Fluorine-doped carbon can possess different types of C–F bonds including semi-ionic, weakened covalent CF_x, and CF covalent bonds [49]. Here the characterization of the surface chemical compositions of the virgin and fluorinated samples was studied by XPS analysis. For the fluorinated sample, complementary

analyses regarding the F/C atomic ratio were also performed, considering the weight uptake during the TGA experiments. In previous work we have shown the XPS survey spectrum for the virgin and fluorinated sample and discussed the TGA experiments [50]. As expected, the peaks of F1s confirmed the presence of fluorine atoms in the fluorinated samples, and the peak intensities increased with fluorination level. Table 6-2 lists the atomic ratio of each element on the surface of the virgin and fluorinated samples. The surface carbon concentration of the samples decreases after fluorination, whereas the fluorine content increases from 5.53% for SiCDC-LF to 7.48% and 22.46% for SiCDC-MF and SiCDC-HF, respectively. It can be also seen that the F/C atomic ratio of the samples increases significantly for the more highly fluorinated sample. In addition, the O1s peaks of the fluorinated SiCDCs slightly increases with the increase in the fluorination level, however the O1s peak of high fluorinated SiCDC decreases on fluorination.

Table 6-2. XPS surface elemental analysis of virgin and fluorinated samples.

Samples	C1s	O1s	F1s	O1s/ C1s	F1s/ C1s
	atomic percent (%At)	atomic percent (%At)	atomic percent (%At)	(atomic ratio)	(atomic ratio)
virgin	96.90	3.10	-	0.0320	-
SiCDC - LF	89.56	4.91	5.53	0.0548	0.0617
SiCDC - MF	85.80	6.72	7.48	0.0783	0.0872
SiCDC - HF	73.08	4.46	22.46	0.0610	0.3073

The changes in the chemical bonds of the SiCDCs after fluorination were also studied by C1s spectra deconvolution, and the results along with the peak assignments are reported in Table 6-3. Figure 6-1 shows the XPS C1s spectra of the fluorinated samples at different levels of fluorination. In the C1s spectra of the samples, different types of carbon-fluorine bonds are observed, including semi-ionic C---F, weakened covalent C--F, covalent C-F, and CF_2. It is

observed that the amount of the weakened covalent C---F bonds increase in more highly fluorinated samples, while the amount of semi-ionic bondings in these samples decreases. The F1s peaks were also investigated and the variation in the F1s peaks corresponded well with the variation of the C1s peaks on fluorination. The XPS F1s spectra of the fluorinated confirmed that the weakened covalent carbon-fluorine bonds were more dominant when the fluorination level increased.

Table 6-3. Binding energy, assignments, and composition of fluorinated bonds from C1s peak.

Binding energy (eV)	**Assignment**	**Concentration of fluorinated functions (%)**		
		SiCDC - LF	**SiCDC - MF**	**SiCDC - HF**
287.9	semi-ionic C---F	34.4	28.2	13.5
288.6	weakened covalent C--F	35.2	31.1	77.8
290.1	C-F	20.8	26.4	7.0
291.5	CF_2	9.6	14.3	1.7

MAS-NMR spectroscopy on ^{19}F nucleus was also used to identify the various fluorinated groups and the nature of C-F bonds for the LF, MF and HF samples. Deconvolution of the NMR spectra, as shown in Figure 6-2, led to identification of the different covalence of carbon-fluorine bonds and relative contents in the bulk material. The CF_3 and CF_2 groups correspond to the -5 ppm line and -45 ppm broad line respectively. These shifts are likely to appear in case of decomposition. The content of CF_3 groups were in limit of detection (<1%) while CF_2 content strongly increased from 3% for LF sample to 29% for the MF sample. Main functions were C-F; two covalent bonds are found and can explain the broadness of the spectra. The weakened covalent C-F and covalent CF represented by -74 and -135 ppm bands respectively. Ghimbeu et al. [43] indicated -190 ppm/$CFCl_3$ ie -115 ppm/CF_3COOH line as the most covalent bond. This synthesis enabled to obtain strongest bond. Semi-ionic bond

were in high content, up to 70% with no significant evolution. It has been observed that the covalent C-F decreases from 32% to 1% with increase in the fluorination level. Such drop is also observed in the XPS analysis (Table 6-3). Furthermore it is also simultaneous to the increase of the CF_2 groups. Thus, it is likely that covalent C-F bonds are converted to CF_2 groups similar to the observations from the XPS analysis, as both techniques are sensitive to surface groups. Therefore strengthening of the C-F bonds is important in the surface, and bulk functions are mainly semi-ionic, and CF_2 groups are originating from the covalent C-F bonds.

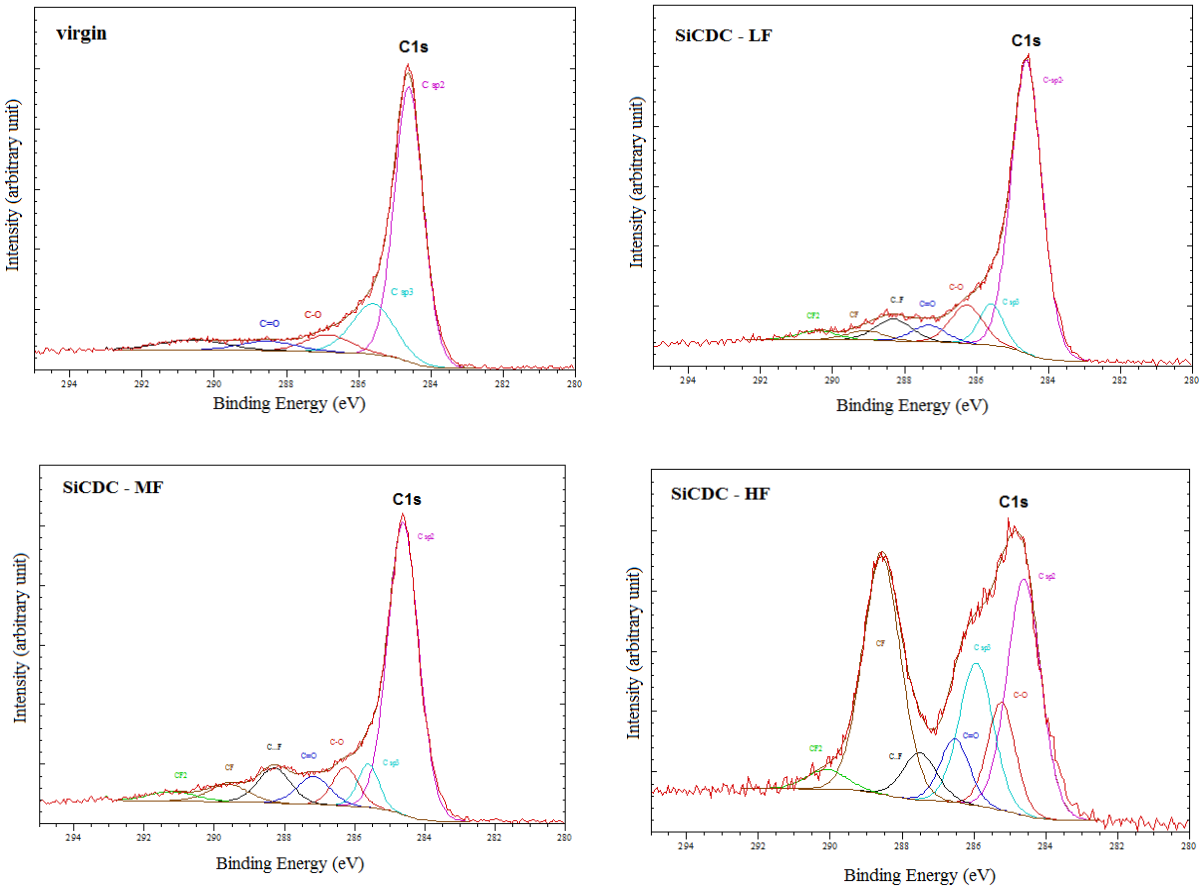

Figure 6-1. XPS C1s curve fit spectra for virgin and fluorinated samples.

6.3.2 Influence of fluorination on microporosity

The textural properties of the materials were assessed using the experimental adsorption equilibrium of argon at 87 K and CO_2 at different temperatures for the virgin and fluorinated samples. The details of the influence of fluorination on the textural properties of the samples have been presented in our previous work [50]. The argon and CO_2 adsorption isotherms keep the same shape, however show lower adsorption capacity of argon and CO_2 in the

fluorine-doped SiCDC samples, compared to virgin sample [50]. This has an impact on the textural properties (pore volume and surface area).

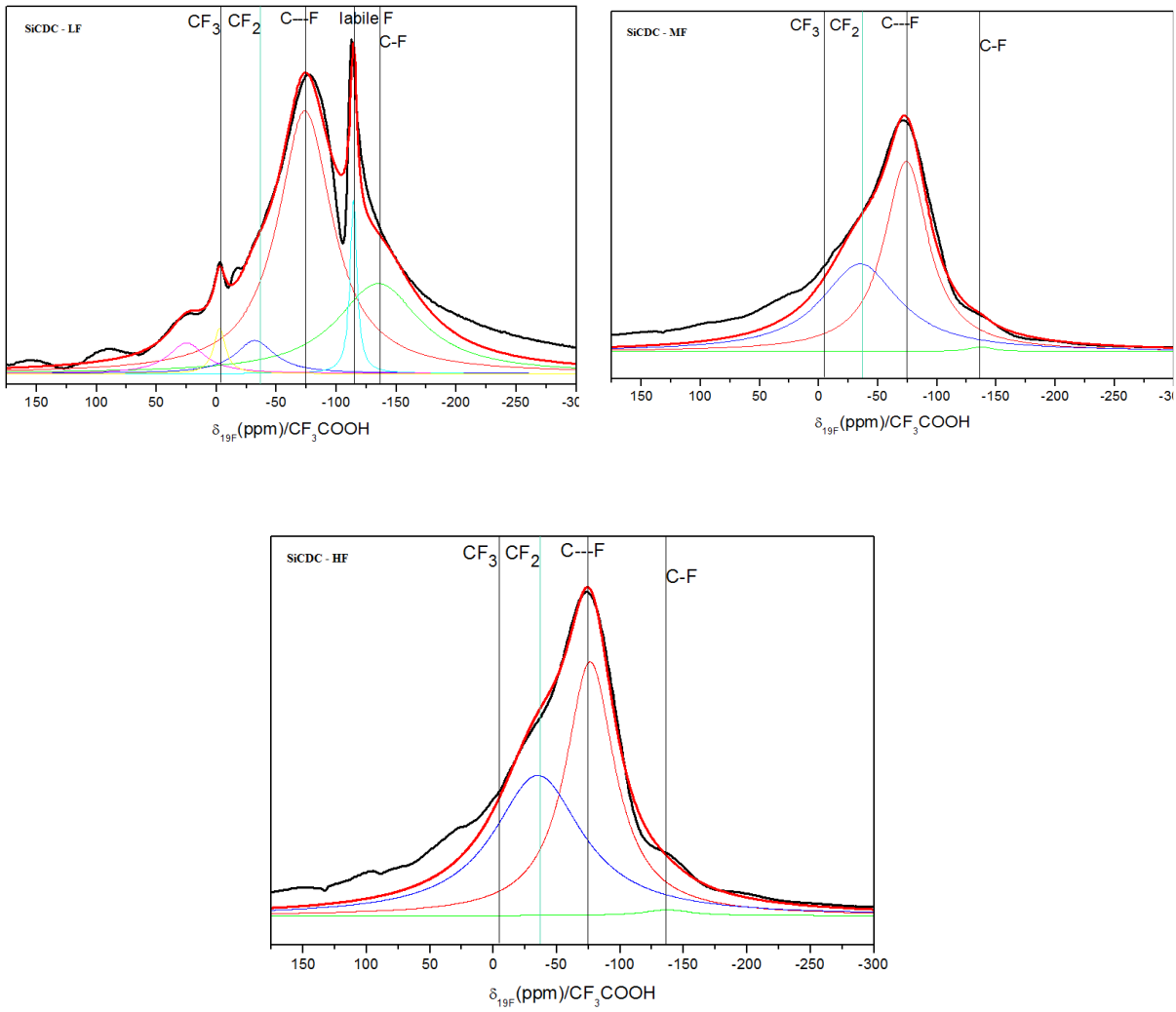

Figure 6-2. 19F MAS NMR spectra of the fluorinated SiCDCs.

We determined the micropore volume, surface area, and pore size distribution (PSD) of the samples with the aid of density functional theory (DFT). Our studies have shown that increasing fluorination level leads to decreasing specific surface area and total pore volume. In Figure 6-3, the PSD of the samples obtained from argon and CO_2 adsorption isotherms using density functional theory (DFT) is presented. As can be seen in Figure 6-3, the porosity based on the argon adsorption isotherms comprises pores in the range of 0.4–1.5 nm. Further, the microporous nature of carbon is preserved after fluorination. The inset in Figure 6-3 illustrates the presence of the ultra-micropores, whose presence in SiCDC has also been shown and discussed in our previous works [50, 51, 53]. From the PSD based on the argon

adsorption, it is observed that increasing the level of fluorination for SiCDCs narrows the range of the pore size distribution. It is seen that fluorination of the SiCDCs has little effect on the ultra-microporosity of the low fluorinated sample, while higher levels of fluorination decrease the ultra-microporosity of SiCDCs significantly. The surface areas obtained from the CO_2 isotherm are larger than those determined from argon adsorption, indicative of some inaccessibility of Ar possibly related to ultra-micropores [50]. Due to the limitation of the DFT model for the fluorinated samples which considers only carbon-gas interactions, the textural properties of the virgin and fluorinated SiCDCs were further evaluated by the analysis of the argon and CO_2 isotherm by the Dubinin–Radushkevich (DR) approach in our previous work [50]. Nevertheless, despite the abovementioned weakness of the DFT method, it was found that the values of the surface area and pore volume obtained from the DR equation were close to the values obtained by the DFT method, with similar trend for both virgin and fluorinated SiCDCs.

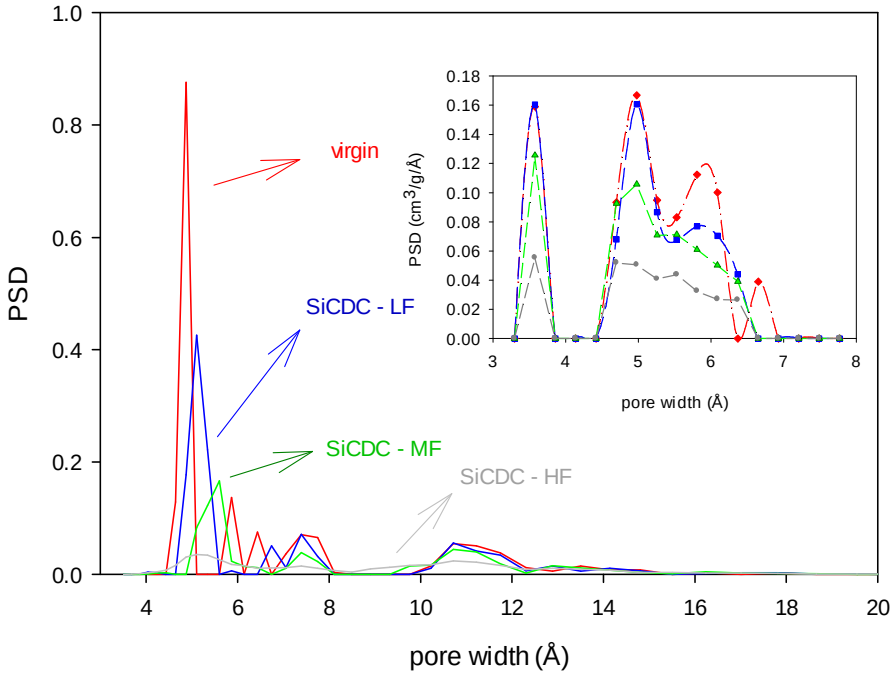

Figure 6-3. Argon and CO_2 (inset) based PSD of the virgin and fluorinated SiCDC samples [50].

6.3.3 Water adsorption isotherms and their modelling

Both water adsorption and desorption isotherms were measured for the virgin and fluorinated samples. The isotherms of the virgin and fluorinated samples which are shown in Figure 6-4

are of type V which is typical of microporous materials having low affinity for water. The adsorption isotherm of the virgin sample has a steep rise at relative pressures around 0.5, while the isotherm of fluorinated samples rises near relative pressures of 0.2, and the water uptake is steeper for the fluorinated samples compared to the virgin sample at low relative pressures.

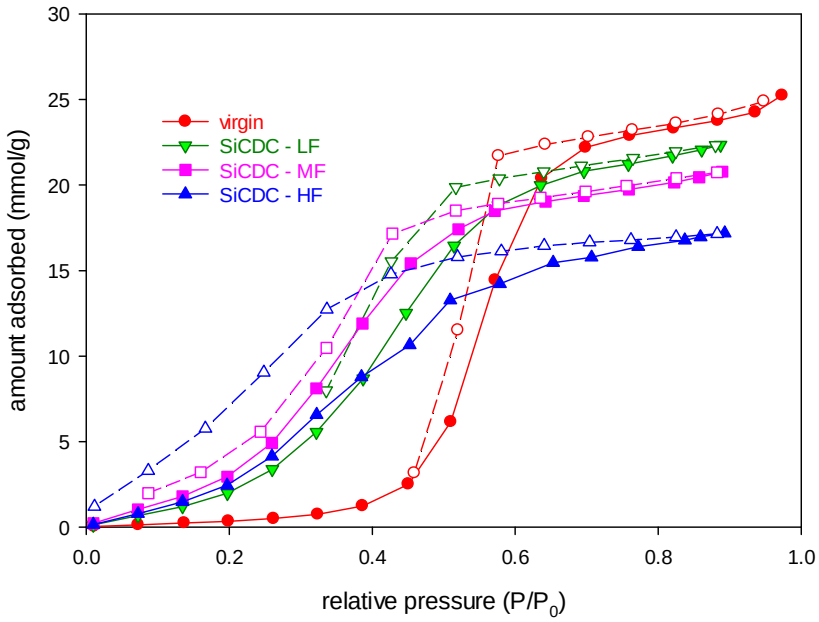

Figure 6-4. Experimental adsorption/desorption isotherms of water vapor at 303 K on the virgin and fluorinated samples.

To extract meaningful fundamental information about the water adsorption behaviour, some of the isotherm models available in the literature including the DS equations, the BEM model, and the Talu-Meunier model (association theory) reviewed above are fitted to the experimental water adsorption isotherms measured for virgin and fluorinated SiCDCs. The fit to the experimental data is presented in Figure 6-5 as continuous lines. The fitting parameters for each sample are provided in Table 6-4. The parameters a_0 and c are common to DS and BEM models, in which a_0 is the fitting parameter that can be related to the physical properties and the amount of the oxygen-containing adsorption sites of the samples, while c essentially represents adsorption equilibrium constant.

Table 6-4. Fitting parameters obtained using different models for virgin and fluorinated samples.

Model	Parameters	Virgin	SiCDC-LF	SiCDC-MF	SiCDC-HF
DS-1	a_0 *(mmol/g)*	1.086476	5.177257	6.594458	6.489505
	c	1.626421	1.587558	1.672236	1.507419
DS-2	a_0 *(mmol/g)*	0.355698	1.151342	1.03740	1.429344
	c	2.350311	3.526905	4.75492	3.755808
	k (g/mmol)	0.021208	0.030553	0.03711	0.041824
	a_s *(mmol/g)*	27.34814	23.87713	21.54163	18.01155
BEM	a_0 *(mmol/g)*	0.647607	4.266056	5.870931	5.682993
	c	1.751096	1.703755	1.777466	1.598379
	k (g/mmol)	0.096161	0.128947	0.151618	0.139593
	a_c *(mmol/g)*	34.40585	28.45941	24.97401	22.03722
	a_s *(mmol/g)*	25.17325	22.91005	21.15343	17.71723
Talu-Meunier	N_m	26.62415	24.67927	22.88964	19.72678
	H_0	5.703109	1.074774	0.671891	0.73091
	K	2.239971	0.569971	0.410719	0.397227

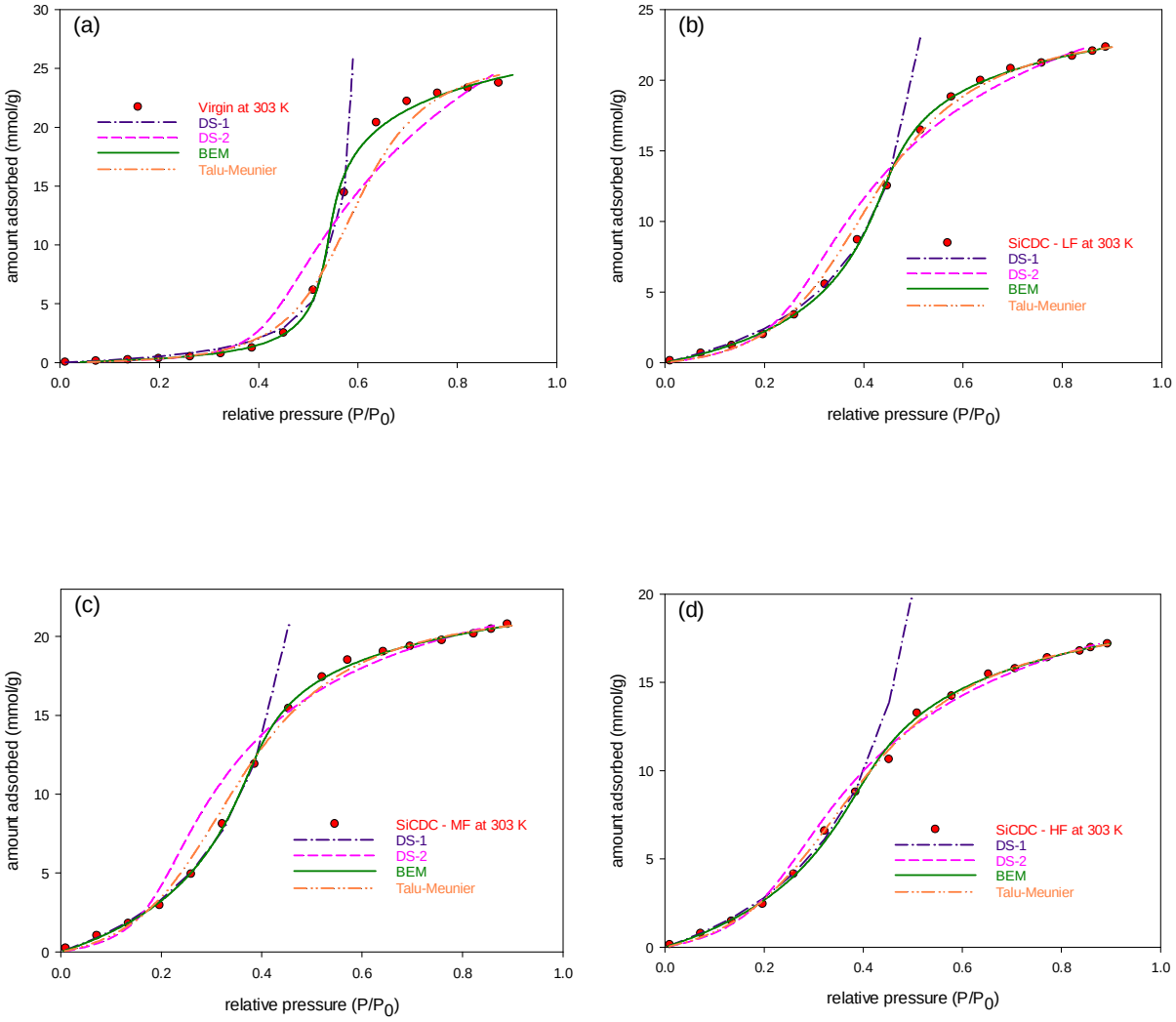

Figure 6-5. Fit of different (lines) to experimental adsorption isotherms of water vapor at 303 K for the virgin and fluorinated samples.

The higher amount adsorbed of H_2O at low relative pressures in the fluorine-doped samples may be correlated with the a_0 values in these samples obtained from data modelling and presented in Table 6-4. This suggests increase in oxygen-containing adsorption sites in the fluorinated samples, in which the amount of these oxygen-containing adsorption sites control the relative pressures at which water adsorption starts. The minimal uptake of water at low relative pressures is also evident from the low values of a_0 obtained from the DS and BEM models presented in Table 6-4 indicating low surface concentration of the primary adsorption centres. It is apparent that DS-1, as is well known, is applicable only for the initial part of the isotherm upswing, which corresponds to relative pressure of up to 0.5 for the virgin SiCDC

and for fluorine-doped SiCDCs up to around 0.3, however the application of DS-2 model gives better correlation over the entire pressure range, but is still less satisfactory for all samples, particularly for the virgin sample. In all cases, there appears to be an overestimation form the DS-2 model during the first part of the steeply rising portion of the isotherm and an underestimation for the latter portion.

The association theory of Talu and Meunier [35] has been also implemented to investigate the water adsorption isotherms. The fitted isotherms based on the Equation 6-4 (solid lines in Figure 6-5) fit the measured water isotherms for MF and HF samples reasonably well, with the parameters listed in Table 6-4, however the fit is not satisfactory for the virgin and LF samples. The low H_0 and K values for the fluorine-doped samples compared to virgin sample suggest that the fluorine-doped SiCDCs have higher affinity for water molecules. Although these parameters can be loosely connected to surface properties of the samples, they are implicitly related to the shape of the isotherm, such as the pore filling pressure and the steepness of the isotherm [54].

We observe that the BEM model produces a very satisfactory fit for all virgin and fluorinated SiCDC samples, over the entire pressure range. The relevant isotherm parameters pertaining to Figure 6-5 are given in Table 6-4. Here, the trends in the values of a_0 and a_s, are compared with the sample characterization results from XPS analysis and the argon adsorption at 87 K respectively. It can be seen that the value of a_0 increases with the level of fluorination, however for SiCDC-MF, it is larger compared to SiCDC-LF and SiCDC-HF samples. This is consistent with our observations in XPS analysis in which the oxygen content and O/C atomic ratio for SiCDC-MF sample are larger compared to other samples (The atomic ratio of oxygen to carbon atoms (O/C) obtained from XPS is presented in Table 6-2). As shown in Figure 6-6(a) where the a_0 values are plotted against (O/C) atomic ratio, the a_0 values obtained from DS-1, DS-2 and BEM models are reasonably close for small amounts of surface oxygen but deviate greatly for the high values of O/C atomic ratio. It can be seen that at the high values of O/C atomic ratio, the a_0 values are almost constant which might be due to the oxygen-saturated surfaces in which as oxygen is increased, the oxygen-containing primary sites become close to each other and the neighbour sites act as one site, and therefore the a_0 values remain almost constant. An interesting aspect of the results in Table 6-4 is that the values of the equilibrium constant at a site, c, are essentially constant, except for a slight

drop for the HF sample, supporting the above argument of a_0 representing the concentration of primary sites. The Henry's law constant based on the BEM equation was also calculated and it was observed that at C_μ=0, $\left[\mathrm{dC}_\mu / \mathrm{dh}\right]_{C\mu=0}$, which is equal to the product of c and a_0, is highest for the MF sample, exceeding that for the LF and HF samples. This is due to the largest amount of oxygen-containing adsorption sites in MF sample as shown in XPS analysis causing stronger solid-fluid interactions.

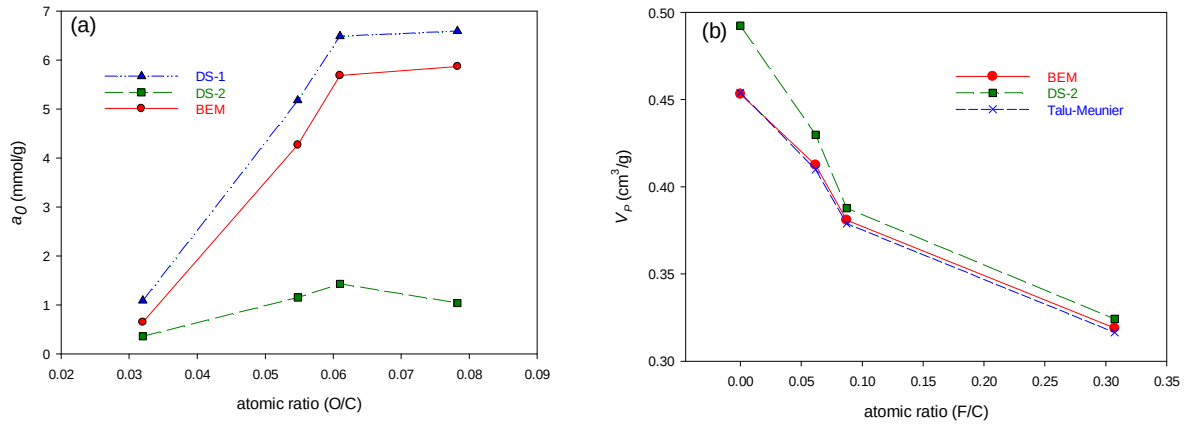

Figure 6-6. (a) Variation of a_0 values with (O/C) atomic ratio, dependency on isotherm analysis, and (b) variation of water-based pore volume of virgin and fluorine-doped samples with (F/C) atomic ratio.

It is noticed that for all of the fluorine-doped SiCDC samples, the saturation adsorption capacity is larger than the pore volume obtained from the argon adsorption isotherms irrespective of the isotherm model. The saturation water adsorption capacity (at P/P_0 = 1) was determined based on the DS-2 and BEM isotherm model parameters, and is given in Table 6-4. Assuming that $\rho_{H_2O} = 1\ \mathrm{g/cm^3}$, the water-based pore volume of the samples was determined from different models. The variation of the water-based pore volume of virgin and fluorine-doped samples with (F/C) atomic ratio is shown Figure 6-6(b). It is observed that, the water-based pore volumes based on the both DS-2, Talu-Meunier and BEM models are larger than the micropore volumes determined based on the argon adsorption (Table 6-1) for the fluorine-doped samples, indicating a pore accessibility problem for argon at 87 K, and that the fluorine-doped SiCDCs have lower pore accessibility for argon at 87 K compared to H_2O at 303 K. Inaccessibility of the internal pore structure for argon at low temperature in fluorine-doped SiCDCs is most probably because the surface functional groups for the

fluorinated samples block the pores for an electrically neutral argon molecule but allow polar H_2O molecules to grow into clusters and migrate into the internal volume of the pores. Webster et al. [55] have reported two smallest minimum molecular dimensions of H_2O molecule along the symmetry axes as 2.9 and 3.2 Å respectively which are smaller than argon size (3.4 Å). This is indicative of the accessibility of H_2O to the pores through the pore necks smaller than 3.4 Å in size which are responsible for the argon inaccessibility. It is also observed that there is a relation between the increasing fluorination level and argon accessibility, in which the difference between the water-based and argon-based pore volume for high fluorinated SiCDC-HF is larger than LF and MF samples. This indicates that HF sample has the least argon accessibility possibly due to the presence of more pore necks in the HF sample that are smaller than 3.4 Å.

6.3.4 Effect of fluorination on the hydrophobicity of SiCDCs

In order to investigate the effect of fluorine-doping on hydrophobicity/hydrophilicity of the SiCDC samples, we have calculated the value of d^2C_μ/dh^2 per site at C_μ=0 based on the BEM equation as follows

$$\frac{1}{a_0}[\mathrm{d}^2C_\mu/\mathrm{d}h^2]_{C_\mu=0} = 2c^2(1-\exp(-k^2a_c^2)) \tag{6-7}$$

which indicates that $[d^2C_\mu/dh^2]/a_0 > 0$ for all samples and equal to 6.13, 5.81, 6.32, and 5.11 for the virgin, SiCDC-LF, SiCDC-MF, and SiCDC-HF respectively. This behaviour indicates that hydrophobic character of the virgin, low and medium fluorinated SiCDC samples does not change significantly and remains almost constant after fluorination, while the decrease in the value of $[d^2C_\mu/dh^2]/a_0$ at C_μ=0 for SiCDC-HF is a clear indication of decrease in the hydrophobicity of the high fluorine-doped SiCDC sample. This behaviour is probably due to the negligible effect of fluorine at low (6.2%) and medium (8.7%) levels of fluorination while at high level fluorination of 30.7%, the effect of fluorine is more prominent which reduces the hydrophobicity. The decreased hydrophobic character of HF sample is also consistent with the XPS and NMR analysis observation in which strong C-F covalent bonds decrease in HF sample while weakened covalent C–F bonds significantly increase. Parmentier et al. [49] have argued that the weakened covalent C–F bonds react with water during their contact with water and are converted into C–OH groups. However Li et al. [48], who have reported

fundamentally different isotherms for the fluorinated microporous carbon fibers suggest fluorination can donate perfect hydrophobicity to the carbonaceous microporous system in which fluorinated carbon micropores repel water almost completely without formation of water clusters. While the nature of the C-F bonding in their experiments is not discussed by Li et al. [48], we may speculate that the increased hydrophobicity in their experiments is due to increase in strong C-F bonds.

We have also plotted the pore volume and surface area-normalised isotherms of H_2O at 303 K, based on the structural properties obtained from argon adsorption to investigate the effect of fluorine-water and fluid-fluid interactions in the fluorine-doped and virgin SiCDC samples. Figure 6-7a and b show that the normalised isotherms differ from each other, with the fluorine-doped isotherms shifting to higher adsorbed value compared to the virgin samples, and adsorption branch of the virgin sample is below the branches of those fluorine-doped samples. Further, it would appear that the adsorbed volume at high relative pressure is higher than the pore volume of the fluorinated samples measured by argon adsorption. This implies that fluorine functional groups in fluorinated samples block the pores in the SiCDC sample for argon molecules while allowing H_2O molecules to grow into clusters as discussed in section 6.3.3. Due to the pore accessibility problem of argon, the water-based pore volume normalised isotherms of H_2O at 303 K are also presented in Figure 6-8.

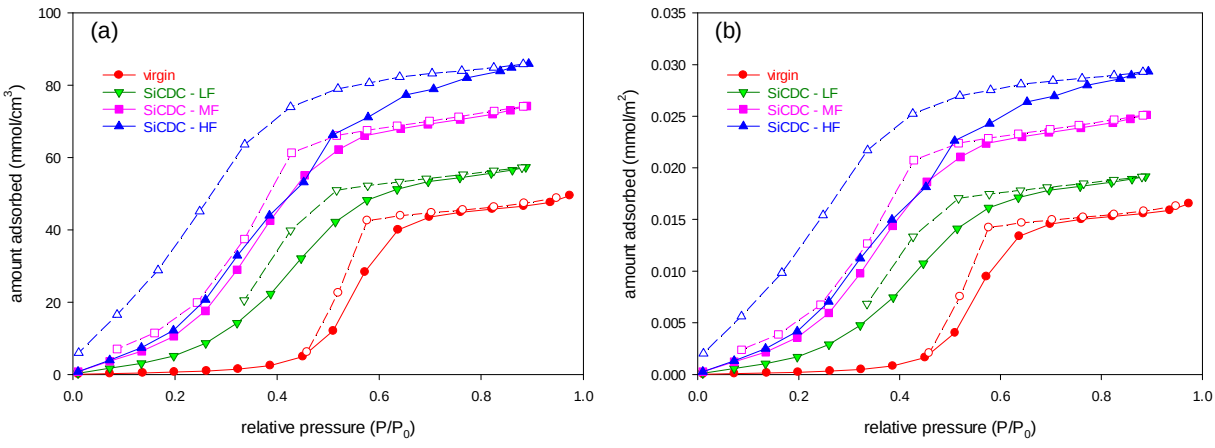

Figure 6-7. Experimental adsorption/desorption isotherms of water vapor at 303 K normalised by argon-based (a) pore volume, and (b) surface area on virgin and fluorinated samples.

It can be seen in Figure 6-8 that the isotherms are overlapping at high relative pressures as expected, since at high pressures the water density (used as basis for calculating the water-based pore volume) is approached. On the other hand, at low relative pressures the adsorbed amount of water is higher in fluorine-doped samples compared to the virgin SiCDC sample, which indicates the increase of the fluorine-water and fluid-fluid interactions in fluorine-doped SiCDC samples as fluorination level increases which shifts the water amount adsorbed in the normalised isotherms to higher adsorbed amount of H_2O. The increase of the fluorine-water and fluid-fluid interactions is also evident from the desorption branch of the fluorinated SiCDC samples which displays higher water uptake than the virgin sample in the low relative pressure regions. The desorption branches show hysteresis due to the strong hydrogen bonds formed between the water molecules. The change of the shape of water adsorption hysteresis reflects the variation of the surface chemistry and composition of the carbon pores as discussed in XPS and NMR analysis. Although all samples show remarkable hysteresis, as seen in Figures 6-4 and 6-8, the desorption equilibrium of fluorinated samples exhibit higher water content than virgin sample and the width of the hysteresis loops increases with increasing level of fluorination. Parmentier et al. [49] have also noted such hysteresis for water adsorption on virgin and fluorinated carbons, showing lower water adsorption on fluorinated samples, indicative of increased hydrophobicity, but higher adsorption on desorption branch, indicating increased hydrophilicity.

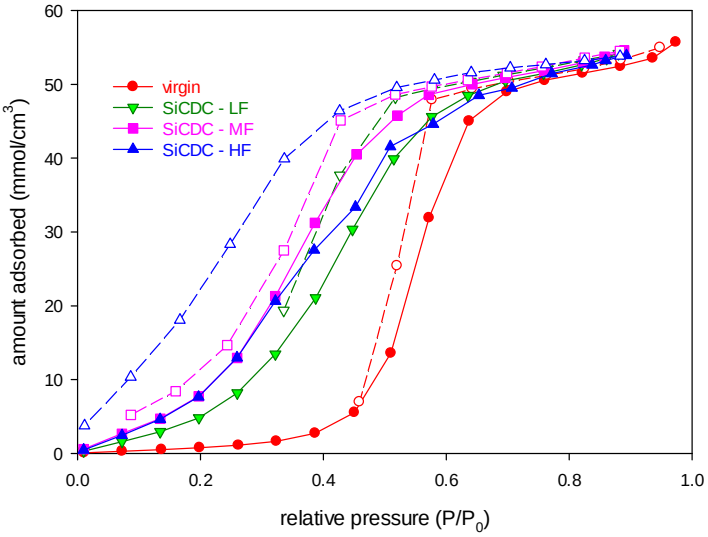

Figure 6-8. Experimental adsorption/desorption isotherms of water vapor at 303 K normalised by water-based pore volume.

6.3.5 Comparison with simulation

In the recent work from this group [41], the atomistic models of fluorine-doped SiCDC at three different levels of fluorination with F/C atomic ratios of 0.019, 0.053, and 0.1 were developed based on a hybrid reverse Monte Carlo (HRMC) constructed model of SiCDC [56]. The details of the atomistic models of fluorinated SiCDCs are provided elsewhere [41]. In our previous work [50], it was shown that although both experiment and simulation show similar decreasing trends for the variation of pore volume and surface area with increasing fluorination level, the experimental values of pore volume and surface area were considerably lower than those predicted by the simulations, suggesting that the siting of the fluorine in the simulation differs from that attained in the experiment.

Here we compare the water-based simulation results with our experimental findings to demonstrate the effect of fluorination on water vapor adsorption. Farmahini et al. [41] have shown that for the virgin sample the pore filling process does not start until the pressure is at the experimental saturation pressure (P/P_0 <1.0), while in our study we have seen a sudden increase of water adsorption in the experimental virgin SiCDC. This pattern in our experimental results is similar to the GCMC simulations for the activated carbons in which it is shown a pore filling mechanism gives rise to the amount of water adsorbed at medium relative pressure [28, 57]. Nguyen and Bhatia [1] have also reported the same pattern for the activated carbon fibre (ACF-15) model, however Farmahini and Bhatia [58] have demonstrated that in the absence of activated sites, pore filling of amorphous SiCDC and activated carbon fibre does not occur until pressure exceeds the saturation pressure. Therefore the steep water uptake at medium relative pressure in our experimental virgin SiCDC might be due to the existence of significant numbers of oxygen-primary adsorption sites which act as nuclei for the formation of H_2O cluster. These oxygen-containing sites also shown in the XPS analysis encourage the growth of the water clusters leading to the carbon pore filling. In simulation works from Brennan et al. [24] and Liu and Monson [59], it is also shown that H_2O adsorption is strongly enhanced in the presence of activated surface sites.

In the Farmahini et al. [41] work, their GCMC simulations have also shown that fluorination significantly enhances water uptake and the amount of H_2O adsorbed in the fluorine-doped increases with the level of fluorination, consistent with our observation of enhancement of water uptake for low relative pressures. However they have observed that for the highly

fluorinated SiCDC sample, $d^2C_\mu/dh^2 < 0$ at low relative pressures an indication of hydrophilicity while in our experiments $d^2C_\mu/dh^2 > 0$ for virgin and all of the fluorine-doped samples at low relative pressures and the hydrophobicity is almost constant for LF and MF samples. Experimental results also show larger amount of adsorbed H_2O compared to the simulations for the fluorine-doped SiCDCs while the experimental values of argon-based pore volume and surface area are considerably lower than those predicted by the simulations. This might be due to the differences in SiCDC model constructed by simulation and experimentally synthesized SiCDC and fluorine-doped samples, and the difference in the siting of the fluorine in simulation and experiment. The lower argon-based pore volume in experimental samples compared to those obtained from simulation also suggests the accessibility problem for argon in the experimental virgin and fluorine-doped samples. The larger amount of adsorbed H_2O in experiment compared to the simulation is due to the presence of oxygen-primary sites in experimental samples leading to the pore-filling below the saturation pressure while in SiCDC model constructed by simulation pore-filling does not occur below the saturation pressure.

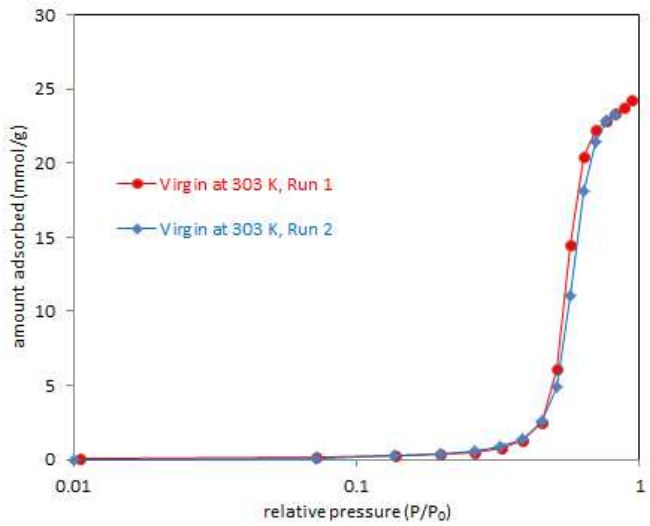

Figure 6-9. Experimental reproducibility runs for water vapor at 303 K.

As a test of the reproducibility of the experimental data, some of the experimental runs were repeated and the reproducibility of the data were checked. As an example, in Figure 6-9, two different runs on virgin sample at 303 K are shown. We did not observe significant differences in the reproducibility runs and the experimental data were repeatable.

6.4 Summary and conclusions

To show the role of fluorine doping on the adsorption behaviour and the hydrophilic/hydrophobic character of the synthesized silicon carbide-derived carbon, we successfully fluorinated the synthesized SiCDC samples at three different level at room temperature. The XPS and NMR analysis confirmed that different C-F bonds were created irrespective of the fluorination level showing that strong covalent C-F bonds decrease on fluorination while C-F bonds with weakened covalence increase. Water adsorption isotherms are volumetrically measured on fluorinated and virgin SiCDC samples. The hydrophilic/hydrophobic nature of the fluorinated SiCDC has been evaluated by water adsorption and compared with the virgin SiCDC. It is found that the amount of water adsorbed is directly related to the fluorination level. The weakening of the hydrophobic character of the high fluorinated samples is evidenced by calculating the value of d^2C_μ/dh^2 at C_μ=0 which is lower than the values obtained for the LF and MF samples supporting the presence of the more hydrophilic surface groups, and the prominent effect of fluorine in HF sample. The decreased hydrophobicity in highly fluorinated sample were attributed to the decreased amount of strong C–F bonds on fluorination along with the increase of C-F bonds with weakened covalence, as observed in the XPS and NMR analysis. It appears that in the pore volume and surface area-normalised isotherms, the fluorine-doped isotherms shift to higher adsorbed value compared to the virgin samples and adsorption/desorption branch of the virgin sample is always below the branches of those fluorinated samples. The findings from this research support the recent molecular simulation studies of water adsorption in virgin and fluorinated SiCDCs presented from this group [41]. We have applied different semi-empirical model equations to the water adsorption isotherms of virgin and fluorinated SiCDCs that were originally developed to interpret the adsorption isotherms of water on porous carbonaceous materials. We conclude that the modified BEM model equation proposed by Barton et al. [33] is one of the most suitable equations for the water adsorption on the virgin and fluorinated SiCDCs. It was noticed that for the fluorinated SiCDCs, irrespective of the isotherm model, the water-based pore volumes are larger than the pore volumes obtained based on the argon adsorption. This is likely due to the blockage of fluorine functional groups for nonpolar argon molecules while allowing H_2O molecules to grow into clusters in the internal volume of the pores. Further, it is shown that increasing fluorination level gives rise to the pore accessibility problem of argon at 87 K. The adsorption isotherms

of water on virgin and fluorine-doped SiCDCs have shown perceptible adsorption hysteresis, in which the desorption on fluorinated samples exhibit higher amount of water, and the width of the hysteresis loops increase with increasing the level of fluorination due to the variation of the surface composition of carbonaceous pores.

6.5 References

[1] Nguyen TX, Bhatia SK. How Water Adsorbs in Hydrophobic Nanospaces. The Journal of Physical Chemistry C. 2011;115(33):16606-12.

[2] Bhatia S, Nguyen T. Potential of silicon carbide-derived carbon for carbon capture. Ind Eng Chem Res. 2011;50(17):10380-3.

[3] Ohba T, Kanoh H, Kaneko K. Affinity transformation from hydrophilicity to hydrophobicity of water molecules on the basis of adsorption of water in graphitic nanopores. J Am Chem Soc. 2004;126(5):1560-2.

[4] Do D, Junpirom S, Do H. A new adsorption–desorption model for water adsorption in activated carbon. Carbon. 2009;47(6):1466-73.

[5] Webley PA. Adsorption technology for CO2 separation and capture: a perspective. Adsorption. 2014;20(2-3):225-31.

[6] McBain JW, Porter J, Sessions R. The nature of the sorption of water by charcoal. J Am Chem Soc. 1933;55(6):2294-304.

[7] Pierce C, Smith RN. The Adsorption–Desorption Hysteresis in Relation to Capillarity of Adsorbents. The Journal of Physical Chemistry. 1950;54(6):784-94.

[8] Dubinin M. Water vapor adsorption and the microporous structures of carbonaceous adsorbents. Carbon. 1980;18(5):355-64.

[9] Dubinin M, Serpinsky V. Isotherm equation for water vapor adsorption by microporous carbonaceous adsorbents. Carbon. 1981;19(5):402-3.

[10] Horikawa T, Sekida T, Hayashi Ji, Katoh M, Do DD. A new adsorption–desorption model for water adsorption in porous carbons. Carbon. 2011;49(2):416-24.

[11] Barton SS, Evans MJ, MacDonald JA. The adsorption of water vapor by porous carbon. Carbon. 1991;29(8):1099-105.

[12] Tao Y, Muramatsu H, Endo M, Kaneko K. Evidence of Water Adsorption in Hydrophobic Nanospaces of Highly Pure Double-Walled Carbon Nanotubes. J Am Chem Soc. 2010;132(4):1214-5.

[13] Gregg SJ, Sing KSW. Adsorption, Surface Area and Porosity. Academic New York 1982.

[14] Bradley R, Rand B. On the physical adsorption of vapors by microporous carbons. J Colloid Interface Sci. 1995;169(1):168-76.

[15] Vartapetyan RS, Voloshchuk AbM. The mechanism of the adsorption of water molecules on carbon adsorbents. Russ Chem Rev. 1995;64(11):985.

[16] Alcañiz-Monge J, Linares-Solano A, Rand B. Water adsorption on activated carbons: study of water adsorption in micro-and mesopores. The Journal of Physical Chemistry B. 2001;105(33):7998-8006.

[17] Horikawa T, Sakao N, Sekida T, Hayashi Ji, Do D, Katoh M. Preparation of nitrogen-doped porous carbon by ammonia gas treatment and the effects of N-doping on water adsorption. Carbon. 2012;50(5):1833-42.

[18] Müller EA, Gubbins KE. Molecular simulation study of hydrophilic and hydrophobic behavior of activated carbon surfaces. Carbon. 1998;36(10):1433-8.

[19] McCallum C, Bandosz T, McGrother S, Müller E, Gubbins K. A molecular model for adsorption of water on activated carbon: comparison of simulation and experiment. Langmuir. 1999;15(2):533-44.

[20] Hummer G, Rasaiah JC, Noworyta JP. Water conduction through the hydrophobic channel of a carbon nanotube. Nature. 2001;414(6860):188-90.

[21] Slasli A, Jorge M, Stoeckli F, Seaton N. Water adsorption by activated carbons in relation to their microporous structure. Carbon. 2003;41(3):479-86.

[22] Striolo A, Chialvo AA, Cummings PT, Gubbins KE. Water adsorption in carbon-slit nanopores. Langmuir. 2003;19(20):8583-91.

[23] Jorge M, Schumacher C, Seaton NA. Simulation study of the effect of the chemical heterogeneity of activated carbon on water adsorption. Langmuir. 2002;18(24):9296-306.

[24] Brennan JK, Thomson KT, Gubbins KE. Adsorption of water in activated carbons: effects of pore blocking and connectivity. Langmuir. 2002;18(14):5438-47.

[25] Iiyama T, Nishikawa K, Suzuki T, Kaneko K. Study of the structure of a water molecular assembly in a hydrophobic nanospace at low temperature with in situ X-ray diffraction. Chem Phys Lett. 1997;274(1):152-8.

[26] Sliwinska-Bartkowiak M, Dudziak G, Sikorski R, Gras R, Gubbins K, Radhakrishnan R. Dielectric studies of freezing behavior in porous materials: Water and methanol in activated carbon fibres. Phys Chem Chem Phys. 2001;3(7):1179-84.

[27] Sanfelix PC, Holloway S, Kolasinski K, Darling G. The structure of water on the (0001) surface of graphite. Surf Sci. 2003;532:166-72.

[28] Kimura T, Kanoh H, Kanda T, Ohkubo T, Hattori Y, Higaonna Y, et al. Cluster-associated filling of water in hydrophobic carbon micropores. The Journal of Physical Chemistry B. 2004;108(37):14043-8.

[29] Lodewyckx P. The effect of water uptake in ultramicropores on the adsorption of water vapour in activated carbon. Carbon. 2010;48(9):2549-53.

[30] Kockrick E, Schrage C, Borchardt L, Klein N, Rose M, Senkovska I, et al. Ordered mesoporous carbide derived carbons for high pressure gas storage. Carbon. 2010;48(6):1707-17.

[31] Rose M, Kockrick E, Senkovska I, Kaskel S. High surface area carbide-derived carbon fibers produced by electrospinning of polycarbosilane precursors. Carbon. 2010;48(2):403-7.

[32] Furmaniak S, Gauden PA, Terzyk AP, Rychlicki G. Water adsorption on carbons—Critical review of the most popular analytical approaches. Adv Colloid Interface Sci. 2008;137(2):82-143.

[33] Barton S, Evans M, MacDonald J. An equation describing water vapour absorption on porous carbon. Carbon. 1992;30(1):123-4.

[34] Gauden PA. Does the Dubinin–Serpinsky theory adequately describe water adsorption on adsorbents with high-energy centers? J Colloid Interface Sci. 2005;282(2):249-60.

[35] Talu O, Meunier F. Adsorption of associating molecules in micropores and application to water on carbon. AIChE J. 1996;42(3):809-19.

[36] Do D, Do H. A model for water adsorption in activated carbon. Carbon. 2000;38(5):767-73.

[37] Neitsch M, Heschel W, Suckow M. Water vapor adsorption by activated carbon: a modification to the isotherm model of Do and Do. Carbon. 2001;39(9):1437-8.

[38] Yao X, Li L, Li H, He S, Liu Z, Ma W. A new model for calculating the adsorption equilibrium constant of water vapor in micropores of activated carbon. Computational Materials Science. 2014;89:137-41.

[39] Lee Y-S. Syntheses and properties of fluorinated carbon materials. J Fluorine Chem. 2007;128(4):392-403.

[40] Touhara H, Okino F. Property control of carbon materials by fluorination. Carbon. 2000;38(2):241-67.

[41] Farmahini AH, Sholl DS, Bhatia SK. Fluorinated carbide-derived carbon: more hydrophilic, yet apparently more hydrophobic. J Am Chem Soc 2015;137: 5969-5979.

[42] Ghimbeu CM, Gadiou R, Dentzer J, Schwartz D, Vix-Guterl C. Influence of surface chemistry on the adsorption of oxygenated hydrocarbons on activated carbons. Langmuir. 2010;26(24):18824-33.

[43] Ghimbeu CM, Guerin K, Dubois M, Hajjar-Garreau S, Vix-Guterl C. Insights on the reactivity of ordered porous carbons exposed to different fluorinating agents and conditions. Carbon. 2015;84:567-83.

[44] Im JS, Jung MJ, Lee Y-S. Effects of fluorination modification on pore size controlled electrospun activated carbon fibers for high capacity methane storage. J Colloid Interface Sci. 2009;339(1):31-5.

[45] Leroux F, Dubois M. Origin of the highly enhanced porosity of styryl LDH hybrid-type carbon replicas and study of a subsequent fluorination at low-temperature. J Mater Chem. 2006;16(46):4510-20.

[46] Jung M-J, Jeong E, Kim S, Lee SI, Yoo J-S, Lee Y-S. Fluorination effect of activated carbon electrodes on the electrochemical performance of electric double layer capacitors. J Fluorine Chem. 2011;132(12):1127-33.

[47] Fulvio PF, Brown SS, Adcock J, Mayes RT, Guo B, Sun X-G, et al. Low-temperature fluorination of soft-templated mesoporous carbons for a high-power lithium/carbon fluoride battery. Chem Mater. 2011;23(20):4420-7.

[48] Li G, Kaneko K, Ozeki S, Okino F, Touhara H. Water rejective nature of fluorinated microporous carbon fibers. Langmuir. 1995;11(3):716-7.

[49] Parmentier J, Schlienger S, Dubois M, Disa E, Masin F, Centeno TA. Structural/textural properties and water reactivity of fluorinated activated carbons. Carbon. 2012;50(14):5135-47.

[50] Shahtalebi A, Mar M, Guérin K, Bhatia SK. Effect of fluorine doping on structure and CO 2 adsorption in silicon carbide-derived carbon. Carbon. 2016;96:565-77.

[51] Shahtalebi A, Farmahini AH, Shukla P, Bhatia SK. Slow diffusion of methane in ultra-micropores of silicon carbide-derived carbon. Carbon. 2014;77:560-76.

[52] Mowla D, Do D, Kaneko K. Adsorption of water vapor on activated carbon: a brief overview. Chem Phys Carbon. 2003;28:229-.

[53] Shahtalebi A, Shukla P, Farmahini AH, Bhatia SK. Barriers to diffusion of CO 2 in microporous carbon derived from silicon carbide. Carbon. 2015;88:1-15.

[54] Wang H-J, Kleinhammes A, McNicholas TP, Liu J, Wu Y. Water adsorption in nanoporous carbon characterized by in situ NMR: measurements of pore size and pore size distribution. The Journal of Physical Chemistry C. 2014;118(16):8474-80.

[55] Webster CE, Drago RS, Zerner MC. Molecular dimensions for adsorptives. J Am Chem Soc. 1998;120(22):5509-16.

[56] Farmahini AH, Opletal G, Bhatia SK. Hybrid Reverse Monte Carlo Modeling of Silicon Carbide-Derived Nanoporous Carbon. J Phys Chem C 2013; 117, 14081−14094.

[57] Brennan JK, Bandosz TJ, Thomson KT, Gubbins KE. Water in porous carbons. Colloids Surf A Physicochem Eng Asp. 2001;187:539-68.

[58] Farmahini AH, Bhatia SK. Differences in the adsorption and diffusion behaviour of water and non-polar gases in nanoporous carbon: role of cooperative effects of pore confinement and hydrogen bonding. Mol Simul. 2015;41(5-6):432-45.

[59] Liu J-C, Monson P. Monte Carlo simulation study of water adsorption in activated carbon. Ind Eng Chem Res. 2006;45(16):5649-56.

Chapter 7 : Conclusions and Recommendations

7.1 Conclusions

In this thesis the adsorption behaviour of CH_4 and CO_2 on carbide-derived carbons and the effect of fluorine-doping on the hydrophilicity/hydrophobicity and water vapor adsorption were investigated both experimentally and theoretically.

In Chapter 2, the literature concerning the characterisations of the carbide-derived carbons (CDCs), the adsorption equilibrium and kinetics on the porous materials, the experimental techniques for the adsorption equilibrium and kinetics measurements, and water adsorption on carbonaceous materials were reviewed.

In Chapter 3 and 4, the microstructure characterizations of the SiC-DC samples synthesized at 1073 K using different analysis techniques were presented. The HRTEM images have shown the existence of grains in the highly amorphous structure of synthesized SiC-DC particles. The XRD and Raman spectra have confirmed the amorphous nature of SiC-DCs. The CO_2 adsorption at 273 K has shown the presence of significant ultra-microporosity while such ultra-microporosity is not observed in characterisations based on the argon adsorption at 87 K. The FWT-NLDFT approach and structural data (pore size and pore wall thickness distributions) obtained from interpreting experimental sub-atmospheric adsorption isotherms of argon at 87 K were used to predict the low pressure CO_2 isotherm at 273 K and high pressure adsorption isotherms of CH_4 at 313 and 333 K in the SiC-DC. It is shown that FWT-NLDFT model satisfactorily predicts all experimental data, however for sub-atmospheric CO_2 adsorption at 273 K, under-prediction is observed at very low pressure indicating that the synthesized SiC-DC has lower pore accessibility for argon at 87 K at low pressures compared to CO_2 at 273 K.

Adsorption kinetics has been studied at different temperature over a wide range of loading, and interpreted by a bidisperse structure model for the SiC-DC assuming that ultra-micropores have topologically connected networks in small independent grains, with the larger micropores forming the inter-granular space as particle-scale pathways. A dual Langmuir–Henry adsorption isotherm has been found to fit the equilibrium adsorption data for CH_4 and CO_2 at different temperatures and up to atmospheric pressure very well, consistent with the bididpserse structure model. In this bidisperse pore structure model, it is considered that the Langmuirian part of the isotherm corresponds to the adsorption in the

grains, and the Henry law part corresponds to the diffusion at the particle scale in the larger micropores. This model is found to correlate experimental data for transient uptake kinetics of CH_4 in SiC-DC, more satisfactorily than alternative micropore diffusion models involving only one diffusional length scale. For CO_2, it is found that the adsorption kinetics is strongly influenced by a barrier resistance at the grain surface, and the uptake of CO_2 occurs through a rapid diffusion in the large particle-scale micropores, and a combination of barrier resistance at the grain surface and diffusional resistance in the grain interior. It is shown that the extracted micropore and ultra-micropore transport parameters, and barrier mass transfer coefficients have strong dependence on temperature and loading, and follow Arrhenius law in the studied temperature range. The activation energies for the diffusion of CH_4 and CO_2 in the grains are comparable to literature results for carbon molecular sieves, in agreement with our model considering the grains to be ultra-microporous. It is also shown that activation energies for the interfacial mass transfer of CO_2 at the grain surface are also consistent with literature results for the interfacial barrier in carbon molecular sieves.

In this thesis, the MD and GCMC simulations are also performed to validate the experimental results. The self-diffusions of CH_4 and CO_2 in the HRMC model of SiC-DC over a wide range of temperatures have been also investigated using EMD simulations. A comparison of experimental uptake-based data with simulation results reveals that CO_2 diffusivities obtained from EMD simulations are two orders of magnitude larger than the particle scale diffusion coefficients, while for CH_4 there is a remarkable agreement between simulation dynamics and the uptake-based diffusivities. From the difference between the activation energies obtained from the kinetic uptake measurements with those of MD simulations and QENS measurement, it is concluded that there are some internal barriers and structural constrictions which are not captured by MD simulation and QENS. The long range barriers for CO_2 are demonstrated to be responsible for the particle scale diffusivity of CO_2 being about two orders of magnitude smaller than that of CH_4. It is also shown that there is excellent agreement between GCMC simulation isotherm and experimental adsorption isotherms indicating that HRMC model is able to provide accurate predictions for CO_2 adsorption equilibrium over a wide range of temperatures up to atmospheric pressure. It is shown that isosteric heats of adsorption obtained from simulation are in good agreement with those obtained from fitting of the dual Langmuir–Henry equation to experimental isotherm data and are in the usual range of heats of adsorption for microporous carbons.

The effect of fluorine functionalisation on the microstructure of fluorinated SiC-DCs has been also investigated in this thesis using different characterization techniques. As seen in Chapter 5 of this thesis, the HRTEM/SAED images and Raman spectra show the highly amorphous nature of the virgin and fluorinated SiCDCs. The formation of C-F bonds in all fluorinated samples is seen in FTIR spectroscopy. Thermogravimetric analysis (TGA) experiments were also carried out, in order to evaluate the thermal stability of the fluorinated carbon. The TGA curves show that the higher levels of fluorination leads to more stable C-F bonds. It is shown that the fluorine doping of SiC-DC does not collapse its microstructure significantly. It is illustrated that increasing the level of fluorination narrows the range of the pore size distribution of the samples. It is shown that fluorination of the SiCDCs has little effect on the ultra-microporosity of the low fluorinated sample, while higher levels of fluorination decrease the ultra-microporosity of SiCDCs significantly. As discussed in Chapter 5, the decreases of pore volume, and surface area on fluorination is in agreement with simulation studies. Comparison of the experimental adsorption isotherms and kinetic uptake of CO_2 in fluorinated SiC-DC with virgin SiC-DC shows that fluorination causes slower CO_2 adsorption kinetics and reduces equilibrium uptake which is in agreement with simulation studies. It is shown that activation energy barriers for CO_2 diffusion and heats of adsorption obtained from fitting of the dual Langmuir–Henry equation to CO_2 experimental isotherm data decrease on fluorination.

Due to the significance of water adsorption, Chapter 6 of this thesis is devoted to the water vapor adsorption and the effect of fluorine doping of microporous SiC-DC on its hydrophobic/hydrophilic character. Different semi-empirical models were applied to the experimental water adsorption isotherms of the virgin and fluorine-doped SiCDCs to analyse the effect of fluorination on the adsorption mechanism. The surface chemistry of the virgin and fluorinated samples are characterized by X-ray photoelectron spectroscopy (XPS) and ^{19}F nuclear magnetic resonance (NMR) analysis techniques. The XPS and NMR analysis confirmed that different C-F bonds were created indicating that covalent C-F bonds decrease while C-F bonds with weakened covalence increase on fluorination. It is shown that the virgin and fluorine-doped SiCDCs present distinct surface chemistries in terms of the nature and quantity of the C-F bonds. It is illustrated that the water adsorbed amounts of fluorine-doped samples are larger than the virgin SiCDC, high level of fluorination decreases the hydrophobicity. It is also demonstrated that fluorine functionalisation blocks the carbon pores

for the nonpolar argon molecules while allowing H_2O molecules to grow into clusters in the internal volume of the micropores.

7.2 Recommendations

There are a number of potential works in pursuit of this thesis which could improve our understanding of the structural and adsorption properties (both equilibrium and kinetics) of microporous CDCs. The following topics are recommended for further investigations:

- This thesis mostly focuses on the pure gases due to the limited timeframe however adsorption and diffusion of gas mixtures such as CO_2/H_2O binary mixture on both virgin and fluorine-doped SiCDCs can provide more insight for the potential industrial application of CDCs. The diffusion mechanism of H_2O in the microporous SiCDCs also needs further investigation. The development of new model for the investigation of the H_2O adsorption kinetics might be necessary.
- In this thesis we have analysed the adsorption equilibrium and kinetics of CH_4, however the investigation of the adsorption and transport of larger molecules and other hydrocarbons is also recommended for the future studies. Investigating the effect of SiCDC structure and microporosity on the diffusion and activation energy barrier of these molecules and comparing it with the results reported in this thesis can provide more insight into the structural properties and the characteristics of CDCs.
- Experiments on adsortpion equilibrium and kinetics of hydrogen and deuterium in microporous CDCs at very low temperatures is also an interesting topic and recommended to analyse the selectivity for the deuterium over hydrogen in CDCs.
- The kinetics model can be also further improved by considering the effect of structural heterogeneity on transport including the effect of the distribution of diffusion coefficients and energy barriers.